Search for physics beyond the Standard Model in di-lepton final state with the ATLAS experiment

Inauguraldissertation
der Philosophisch-naturwissenschaftlichen Fakultät
der Universität Bern

vorgelegt von

Rimoldi Marco

von Italien

Leiter der Arbeit:

Prof. Dr. Antonio Ereditato

Prof. Dr. Michele Weber

Albert Einstein Center for Fundamental Physics
Laboratorium für Hochenergiephysik
Physikalisches Institut

Search for physics beyond the Standard Model in di-lepton final state with the ATLAS experiment

Inauguraldissertation
der Philosophisch-naturwissenschaftlichen Fakultät
der Universität Bern

vorgelegt von

Rimoldi Marco
von Italien

Leiter der Arbeit:
Prof. Dr. Antonio Ereditato
Prof. Dr. Michele Weber
Albert Einstein Center for Fundamental Physics
Laboratorium für Hochenergiephysik
Physikalisches Institut

Von der Philosophisch-naturwissenschaftlichen Fakultät angenommen.

Der Dekan
Prof. Dr. Gilberto Colangelo

Bern,20. July 2018

Abstract

The Large Hadron Collider and its experiments are the largest ongoing particle physics research project in the world. In this thesis I present a search accomplished with the LHC and the ATLAS detector to look for new physics beyond that described by the so-called Standard Model of particle and interactions. The data analysis reported here was performed on a sample corresponding to 36.1 fb^{-1} of integrated luminosity from LHC pp collision at $\sqrt{s} = 13$ TeV recorded by ATLAS. The study focuses on the final state events with two leptons (electrons or muons) of opposite electric charge. In the final event selection, the number of observed events potentially indicating the existence of new physics was found to be consistent with the Standard Model expectation. Limits for different types of models involving the existence of new particles from Dark Matter and Supersymmetry were set. The results on SUSY are interpreted taking into account only the lightest top squark ($\tilde{t}_1$) and the lightest neutralino ($\tilde{\chi}_1^0$). Furthermore, limits are also set on the production cross-section of colour-neutral mediators decaying into Dark Matter particles produced in association with top quark pairs. For a massless neutralino, top squark masses below 720 GeV are excluded at 95% Confidence Level. Neutralino masses below 300 GeV for $m(\tilde{t}_1) = 650$ GeV are excluded as well. Similar limits are also set on a possible phenomenological Minimal Supersymmetric Standard Model. Assuming Dark Matter models, limits are obtained both as a function of the mediator mass and of the Dark Matter particle mass. For 1 GeV Dark Matter mass particle, scalar mediator masses up to 50 GeV are excluded. Limits on the spin-independent Dark Matter–nucleon scattering cross-section are set to compare with past fixed target experiments. As a related experimental activity, I also investigated a new pixel silicon sensor technology for the upgrade of the ATLAS inner detector. Using this new technique, both the pixel sensor and the read-out chip are implemented in the same silicon bulk. Sensors of this technology were tested during a beam test at the H8 line at the CERN Super Proton Synchrotron measuring excellent performance and a high 99.6% efficiency also after irradiation.

Contents

Introduction

In the last century, high energy physics has made extraordinary steps toward the understanding of the nature of elementary particles and of their fundamental interactions. The Standard Model of particle and interactions provides a convincing description of the all known subatomic particles (fermions and quarks) and their quantum interactions (strong, weak and electromagnetic). Nevertheless, the Standard Model is incomplete, due to a number of open questions that are currently unanswered; neutrinos were supposed to be massless but a very small mass is needed to be introduced after the discovery of neutrino flavour oscillations. Another open issue is the observed imbalance of matter with respect to antimatter in the universe. No sufficient mechanism to explain this asymmetry is present. In addition, the Standard Model is not a Grand Unified Theory (GUT) i.e. a model in which at high energy the gauge interaction constants are merged into one. I would like to highlight in particular other two open questions: the first one is the large difference in energy between the electroweak energy scale ($\lambda_{EW} \approx 100$ GeV) and the scale of the GUT ($\lambda_{GUT} \approx 10^{16}$). This is called the hierarchy problem and it causes that the Standard Model cannot be extended up to the Planck scale without a precise tuning of its parameters in order to fit with the experimental observations. Secondly, in the Standard Model there is no suitable particle candidate for Dark Matter (DM) and even more an explanation of Dark Energy (DE). DM and DE contribute to the 26.8% and 68.3%, respectively, to the total mass-energy balance in the present-day universe. The accurate determination of these abundances comes from global fits of cosmological parameters while the nature of the DM remains largely unknown [1, 2].

The two latest presented open questions can be addressed at the Large Hadron Collider (LHC), the largest ongoing particle physics research project in the world, located at CERN[1] in Geneva. On February 2013, the first data taking period of the LHC, called Run 1, successfully ended whereby it was shut down for planned upgrades and improvements. At the beginning of my Ph.D. work in early 2015, the second data taking period (Run 2) of the LHC started. The centre mass energy was increased with respect to Run 1 from 8 TeV to 13 TeV allowing the experiments to push the discovery sensitivities for new particles beyond the Standard Model to higher value overcoming their limits set with previous studies. In this thesis, I analysed the *pp* collisions data collected during 2015 and 2016 by the ATLAS experiment corresponding to 36.1 fb^{-1} of integrated luminosity.

Many types of theory beyond the Standard Model are proposed which foresee DM particle candidates and resolve the hierarchy problem. One of the best motivated particle candidates for DM is a weakly interacting massive particle (WIMP) [3]. If this is the case, then it may be possible to produce these particles directly at the LHC. A recently proposed benchmark models for DM production assume the existence of a mediator particle which couples both the Standard Model particles and the DM particles. In this model, the DM particle is produced through the exchange of a spin-0 mediator, which can be either a colour-neutral scalar or pseudoscalar particle, denoted (ϕ/a) respectively. The couplings of the mediator to the Standard Model

[1] *Organisation européenne pour la recherche nucléaire*

fermions are severely restricted by precision flavour measurements. An ansatz that automatically relaxes these constraints is Minimal Flavour Violation [4]. The production of DM in association with top-quark is expected to be enhanced with respect to that of other Standard Model particles under the assumption of a Yukawa-type coupling between the mediator (ϕ/a) and the Standard Model particles. It follows that colour-neutral mediators would be considerably produced in association with heavy-flavour quarks. The presence of heavy quarks (top or bottom quarks) makes this model very interesting to address at the LHC.

A further remarkable UV-complete theory is Supersymmetry (SUSY) [5–10]. SUSY postulates the existence of new set of particles which are not yet observed. In particular, for each fermion (boson) of the SM, a Supersymmetric partner is foresee with spin differing by half an integer. If SUSY is realised in nature, it must be a broken symmetry to push the mass of the superpartners to higher values than their Standard Model counterparts. Differently from the Standard Model electroweak sector, the actual mechanism by which SUSY is broken is unknown and this is translated in 105 parameters which describe the low energy effect of the breaking mechanism. SUSY also predicts the matching of all the coupling constant of the fundamental force at an energy of about 10^{15} GeV. The introduction of these new particles allows the cancellations of the divergences without large fine-tuning, solving in this way the hierarchy problem. The largest contribution for this cancellation comes from the SUSY partner of the top quark: the top squark $\tilde{t}_1$. At the LHC, it is possible to search for the $\tilde{t}_1$ via its decay productions with the cross section production that depends on the assumed $\tilde{t}_1$ mass. In addition, if R-parity [11] is assumed to be conserved, the *"lightest supersymmetric particle"*, or LSP, can be an attractive non-baryonic dark matter candidate [12, 13]. The 105 MSSM parameters can be reduced to 19 taking into account several phenomenological constraints. This 19 parameters model is called the "phenomenological" Minimal Supersymmetric Standard Model or pMSSM.

The idea behind my research program is to select top-quark associated production of DM and SUSY particles decays involving final state signature with two leptons of opposite electric charge (electrons or muons) and large missing transverse energy. The requirement of the two leptons allows to reduce the contribution of Standard Model processes since it permits to have a clear signature in a detector.

By the end of Run 2 in late 2018, the LHC is expected to have delivered more than 150 fb^{-1} to the ATLAS and CMS experiments. During 2019 and 2020, the Long Shutdown 2 is planned during which the LHC centre of mass energy will be increased to 14 TeV, reaching the nominal LHC energy. During the following years, 2021–2023, the Run 3 will collect more than 300 fb^{-1}. At this point both the LHC and the detectors will require major upgrades in order to maintain their performance. The upgrade project of the LHC, called the High Luminosity-LHC (HL–LHC), is planned to be ready during late 2026 pushing the instantaneous luminosity up to $7.5 \cdot 10^{34}\,\text{cm}^{-2}\text{s}^{-1}$, with the goal to deliver more than 3000 fb^{-1} during 10 years of operation. During the LS3 period, which is scheduled between 2024 and mid 2026, major upgrades of the ATLAS detector are planned in order to be ready for the HL-LHC start. The upgrades are required to cope with increased particle multiplicity, the large pile-up and huge radiation doses. The main component of these upgrades, is a fully silicon based detector called Inner Tracker (ITk) that will replace the current ATLAS Inner Detector. The current design of ITk foresees a Pixel Detector in the inner part and a strip detector in the outer one. I decided to investigate a new approach towards a pixel silicon sensor for the outer layer of the ITk Pixel Detector: a "monolithic sensor" where the pixel sensor and the read-out chip are implemented in the same silicon bulk thus reducing the intrinsic electronic noise and power consumption. In addition, the absence of the bump bonding process make the production easier and with lower cost. I tested prototypes in a beam test at the H8 line at CERN Super Proton Synchrotron (SPS). I also developed an irradiation campaign at the Bern cyclotron aiming to test the performance and the radiation hardness of this sensor.

The thesis is organized in the following way: In Chapter 1, the theoretical aspects of the Standard Model are presented with also the details of Supersymmetry theory. A more general model concerning the direct production of DM at the LHC is also described.
Chapter 2 describes the Large Hadron Collider and the ATLAS detector. The general features of the event reconstruction in the ATLAS environment and their performance are also presented.
Chapter 3 presents the search for new physics beyond the Standard Model in the final state with two leptons (electrons and muons).
Chapter 4 presents the HL-HLC project and in particular the new Inner Tracker (ITk) of the ATLAS Detector. Beam test results for a monolithic CMOS pixel sensor are presented. In Chapter 5, is reported a sensitivity prospect for top squark pair production in compress mass spectra in the High Luminosity LHC scenario. In Chapter 6 presents the conclusions of this thesis .

Chapter 1

The Standard Model and beyond

The Standard Model (SM) of particle physics is an elegant and concise theory of elementary particles and their interactions [14–17]. It's based on the existence of local gauge symmetries that explain the interactions between fermions (quarks and leptons) through to the force-mediating fields to which correspond to vector bosons. The non-abelian gauge field of the SM is invariant under the symmetry group

$$SU(2)_L \otimes U(1)_Y \otimes SU(3)_C \tag{1.1}$$

where L,Y and C are the weak isospin, the hypercharge and the colour charge. The formalism of the Standard Model can be summarised using

$$\mathcal{L} = -\frac{1}{4}F^a_{\mu\nu}F^{a\mu\nu} \tag{1.2}$$

$$+ i\bar{\psi}_i \not{D}\psi_i + \text{h.c.} \tag{1.3}$$

$$+ i\bar{\psi}_i y_{ij}\psi_y\phi + \text{h.c.} \tag{1.4}$$

$$+ |D_\mu\phi|^2 - V(\phi) \tag{1.5}$$

Equation 1.2 is the kinetic terms for the gauge sector. The index a runs over all the component of the electroweak and strong gauge fields. Equation 1.3 describes the interaction between fermion, matter fields ψ, and bosons, gauge fields which are contained in the covariant derivative term. Equation 1.4 is the Yukawa sector and incorporates the interaction between the matter fields and the Higgs field, ϕ, which are thought to be responsible for giving fermions their mass when SSB in the electroweak sector occurs. The fourth descibes the Higgs sector itself with the kinetic term and the SM Higgs potential $V(\phi) = -\mu^2|\phi|^2 + \lambda|\phi|^4$. The prediction capabilities of the above Lagrangian are experimentally verified to an incredible degree by a lot of experiments and across a wide range of energy scales. Figure 1.1 shows the cross section measurements for various SM process obtained by the ATLAS experiment during proton-proton collision. The consistency between the SM theory prediction (grey box) and the experimental measurement at different center mass energies $\sqrt{s} = 7, 8, 13\,\text{TeV}$ (blue, orange and purple respectively) is a remarkable achievements for the modern particle physics.

After the recent discovery of the Higgs Boson in 2012 [18, 19], the SM add another important piece to the comprehension of the nature. Despite being a very successful theory which makes detailed, precise and quantitative predictions (Figure 1.1), the SM is not without its limitations, it is however the starting point for the comprehension of the backgrounds in the search for new physics. Supersymmetry (SUSY) is one of the most compelling extensions of the SM that can solve some of the its limitations.

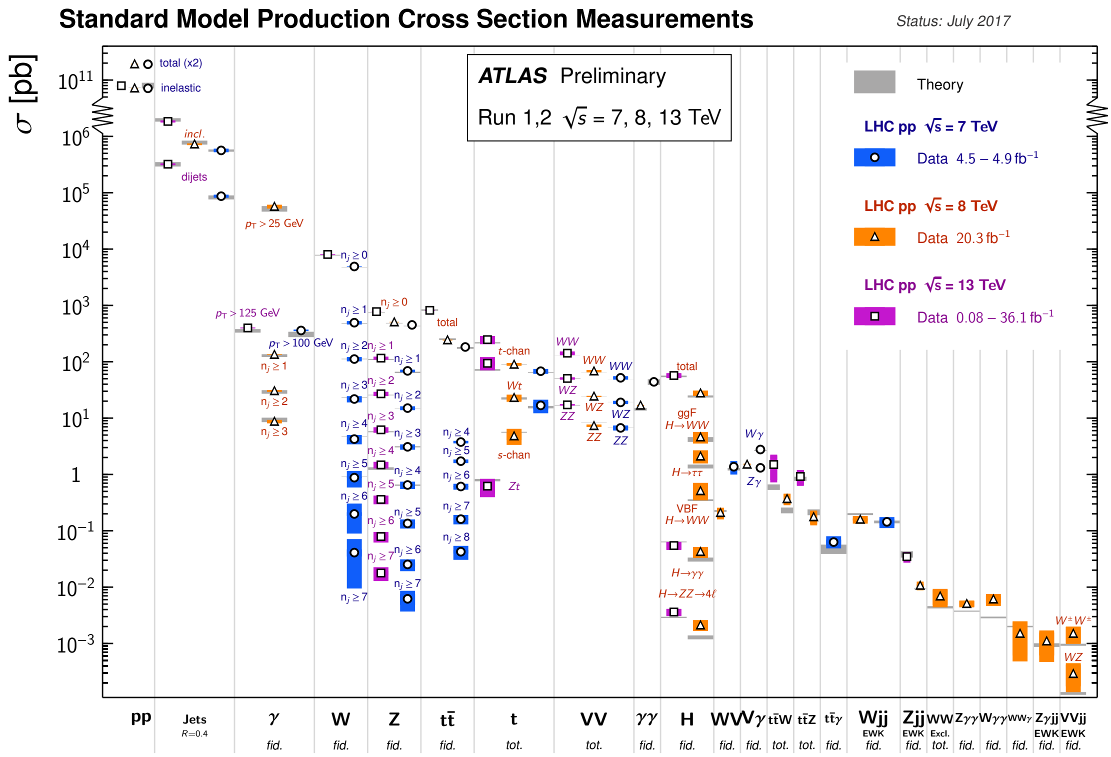

FIGURE 1.1: Summary of several Standard Model total and fiducial production cross section measurements, compared to the corresponding theoretical expectations at $\sqrt{s} = 7, 8, 13$ TeV center mass energy. Taken from [20].

The main elementary constituents of matter are point-like spin-$\frac{1}{2}$ particles called *fermions*. They are governed by Fermi-Dirac statistics and obey to the Pauli exclusion principle. The interaction between the fermions are controlled by *bosons* which are the mediators of the fundamental forces. The bosons are integer spin particles and follow the Bose-Einstein statistics.

1.1 Fermions

The fermionic sector of the SM can be divided into *quarks*, of which the proton and neutron are composed of, and *leptons*, such as the electron and the corresponding neutrino. Each of the two families can be naturally organised into three generations of increasing mass. Each generation is composed of two doublets, one for fermions and the other for quarks. All of the stable matter is made up by quarks of the first generation (*up* and *down*), electrons and neutrinos. The second and third generations of fermions are unstable particles and decay into lighter particles.

In the leptonic sector, each doublet is composed of an electrically charged particle (l) and the corresponding neutrino (ν_l). A leptonic number can be assigned to each of the particles: $+1$ for leptons and -1 for anti-leptons. As lepton number violating processes are not observed in nature, it is conserved in the SM. In Table 1.1 the three lepton generations are presented with their mass and electric charge.

[1] The mass of the neutrino depends on the mass hierarchy. The flavour eigenstates (ν_e,ν_μ,ν_τ) don't correspond directly to the mass eigenstate (ν_1,ν_2,ν_3).

Generation	Lepton	Symbol	Mass	Electric charge [e]
1^{st}	Electron	e	0.511 MeV	-1
	Electron-neutrino	ν_e	< 2 eV [1]	0
2^{nd}	Muon	μ	105.7 MeV	-1
	Muon-neutrino	ν_μ	< 0.19 eV[1]	0
3^{rd}	Tau	τ	1776.8 MeV	-1
	Tau-neutrino	ν_τ	< 18.2 eV[1]	0

Table 1.1: Leptons in the SM. Particle masses. Taken from [21].

Quarks, too, fall into three generations of increasing mass (Table 1.2). In this case the quarks carry fractional electric charges and the doublets are formed by an *up-type* quark with $+2/3$ electric charge and by a *down-type* with $-1/3$ electric charge.

Generation	Quark	Symbol	Mass	Electric charge [e]
1^{st}	Up	u	$2.3^{+0.7}_{-0.5}$MeV	$+2/3$
	Down	d	$4.8^{+0.7}_{-0.3}$ MeV	$-1/3$
2^{nd}	Charm	c	95 ± 5 MeV	$+2/3$
	Strange	s	1.275 ± 0.025 GeV	$-1/3$
3^{rd}	Top	t	173.1 ± 0.6 GeV	$+2/3$
	Bottom	b	4.18 ± 0.03 GeV	$-1/3$

Table 1.2: Quarks in the SM. Particle masses. Taken from [21].

In the SM, quarks carry also another conserved quantum number called *colour*. Each quark comes with three different colours (red (R), green (G) and blue (B)) and this triples the number of the quarks present in nature. Experimental results suggest that all naturally occurring particles are colour singlets and that no colourful states can be produced. This characteristic is called colour-confinement and is the reason why quarks have not been observed as free particles. Quarks can be found in colourless bound states called *hadrons*. The simplest hadron is a *meson* and it is a combination of a quark and an anti-quark of the same colour ($q\bar{q}$). Examples of mesons are the pion $\pi^+(u\bar{d})$ with mass of 139.5 MeV or the $J/\psi(c\bar{c})$ with mass of 3.096 GeV. *Baryons* are bound states of three different coloured quarks or anti-quarks (qqq or $\bar{q}\bar{q}\bar{q}$). Protons (uud) and neutrons (udd) are examples of baryons.

1.2 Bosons

Three fundamental forces are described in the SM: electromagnetic (EM), weak and strong (Table 1.3). Each of the forces has a corresponding associated bosons. They can interact between each other and they mediate the interactions between fermions. The forces have very different strengths which are determined by the coupling constant and can span several orders of magnitude.

The photon is a massless, electrically neutral, spin 1 boson that mediates the electromagnetic interactions. Photons only couple to electrically charged particles. Both quarks and charged

Interaction	Boson		Mass [GeV]	Electric charge [e]	Colour charge
Eletromagnetic	photon	γ	0	0	
Weak	W bosons	$W^{\pm}$	80.385 ± 0.015	± 1	
	Z boson	Z^0	91.1876 ± 0.0021	0	
Strong	gluons ($\times 8$)	g	0	0	R,G,B

TABLE 1.3: Stardard Model bosons properties. Taken from [21]

leptons ($e^{\pm}$, $\mu^{\pm}$, $\tau^{\pm}$) can interact electromagnetically. Quantum electrodynamics (QED) describes this interaction in a $U(1)$ gauge theory. The conserved quantity is the electric charge. The distance range of the EM interaction is infinite and the force decreases proportionally to $1/r^2$.

The weak force is best known for its role in nuclear decay ($n \to p\, e^-\, \bar{\nu}_e$) and in the neutral current interaction of the neutrino $e^- \nu_e \to e^- \nu_e$. The weak charged current interaction is carried by the $W^{\pm}$ bosons, with mass equal to 80.4 GeV. It is responsible for the transition between up-type and down-type quarks and between charged leptons and the corresponding neutrinos. The Z^0 boson, with mass of 91.2 GeV, is responsible for the neutral weak current. The range of the weak interaction is related to the masses of the heavy weak bosons and therefore is very short (10^{-16} m).

In 1968, Sheldon Glashow, Abdus Salam and Steven Weinberg unified the electromagnetic and the weak interaction by showing them to be two aspects of a single force, now termed as the Electroweak force. Mathematically, the symmetry group of the electroweak interaction is $SU(2)_L \otimes U(1)_Y$ where L and Y are the weak isospin and the hypercharge respectively. The corresponding gauge bosons are the three W bosons of weak isospin from SU(2) (W_1, W_2, and W_3), and the B^0 boson of weak hypercharge from U(1), respectively, all of which in the theory are massless. The physical bosons massive states $\gamma, W^{\pm}, Z^0$ are a linear combination of the W_i and B_0 fields.

$$W^{\pm} = \frac{(W^1 \mp W^2)}{\sqrt{2}}, \qquad \begin{pmatrix} Z^0 \\ \gamma \end{pmatrix} = \begin{pmatrix} \cos\theta_W & -\sin\theta_W \\ \sin\theta_W & \cos\theta_W \end{pmatrix} \begin{pmatrix} W^3 \\ B^0 \end{pmatrix} \tag{1.6}$$

with the Weinberg angle θ_W defined by:

$$\sin\theta_W = \frac{e}{g_2} \qquad m_Z = \frac{m_W}{\cos\theta_W} \tag{1.7}$$

e is the electric charge and it is the coupling of the electromagnetic interaction and g_2 is the gauge coupling constant for $SU(2)_L$.

With electroweak symmetry breaking, a scalar Higgs boson is added and it gives mass to the $W^{\pm}$ and Z^0 via the Brout-Englert-Higgs mechanism [22–24] without breaking the underlying symmetry. The last particle of the SM is the recently discovered Higgs boson which is the manifestation of the Spontaneous Symmetry Breaking (SSB) in the electro-weak sector, delivering mass to other W and Z bosons. In the SM, the Higgs field couples to fermions through a Yukawa interaction coupling strength which is proportional to the mass of the fermions.

The discovery of the Higgs boson has been independently confirmed by ATLAS [25] and CMS [26] experiments at CERN in July 2013. Since then, the ATLAS and CMS collaborations started the characterisation of this new boson particle. The precise measurement of the Higgs mass (Fig 1.2) and, in particular, of the coupling to SM particles (Fig 1.3) is very important as a sign for new physics beyond the SM. ATLAS and CMS have published a combined measurement of the Higgs boson mass [27], using LHC Run 1 data focusing on $H \to \gamma\gamma$ and $H \to ZZ \to 4\ell$ channels , where Run 1 indicates the LHC proton-proton (pp) data taking period in 2011 and 2012 at centre-of-mass energies $\sqrt{s} = 7$ and 8 TeV. The result of the combination gives a Higgs mass measurement of $m_H = 125.09 \pm 0.21\,(stat) \pm 0.11\,(syst)$ GeV. The individual mass measurement analysis can be seen in Fig 1.2.

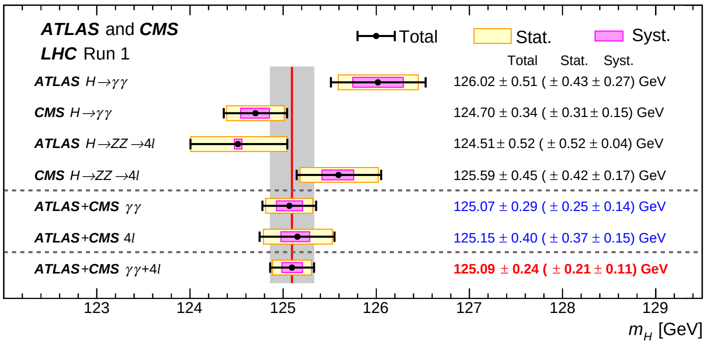

FIGURE 1.2: Summary of Higgs boson mass measurements from the individual analyses of ATLAS and CMS. The systematic (narrower, magenta-shaded bands), statistical (wider, yellow-shaded bands), and total (black error bars) uncertainties are indicated. The (red) vertical line and corresponding (gray) shaded column indicate the central value and the total uncertainty of the combined measurement, respectively. Taken from [27]

The strong interaction is an attractive force between quarks and is responsible for the binding quarks to form hadrons and mesons. The mediators of the strong interaction are eight massless, electrically neutral, spin 1 bosons called *gluons*. They couple to the colour charge and mediate the interaction between quarks. Gluons have colours and can interact directly with each other. Strong interactions are described by the Quantum-Chromo-Dynamics (QCD) theory. An important property of QCD is that the gauge coupling is dependent upon the momentum transfer of a process Q^2:

$$g^2(Q^2) = \frac{4\pi}{\beta_0 \ln\left(\frac{Q^2}{\Lambda^2_{\text{QCD}}}\right)} \qquad \alpha_s = \frac{g^2}{4\pi} \tag{1.8}$$

Equation 1.8 leads to two important consideration:

- `Asymptotic freedom` shows that in the limit of high energy, $Q^2 \to \infty$, the strong coupling tends to 0. It is in this regime that QCD calculations can be computed perturbatively (pQCD) and quarks and gluons can be treated as quasi-free particles.
- `Confinement:` In the other direction $Q^2 \to \Lambda^2_{\text{QCD}}$ the strong coupling constant tends to ∞. The consequence of this, is that in nature only singlet state of colour are observed, as at low energies coloured states hadronise. This implies that in a particles detector bare quarks and gluons are observed as a flow of hadrons knowns as jet.

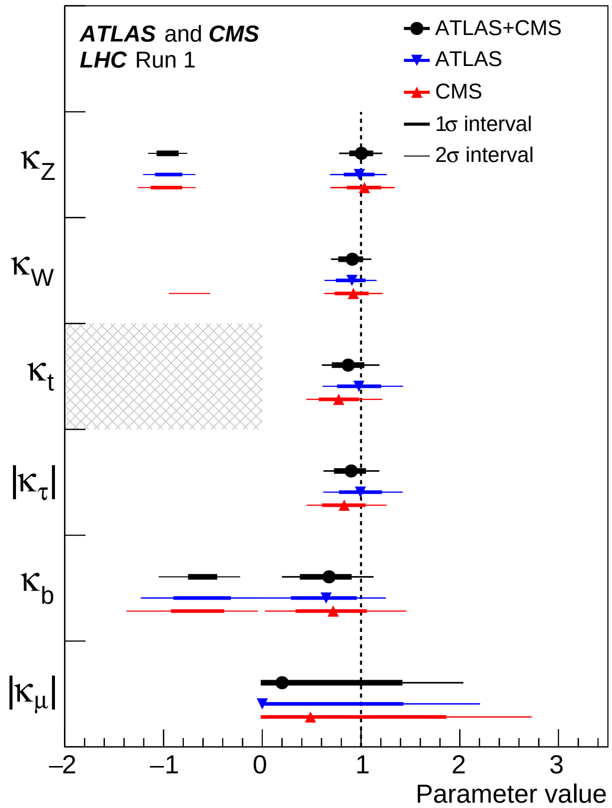

FIGURE 1.3: Best fit values of the signal strengths for the combination of ATLAS and CMS data, and separately for each experiment, for the parameterisation assuming the absence of BSM particles in the loops, $B_{BSM} = 0$. The hatched area indicates the non-allowed region for the parameter that is assumed to be positive without loss of generality. The error bars indicate the 1σ (thick lines) and 2σ (thin lines) intervals. When a parameter is constrained and reaches a boundary, namely $|k_\mu| = 0$, the uncertainty is not defined beyond this boundary. For those parameters with no sensitivity to the sign, only the absolute values are shown. [28]

1.3 Open questions in the Standard Model

The Standard Model is believed to be only a low-energy realisation of a more general theory. If fact, if we consider higher energies up the Grand Unified Theory (GUT) ($\lambda_{GUT} \approx 10^{16}$ GeV) or at the Planck scale ($\lambda_{Planck} \approx 10^{19}$ GeV), number of conceptual problems start to appear.

A first problem comes from the very large difference in energy between the electroweak energy scale ($\lambda_{EW} \approx 100$ GeV) and the scale of the GUT ($\lambda_{GUT} \approx 10^{16}$). This is called the hierarchy problem and it causes that the Standard Model cannot be extended up to the Planck scale without a precise tuning of its parameters in order to fit with the experimental observations. Each particle that couples to the Higgs field has a Yukawa coupling Λ_f that enter in the definition of the interaction term in the Lagrangian: $\mathcal{L}_{Yukawa} = -\Lambda_f \bar{\psi} H \psi$. Furthermore, the mass of a fermion is proportional to its Yukawa coupling and this implies that the most massive particles are coupled more to the Higgs boson. Then, the most significant corrections to the Higgs mass will originate from the heaviest particles, most prominently the top quark. The correction to m_H^2 from a loop containing a Dirac fermion is given by:

$$\Delta m_H^2 \simeq \frac{|\lambda_f|^2}{16\pi^2} \left[-2\Lambda^2 - 6m_f^2 \ln\left(\frac{\Lambda}{m_f}\right) + ... \right] \tag{1.9}$$

Where λ_f is the Yukawa coupling of a fermion f and Λ^2 is the ultraviolet cut-off used to regulate the loop integral. Hence, nothing prevents the Higgs boson mass from diverging quadratically in Λ. In the assumption that the SM is valid up to the GUT (or Planck) energy scale and in order to obtain the experimentally measured value of the Higgs Boson mass a 16 digit fine tuning of these enormous correction is needed.

This large correction is in disagreement with the concept of *naturalness*. A quantitative definition of the naturalness of a particle physics theory can be given with respect to the amount of fine-tuning needed to achieve the electroweak symmetry breaking at the observed energy scale, represented by the Z boson mass [29,30].

Another important missing piece in the SM is a candidate for Dark Matter (DM). Proof of the existence of DM arises from gravitational evidence across a wide range of astrophysical and cosmological observations [1,2,31,32]. All of the known SM particles are excluded. Of the many types of DM candidate proposed, weakly interacting massive particle (WIMP) is motivated to be a theoretically convincing candidate [3].

Futhermore, the SM also does not provide any indication into the nature of Dark Energy (DE). DE is a term that refers to the accelerating expansion of the universe. This phenomena was discovered in 1988 [33, 34] and in the context of a homogeneous and isotropic universe, this implied that a repulsive force, identified with DE, causes the Universe to expand in an accelerated rate.

Moreover gravity is not included in any quantum field theory in the SM.

In the current form of the SM, the neutrinos are massless, but it is now known that neutrinos have non-zero mass since neutrino flavour oscillations have been thoroughly confirmed. The implication of the neutrino oscillation is that neutrinos have both flavour and mass eigenstates. The flavour of the neutrino is free to oscillate with a rotation matrix called Pontecorvo-Maki-Nakagawa-Sakata (PMNS) matrix [21]. The discovery of neutrino oscillations showing that neutrinos have mass led to the Nobel Price to Takaaki Kajita and Arthur B. McDonald in 2015 [35]. The masses of the neutrinos have not yet been experimentally quantified, but only the relative magnitude of the masses has been measured [21].

Another important open question is the matter-antimatter asymmetry, that is, the imbalance of matter respect to antimatter in the universe. The SM predicts that matter and antimatter should have been created in equal amounts, however there is a negligible remaining amount of antimatter in the visible universe. Yet, no mechanism sufficient to explain this asymmetry exists in the Standard Model.

Some of these shortcomings could be remedied by the existence of new particles at the TeV scale, which motivates extensive searches for physics Beyond the Standard Model (BSM) at the Large Hadron Collider (LHC).

1.4 Supersymmetry: A Natural extension of the Standard Model

In the last decades many attractive extensions of the SM have been developed. One of the most compelling of such theories is Supersymmetry (SUSY) [5–10].

SUSY is a space-time symmetry which for each SM particle postulates the existence of a partner particle whose spin differs by one-half unit (superpartner). The introduction of a symmetry of this form is not arbitrary. In fact the Coleman-Mandula theorem [36] states the impossibility of combining space-time and internal symmetries in any but a trivial way. The theorem postulates that the only non-trivial mix of Poincaré and internal symmetry is the product of the two (*Poincaré* $\times$ *Internal*). Thankfully this theorem was written considering only bosonic internal symmetries namely it deals only with transformations that transform bosons into bosons and fermions into fermions and are therefore generated by operators that satisfy commutation relations. When considering a fermionic operator, the Coleman-Mandula theorem no longer prevents the inclusion of this symmetry. The operator Q that generates such transformation must be an anti-commuting spinor with:

$$Q\,|\text{Boson}\rangle = |\text{Fermion}\rangle\,, \qquad Q\,|\text{Fermion}\rangle = |\text{Boson}\rangle \tag{1.10}$$

The new symmetry introduces a group orthogonal to the SM implying that the SM quantum number of a particle will not change when that particle undergoes a SUSY transformation. The superpartners have identical mass and quantum numbers but differ due to their spin. The SM particles and their superpartners can be organised in two types of supermultiplet, chiral multiplets or gauge multiplets. The SM fermions are one component of a chiral multiplet, with the other one being their scalar superpartner. The naming convention for the superpartner in a chiral multiplet is to add the pre-fix "s" for scalar. For example the *stop* is the superpartner of the top quark. The SM boson and the relevent spin-$\frac{1}{2}$ are included in a gauge multiplet. The naming convention add the suffix "ino" to the SM boson name. *Gluino* (*Photino*) is the superpartner of the gluon (photon). The scalar Higgs boson is represented in a chiral multiplet. Actually, it turns out that one chiral multiplet is not enough for two reasons: first, is that if there were only one chiral supermultiplet, the electroweak gauge symmetry would suffer a gauge anomaly, secondly in a supersymmetric theory up-type quark can receive mass only from a $Y = 1/2$ Higgs while down-type quarks receive mass from $Y = -1/2$ Higgs, therefore two different Higgs are necessaries. These are noted as (H_u^+, H_u^0) for the up-type and (H_d^0, H_d^-) for the down-type.

The introduction of scalar superpartners for each SM fermions allow to solve the *"hierarchy problem"* (Section 1.3). The correction at one-loop to the Higgs mass for a scalar particle is given by:

$$\Delta m_H^2 \simeq \frac{g_s}{16\pi^2}\left[2\Lambda^2 - 4m_s^2 \ln\left(\frac{\Lambda}{m_s}\right) + ...\right] \tag{1.11}$$

For every particle loop of particles there is a corresponding sparticles loop which provide a correction with the opposite sign. If the sparticle masses were the same as the SM, the cancellation would be exact. If supersymmetry were an exact symmetry of nature, sparticles would have been already discovered. Therefore, if supersymmetry exists, it is a broken symmetry and the mass scale of the SUSY particles is not known *a priori*. Nevertheless, there are theoretical arguments that favour a relatively low mass scale of O(1 TeV)

In this thesis we will refer to the Minimal Supersymmetric extension of the Standard Model i.e. the *MSSM*. It is called minimal since it introduces the minimal number of new particles necessary to build a supersymmetric theory. It is based on few basic assumptions.

1. The symmetry can be written as $SU(3)_C \otimes SU(2)_L \otimes U(1)_Y \otimes SUSY$.
2. Three generations of spin-1/2 quarks and leptons as in the SM with no right-handed neutrino. The left and the right-handed chiral fields belong to chiral supermultiplets together with their spin-0 SUSY partners (squark and sleptons). Two chiral multiplet for the Higgs sector (H_u^+, H_u^0) and (H_d^0, H_d^-) and their spin 1/2 superpartners, the *higgsinos*. The higgsinos will mix with bino and winos to give the mass eigenstates (4 neutralinos and 2 charginos).
3. The introduction of gauge-invariant and renormalizable interactions into SUSY models can violate the conservation of baryon number (B) and lepton number (L), resulting in a proton lifetime shorter than current experimental limits [37]. This is solved by assuming that R-parity [11], defined as $R = (-1)^{3(B-L)+2S}$, is conserved. B and L are respectively the baryon and the lepton number, and S the spin. An important phenomenological consequences of this quantum number conservation are:
   - All sparticles can only be produced in pairs.
   - The lightest sparticle with $P_R = -1$, called the *"lightest supersymmetric particle"* or LSP, is stable. If the LSP is electrically neutral, it interacts only weakly with ordinary matter, and so, in cosmology, can be an attractive non-baryonic dark matter candidate [12, 13].
   - Each sparticle other than the LSP must eventually decay into a state that contains an odd number of LSPs (usually just one).

In the *MSSM*, the superpartners listed in Table 1.4 and 1.5 are the gauge eigenstates.

Names		spin 0	spin 1/2	$SU(3)_C$, $SU(2)_L$, $U(1)_Y$
squarks, quarks	Q	$(\tilde{u}_L \;\; \tilde{d}_L)$	$(u_L \;\; d_L)$	$(\mathbf{3},\, \mathbf{2},\, \frac{1}{6})$
(×3 families)	$\bar{u}$	$\tilde{u}_R^*$	$u_R^\dagger$	$(\overline{\mathbf{3}},\, \mathbf{1},\, -\frac{2}{3})$
	$\bar{d}$	$\tilde{d}_R^*$	$d_R^\dagger$	$(\overline{\mathbf{3}},\, \mathbf{1},\, \frac{1}{3})$
sleptons, leptons	L	$(\tilde{\nu} \;\; \tilde{e}_L)$	$(\nu \;\; e_L)$	$(\mathbf{1},\, \mathbf{2},\, -\frac{1}{2})$
(×3 families)	$\bar{e}$	$\tilde{e}_R^*$	$e_R^\dagger$	$(\mathbf{1},\, \mathbf{1},\, 1)$
Higgs, higgsinos	H_u	$(H_u^+ \;\; H_u^0)$	$(\tilde{H}_u^+ \;\; \tilde{H}_u^0)$	$(\mathbf{1},\, \mathbf{2},\, +\frac{1}{2})$
	H_d	$(H_d^0 \;\; H_d^-)$	$(\tilde{H}_d^0 \;\; \tilde{H}_d^-)$	$(\mathbf{1},\, \mathbf{2},\, -\frac{1}{2})$

TABLE 1.4: Chiral supermultiplets in the Minimal Supersymmetric Standard Model (*MSSM*). The spin-0 fields are complex scalars, and the spin-1/2 fields are left-handed two-component Weyl fermions.

Taking into account all the new particles introduced in the *MSSM*, additional 105 parameters (masses, phases and mixing angles) need to be introduced. This abundance of free parameters make any phenomenological analysis a daunting task. Several phenomenological constraints allow for the justification of some assumptions and the 105 *MSSM* parameters can be reduced

Names	spin 1/2	spin 1	$SU(3)_C$, $SU(2)_L$, $U(1)_Y$
gluino, gluon	$\tilde{g}$	g	(**8**, **1** , 0)
winos, W bosons	$\tilde{W}^{\pm}$ $\tilde{W}^0$	$W^{\pm}$ W^0	(**1**, **3** , 0)
bino, B boson	$\tilde{B}^0$	B^0	(**1**, **1** , 0)

Table 1.5: Gauge supermultiplets in the Minimal Supersymmetric Standard Model.

to 19. This 19-parameter model is called the "phenomenological"*MSSM* or *pMSSM* [38, 39] and is justified by the following assumptions:

- **No new source of CP violation.**
  The experimental limits on the electron and neutron electric moments constrain the new sources of CP violation. Assuming that all the phases in the soft SUSY breaking potential are zero eliminates all the new sources of CP-violation and leads to a drastic reduction of the number of parameters.
- **No FCNC.**
  The matrices for the sfermion masses and for the trilinear couplings are all diagonal, implying the absence of FCNC (flavour-changing neutral current) processes at the tree-level.

The 19 parameters are:

$\tan\beta$: the ratio of the vev the two Higgs doublet fields ($\tan\beta = v_u/v_d$) with ($0 < \beta < \pi$ 2).

M_A : The mass of the pseudoscalar Higgs Boson.

μ : The higgs higgsino mass parameter.

M_1, M_2, M_3 : bino, wino, gluino mass parameters.

$M_{\tilde{q}}, M_{\tilde{u}_R}, M_{\tilde{d}_R}, M_{\tilde{l}}, M_{\tilde{e}_R}$: first and second generation sfermion masses.

$M_{\tilde{Q}}, M_{\tilde{t}_R}, M_{\tilde{b}_R}, M_{\tilde{L}}, M_{\tilde{\tau}_R}$: third generation sfermion masses.

A_t, A_b, A_τ third generation trilinear gauge coupling.

The $M^2_{H_u}, M^2_{H_d}$ and B are fixed through electroweak symmetry breaking conditions and M_A. This type of model has much more predictability and is much easier to discuss phenomenologically.

1.5 Mass Eigenstate of SUSY particles

After taking into account the electroweak SSB and the supersymmetry breaking effects, particles with the same quantum numbers will in general mix. The resulting masses and mixing are presented next.

Higgs Sector

The Higgs fields in the *MSSM*, as already mentioned in Section 1.4, consist of two complex $SU(2)_L$ doublets with 8 real, scalar degrees of freedom. After SSB, three of the degree of freedom become the longitudinal modes of the Z and W. The remaining five Higgs scalar mass eigenstates consist of two neutral scalars h^0 and H^0, one pseudoscalar neutral A^0 and two charged scalars $H^{\pm}$, with masses given by;

$$m^2_{A^0} = 2|\mu|^2 + m^2_{H_u} + m^2_{H_d} \tag{1.12}$$

$$m^2_{h^0,H^0} = \frac{1}{2}\left(m^2_{A^0} + m^2_Z \mp \sqrt{(m^2_{A^0} - m^2_Z)^2 + 4m^2_Z m^2_{A^0}\sin^2(2\beta)}\right) \tag{1.13}$$

$$m^2_{H^{\pm}} = m^2_{A^0} + m^2_W \tag{1.14}$$

The Higgs scalar sector is also related to the mass of the Z by:

$$m_Z = 2\frac{m^2_{H_d} - m^2_{H_d}\tan^2\beta}{\tan^2\beta - 1} - 2\mu^2 \tag{1.15}$$

Charginos

The chargino mass eigenstates $\left[\tilde{\chi}^{\pm}_1, \tilde{\chi}^{\pm}_2\right]$ depend on the parameters M_2, μ and $\tan\beta$. They are obtained diagonalising a 2×2 complex mass matrix:

$$\begin{bmatrix} M_2 & \sqrt{2}M_W \sin\beta \\ \sqrt{2}M_W \cos\beta & \mu \end{bmatrix} \tag{1.16}$$

This leads to the two chargino masses:

$$\begin{aligned} m_{\tilde{\chi}^+_{1,2}} =& \frac{1}{\sqrt{2}}\Big[M_2^2 + \mu^2 + 2M_W^2 \\ & \mp \{(M_2^2 - \mu^2)^2 + 4M_W^4\cos^2 2\beta + 4M_W^2(M_2^2 + \mu^2 + 2M_2\mu\sin 2\beta)\}^{1/2}\Big]^{1/2} \end{aligned} \tag{1.17}$$

In the limit of $\mu >> M_2, M_Z$ the mass of the two charginos reduces to:

$$\begin{aligned} m_{\tilde{\chi}^{\pm}_1} &\simeq M_2 - \frac{M_W^2}{\mu^2}(M_2 + \mu\sin 2\beta) \\ m_{\tilde{\chi}^{\pm}_2} &\simeq |\mu| - \frac{M_W^2}{\mu^2}\epsilon_\mu(M_2\sin 2\beta + \mu) \end{aligned} \tag{1.18}$$

For $\mu \to \infty$, the lightest chargino corresponds to a pure Wino state with $m_{\tilde{\chi}^{\pm}_1} \simeq M_2$ and the heavier chargino corresponds to a pure Higgsino state with $m_{\tilde{\chi}^{\pm}_2} \simeq |\mu|$.

Neutralinos

The neutralino mass eigenstates $\left[\tilde{\chi}^0_1, \tilde{\chi}^0_2, \tilde{\chi}^0_3, \tilde{\chi}^0_4\right]$ are obtained by diagonalising a 4×4 complex mass matrix considering the gauge eigenstate basis $\left[\tilde{B}, \tilde{W}, \tilde{H}^0_d, \tilde{H}^0_u\right]$. The matrix depends on $M_1, M_2, \tan\beta, \mu$:

$$\begin{bmatrix} M_1 & 0 & -M_Z\cos\beta\sin\theta_W & M_Z\sin\beta\sin\theta_W \\ 0 & M_2 & M_Z\cos\beta\cos\theta_W & -M_Z\sin\beta\cos\theta_W \\ -M_Z\cos\beta\sin\theta_W & M_Z\cos\beta\cos\theta_W & 0 & -\mu \\ M_Z\sin\beta\sin\theta_W & -M_Z\sin\beta\cos\theta_W & -\mu & 0 \end{bmatrix} \tag{1.19}$$

In the limit of large value of $|\mu|$ the mass of the neutralino can be simplified to:

$$m_{\tilde{\chi}_1^0} = M_1 - \frac{M_Z^2}{\mu^2}\,(M_1 + \mu \sin 2\beta) \sin^2\theta_W \tag{1.20}$$

$$m_{\tilde{\chi}_2^0} = M_2 - \frac{M_Z^2}{\mu^2}\,(M_2 + \mu \sin 2\beta) \cos^2\theta_W \tag{1.21}$$

$$m_{\tilde{\chi}_3^0} = |\mu| + \frac{1}{2}\frac{M_Z^2}{\mu^2}\epsilon\,(1 - \sin 2\beta)\left(\mu + M_2\sin^2\theta_W + M_1\cos^2\theta_W\right) \tag{1.22}$$

$$m_{\tilde{\chi}_4^0} = |\mu| + \frac{1}{2}\frac{M_Z^2}{\mu^2}\epsilon\,(1 + \sin 2\beta)\left(\mu - M_2\sin^2\theta_W - M_1\cos^2\theta_W\right) \tag{1.23}$$

In general the parameter μ, M_1 and M_2 are completely arbitrary. However if one consider the GUT (Grand Unification Theories), M_1 and M_2 are equal at large scale $M_1(\Lambda_{GUT}) = M_2(\Lambda_{GUT})$ while at the Z mass (m_Z) scale the relation is:

$$M_1(m_Z) \simeq \frac{1}{2}M_2(m_Z) \tag{1.24}$$

In the limit $|\mu| \to \infty$, the first two neutralino are pure gaugino states with masses of $m_{\tilde{\chi}_1^0} \simeq M_1$ and $m_{\tilde{\chi}_2^0} \simeq M_2$, while the two others neutralino are pure higgsino states, with masses $m_{\tilde{\chi}_3^0} \simeq m_{\tilde{\chi}_4^0} \simeq |\mu|$.

Squarks

In the most general case, the squark can be obtained by diagonalising two 6×6 squark mass squared matrices, one for the up-type and one for the down-type. If we ignore intergenerational mixing, that can cause severe problems due to large loop contributions to FCNC process, the two 6×6 matrices can be decomposed into a series of 2×2 matrices, each of which describes squarks of a specific flavour. In particular for the third generation squarks, the squared mass matrix can be approximately written as:

$$\begin{bmatrix} M^2_{\tilde{t}_\mathrm{L},\tilde{b}_\mathrm{L}} + m^2_{t,b} & m_t(A_{t,b} - \mu r_{t,b}) \\ m_{t,b}(A_{t,b} - \mu r_{t,b}) & M^2_{\tilde{t}_\mathrm{R},\tilde{b}_\mathrm{R}} + m^2_{t,b} \end{bmatrix} \tag{1.25}$$

where $M_{\tilde{t}_\mathrm{L}}, M_{\tilde{b}_\mathrm{L}}, M_{\tilde{t}_\mathrm{R}}, M_{\tilde{b}_\mathrm{R}}$ are the sfermion masses. Due to the large contribution of m_t, mixing is particularly strong in the stop sector. This generates a large splitting between the two stop mass eigenstates ($\tilde{t}_1$,$\tilde{t}_2$), justifying the possibility of a light stop.

Gluinos

Excluded from this mixing argument are the gluinos which are colour octet fermions and therefore do not have the appropriate quantum number to mix with any other particle. The gluino mass parameter M_3 is related to the bino (M_1) and wino(M_2) mass parameters by:

$$M_3 = \frac{\alpha_s}{\alpha}\sin^2\theta_W M_2 = \frac{3}{5}\frac{\alpha_s}{\alpha}\cos^2\theta_W M_1 \tag{1.26}$$

This equation implies a rough prediction $M_3 : M_2 : M_1 \approx 6 : 2 : 1$. It is therefore reasonably to suspect that the gluino is considerably heavier than the lighter neutralinos and charginos.

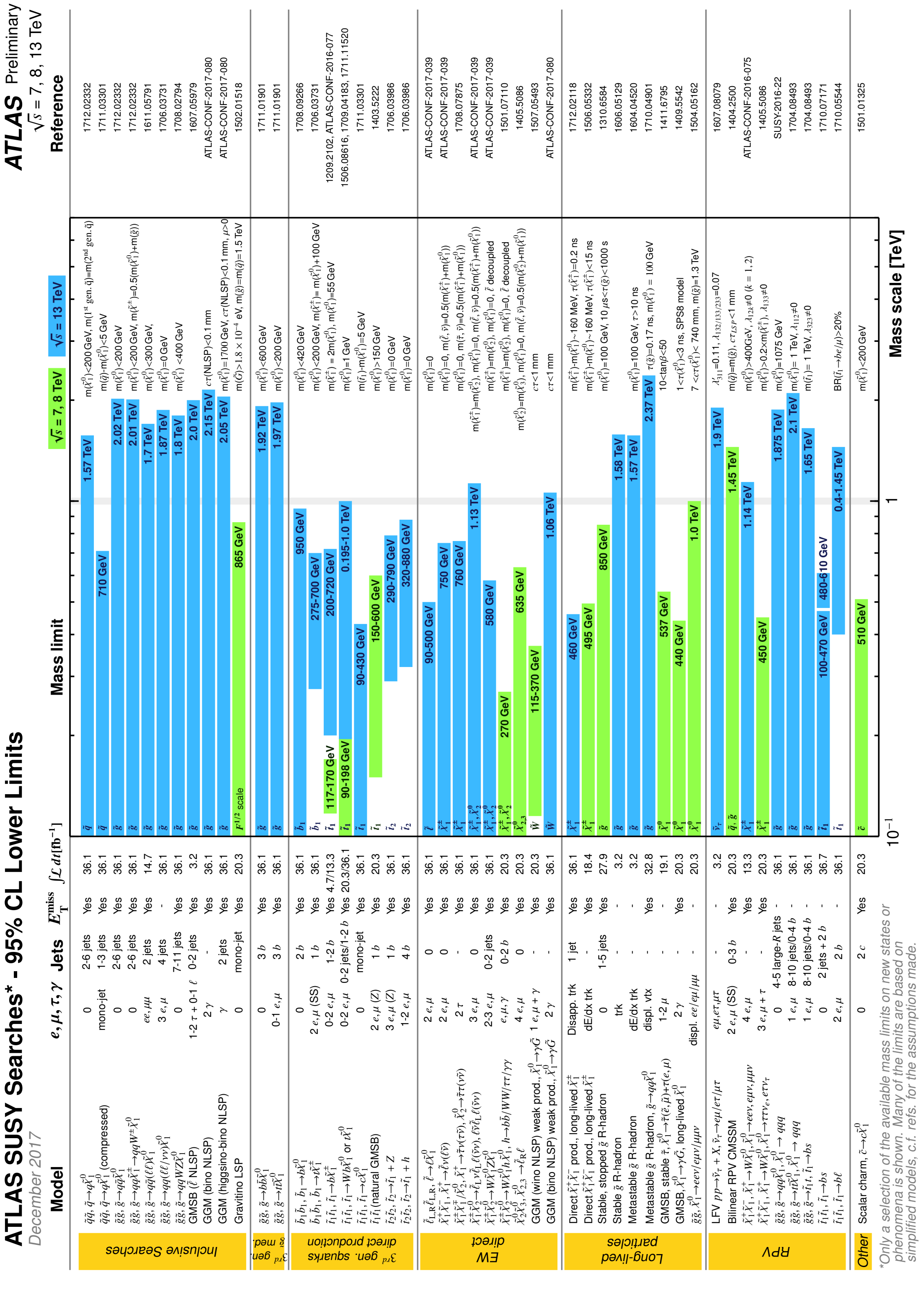

FIGURE 1.4: Mass reach of ATLAS searches for Supersymmetry. Only a representative selection of the available results is shown.

1.6 Top squark phenomenology

The third generation squarks have an important role in the loop corrections of the Higgs mass solving the hierarchy problem, therefore it is important to study these particles. $\tilde{t}_1$ and $\tilde{b}_1$ are expected to be the lightest of the squarks and, if so their production would be abundant at the LHC.

Top squark production:

At the LHC the top squark $\tilde{t}_1$ can be produced by two mechanisms:

1. Via **Gluino decay** ($q\bar{q} \rightarrow \tilde{g}\tilde{g}$ and $\tilde{g} \rightarrow \tilde{t}_1\tilde{t}_1$): This production mechanism happens if the gluino is heavier enough to decay into a $\tilde{t}_1$ $\tilde{t}_1$ pair but light enough to be produced at a significant rate.

2. **Direct production** ($q\bar{q} \rightarrow \tilde{t}_1\tilde{t}_1$)**:** If the gluinos are just a few TeV heavier than the top squark, the production cross section is too small, only direct production is left.

The direct production's diagrams can be obtained substituting in the $t\bar{t}$ ones the respective supersymmetric partners. The cross section of this process (Figure 1.5) is calculated at the next-to-leading order (NLO), including the resummation of soft-gluon emission calculated at NLO + next-to-leading Log order (NLL) [40–45].

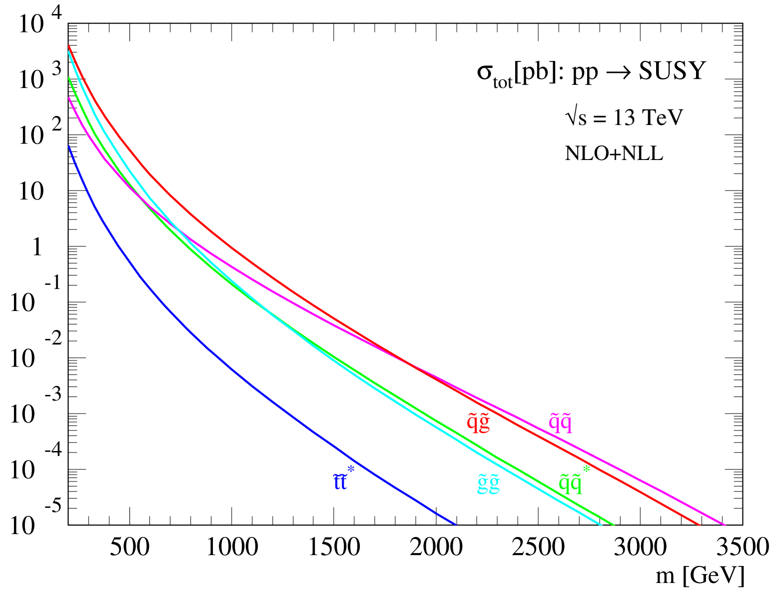

FIGURE 1.5: NLO+NLL production cross sections for the case of equal degenerate squark and gluino masses as a function of mass at $\sqrt{s} = 13$ TeV [45].

Top squark decay modes

In this work, results will be presented in either simplified models [46–48], in which the masses of all sparticles are set to high values except for the few sparticles involved in the decay chain of interest, or models based on the pMSSM, in which all of the 19 parameters are set to fixed values, except for two which are scanned. This set of models was chosen to give a broad coverage of the possible stop decay patterns and phenomenology that can be realised in the MSSM, in order to best demonstrate the sensitivity of the search for direct stop production. The simplified models used are designed with a goal of covering distinct phenomenologically different regions of pMSSM parameter space. Three different models are considered, where each signal scenario is defined by the nature of the lightest supersymmetric particle (LSP) and the next-to-lightest (NLSP) supersymmetric particle.

The Pure bino LSP

This is a simplified model where the only light sparticles are the top squark ($\tilde{t}_1$) and the lightest neutralino ($\tilde{\chi}_1^0$) as NLSP. The top quarks decay in the lightest neutralino with the 100% BR. A schematic representation of the parameter space ($m_{\tilde{t}_1}, m_{\tilde{\chi}_1^0}$) is given in Figure 1.6 with the three different decay modes available.

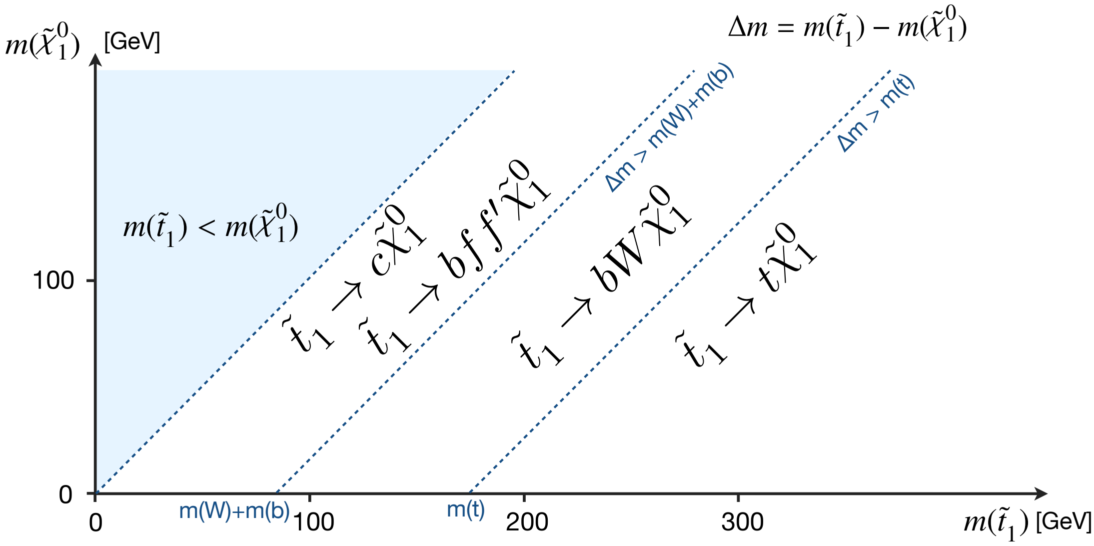

FIGURE 1.6: Schematic representation of all possible decays of the top squark. The dashed line indicate the kinematic boundaries for the various decay channels. The region $m(\tilde{t}_1) < m(\tilde{\chi}_1^0)$ is kinematically forbidden.

- **Two Body Decay**
  The decays $\tilde{t}_1 \to t\tilde{\chi}_1^0$ and $\tilde{t}_1 \to b\tilde{\chi}_1^\pm$ (Figure 1.7(a) and 1.7(b) respectively) where t and b represent either the quark or the anti-quark, depending on the charge conjugation, dominate when they are kinematically accessible, ie, when the mass difference between the $\tilde{t}_1$ and the $\tilde{\chi}_1^0$ is larger that the top mass ($\Delta m(\tilde{t}_1, \tilde{\chi}_1^0) > m_t$). The final state consists of multi jets including b-jets, leptons and $E_{\mathrm{T}}^{\mathrm{miss}}$. Since the lightest chargino is generally heavier than the lightest neutralino, the lightest chargino can decay further throught $\tilde{\chi}_1^0$ and W boson via $\tilde{\chi}_1^\pm \to \tilde{\chi}_1^0 ff'$ where f and f' are any SM fermions. The branching ratio to fermion flavour depends on the corresponding scalar fermion masses.
  If the above two body decay and the three-body decay modes shown below are all kinematically suppressed the top squark can decay via $\tilde{t}_1 \to c\tilde{\chi}_1^0$ if $\Delta m(\tilde{t}_1, \tilde{\chi}_1^0) > m_c$ through a loop diagram. This topology is possible in a limited parameter space.

- **Three Body Decay**
  For intermediate mass differences the top quark is produced off-shell ($m_{\tilde{\chi}_1^0} + m_W + m_b < m_{\tilde{t}} < m_{\tilde{\chi}_1^0} + m_t$) and the three-body decay $\tilde{t}_1 \to bW\tilde{\chi}_1^0$ is possible (Figure 1.7(c)). This process can be dominant when the two-body decay modes are kinematically forbidden.

- **Four Body Decay**
  For smaller mass differences, both the W and the top quark are off-shell. The four-body decay channel $\tilde{t}_1 \to bff'\tilde{\chi}_1^0$, where f and f' are two fermions from the W^* decay (real

or virtual), is assumed to occur. In this search, f and f' are a lepton and its associated neutrino.

Previous ATLAS [49, 50] and CMS [51–63] analyses have set exclusion limits at 95% confidence level (CL) on the signal scenarios considered here. When considering simplified models including the $\tilde{t}_1 \to t\tilde{\chi}_1^0$ decay, top squark masses up to about 850 GeV have been excluded for a nearly massless lightest neutralino (Figure 1.8).

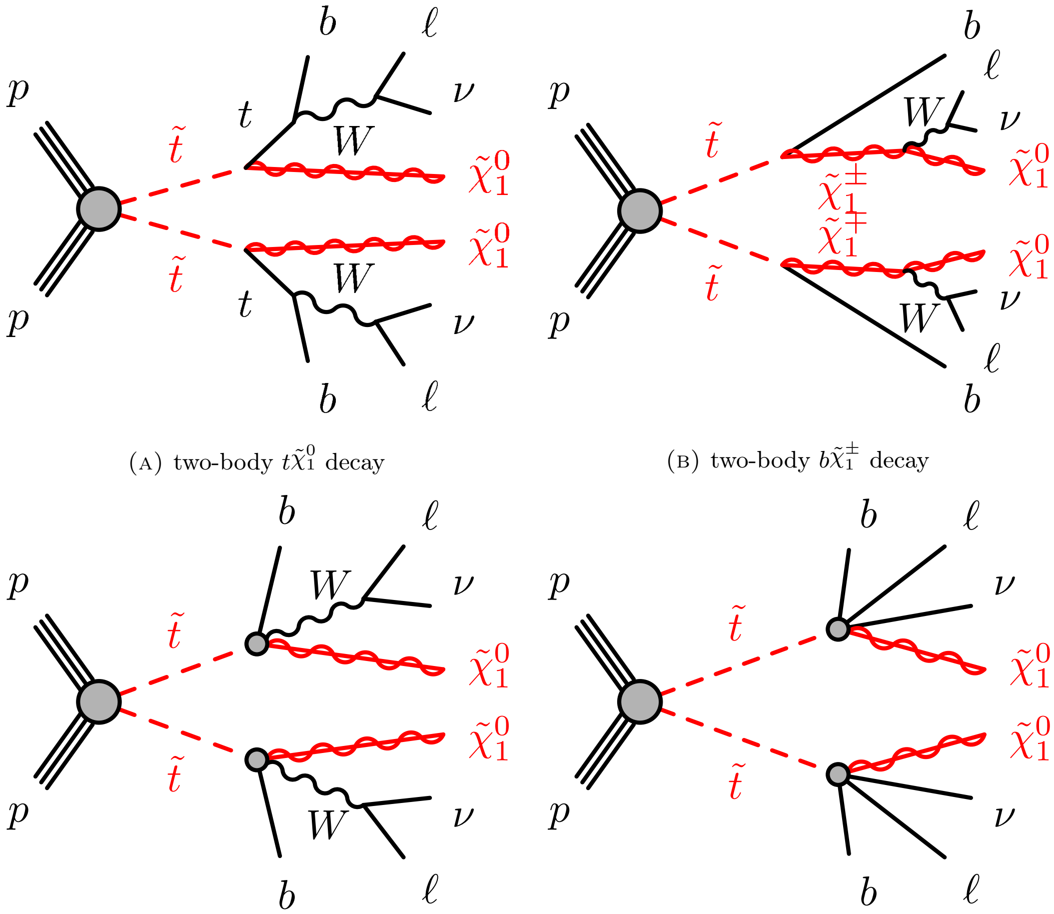

(A) two-body $t\tilde{\chi}_1^0$ decay

(B) two-body $b\tilde{\chi}_1^{\pm}$ decay

(C) three-body $bW\tilde{\chi}_1^0$ decay

(D) four-body $b\ell\nu\tilde{\chi}_1^0$ decay

FIGURE 1.7: Diagrams representing the four main signals targeted by the analyses: (A) the two-body decay into an on-shell top quark and the lightest neutralino ($\tilde{t}_1 \to t\tilde{\chi}_1^0$), (B) the decay of the top squark via the lightest chargino ($\tilde{t}_1 \to b\tilde{\chi}_1^{\pm}$) (C) the three-body decay mode into an on-shell W boson, a b-quark and the lightest neutralino ($\tilde{t}_1 \to bW\tilde{\chi}_1^0$) and (D) the four-body decay mode ($\tilde{t}_1 \to bff'\tilde{\chi}_1^0$) where the two fermions f and f' are a lepton with its neutrino in this article.

Pure b-$\tilde{\chi}_1^{\pm}$ model

The lightest chargino ($\tilde{\chi}_1^{\pm}$) is added between the top squarks and the neutralino (Figure 1.7(b)). The decay mode $\tilde{t}_1 \to b + \tilde{\chi}_1^{\pm}$ with $\tilde{\chi}_1^{\pm} \to W(*) + \tilde{\chi}_1^0$ is assumed with 100% BR. The kinematics of this decay depend upon the masses of the mass of the $\tilde{t}_1$,$\tilde{\chi}_1^{\pm}$ and $\tilde{\chi}_1^0$ and their respective mixings and different hypothesis has been used: fixed $\tilde{\chi}_1^{\pm}$ mass (106 GeV, 150 GeV), $m(\tilde{\chi}_1^{\pm}) \sim 2 \times m(\tilde{\chi}_1^0)$, fixed $\Delta m(\tilde{t}_1, \tilde{\chi}_1^{\pm}) = 10$ GeV, or fixed $\Delta m(\tilde{\chi}_1^{\pm}, \tilde{\chi}_1^0) = 5$ GeV. The respective exclusion limits are presented in Figure 1.9.

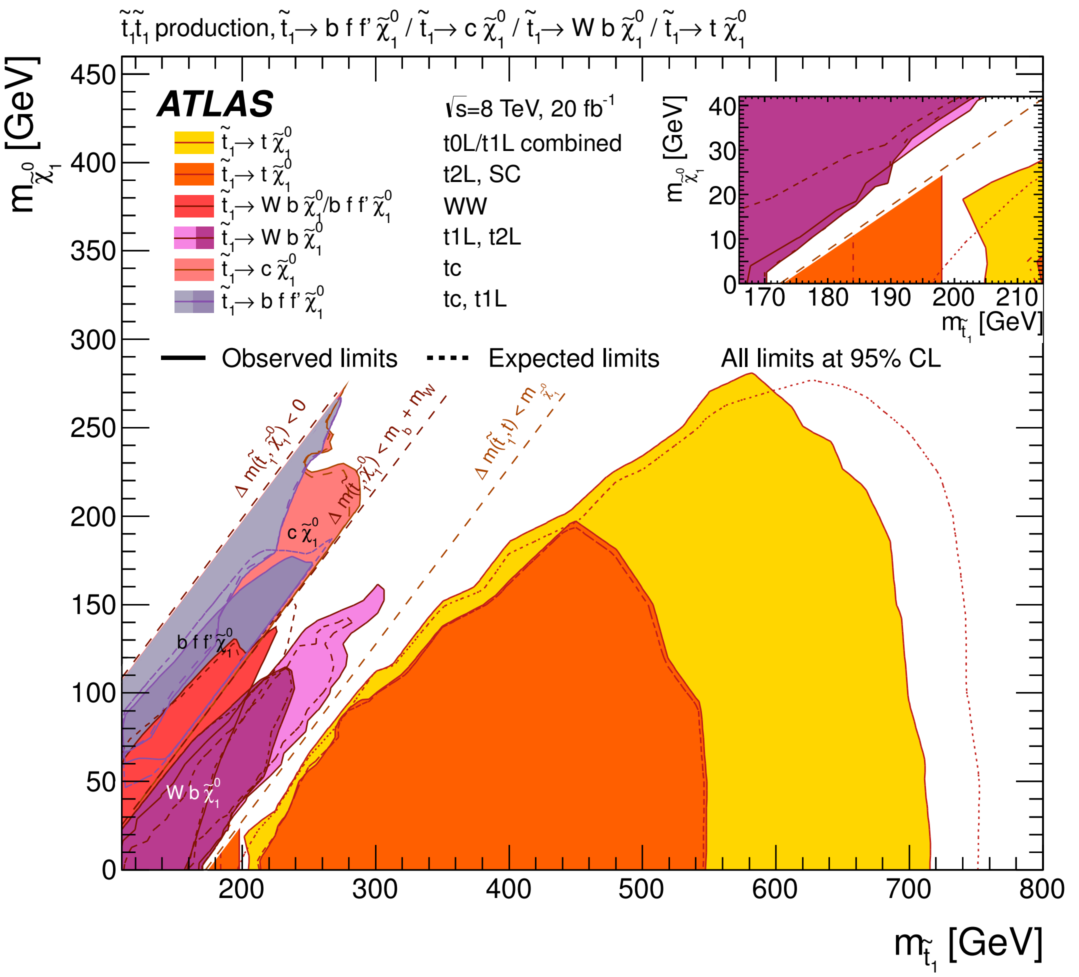

FIGURE 1.8: Summary of the dedicated ATLAS searches for top squark (stop) pair production based on 20 fb-1 of pp collision data taken at $\sqrt{s} = 8$ TeV. Exclusion limits at 95% CL are shown in the $\tilde{t}_1$-$\tilde{\chi}_1^0$ mass plane. The dashed and solid lines show the expected and observed limits, respectively, including all uncertainties except the theoretical signal cross section uncertainty (PDF and scale). Four decay modes are considered separately with 100% BR: $\tilde{t}_1 \to t+\tilde{\chi}_1^0$ (where the $\tilde{t}_1$ is mostly right), $\tilde{t}_1 \to W + b + \tilde{\chi}_1^0$ (3-body decay for $m(\tilde{t}_1) < m(top) + m(\tilde{\chi}_1^0)$), $\tilde{t}_1 \to c + \tilde{\chi}_1^0$ and $\tilde{t}_1 \to f + f' + b + \tilde{\chi}_1^0$ (4-body decay). The latter two decay modes are superimposed. The region $\tilde{t}_1$ mass below 100 GeV has not been considered for the 4-body decay. This plot is taken from [64]

A phenomenological MSSM (pMSSM) model: Wino NLSP.
This model assumes that: the $\tilde{t}_1$ is composed mainly by $\tilde{t}_L$; the chargino $\tilde{\chi}_1^{\pm}$ is wino-like and is mass degenerate with the neutralino $\tilde{\chi}_2^0$; the lightest neutralino $\tilde{\chi}_1^0$ is bino-like and is the LSP (see Equation 1.18 and 1.20) with $M_2 = 2 \times M_1$ and $m_{\tilde{t}_1} > M_1$. This model was constructed by performing a two-dimensional scan of the pMSSM parameters M_1 (Bino mass) and $M_{\tilde{Q}L3}$ [65]. The gluino mass $M_3 = 2.2$ TeV and $M_S = \sqrt{m_{\tilde{t}_1} m_{\tilde{t}_2}} = 1.2$ TeV are fixed in order to evade the current gluino and stop mass limits.

The mixing parameter between the superpartners of the left-handed and right-handed state are set to $X_t/M_S = \sqrt{6}$, where $X_t = A_t - \mu \tan\beta$ and A_t is the trilinear coupling parameter in the top-squark sector. The value of $\tan\beta$ is fixed to 20. All the other pMSSM masses are set greater than 3 TeV.

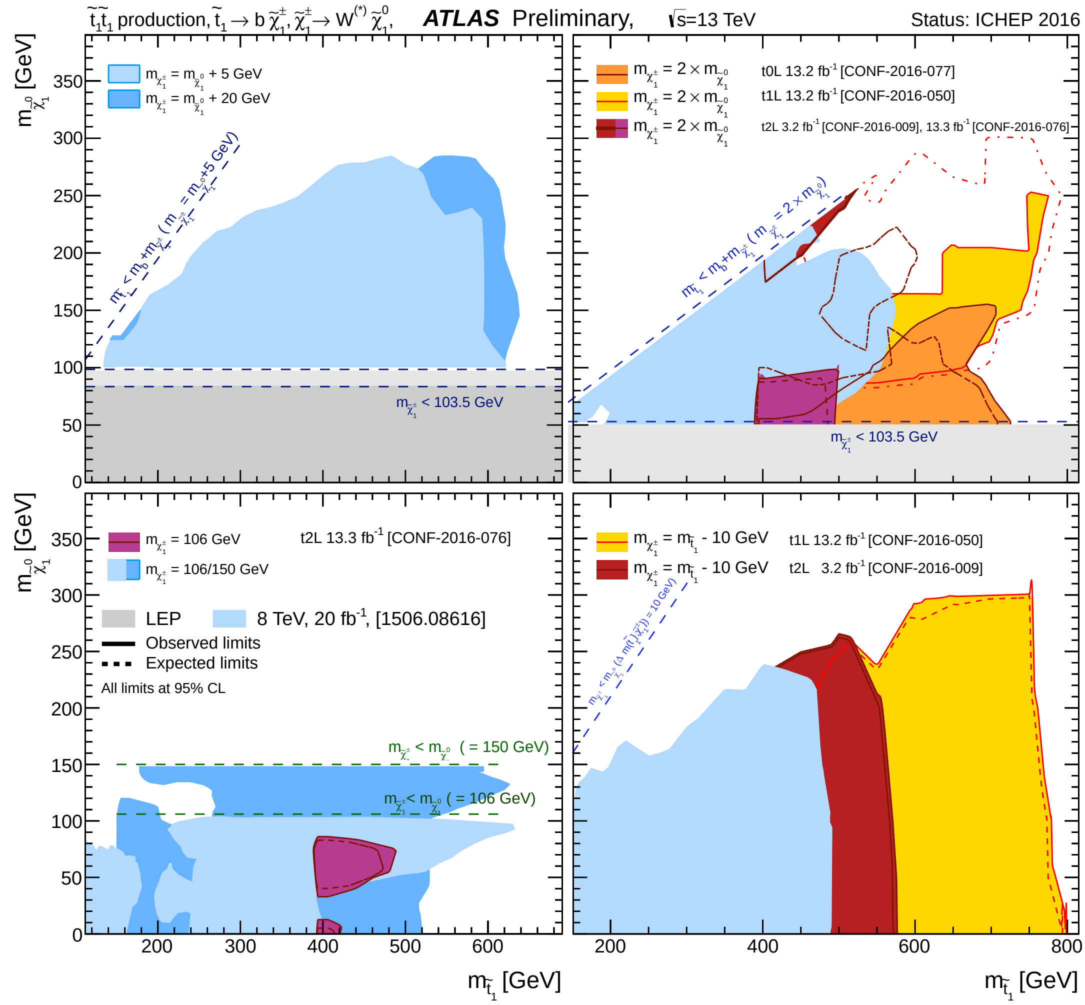

FIGURE 1.9: Summary of the dedicated ATLAS searches for top squark (stop) pair production based on $13 fb^{-1}$ of pp collision data taken at $\sqrt{s} = 13$ TeV. Exclusion limits at 95% CL are shown in the $\tilde{t}$ -$\tilde{\chi}_1^0$ mass plane.

In this model additional decay modes for the $\tilde{t}_1$ are available: (A) $\tilde{t}_1 \to t\tilde{\chi}_1^0$, (B) $\tilde{t}_1 \to b\tilde{\chi}_1^\pm$ with $\tilde{\chi}_1^\pm \to W\tilde{\chi}_1^0$ and (C) $\tilde{t}_1 \to t\tilde{\chi}_2^0$, with $\tilde{\chi}_2^0 \to h/Z\tilde{\chi}_1^0$. In a large fraction of the phase space, the stop decays prevalently via $b\tilde{\chi}_1^\pm$ and $t\tilde{\chi}_2^0$ $(BR(\tilde{t}_1 \to b\tilde{\chi}_1^\pm) \sim 66\%, BR(\tilde{t}_1 \to t\tilde{\chi}_2^0) \sim 33\%)$. . Since the coupling of $\tilde{t}_\mathrm{L}$ to the wino states is larger than the one to the bino state, the stop decay into the bino state $(\tilde{t}_1 \to t\tilde{\chi}_1^0)$ is suppressed. The BR can be significantly different in the regions of phase space where one of the decays is kinematically inaccessible. In the case that $\Delta m(\tilde{t}_1, \tilde{\chi}_2^0) < m_{top}$ the decay $\tilde{t}_1 \to t\tilde{\chi}_2^0$ is suppressed while the $\tilde{t}_1 \to b\tilde{\chi}_1^\pm$ decay is enhanced. Similarly the $\tilde{t}_1 \to b\tilde{\chi}_1^\pm$ decay is suppressed near the boundary of $m_{\tilde{t}_1} = m_b + m_{\tilde{\chi}_1^\pm}$ while the $\tilde{t}_1 \to t\tilde{\chi}_1^0$ is enhanced.

The branching fraction of decay of the $\tilde{\chi}_2^0 \to h/Z\tilde{\chi}_1^0$ depends on the sign of μ as shown in Figure 1.10. The $\tilde{\chi}_2^0$ decays into the lightest Higgs boson and the LSP $(BR(\tilde{\chi}_2^0 \to h\tilde{\chi}_1^0) \sim 95\%)$ if $\mu > 0$ and decays into a Z and the LSP $(BR(\tilde{\chi}_2^0 \to Z\tilde{\chi}_1^0) \sim 75\%)$ if $\mu < 0$. The two scenarios were considered separately in the analysis presented in Chapter 3.

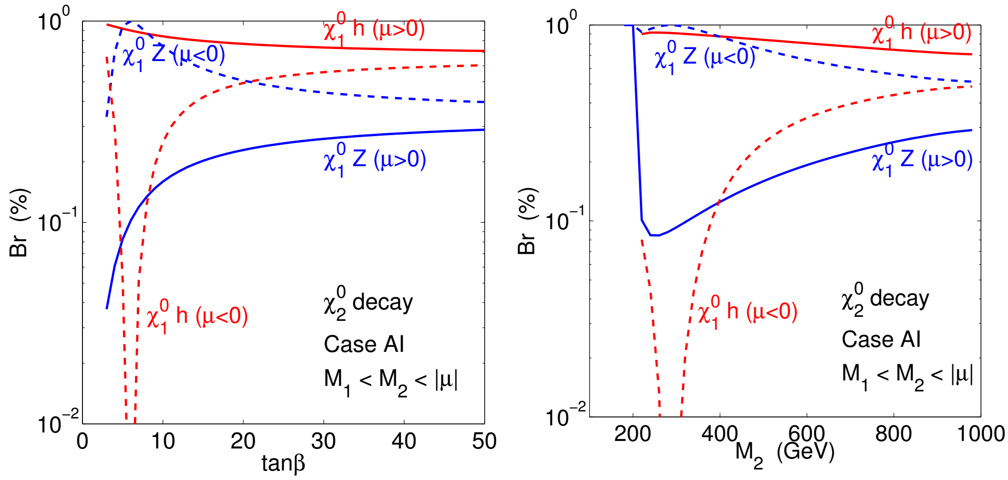

FIGURE 1.10: Wino-like NLSPs and Bino-like LSP: Decay branching fractions of $\tilde{\chi}_2^0$ (a) versus M_2 for $\tan\beta = 10$, and (b) versus $\tan\beta$ for $M_2 = 500$ GeV. Two-body on-shell inclusive decays are labelled by $\tilde{\chi}_1^0 Z$ and $\tilde{\chi}_1^0 h$. Solid lines are for $\mu > 0$ and dashed lines are for $\mu < 0$. Other parameters are set as $M_1 = 100$ GeV, $|\mu| = 1$ TeV [66].

1.7 Dark Matter

The understanding of dark matter (DM) is one of the priorities in modern physics and the investigation of its nature is fundamental for science. As previously mentioned, proof of the existence of DM arises from gravitational evidence across a wide range of astrophysical and cosmological systems [1, 2]. This area of research is subject to an intense effort based on a wide range of complementary experimental techniques and approaches. Direct DM detection experiments rely on the scattering of DM particles from the halo of the Milky Way in a detector on Earth via nucleon scattering ($\chi+N \to \chi+N$). Indirect DM detection experiments investigate the annihilation and decay of DM through the observation of photons, charged cosmic rays and neutrinos coming from our Galaxy and throughout the cosmos, ($\chi+\chi \to SM+SM$) where SM represents any Standard Model particles. Of the many types of DM candidate proposed, weakly interacting massive particles (WIMPs) [3] are among the most compelling from a theoretical perspective, assuming they are consistent with the expected DM density. If WIMPs are the manifestation in nature of DM, then it may be possible to produce them directly at the LHC ($pp \to \chi+\chi+X$). Since the DM will be observed as missing transverse momentum, an additional object (a jet, a photon or a gauge boson) must be used to define the search strategy.

When looking for DM, the experimental reach can be casted in terms of specific models of DM which are UV-complete. These models usually have a number of additional new particles with more significant interactions with the SM than the DM itself. The canonical example of this sort is the R-parity conserving SUSY model which provide the neutralino $\tilde{\chi}_1^0$ as a natural WIMP candidate for DM. Despite the advantage of UV-complete models, interpreting results in this way has some drawbacks: the results may be difficult to be re-casted to new available models. Focusing on this specific high-energy models, the risk is to overlook other experimentally interesting channels and to tune the experimental selection criteria reducing the sensitivity to other types of dark matter. A more general approach to introduce DM candidates in a theoretical framework is based on Effective Field Theories (EFT). The EFT approach assumes contact term interactions between dark matter and SM particles with the particle(s) connecting the two sectors integrated out of the low-energy spectrum. In this case, the missing energy distribution of the signal is determined by the nature and the mass of the Dark Matter particles and the Lorentz structure of the interaction. Only the overall production rate is a free parameter to be constrained or measured. EFTs are valid only if the interaction energy between the SM and DM particles is much lower than the collision energy, but they have the advantage to probe DM-SM couplings in a model-independent way.

1.8 Dark Matter plus Heavy Flavour phenomenology

The set of models considered in Chapter 3 are based on a bottom-up approach which embeds either SUSY or EFT characteristics. Often referred to as *simplified models*, these allow the study of different possible signatures focusing on the final state kinematics.

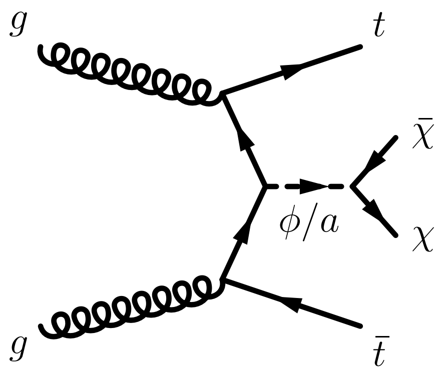

FIGURE 1.11: Representative diagrams at the lowest order for colour-neutral spin-0 mediator associated production with top quarks

Thanks to the reduced set of parameters, simplified models provide a very effective mapping of the phenomenological space accessible to experimentation and to define the set of signatures with the highest potential for discovery. In this type of DM search, a mediator-based approach is considered: the DM candidate is a fermionic particle produced via the decay of a spin-0 mediator. The mediator is responsible to the connection between the DM sector with the SM. The considered mediator is a spin-0 particle which can be either a colour-neutral scalar or pseudoscalar particle (ϕ and a respectively). The couplings of the mediator to the SM fermions are severely restricted by precision flavour measurements. An ansatz that automatically relaxes these constraints is Minimal Flavour Violation [4]. This assumption implies that the interaction between any new neutral spin-0 state and SM matter is proportional to the fermion masses via Yukawa-type couplings. It follows that colour-neutral mediators would be sizeably produced through loop-induced gluon fusion or in association with heavy-flavour quarks. The DM candidate arises from the decay of the mediator ($\phi/a \to \chi\chi$) and the signature will be characterised by the presence of large $E_{\mathrm{T}}^{\mathrm{miss}}$ from the undetected DM candidate, and a top-quark pair $\left(t\bar{t}{+}E_{\mathrm{T}}^{\mathrm{miss}}\right)$. Following the notation of Ref. [67], the considered model has four parameters: the mass of the mediator m_ϕ or m_a, the DM mass m_χ, the DM–mediator coupling g_χ, and the flavour-universal SM mediator coupling g_q. The mediator width is assumed to be the minimal width, which is the one calculated from the masses and couplings assumed by the model. The mediator can decay into SM particles or into DM particles. This search is sensitive to decays of the mediator into a pair of DM particles. Off-shell DM production is also taken into account. The effective production cross-section of DM particles at pp colliders is a function of the production cross-section of the mediator, depending on g_q, and on the branching ratio for the mediator to decay into a pair of DM particles, which is a function of g_q and g_χ. The cross-section for DM production is therefore proportional to the squared product of the couplings $(g_q \cdot g_\chi)^2$, and an additional assumption of $g_q = g_\chi = g$ is made to reduce the number of parameters. Since the cross-section of annihilation and scattering from nucleons has the same functional dependence on the couplings, the same assumption is made when the results are compared to non-collider experiments.

Chapter 2

The Large Hadron Collider and the ATLAS detector

In this chapter a brief introduction to the Large Hadron Collider (LHC) [68] and its physics environment is given, together with a description of the ATLAS detector [69]:

2.1 The Large Hadron Collider

The LHC is a collider machine based at CERN (*Conseil Européen pour la Recherche Nucléaire*)[1], near Geneve. The LHC uses a 26.7 km tunnel at the border between Switzerland and France that was built between 1984 and 1989 for the LEP (Large Electron-Positron Collider) [70] and it is located underground between 50 m and 175 m depth. The first official recognition of the concept of the LHC was made by CERN and the European Committee for Future Accelerators (ECFA) in Lausanne, Switzerland in March 1984 [71]. The approval of the LHC project in December 1994 by the CERN Council [72] brought LEP to be decommissioned in 2000 to give way to the LHC. After some problems during the commissioning time, the LHC was ready to operate during late 2009.

In Figure 2.1 the full CERN complex is showed with also the LHC which is a two-ring synchrotron counter-rotating particle accelerator. Its 1232 dipole magnets bend the two beams into their circular orbit, whereas its 392 quadrupole magnets focus the beams near the four interaction points (IPs) where the collision occur.
The dipoles magnetic field required to bend the proton path is 8.33 T. The resulting current and material requirements are beyond the capabilities of traditional electromagnets, thus, NbTi superconducting magnets that operate at 1.9 K are used instead. This is accomplished by using an elaborate cryogenics system, with liquid helium cooling the magnets to their operating temperature. The acceleration is provided by 400 MHz radio-frequency (RF) cavities, that also compensate for the energy loss, keeping the beam energy constant. In order to avoid collision of the proton beam with gas molecules, the beam-pipes are kept in a ultra-high vacuum(10^{-13} atm). A succession of small to large accelerators (Figure 2.1) is used to accelerate the protons to the energy needed for injection into the LHC. Protons are first accelerated through *LINAC-2* up to 50 MeV and then pass to PSB (Proton Synchrotron Booster) where the beams reach 1.4 GeV. The last two steps are the PS (Proton Synchrotron) and the SPS (Super Proton Synchrotron).

[1] CERN was founded in 1954 and it is the largest institution for particle physics research

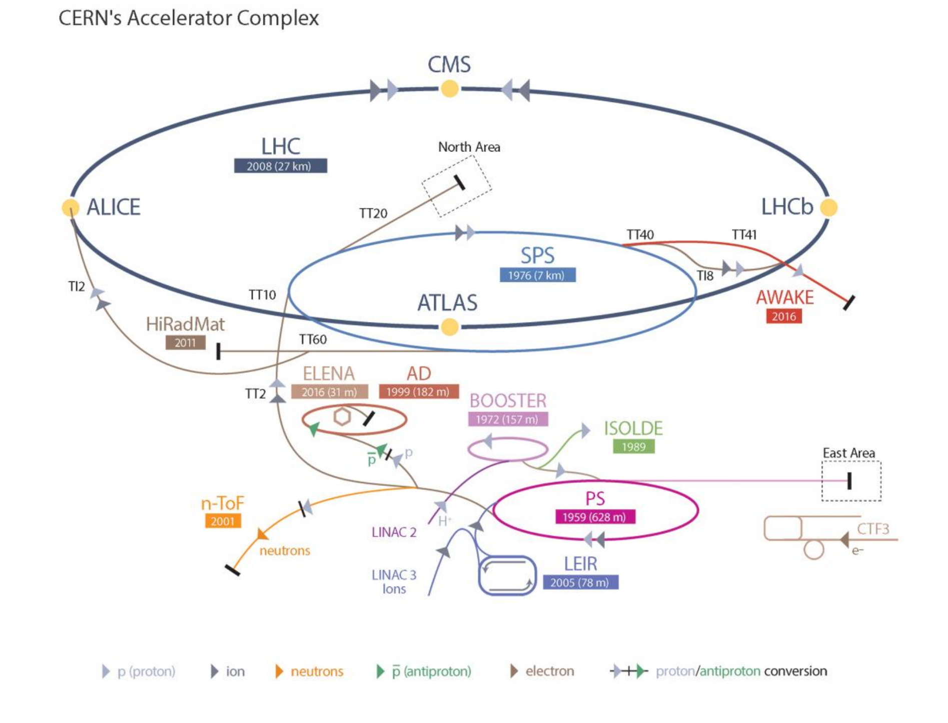

Figure 2.1: The CERN accelerator complex, showing the multi-stage system of injectors which are used to fill the LHC. A subset of the many experiments supported by these accelerators is also shown [73]

The injection of the particle beam in the LHC occurs at an energy of 450 GeV. These beams consist in bunches of protons with a length corresponding to 1.71 ns (reduced to 1.06 ns for collisions) and spaced by 25 ns. The size and the frequency of these bunches is directly relevant to the rate of interesting collisions.

For the purpose of gathering the information about what happened in the collisions, four detectors are built at the IPs, as illustrated in Figure 2.1. These are ATLAS[2] [69], ALICE[3] [74],CMS [4] [75], and LHCb [5] [76].

ALICE is designed to primarily look at heavy ion collisions. LHCb is specialised to look at hadrons containing the bottom quark while the ATLAS and CMS detectors are general purpose detectors, built to be able to discover a broad spectrum of possible new physics.

Run 1 of the LHC data taking took place from March 2010 to early 2013 colliding two proton beams at a centre of mass energy of 7 TeV (2010-2011) and 8 TeV (2012-2013). Afterwards, the machine was upgraded for two years and was restarted at the beginning of 2015 for Run 2 of LHC data taking, reaching a centre of mass energy of 13 TeV. Future upgrades will increase the centre mass energy to 14 TeV (see Chapter 4). In addition to producing proton-proton collisions, the LHC is also used for proton-ion and ion-ion collisions. While these types of collision are very interesting and have led to very important results [77, 78], they will not be considered further.

The event rate for a given physics process at the LHC is proportional to the cross section σ of the considered process and the instantaneous luminosity $\mathcal{L}$ of the machine:

$$\frac{dN}{dt} = \sigma \times \mathcal{L} \tag{2.1}$$

[2] ATLAS, A Toroidal LHC ApparatuS
[3] ALICE, A Large Ion Collider Experiment
[4] CMS, Compact Muon Spectrometer
[5] LHCb, Large Hadron Collider beauty experiment

The total number of events N produced during data-taking is obtained integrating Equation 2.1 with respect to time.

$$N = \sigma \times \int \mathcal{L} dt = \sigma \times L \tag{2.2}$$

where L is the integrated luminosity ($barn^{-1}$).
A measurement of intensity of the collision rate is the instanteous *luminosity*, which depends only on parameters of the beam:

$$\mathcal{L} = \frac{N_b^2 n_b f_r \gamma_r}{4\pi \epsilon_n \beta^*} F \tag{2.3}$$

where:

- N_b is the bunch intensity, as average charge protons per bunch.
- n_b is the number of colliding bunches per beam. The number of bunches depends on the filling scheme of the LHC and the maximum varied during 2015 (2232 bunches) and 2016 (2208 bunches) following the environment of the LHC machine.
- f_r is the revolution frequency (11245 Hz). This value cannot be changed since is related to the LHC perimeter and the speed of the circulating protons.
- γ_r is the relativistic gamma factor (∼7000),
- ϵ_r (emittance) and β^* (β function) express the size and shape of the beam at the interaction points.
- F is a factor that take into account the fact that the collisions do not occur head-on but at a crossing angle to minimized interaction between the non-colliding bunches.

The main parameters of the LHC during Run 1 and 2 are shown in Table 2.1. The luminosity is determined using counting rates measured by the luminosity detectors, and is based on a preliminary analysis of Van-der-Meer beam-separation scans during 2015 and 2016. The other important parameter in Equations 2.1 and 2.2 is the cross-section σ. The cross section is a measure of the probability of a specific scattering process, under some given set of initial and final conditions. In Figure 2.2 the cross section for different process in function of the centre of mass energy for proton-antiproton collisions until 4 TeV and proton-proton above that is presented. The calculation of this value take into account the factorization theorem in order to divide the interesting hard scattering process and the soft reactions.

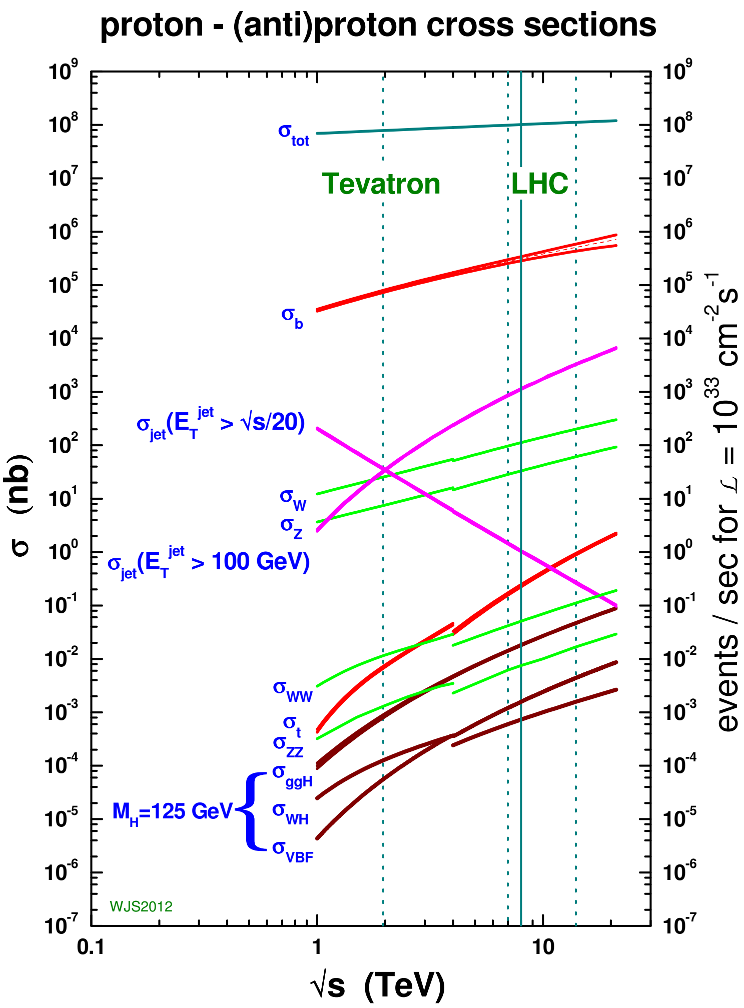

Figure 2.2: Standard model cross sections at the Tevatron and LHC colliders. These cross sections are calculated either at NLO or NNLO pQCD, using MSTW2008 (NLO or NNLO) [79] parton distributions, with the exception of the total hadronic cross section which is based on a parametrisation of the Particle Data Group. The discontinuity in some of the cross sections at 4 TeV is due to the switch from proton-anti-proton to proton-proton collisions at that energy. [80]

	Run 1	Run 2	
	2012	2015	2016
Energy [TeV]	4	6.5	6.5
Bunch Spacing [ns]	50	25	25
Maximum Colliding Bunches n_b	1380	2232	2208
β^* [cm]	60	80	40
Crossing angle[μrad]	290	290	140
Emittance ϵ_r [μm]	2.	3.5	2.5
Max bunch population [$10^{11} p/bunch$]	1.6	1.15	1.15
Max. no of bunches per injected train	144	144	96
Max. stored energy [MJ]	140	270	265
Peak luminosity [$10^{34} cm^{-2} s^{-1}$]	0.7	0.5	1.4

Table 2.1: Overview of performance related parameters at the LHC during 2012 (Run 1) and 2015-16 (Run 2).

2.2 The ATLAS Detector

The ATLAS detector [81–83] is one of the two general purpose detectors at the LHC. It is located at LHC Point 1, below the CERN main site located in Meyrin, Switzerland. ATLAS is 25 meters high, 44 meters long and weights 7000 tonnes. Figure 2.3 illustrates the overall layout including the various sub-detectors.

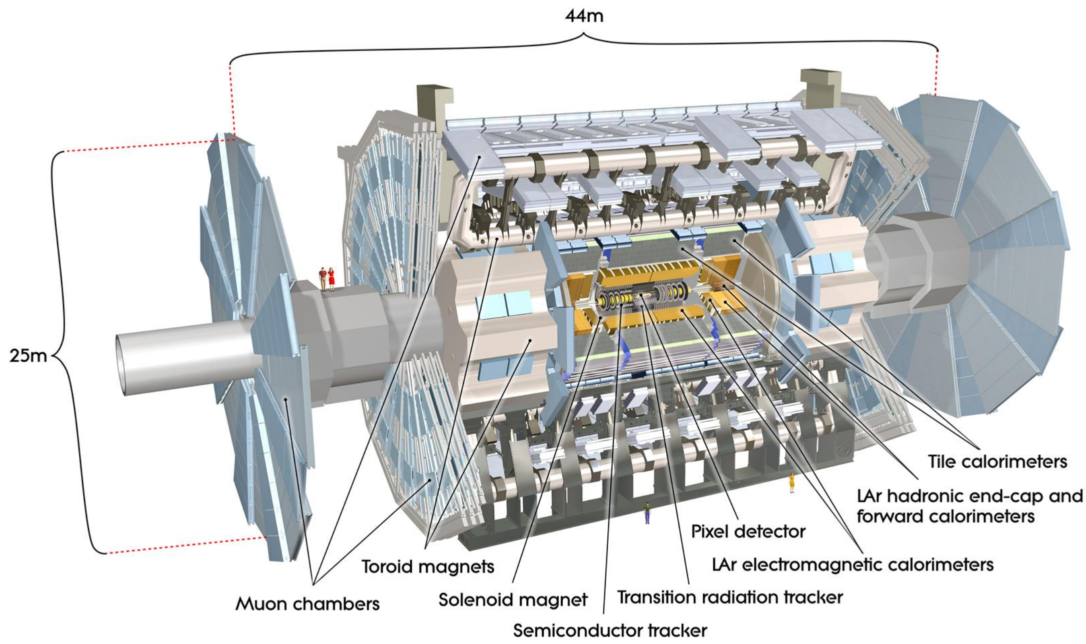

FIGURE 2.3: The ATLAS detector and its subdetectors. [81–83]

ATLAS uses a right-handed coordinate system with its origin at the nominal Interaction Point (IP) in the centre of the detector and the z-axis along the beam pipe. The x-axis points from the IP to the centre of the LHC ring, and the y-axis points upward. Cylindrical coordinates (r, ϕ) are used in the transverse plane, ϕ being the azimuthal angle around the z-axis. The pseudorapidity is defined in terms of the polar angle θ as

$$\eta = -\ln\left[\tan\left(\frac{\theta}{2}\right)\right] \tag{2.4}$$

The difference of pseudorapidity of two particles is independent of the Lorentz boosts along the beam axis. The distance in pseudorapidity-azimuthal angle space is defined as $\Delta R = \sqrt{\Delta\eta^2 + \Delta\phi^2}$. The cylindrically shaped of the ATLAS Detector is designed to be as close to hermetic as possible in order to reconstruct and identify nearly every energetic particles produced in the event. The design of the detector has been chosen in order to handle the expected high luminosity and high pileup conditions.
The detector structure and each sub detector can be divided into two parts:

- **Barrel**: The *Barrel* is the central part of the detector and consists of a cylindrically symmetrical structure that covers a pseudorapidity range of approximately $|\eta| < 1.4$.
- **End-Caps**: On either side of the Barrel, two cylindrical structures are present in order to guarantee longitudinal hermeticity. These structures are called *End-Caps* and they cover

a pseudorapidity range of approximately $1.5 < |\eta| < 4.7$ with some overlap with the barrel coverage.

The ATLAS Detector is composed of layers of various sub detectors, each with its own purpose. In the innermost part, immersed in a 2 T uniform magnetic field, is the tracking system which provides pattern recognition, momentum and vertex measurements, and electron identification with a coverage of $|\eta| < 2.5$. This is achieved with a combination of discrete, high-resolution semiconductor pixel and strip detectors in the inner part of the tracking volume, and a straw-tube tracking detector with the capability to generate and detect transition radiation in its outer part.
After the tracking detectors, a calorimetric system is located with a total coverage of $|\eta| < 4.9$. A combination of high granularity liquid-argon (LAr) electromagnetic sampling calorimeters (in the inner part) and scintillator-tile calorimeters (TILE) are used.
The muon spectrometer, which provides coverage for $|\eta| < 2.7$, is in the outermost part of the detector bathed in a toroidal magnetic field. Multiple-scattering effects are thereby minimised, and excellent muon momentum resolution is achieved with three layers of high precision tracking chambers. The muon spectrometer defines the overall dimensions of the ATLAS detector. The overall ATLAS detector nominal performance are listed in Table 2.2.

Detector Component	**Resolution**	$|\eta|$ Coverage
Tracking	$\sigma_{p_T}/p_T = 0.05\%\, p_T \otimes 1\%$	< 2.5
EM calorimetry	$\sigma_E/E = 10\%\sqrt{E} \otimes 0.7\%$	< 3.2
Hadronic calorimetry		
Barrel and end-cap	$\sigma_E/E = 50\%\sqrt{E} \otimes 3\%$	< 3.2
Forward	$\sigma_E/E = 100\%\sqrt{E} \otimes 10\%$	$3.1 < |\eta| < 4.9$
Muon Spectrometer	$\sigma_{p_T}/p_T = 10\%\, p_T$ at $p_T = 1\text{TeV}$	< 2.5

TABLE 2.2: Nominal performance of the ATLAS detector. Note that, for high-p_T muons, the muon-spectrometer performance is independent of the inner-detector system. The units for E and p_T are in GeV.

The LHC provides collision every $25\,ns$, which converts into a bunch crossing rate of 40 MHz. At this frequency the output rate cannot be entirerly recorded. For this reason, an online event selection is used called *trigger system* to select only the most interesting collisions, where a hard scattering has occurred between the partons inside the protons, from the elastic collisions background[6]. The trigger system consists of a hardware based Level-1 (L1) trigger and a software-based high-level trigger (HLT) that reduces the event rate from the bunch crossing rate of 40 MHz to an average recording rate of a few hundred Hz.

2.3 The Inner Detector

The Inner Detector (ID), Figure 2.4, is the innermost detector and consist of three parts: the Pixel Detector plus the Insertable B-Layer (IBL), the Semi Conductor Tracker (SCT) and the Transition Radiation Tracker (TRT). All of these sub-detectors are immersed in a 2 T magnetic field produced by a thin solenoid magnet which surrounds the Inner Detector. The ID must provide excellent spatial resolution to make the reconstruction of the tracks and momentum of particles spanning a large energy region possible. The ID is subject to large doses of highly energetic particles, and must be radiation-hard in order to survive such a harsh environment: at design luminosity, it will see around 40 billion charged particles per second. A schematic view of

[6]Typically, interaction with low momentum transfer between the protons.

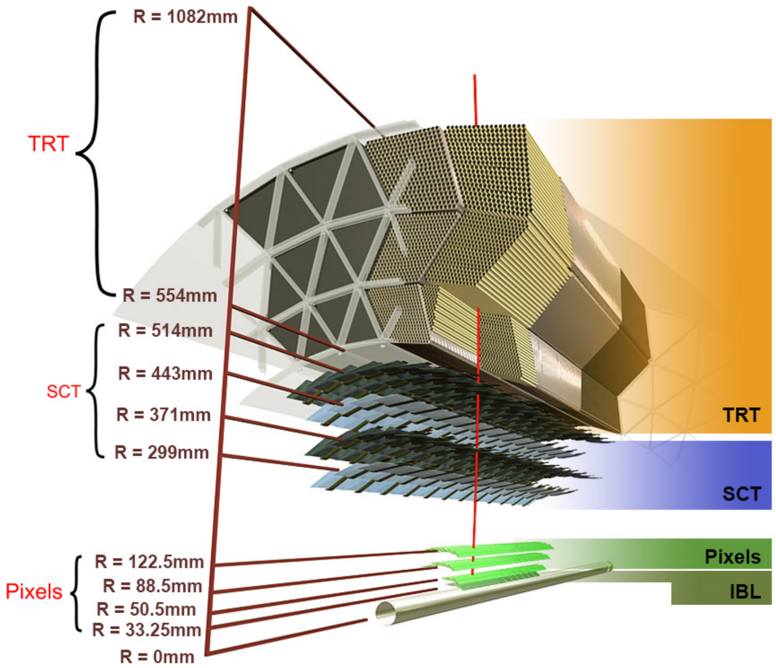

FIGURE 2.4: Illustration of the barrel part of the Run 2 Inner Detector with the additional layer of IBL.

the barrel part of the ID is shown in Figure 2.4. During the first LHC long shutdown 1 (LS1) the Insertable B-Layer (IBL) [84] was added to the detector. The introduction of the IBL provided an additional layer of pixel sensors at a radius of 3 cm away from the beam. This extra layer of pixels provides further tracking information, allowing for improved identification of secondary vertices, greatly improving flavour tagging.

Pixel Detector: The detector closest to the beam pipe is the Pixel Detector: it consist of 1744 pixel sensors of $250\mu m$ thickness and dimensions $19 \times 63\,mm^2$. Each sensor has 46 080 read-out channels, thus making up more than 80.4 million read-out channels in total. The layer closest to the beam-line, at a radius of $5.05\,cm$, is called the *b-layer*. The other layers, at radii of 8.85 and 12.3 cm respectively, are called *layer 1* and *layer 2*. The three end-cap disks are located at ±49.5, ±58.0 and ±65.0 cm along the z axis. The pixel layers have an intrinsic resolution of $10\,\mu m$ in the $R-\phi$ plane orthogonal to the beam axis ($z-\phi$ plane for the end-cap disks) and $115\,\mu m$ along z (R for the end cap disks).
Insertable B-Layer is an additional layer of pixel sensors designed to fit between the *b-layer* of the existing Pixel detector and a new beam pipe of reduced inner radius of 23.5 mm. It consists of 14 carbon-fibre staves, providing full azimuthal (ϕ) hermeticity for high transverse momentum ($p_{\mathrm{T}} > 1\,\mathrm{GeV}$) particles and longitudinal coverage up to $|\eta| < 3$. Each stave has 20 pixel sensor modules and carries the electrical services and cooling pipes serving them. Two module types [85] are installed on each stave. A total of 12 double-chip (DC) planar n-in-n sensors similar to those implemented in the Pixel detector, each bump-bonded to two FE-I4B read-out chips, populate the central stave region. Four single-chip (SC) 3D sensors, adopted for the first time in a collider tracking detector and each bump-bonded to one FE-I4B chip, populate each end of the stave. The staves are mounted with the sensors facing the beam pipe and are inclined by 14° with respect to the radial direction to achieve an overlap of the active area.
Semi Conductor Tracker (SCT), placed after the Pixel Detector, completes the high precision tracking, with eight hits per tracks expected. The barrel consists in 4 cylindrical layers of modules of silicon microstrips, each made up by two sensor at a 40 mrad stereo angle in order to measure

also the z coordinate. The pitch of the strips is about $40\mu m$. The end-cap is composed of 9 disks. The intrinsic resolution of the SCT is 17 μm in the $R-\phi$ plane and 580 μm in η. The total number of channels is approximately 6.3 million.
Transition Radiation Tracker (TRT) surrounds the SCT. It uses a gas-filled polyamide drift straw tubes technology and allows for pion versus electron separation by absorbing and measuring transition-radiation photons. It has been designed to provide a large number of measured space-points and to enhance the electron identification capabilities in $|\eta| < 2$ region. It is constituted of straw tubes of about 4 mm diameter, that provide a large numbers of measured points (~ 30 hits). The TRT only provides $R-\phi$ information in the barrel region and $z-\phi$ information the end-cap. In the barrel region the straw (4 mm diameter and 144 cm long) are disposed parallel to the beam axis. In the end-cap region the 37 cm long straw are disposed radially in wheels. The total number of TRT readout channels is approximately 351000. The tubes are filled with non-flammable xenon-based gas (70% Xe, 27% CO_2 and 3% O_2).

2.4 The Calorimetry System

The calorimeter systems (Figure 2.5) are located after the ID and used to measure the energies of electrons, photons and jets. Electrons and photons are identified in the liquid argon (LAr) electromagnetic calorimeters (EM) and in the end-cap region by the LAr electromagnetic end-cap (EMEC). The LAr technology provides excellent performance in terms of energy measurement and shower shape development. Hadron energy is measured in the scintillator Tile Hadronic Calorimeter (TILE). LAr technology is also used in the detection of hadronic activity in the Hadronic End-cap Calorimeter (HEC) and in the Forward Calorimeter (FCal). The calorimeters of ATLAS are not compensating, which means that the response of electrons and photons respect to the hadron is greater than one (i.e. $e/h > 1$). While electromagnetic showers, generated by photons and electron, develop mainly through Bremsstrahlung and pair production in the EM Calorimeter, hadronic showers develop through hadronic interactions between the produced hadron and the nuclei in the absorber medium. Hadronic showers have a significant EM component mainly due to decay of pion decays $\pi_0 \rightarrow \gamma\gamma$ which is not detected in the hadronic calorimeter. This component is responsible to the non compensating ($e/h \neq 1$) properties of the ATLAS hadronic calorimeters.

Liquid Argon (LAr) Calorimeter

The Electromagnetic Calorimeters are lead liquid-Argon detectors with accordion shaped absorbers and electrodes (Figure 2.6). The lead is used as an absorber while the LAr is the active medium. This structure provides full-azimuthal coverage without crack regions. In the barrel, the accordion waves are parallel to the beam axis and their folding angle varies along the radius in order to keep the liquid Argon gap as constant as possible. In the electromagnetic end-caps, the accordion waves run axially and the folding angle varies with radius. The calorimeter is placed into a cryostat which also contains the inner solenoid. The end-caps cryostat contains all the entire end-cap calorimetry system.

The LAr Calorimeter is longitudinally segmented in three layers in the region $0 < |\eta| < 2.5$. The cell granularity of the first layer is:

Thanks to its fine granularity it provides additional rejection power against π^0 decays. The middle layer has a constant cell size of $\Delta\eta \times \Delta\phi = 0.0025 \times 0.0025$. The second layer collects most of the energy of electrons and photons. The last layer is segmented in cells with a granularity of $\Delta\eta \times \Delta\phi = 0.05 \times 0.025$ completing the containment of the electromagnetic showers. For $|\eta| < 1.8$ another layer called presampler is present in front of the calorimeter; it is used to

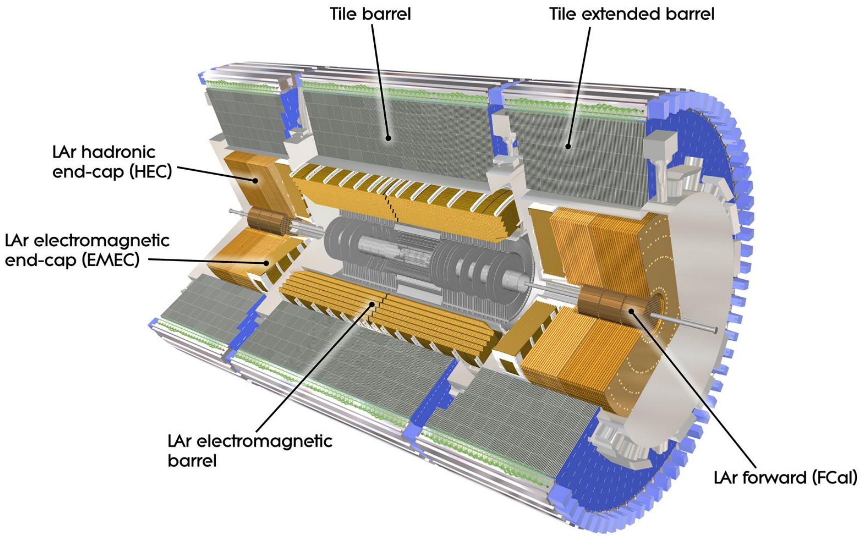

FIGURE 2.5: ATLAS LAr and Tile Calorimeters

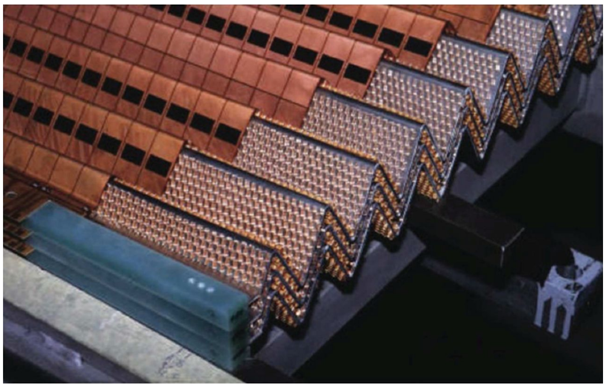

(A)

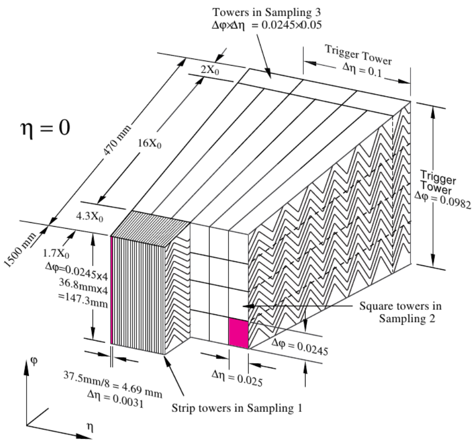

(B)

FIGURE 2.6: (A) Accordion-shaped geometry of the LAr calorimeter. (B) Barrel Module of the electromagnetic calorimeter

$\Delta\eta \times \Delta\phi$	η Coverage
$\lvert\eta\rvert < 1.4$	0.003×0.1
$1.4 < \lvert\eta\rvert < 1.475$	0.025×0.0025
$1.375 < \lvert\eta\rvert < 2.5$	0.003-0.025 $\times$ 0.01
$2.5 < \lvert\eta\rvert < 3.2$	0.1×0.1

TABLE 2.3: Segmentation in η and ϕ of the LAr Calorimeter

recover the energies lost in the ID material and Cryostat. The total depth of the EM calorimeter exceeds 22 radiation lengths(X_0) in the barrel region and 24 in the end-cap.

An incident electron or photon interacts with lead and initiates an electromagnetic shower, whose secondary electrons ionise the active medium. An electrode in the middle of the liquid argon gap is powered on both sides with high voltage and the ionisation electrons drift in gap. The total energy of the incident particle is proportional to the total ionisation energy. The calibration of the electromagnetic calorimeter has a very important impact in the physics results related to electrons and photons.

Barrel EM calorimeter consists of two identical half-barrels, separated by a small gap of 4 mm at $z = 0$. Each half barrel is divided in 16 modules each covering $\Delta\phi = 22.5^o$. Each half barrel consist in 1024 accordion shaped lead absorbers interleaved with the readout electrodes. The readout electrodes consist of three conductive copper layers separated by insulating kapton sheets. The two outer layers are at high voltage whereas the inner layer is used for the readout of the signal via capacitive couplings. Azimuthal segmentation is obtained by grouping together the appropriate numbers of electrodes. For $|\eta| < 0.8$ ($|\eta| > 0.8$) the absorbers are made of lead and have a thickness of 1.53 mm (1.13 mm) respectively. The size of the drift gaps is 2.1 mm.

End-cap Calorimeters are divided into two coaxial wheels: an outer wheel covering the region $1.375 < |\eta| < 2.5$ and a inner wheel covering $2.5 < |\eta| < 3.2$. The end-cap wheels are divided into eight wedge shaped modules. In the outer (inner) wheel of each end-cap, there are 768 (256) absorbers, interleaved with readout electrodes. The absorbers have a thickness of 1.7 mm for $|\eta| < 2.5$ and 2.2 mm for $|\eta| > 2.5$. The same segmentation in depth of the barrel calorimeter is present in the outer wheel, while only two layer for the inner wheel. The $\Delta\phi$ granularity is obtained by gathering the signal from adjacent electrodes.

Presampler (PS) is placed in front of the calorimeter in the region $|\eta| < 1.8$, and is used to correct for the loss of energy upstream the calorimeter. This detector consists of one single layer made of LAr, with a thickness of 1 cm in the barrel region and 0.5 cm in the end-cap. Beyond $\eta = 1.8$ the PS is no longer necessary given the more limited dead material upstream the calorimeter. The PS is made of 32 identical azimuthal sectors, each of them 3.1 m long and 0.28 m wide. Each sector covers the region $\Delta\eta \times \Delta\phi = 1.52 \times 0.2$. The sectors are mounted on rails which are fixed on the barrel internal rings. Each sector contains eight modules, seven of them covering a region of $\Delta\eta \times \Delta\phi = 0.2 \times 0.2$ and the last, located at the edge of the sector, covering a region $\Delta\eta \times \Delta\phi = 0.12 \times 0.2$. Each module is divided into eight cells in η and two cells in ϕ, leading 16 cells per module, except at the ends of the barrel where the modules have a reduced size with only ten cells. In total 7808 readout channels are then needed for the PS. A module of the end-cap PS is made of two active liquid-argon layers each 2 mm thick. Figure shows

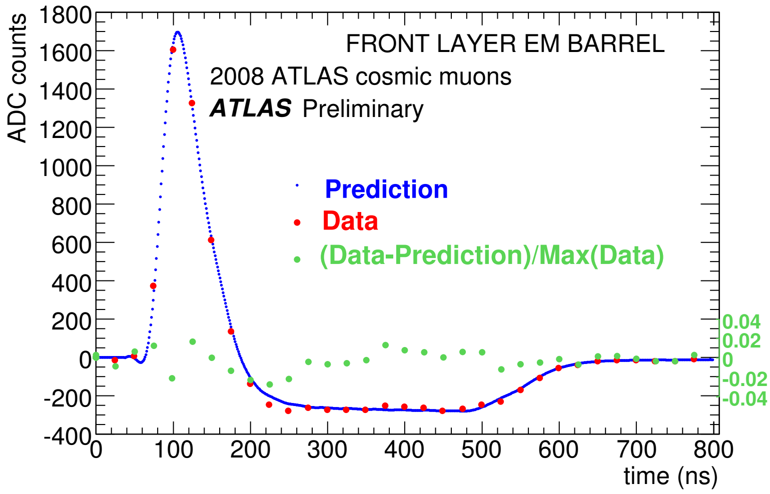

FIGURE 2.7: SignalEM

the typical shape of a ionization pulse produced by a cell in the front layer of the LAr EM calorimeter. The pulse is much longer than the nominal 25 ns bunch spacing of the LHC. The pulse shape is characterised by a positive peak and a negative tail of equal integral. In this way, the out-of-time energy deposition from previous/following bunches is, on average, cancelled out over several bunches.

Hadronic Calorimeter

Unlike the electromagnetic calorimeter, multiple technologies are used for the three sub detectors of the the Hadronic Calorimeter. In the central part known as *Tile Barrel* (up to $|\eta| < 1.0$), and in the *Tile Extended Barrel* ($0.8 < |\eta| < 1.7$), scintillator-tile detectors of easier assembling and lower cost are used. The absorbing material of these calorimeters are composed of steel. The module segmentation of the Tile Barrel and in Tile Extended Barrel is shown in Figure 2.8.

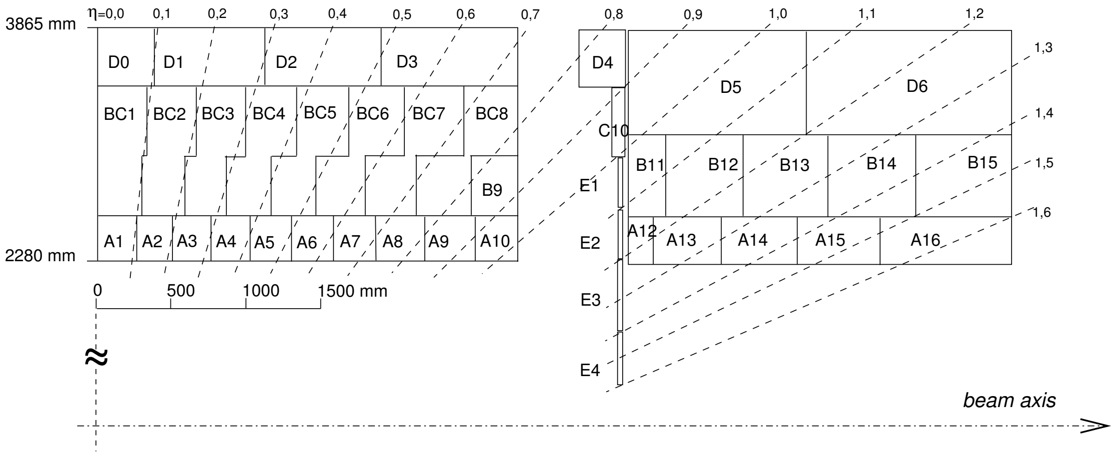

FIGURE 2.8: Segmentation in depth and eta of the tile-calorimeter modules in the central (left) and extended (right) barrels. The bottom of the picture corresponds to the inner radius of the tile calorimeter. The tile calorimeter is symmetric about the interaction point at the origin. [69]

Radially, each module is further segmented into three layers which are approximately 1.5, 4.1 and 1.8 λ (nuclear interaction length for protons) thick for the barrel and 1.5, 2.6 and 3.3 for the extended barrel. The Tile calorimeter has more coarse granularity than the electromagnetic calorimeters, with cells of $0.1 \times \pi/32$ for the first layers in η, ϕ-space. Wavelength shifting fibres coupled to the tiles on either ϕ edge of the cells collect the produced light and are read out via square light guides by two different photomultiplier tubes (PMTs), each linked to one readout channel. In the *end-cap region* the calorimeter technology is similar to that of the EM colorimeter, with an active medium of liquid Argon, but with the passive absorption medium is copper rather than lead. The general layout is shown in Figure 2.5. The hadronic calorimeter adds 9.7 interaction lengths (X_0) in the barrel region and ~ 10 in the end-caps (see Figure 2.9).

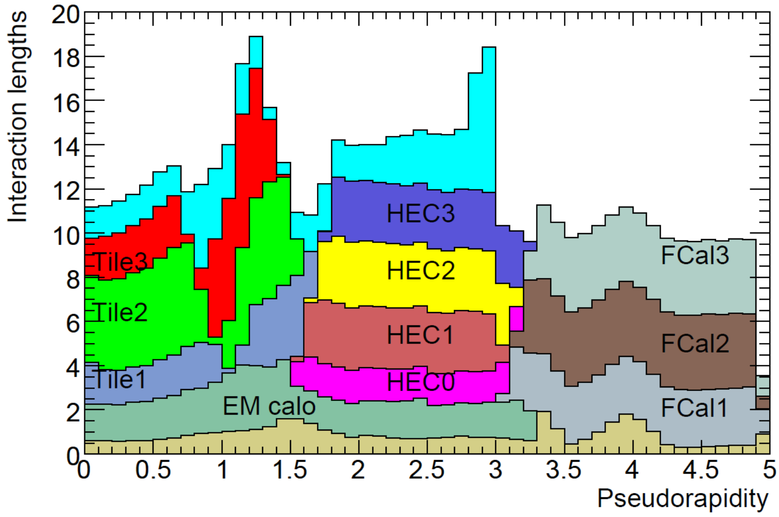

FIGURE 2.9: The number of interaction lengths of material in the ATLAS detector as a function of the pseudorapidity $|\eta|$. The unlabelled cyan region is additional material after the calorimeters and before the muon spectrometer, and is only shown up to $|\eta| = 3.0$. The unlabelled gold area represents additional material before the calorimeters. [69]

2.5 The Muon Spectrometer

The Muon Spectrometer (Figure 2.10) surrounds the calorimeter system. It is designed to detect and measure the momentum of charged particle than are not stopped by the calorimeters in the range $|\eta| < 2.7$. There are two different functions that muon chambers must accomplish: triggering and high precision tracking. The trigger system covers the region up to $|\eta| < 2.4$, and is composed by Resistive Plate Chambers (RPCs) in the barrel and Thin Gap Chamber (TGC) in the end-caps. The triggering system provides bunch-crossing identification (BCID), well-defined p_{T} thresholds and a measurement of the muon coordinate in the direction orthogonal to the chambers dedicated to precision tracking. The tracking is performed by the Monitored Drift Tubes (MDTs) and by Cathod Strips Chambers (CSCs) at large pseudorapidity. High precision mechanical assembly techniques and optical alignment systems provide the essential alignment of the chambers.
The external toroidal magnets use coils consisting of a conductor made of a mixture of aluminium, niobium, titanium and copper, and they extend the magnet system to a total of 26 m length and 20 m diameter. This configuration provides a magnetic field for the Muon Spectrometer of 0.5 T and 1 T in the barrel and end-caps, respectively. The magnet system operates with nominal currents of 8 kA for the solenoid, and of 25 kA for the toroids, respectively. Every toroid has a separate cryogenic system, while in the end-caps the coils have common cryostat. The magnetic field reconstruction relies on Hall sensors distributed throughout the spectrometer volume.

2.6 Trigger and Data Acquisition

The ATLAS Trigger and Data Acquisition (TDAQ) system is schematically represented in Figure 2.11. The TDAQ system controls the recording or the discard of events by ATLAS. A multi-level trigger system, consisting of the Level 1 (L1) hardware trigger and High Level (software) Trigger (HLT) must be passed in order to accept and save on disk an event.

The L1 Trigger has dedicated access to data from the ATLAS calorimeters and the Muon spectrometer. The maximum trigger rate has been raised from 70 kHz in Run 1 to 100 kHz in Run

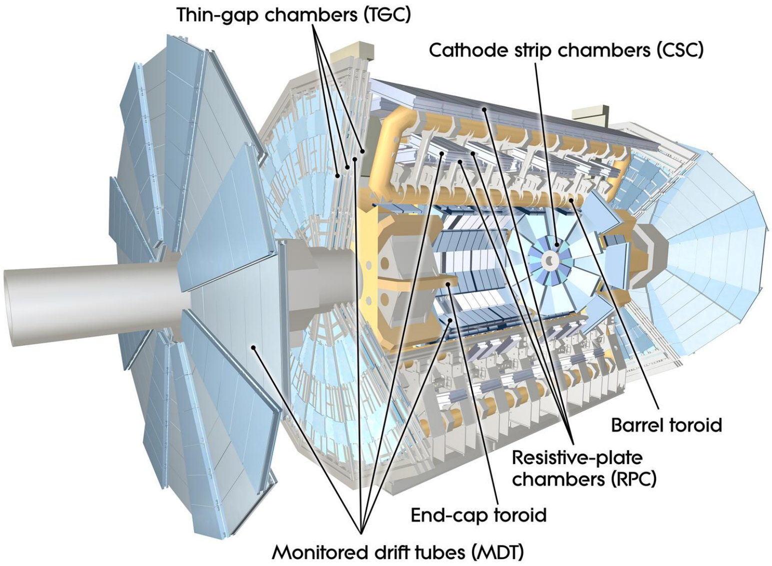

FIGURE 2.10: ATLAS Muon Spectrometer

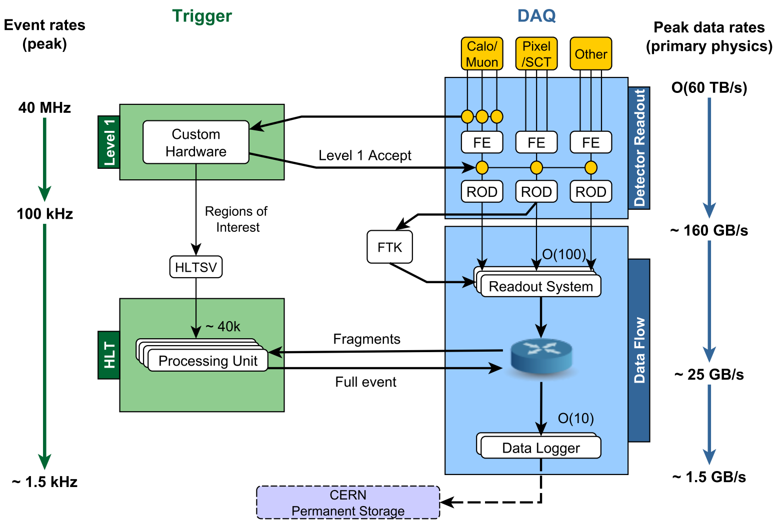

FIGURE 2.11: Functional diagram of the ATLAS Trigger and Data Acquisition system in Run 2 showing expected peak rates and bandwidths through each component.

2 thanks to the upgrade of the Level-1 trigger hardware and in the detector readout.
The Level-1 Calorimeter trigger makes use of reduced granularity information from the electromagnetic and hadronic calorimeters to search for electrons, photons, taus and jets, as well as high total and missing transverse energy ($E_{\mathrm{T}}^{\mathrm{miss}}$). The Level-1 Muon trigger system, which consists of a barrel section and two end-cap sections, provides fast trigger signals from the muon detectors for the Level-1 trigger decision.
A new topological trigger processor (L1Topo) has been installed and validated during the first part of Run 2 and is currently under commissioning. The Level-1 trigger objects from the output merger modules (CMX) of the Level-1 Calorimeter trigger and the Level-1 Muon trigger (MuCTPi) are taken as input for L1Topo. This system allows to apply topological selections at the Level-1 trigger stage combining kinematic information from multiple calorimeter and muon

trigger objects, such as angular separation, invariant mass requirements, or global event quantities such as the sum of the transverse momenta of all Level-1 jet objects.
The Fast TracKer (FTK) [86] project is a fast hardware-based tracking system designed to perform a global track reconstruction receiving input from the ATLAS silicon tracking detectors (Pixel and SCT) after each L1 trigger and provides full-event track information to the HLT. This can be used to improve many trigger selections requiring full-event tracking information, like $b-$jets, which would not be otherwise affordable at HLT. In addition the precise estimation of the pile-up conditions per event can be used to develop pile-up robust trigger strategies. With the Run 2 data taking ongoing, the first boards of FTK are being installed and took ATLAS data in parasitic mode. The full integration within the HLT and the full coverage extension will follow in the next years.

2.7 ATLAS data taking

Run 1 of LHC data taking took place between 2010 and 2013. The total LHC delivered luminosity was $\sim 5.5\,(22.8)$ fb^{-1} during 2011 (2012) at $\sqrt{s} = 7\,(8)$ TeV respectively. Two years later, in 2015, the LHC started the Run 2 data-taking at $\sqrt{s} = 13$ TeV delivering 4.2 fb^{-1} in 2015 and 38.5 fb^{-1} in 2016. In Chapter 3,results are presented using the data collected in the first two years of Run 2. The evolution of the delivered luminosity is shown in Figure 2.12. Figure 2.13(a) and 2.13(b) show the evolution of the peak instantaneous luminosity delivered to ATLAS during stable beams during 2015 and 2016 respectively. The average number of interactions per crossing μ (refereed to as pile-up) is shown Figure 2.13(c) , 2.13(d). As shown in Figure 2.14, the μ distribution is very different between 2015 and 2016. This is due to the improvement of the LHC nominal machine parameters (β^{*}) caused by of the intensity ramp up. The average pile-up was found to be $\langle\mu\rangle = 14$ in 2015 and $\langle\mu\rangle = 24$ in 2016.

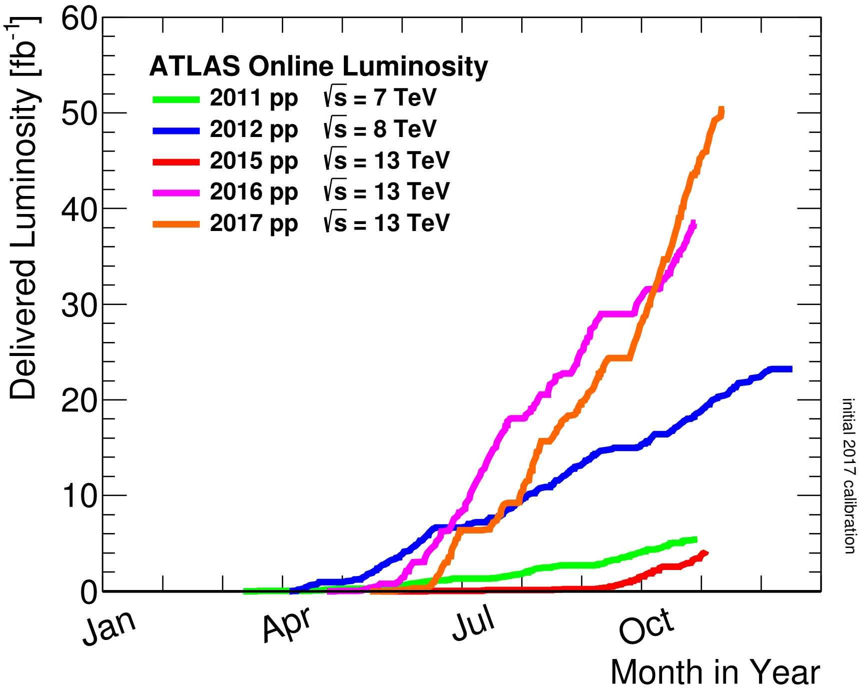

FIGURE 2.12: Cumulative luminosity versus day delivered to ATLAS during stable beams and for high energy p-p collisions.

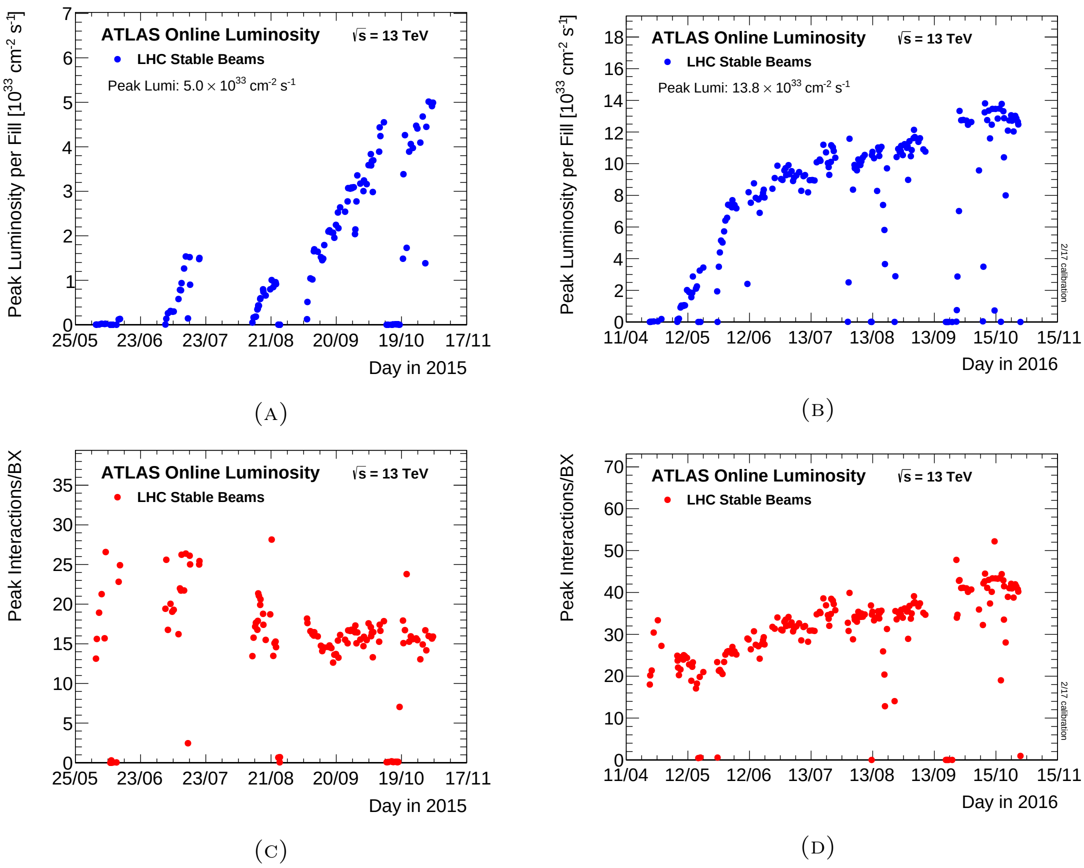

Figure 2.13: (A), (B): The peak instantaneous luminosity delivered to ATLAS during stable beams for pp collisions at 13 TeV centre-of-mass energy is shown for each LHC fill as a function of time in 2015 (2016). (C),(D): The maximum number of inelastic collisions per beam crossing (μ) during stable beams for pp collisions at 13 TeV centre-of-mass energy is shown for each fill in 201 (2016). The number of interactions shown is averaged over all colliding bunch pairs, and only the peak value per fill during stable beams is shown.

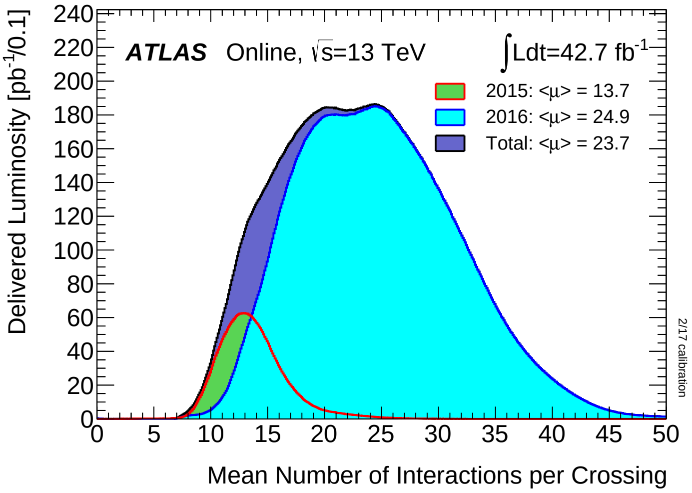

FIGURE 2.14: The luminosity-weighted distribution of the mean number of interactions per bunch crossing for the 2016 pp collision data at 13 TeVcentre-of-mass energy is shown. All data delivered to ATLAS during stable beams is shown, and the integrated luminosity and the mean μ value are given in the figure. The mean number of interactions per crossing corresponds to the mean of the Poisson distribution of the number of interactions per crossing calculated for each bunch. It is calculated from the instantaneous per bunch luminosity as $\mu = L_{bunch} \times \sigma_{inel}/fr$ where L_{bunch} is the per bunch instantaneous luminosity, σ_{inel} is the inelastic cross section which we take to be $80mb$ for 13 TeV collisions, and fr is the LHC revolution frequency.

2.8 Identifying Particles with the ATLAS Detector

ATLAS has an onion-like structure, with different detector layers. The purpose of the design is to be able to discriminate between different types of particles (electrons, muons, taus, photons) or identify a representation of an underlying physical process (jets and b-jets), or the contribution of invisible processes creating an energy imbalance in the event ($E_{\mathrm{T}}^{\mathrm{miss}}$). An illustration of how the various particles are identified in the ATLAS detector is given in Figure 2.15. The behaviour of the most frequently produced stable particles through the layers of the detector are depicted.

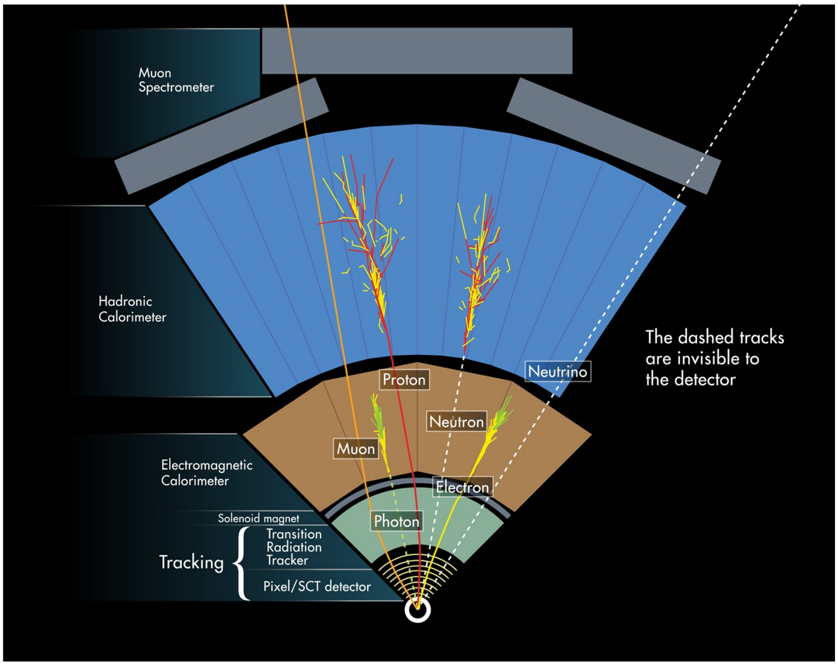

FIGURE 2.15: The identification of various particles with the use of the onion structure of the ATLAS detector

Charged particles, bent by the magnetic field, leaves a track in the inner detector, indicated by full lines. Photon can convert into an electron pair while crossing the inner detector, therefore leaving only hits in some layers of the ID, or be fully stopped in the electromagnetic calorimeter without associated track in the tracker.Anyhow, electrons and photons are fully stopped in the electromagnetic calorimeter, whereas hadrons, such as protons and neutrons, continue and deposit their energy in the hadronic calorimeter. Muons, being minimum ionising particles, leave a small amount of their energy in the inner detector regions, and make it through to the muon spectrometer. In the volume of the muon spectrometer they are bent by the toroidal magnetic field and are measured before they escape the detector. Dashed lines illustrate particles that do not interact with that part of the detector and are effectively invisible. Some particles escape the detector leaving no trace behind,such as neutrinos – they can only be inferred by conservation of energy and momentum and show up as missing energy in some part of the detector.
In this section the definitions of the objects used in the analysis described in Chapter 3 are provided focusing primarily on electrons, muons and jets.

Electrons and Photons

Electrons and photons entering the LAr calorimeter develop EM showers through their interaction with the lead absorbers. The EM showers ionise the LAr in the gaps between the absorbers; the ionisation electrons drift due to the high voltage electric field applied and induce an electrical signal on the electrodes which is proportional to the energy deposited in the active volume of the calorimeter.

The electron reconstruction starts with a cluster building in the EM calorimeter. A sliding window of 5×5 cells is built and the sum of the transverse energy of these cell in all layers of the calorimeter is summed. The total energy depends on η and it is a linear weighted sum of the contribution of the pre-sampler and the three calorimeter layers. If the sum of the energy of the cells in the 5×5 window is above a given threshold a pre-cluster is formed. The pre-cluster and the information provided by the ID are used to built the final electromagnetic cluster. The size of the cluster depends on the particle type.

- **An electron** is reconstructed if at least one well-reconstructed ID track is matched to the seed cluster.
- **A converted photon** is characterised by the presence of at least one track originating inside the tracker volume which matches an electromagnetic cluster.
- **An unconverted photon** is characterised by the absence of matched tracks.

The electron cluster is then rebuilt with size of 3×7 or 5×5 longitudinal towers of cells in the barrel or end-cap region respectively. For converted photons a 3×7 cluster size is used in the barrel, while a 3×5 cluster is associated to unconverted photons. The same cluster size of 5×5 is used in the end-caps for converted and unconverted photons. The choice of the cluster size is a compromise between the attempt to contain the full cluster energy and to reduce the presence of pileup and electronic noise.
The different EM clusters are calibrated following the procedure summarised in Figure 2.16. Full details on calibration procedure are available in Ref. [87]. Data and Monte Carlo (MC) simulation

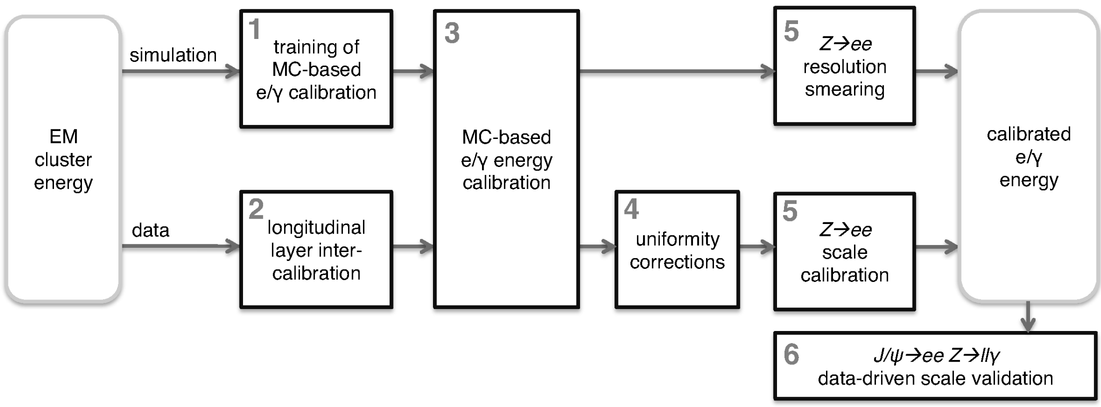

FIGURE 2.16: Schematic overview of the procedure used to calibrate the energy response of electrons and photons in ATLAS. [87]

follow different steps in order to ensure an optimal knowledge of the objects energy. The correct extrapolation of the response in the full p_T range used in the various ATLAS analyses, from a few GeV up to the TeV scale is ensured due to the different energy scales defined using the longitudinal segmentation of the electromagnetic calorimeter.
A set of uniformity corrections is applied to data in specific regions, typically non optimal high voltage regions or cells with problems during signal amplification of the calorimeter. The data and MC energies are corrected using a multivariate (MVA) calibration. The goal of the MVA calibration is to estimate the initial energy of the particles, identifying and if possible removing any dependence of the response with quantities like the impact position on the calorimeter and the shower profile. After all mentioned corrections, electrons response in data and simulation

are matched using the large accumulated sample of $Z \to e^+e^-$ events. A global scale extracted from the Z decay into electrons are applied to data while a smearing correction is applied on MC energies. In fact, the Z invariant mass resolution is typically larger in data than in the Monte Carlo because not all experimental effects are injected in the simulation. After applying all corrections, the di-electron mass distributions in data and simulation agree at the level of 2% in the range $80\,\text{GeV} < m_{ee} < 100\,\text{GeV}$ (Figure 2.17).

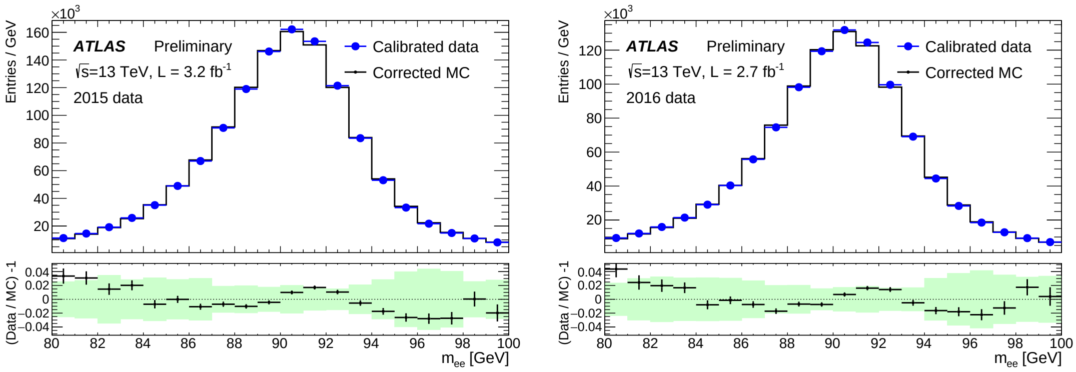

(A) (B)

FIGURE 2.17: Electron pair invariant mass distribution from Zee decays in data compared to simulation after the application of the full calibration, for (A) 2015 dataset and (B) a subset of 2016 dataset. The distributions for the data are shown without applying any background subtraction. The simulation is normalised to data. The bottom panels show the residuals for the data/MC ratios together with the total uncertainty (shaded green band). [88]

In every ATLAS physics analysis, the electron and photon candidates should satisfy a set of identification criteria that require the longitudinal and transverse shower profiles to be consistent with those expected for electromagnetic showers. Apart from this, properties of the tracks in the ID and matching between the track and the energy cluster are used to distinguish electrons from background using a likelihood identification (LH) [89]. Three different identification working points, based on a Likelihood (LH) minimisation, are available for the electrons during Run 2 (`LooseLH`, `MediumLH`, `TightLH`). They are designed to deliver different separation working points between isolated electrons and fake signatures from hadronic jets [90]. Figure 2.18 shows the electron reconstruction and identification efficiencies in $Z \to ee$ events as a function of the transverse energy E_T and pseudorapidity η.
In order to further reject hadronic jets misidentified as electrons, most analyses require electrons to pass one isolation requirement in addition to the identification requirements described above [89]. Both `calorimeter` isolation: based on the sum of the transverse energy deposited in the calorimeter cells in a cone of size ΔR around the electron, or `track` isolation: based on the scalar sum of the transverse momentum of the tracks with $p_\mathrm{T} > 0.4\,\text{GeV}$ in a cone of ΔR around the electron, are used.

Muons

Muon reconstruction is firstly performed independently in the ID and Muon Spectrometer (MS). The information from individual subdetectors is then combined to form the muon tracks that are used in physics analyses. The combined ID–MS muon reconstruction is performed according to various algorithms based on the information provided by the ID, MS, and also from the calorimeters. The muon reconstruction used in this work evolved from the algorithms defined as *Chain 3* in Ref [91]. Four muon types are defined depending on which subdetectors are used in reconstruction:

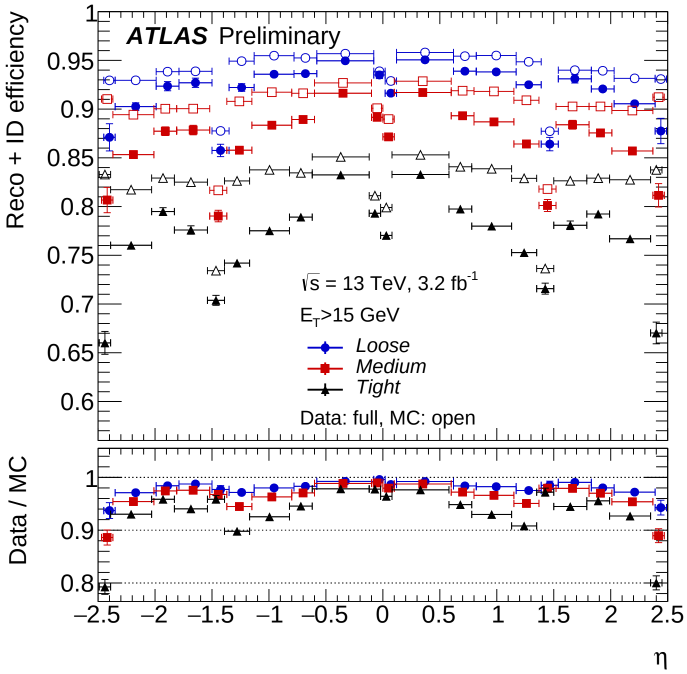

(A)

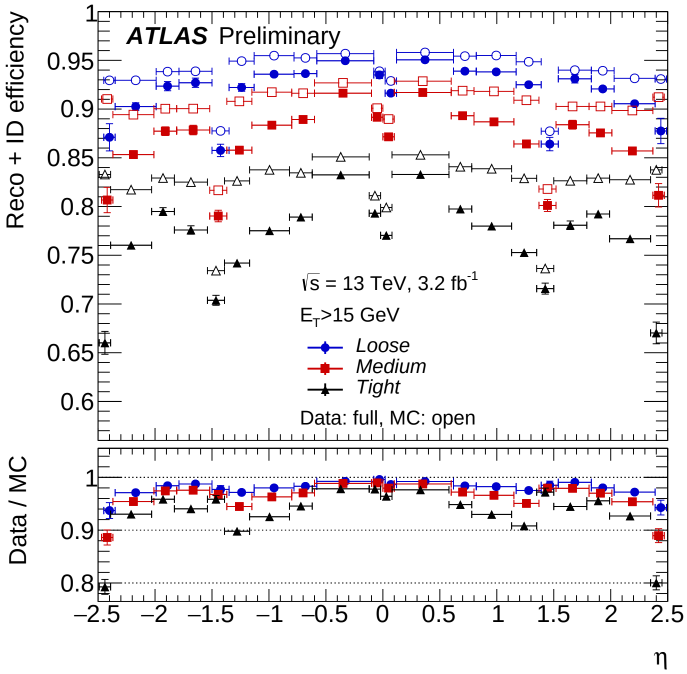

(B)

FIGURE 2.18: Electron reconstruction and identification efficiencies in $Z \to ee$ events as a function of the transverse energy E_T (A) and pseudorapidity η (B). The data efficiencies are obtained from the data-to-MC efficiency ratios measured using J/ψ and Z tag-and-probe, multiplied by the MC prediction for electrons from $Z \to ee$ decays. The uncertainties are obtained with pseudo-experiments, treating the statistical uncertainties from the different (E_T, η) bins as uncorrelated. Two sets of uncertainties are shown: the inner error bars show the statistical uncertainty, the outer error bars show the combined statistical and systematic uncertainty. [89]

- `Stand-alone (SA) Muon`: the muon spectrometer track exists, but there is no inner detector track with which to match it. This is mostly applicable for the region of $2.5 < |\eta| < 2.7$, where the muon spectrometer exists but the inner detector does not.
- `Combined (CB) Muon:` is based on a fully reconstructed track in the muon spectrometer that is matched to an Inner Detector track ($|\eta| < 2.5$)
- `Segment Tagged (ST) Muon:` is a combination of an ID track with a Muon Spectrometer segment. This is primarily useful to recover acceptance in rare areas where only one layer of muon chambers is accessible, or where the muon is very low p_{T}.
- `Calorimeter Tagged (CaloTag) Muon`: the MS tracks do not exist but the ID track and the energy deposit in the calorimeter matches the presence of a MIP. This type of muon has a low purity, and exists primarily for holes in the muon system, most prominently $|\eta| < 1$.

Different muon identification (ID) working points (Figure 2.19) are available by applying quality requirements that suppress background, mainly from pion and kaon decays, while selecting prompt muons with high efficiency and/or guaranteeing a robust momentum measurement. Four working points are available `Tight`, `Medium`, `Loose` and `High-`p_{T} and they are based on the following variables:

- q/p `significance`: defined as the absolute value of the difference between the ratio of the charge and momentum of the muons measured in the ID and MS divided by the sum in quadrature of the corresponding uncertainties.
- ρ' defined as the absolute value of the difference between the transverse momentum measurements in the ID and MS divided by the p_{T} of the combined track.
- normalized χ^2 of the combined track fit.

Seven isolation selection criteria *(isolation working points)* are defined [7], each optimised for different physics scenarios. They are based on two variables:

- A track-based isolation variable, $p_{\mathrm{T}}^{\mathrm{varcone30}}$ is defined as the scalar sum of the transverse momenta of the track with $p_{\mathrm{T}} > 1$ GeV in a cone of $\Delta R = \min(10\ \mathrm{GeV}/p_{\mathrm{T}}^{\mu}, 0.3)$ around the muon of transverse momentum p_{T}^{μ}, excluding the muon track itself. The cone size is chosen to be p_{T}-dependent to improve the performance for muons produced in the decay of particles with a large transverse momentum.
- A calorimeter-based isolation variable $E_{\mathrm{T}}^{\mathrm{topocone20}}$ is defined as the sum of the transverse energy of topological clusters in a cone of size $\Delta R = 0.2$ around the muon after subtracting the contribution from the energy deposit of the muon itself and correcting for pile-up effects.

The isolation selection criteria are determined using the relative isolation variables, which are defined as the ratio of the track- or calorimeter-based isolation variables to the transverse momentum of the muon.

In order to correct for differences in efficiency between data and MC a smearing procedure is applied to the muon p_{T} and multiplicative event weight is applied for each selected muon in MC.

Events with *Cosmic muons*, defined as muons not satisfying the conditions $|z_0| < 1$ mm and $|d_0| < 0.2$ mm, where z_0 and d_0 are the longitudinal and transverse impact parameters with respect to the primary vertex, respectively, are vetoed. An overview of the muon object definitions used in the analysis presented in Chapter 3 are presented in Table 3.2.

[7] *LooseTrackOnly,Loose,Tight,Gradient,GradientLoose,FixedCutTightTrackOnly,FixedCutLoose*

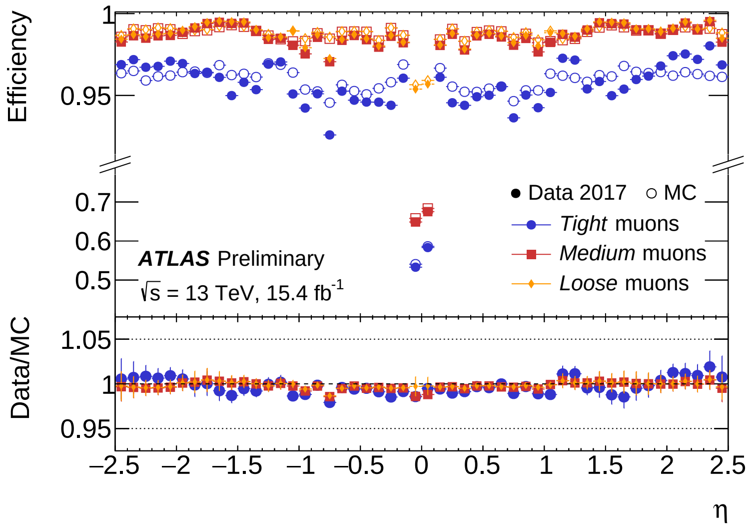

FIGURE 2.19: Muon reconstruction efficiencies for the `Loose`,`Medium`,`Tight` identification algorithms measured in $Z \to \mu^+\mu^-$ events as a function of the muon pseudorapidity for muons with $p_T > 10$ GeV. The prediction by the detector simulation is depicted as open circles, while filled dots indicate the observation in collision data with statistical errors. The bottom panel shows the ratio between expected and observed efficiencies, the efficiency scale factor. The errors in the bottom panel show the quadratic sum of statistical and systematic uncertainty. The results are based on 15.4 fb^{-1} of data collected in 2017. [92]

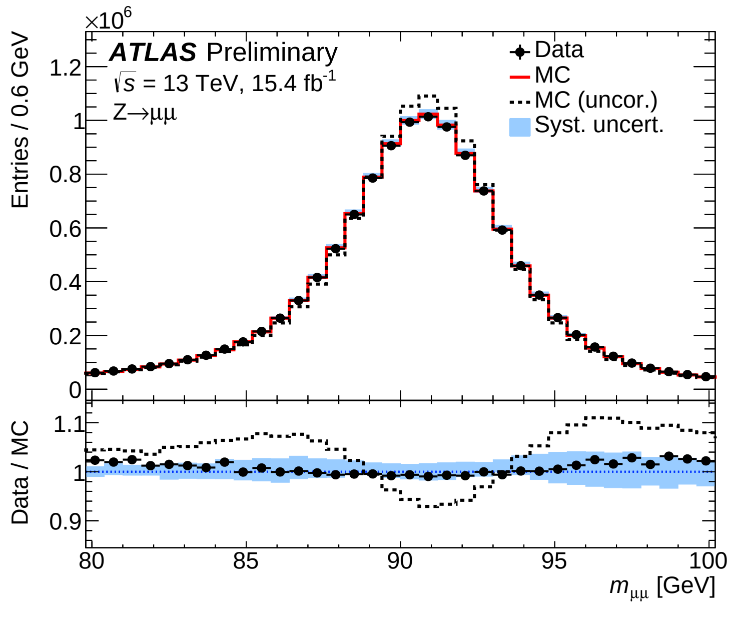

FIGURE 2.20: Dimuon invariant mass distribution of $Z \to \mu^+\mu^-$ candidate events reconstructed with CB muons out of 15.4 fb^{-1} of pp collision data collected in 2017. The upper panels show the invariant mass distribution for data and for the signal simulation plus the background estimate. The points show the data. The continuous line corresponds to the simulation with the momentum corrections (derived from the 2016 dataset) applied while the dashed lines show the simulation when no correction is applied. The band represents the effect of the systematic uncertainties on the momentum corrections. The lower panels show the data to simulation ratios. The simulation distributions are normalised to the data. [93]

Jets

The ATLAS calorimeters have very high lateral granularity and several samplings in depth covering up to $|\eta| < 4.9$. Hadronic jets are the most commonly produced objets in a proton-proton collision and they are the experimental signature of the production of gluons or quarks since they will shower and hadronize almost immediately after being produced. In order to recover gluon or quark information from the hadronic jets, the ATLAS experiment uses an anti-k_t sequential recombination algorithm [94, 95] starting from the positive-energy topological clusters (topo-clusters). Topo-clusters are built from neighbouring calorimeter cells containing a significant energy above a noise threshold that is estimated from measurements of calorimeter electronic noise and simulated pile-up noise. A minimisation procedure is done by iterating over all the topo-clusters, grouping the closest (based upon a p_{T} weighted distance parameter $d_{i,j}$) pair together into one, and iterating until the final set of grouped topo-clusters are all greater than the desired radius R apart. In order to group topo-clusters the distance d_{ij} defined in Equation 2.5, is used.

$$d_{ij} = \min(p_{\mathrm{T}i}^{2p}, p_{\mathrm{T}j}^{2p})\frac{\Delta R_{ij}^2}{R^2} \tag{2.5}$$

$$\Delta R_{ij} = \sqrt{(\Delta\eta)_{ij}^2 + (\Delta\phi)_{ij}^2} \tag{2.6}$$

$$d_{iB} = p_{\mathrm{T}i}^{2p} \tag{2.7}$$

p and R are constants that define the type of algorithm. The traditional k_t algorithm corresponds to a choice of $p = 1$, the Cambridge/Aachen algorithm is $p = 0$, and the anti-k_t algorithm is $p = -1$. Typical values in ATLAS are $R = 0.4$ or $R = 0.6$ for *small jets* and $R = 1.0$ or $R = 1.2$ for *large jets*.

Energy deposits in the calorimeter are calibrated typically at the electromagnetic scale (EM-scale), which is the signal scale that electromagnetic showers deposit in the calorimeter. This means that for hadrons the energy measurement can be underestimated by 55%, because ATLAS has non-compensating calorimeters. In order to recover the jet energy scale to the truth jets reconstructed at the particle-level energy scale, jets need to be calibrated following Figure 2.21. Details on the Jet Energy Scale (JES) can be found in Ref. [96, 97]. Figure 2.22 shows the fractional JES uncertainty of jets function of the jet p_{T}.

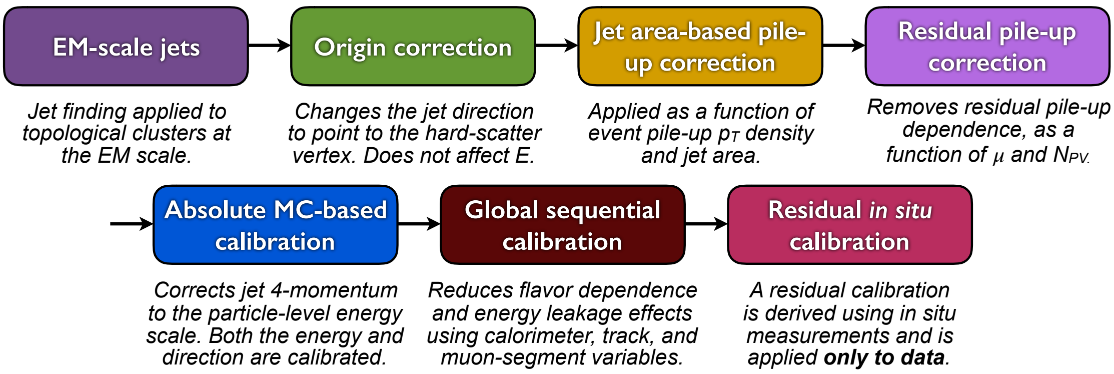

FIGURE 2.21: Calibration stages for EM-scale jets. Other than the origin correction, each stage of the calibration is applied to the four-momentum of the jet. [97]

b-tagged jets

Identification of jets originating from b-quark fragmentation (b-tagging) plays a central role in the ATLAS physics programs. It is essential for many physics analyses for which b-quark(s) in

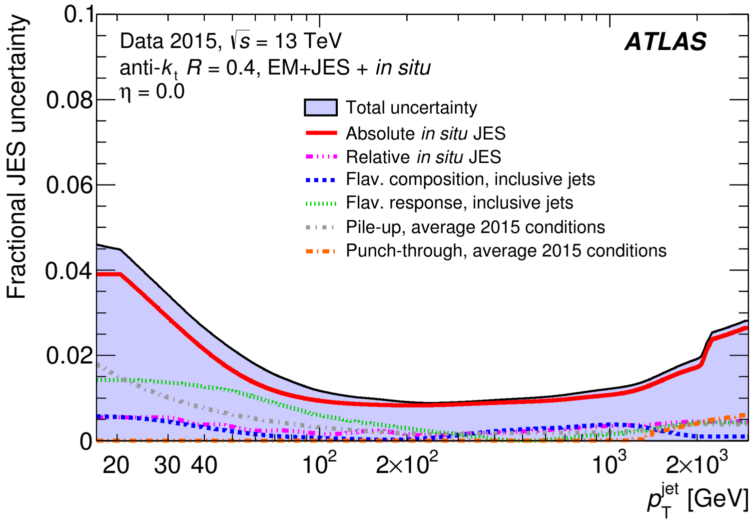

FIGURE 2.22: Combined uncertainty in the JES of fully calibrated jets as a function of jet p_T at $\eta = 0$. Systematic uncertainty components include *pile-up*, *punch-through*, and uncertainties propagated from the Z/γ-jet and *MJB* (absolute in situ JES) and η intercalibration (relative in situ JES). The flavor composition and response uncertainties assume a quark and gluon composition taken from PYTHIA dijet MC simulation (inclusive jets). [97]

their final state are expected, such as: property measurements of the top quark, searches for the Higgs boson decaying to a b-quark pair, and searches for new physics phenomena. Hadrons containing b-quarks have a relatively long lifetime ($\approx 10^{-12}\,s$) and because of the high energy involved they can travel "long distances" ($\approx 1\,mm$) before decaying and leaving a secondary vertex in the ID. Three different algorithm are used to discriminate between b-quarks and light quarks (u,d,s) by using complementary information: impact parameter, secondary vertex, and decay chain.

- The **IP3D** algorithm uses as main variables the value of the longitudinal and transverse impact parameter. The impact parameter is defined as the point of closest approach of the track to the primary vertex and is positive if it is in front and negative if is behind. From the value of the longitudinal (transfer) impact parameter, the corresponding significance $\frac{d_0}{\sigma(d_0)}$ ($\frac{z_0}{\sigma(z_0)}$) is calculated. Probability density function has been defined to discriminate b and light jet hypothesis and combined in a log likelihood ratio discriminant (LLR).

- The **SV1** is another tagging algorithm based on the same secondary vertex finding infrastructure, but it provides a better performance as it is based on a likelihood ratio formalism as it was for IP3D algorithm. Three vertex properties are exploited: firstly the vertex mass, defined as the invariant mass of all charged-particle tracks used to reconstruct vertex. Secondly, the ratio of the sum of the energies of these tracks to the sum of the energies of all tracks in the jet, and finally the number of two-track vertices. In addition, the ΔR between the jet direction and the direction of the line joining the primary vertex and the secondary vertex is used in the LLR.

- **JetFitter** [?] algorithm exploits the topological structure of weak b- and c-hadron decays inside the jet to reconstruct the whole chain decay $PV \to b \to c$ decay. The algorithm tries to find a common line between the primary vertex and the bottom and charm vertices, as well as their position on the line, approximating the b-hadron flight path. The discriminant is based on Neural network using similar variables.

The input variables obtained from the three basic algorithms are combined using a boosted decision tree (BDT) algorithm to discriminate b-jets from light (u,d,s-quark or gluon jets) and c-jets. The default algorithm used in the analysis described in Chapter 3 is called *MV2c10* [98]. This is the output of the BDT trained with $t\bar{t}$ events assigning b-jets as signal and light and c-jet as background. The c-jet fraction of the training for MV2c10 is set at 7% such that the training is performed assigning b-jets as signal and a mixture of 93% light-flavour jets and 7% c-jets as background. Operating points are defined by a single cut value on the MV2c10 output and are chosen to provide a specific b-jet efficiency on a $t\bar{t}$ sample. The value chosen corresponds to 77% b-jet efficiency.

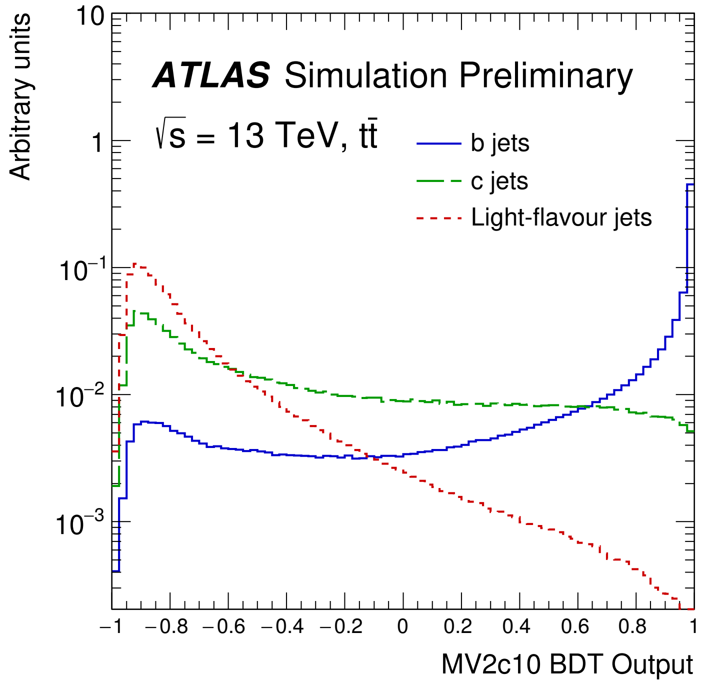

FIGURE 2.23: MV2c10 BDT output for b-(solid blue), c-(dashed green) and light-flavour (dotted red) jets evaluated with $t\bar{t}$ events. [98]

Missing transverse momentum

In proton-proton colliders the fraction of energy the partons have in the collision is unknown, therefore we do not know the initial energy and cannot use the conservation of the momentum. But considering only the transverse plane, the initial sum of the initial momentum is zero. This quantity accounts for all the particles that have not been detected, mainly or other weakly-interacting particles, have not been detected. We can then define the missing transverse energy [99, 100] as :

$$E_{\mathrm{T}}^{\mathrm{miss}} = \sqrt{(E_x^{\mathrm{miss}})^2 + (E_y^{\mathrm{miss}})^2} \tag{2.8}$$

$$\phi^{\mathrm{miss}} = \arctan\left(\frac{E_y^{\mathrm{miss}}}{E_x^{\mathrm{miss}}}\right) \tag{2.9}$$

where $E_{x(y)}^{\mathrm{miss}} = -\sum E_{x(y)}$ and $E_{x(y)}$ is the energy deposit measured in the detector. $E_{\mathrm{T}}^{\mathrm{miss}}$ generated by weakly interaction particles is generally referred as *true missing transverse energy*. *Fake contribution* to the $E_{\mathrm{T}}^{\mathrm{miss}}$ arises from miss-reconstructed physics objects, effects of finite detector resolution, the presence of dead or noisy regions in the detector, cosmic-rays, among others. Particular attention must be placed in the determination of the fake contribution to the $E_{\mathrm{T}}^{\mathrm{miss}}$ coming from pile-up since the introduction of more signals in the detector degrades the $E_{\mathrm{T}}^{\mathrm{miss}}$

resolution. Contribution for the $E_{\mathrm{T}}^{\mathrm{miss}}$ comes from the calorimeters, the muon spectrometers and also from the ID. The x and y contribution to the $E_{\mathrm{T}}^{\mathrm{miss}}$ can be calculated as:

$$E_{x(y)}^{\mathrm{miss}} = E_{x(y)}^{\mathrm{miss},e} + E_{x(y)}^{\mathrm{miss},\gamma} + E_{x(y)}^{\mathrm{miss},\tau} + E_{x(y)}^{\mathrm{miss},jets} + E_{x(y)}^{\mathrm{miss,SoftTerm}} + E_{x(y)}^{\mathrm{miss},\mu} \tag{2.10}$$

where each term is calculated from the negative sum of calibrated cell energies inside the corresponding objects (within $|\eta| < 4.9$), and the $E_{x(y)}^{\mathrm{miss},\mu}$ is calculated from the negative sum of the momenta of muon tracks reconstructed with $|\eta| < 4.9$. The $E_{\mathrm{T}}^{\mathrm{miss}}$ computation used in the analyses presented in Chapter 3 does not compute the separate term for τ leptons, which are instead calibrated as jets. The soft term is constructed from all tracks that are not associated with any reconstructed electron, muon or jet, but which are associated with the primary vertex.

Chapter 3

Search for Beyond Standard Model physics in di-lepton final states

In this chapter, a search accomplished with the LHC and the ATLAS detector to look for new physics beyond the Standard Model is presented. In particular, I look for pair produced top squark and direct DM particles in final states with two opposite charged leptons (electrons or muons). These analyses are based on the 2015 and 2016 pp collision recorded by the ATLAS experiment at $\sqrt{s} = 13$ TeV centre mass energy. I published these searches in two peer review papers in December 2017 and January 2018 on "European Physical Journal C".

- Eur. Phys. J., C77(12):898, 2017. arXiv:1708.03247 [101]
- Eur. Phys. J., C78(1):18, 2018. arXiv:1710.11412. [102]

Both searches are characterized by the presence of large $E_{\mathrm{T}}^{\mathrm{miss}}$, jets and two opposite electric charge leptons. The presence of two leptons in the final state implies a high reduction in statistics but it provides a strong suppression of the reducible backgrounds and, using the kinematics variables of the two leptons, a excellent rejection against SM process can be achieved. Two main models are targeted: the first, is the pair production of the SUSY partner of the top quark ($\tilde{t}_1$); the second model targets a weakly interacting massive dark-matter particle (χ) decaying from a scalar or pseudoscalar mediator (ϕ/a) produced in association with top quark pairs. The phenomenology of this two models are described in Section 1.6 and 1.8. The chosen final state topology allows to develop a common analysis strategy to tackle both of these two models. A very powerful variable that will be used to distinguish between signal and SM backgrounds is the leptonic stransverse mass [103, 104].

3.1 Data samples and event reconstruction

The ATLAS detector collected 4.2 fb^{-1} in 2015 and 38.5 fb^{-1} in 2016 during pp collisions at a centre-of-mass energy of $\sqrt{s} = 13$ TeV, with a peak instantaneous luminosity of $\mathcal{L} = 1.4 \times 10^{34}$ cm^{-2}s^{-1}. In this analysis, only events taken in stable beam conditions, and for which all relevant detector systems were operational, are considered. After data-quality requirements, the data sample amounts to an integrated luminosity of 36.1 fb^{-1}, with an uncertainty of $\pm 3.2\%$. This uncertainty is derived from a van der Meer (vdM) scan similar to that detailed in Ref. [105]. Candidate events are required to have a reconstructed vertex with at least two associated tracks with transverse momentum $p_{\mathrm{T}} > 400$ MeV. The vertex with the highest scalar sum of the squared transverse momenta of the associated tracks is considered the primary vertex of the event. Given the request of two opposite charged leptons in the final state, a particular attention must be put in the definition of the parameters for those particles to be reconstructed. In particular, two candidate types are used for both electrons and muons. The baseline definition consists of a set of loose requirements as reported in Table 3.1 and 3.2 and it is used for pre-selecting the events discarding events with a number of electron and muon different from two. Tighter requirements on the lepton candidates are imposed, which are then referred to as Signal electrons or muons. These requirements are used to further reduce the SM background component keeping the efficiency of selecting SUSY or DM events higher. The definition of the two candidate types are essential to evaluate the background contribution due to jets misidentified as leptons and non-prompt leptons (see Section 3.10).

	Selection
Baseline Electrons	$\|\eta\| < 2.47$ $E^{\text{clust}}/\cosh(\eta) > 7$ GeV `LooseAndBlayerLH` Identification
Signal Electrons	$E^{\text{clust}}/\cosh(\eta) > 20$ GeV `MediumLH` Identification `GradientLoose` isolation

TABLE 3.1: Summary of the electron selections.

	Selection
Baseline Muons	$\|\eta\| < 2.4$ $p_{\text{T}} > 7$ GeV
Signal Muons	$p_{\text{T}} > 20$ GeV `MediumLH` Identification `GradientLoose` isolation

TABLE 3.2: Summary of the muon selections.

Baseline electron candidates are reconstructed from three-dimensional electromagnetic calorimeter energy depositions matched to ID tracks, and are required to have pseudorapidity $|\eta| < 2.47$, $p_{\text{T}} > 7\,\text{GeV}$, and to pass the `LooseAndBlayer` likelihood-based identification requirement (see Section 2.8). The pseudorapidity η is measured from the associated tracks (η^{track}) if the number of hits in the silicon detector are greater than 4 otherwise it is taken from the calorimetry system (η^{clust}).

Baseline muon candidates are reconstructed in the pseudorapidity region $|\eta| < 2.4$ from the muon spectrometer tracks matching ID tracks. They must have transverse momentum (p_{T}) greater than $7\,\text{GeV}$ and must pass the `Medium` identification requirements (See Section 2.8). They are based on requirements on the number of hits in the different ID and muon spectrometer subsystems, and on the significance of the charge-to-momentum ratio (q/p) measurement [91].

Jets are reconstructed from three-dimensional energy clusters in the calorimeter system [106] with the anti-k_t jet clustering algorithm [95, 107] with a radius parameter $R = 0.4$. Only jet candidates with $p_{\text{T}} > 20\,\text{GeV}$ and $|\eta| < 2.8$ are considered. Jets are calibrated as described in Refs. [97, 108], and the expected average energy contribution from pile-up clusters is subtracted according to the jet area [109]. Additional selections are applied to jets with $p_{\text{T}} < 60\,\text{GeV}$ and $|\eta| < 2.4$ in order to reject jets produced in pile-up collisions [110]. The "medium" working point is used for the pile-up rejection, which has an efficiency of about 92% for jets produced by the hard scatter (see Section 2.8). Jets resulting from the hadronisation of b-quarks are identified using the multivariate MV2c10 b-tagging algorithm (See section 2.8). This algorithm is used at a working point that provides 77% b-tagging efficiency in simulated $t\bar{t}$ events. The jets satisfying the b-tagging requirements are referred to as b-jets. Events are discarded if they contain any jet with $p_{\mathrm{T}} > 20\,\mathrm{GeV}$ failing to satisfy basic quality selection criteria that reject detector noise and non-collision backgrounds [111].

	Selection
Jets	$p_{\mathrm{T}} > 20$ GeV $\|\eta\| < 2.5$ MEDIUM JVT if $p_{\mathrm{T}} < 60$ GeV and $\|\eta\| < 2.4$

TABLE 3.3: Summary of the jet selections.

To resolve reconstruction ambiguities, an overlap removal algorithm is applied to candidate leptons and jets. Non-b-tagged jets which lie within $\Delta R = \sqrt{(\Delta y)^2 + (\Delta\phi)^2} < 0.2$ (here y stands for the rapidity) of an electron candidate are removed, and the same is done for jets which lie within 0.2 to a muon candidate and are consistent with the characteristics of jets produced by muon bremsstrahlung. Finally, any lepton candidate which lies within $\Delta R < 0.4$ from the direction of a surviving jet candidate is removed, in order to reject leptons from the decay of a b- or c-hadron. Electrons which share an ID track with a muon candidate are also removed.

Signal electrons must satisfy the `MediumLH` likelihood-based identification requirement as defined in Ref. [112]. Signal electrons must have a transverse impact parameter with respect to the reconstructed primary vertex, d_0, with a significance of $|d_0|/\sigma(d_0) < 5$. Signal Muon candidates are required to have $|d_0|/\sigma(d_0) < 3$. The tracks associated with the electron or muon must have a longitudinal impact parameter with respect to the reconstructed primary vertex, z_0, satisfying $|z_0 \sin\theta| < 0.5$ mm. Isolation criteria are applied to both electrons and muons using the sum of the transverse energy of the calorimeter energy clusters in a cone of $\Delta R_\eta = \sqrt{(\Delta\eta)^2 + (\Delta\phi)^2} = 0.2$ around the electron (excluding the deposit from the electron itself), and the scalar sum of the p_{T} of tracks within a variable-size cone around the lepton (excluding its own track). The track isolation cone radius for electrons (muons) is given by the smaller of $\Delta R = 10\ \mathrm{GeV}/p_{\mathrm{T}}$ and $\Delta R_\eta = 0.2\,(0.3)$. The isolation criteria are optimised such that the isolation selection efficiency is uniform across η, and it increases from 95% for $p_{\mathrm{T}} = 25$ GeV to 99% for $p_{\mathrm{T}} = 60$ GeV in $Z \to \ell\ell$ events.

The missing transverse momentum ($E_{\mathrm{T}}^{\mathrm{miss}}$) is defined as the magnitude of the two-vector $\mathbf{p}_{\mathrm{T}}^{\mathrm{miss}}$ which is the negative vector sum of the transverse momenta of all identified baseline objects (electrons, muons, jets) and an additional soft term. The soft term is constructed from all tracks that are not associated with any reconstructed electron, muon or jet, but which are associated with the primary vertex. In this way, the $E_{\mathrm{T}}^{\mathrm{miss}}$ value is adjusted for the best calibration of the jets and the other identified objects above, while maintaining pile-up independence in the soft term [99, 100].

3.2 The leptonic stransverse mass m_{T2}

The leptonic stransverse mass m_{T2} variable [103, 104] was introduced in the framework of SUSY measurement studies. This variable is used to better identify the case where two identical particles ('legs') are pair produced, and both decay into an invisible particle and to better suppress the SM background. The vector sum of the transverse momenta of the two invisible particles is measured, and constitutes the $E_{\mathrm{T}}^{\mathrm{miss}}$ of the event. The topology is illustrated in Figure 3.1

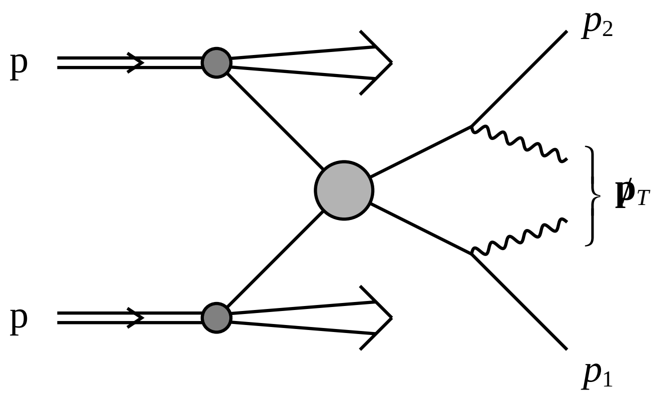

FIGURE 3.1: Diagram of the generic process under consideration [103, 104].

All possible decompositions of the $E_{\mathrm{T}}^{\mathrm{miss}}$ into two transverse vectors, which are interpreted as the transverse momenta of the invisible particles in the two legs of the event are considered. For each test value of the invisible momenta two transverse masses are built with the visible particles in the events and the maximum of the two values is taken. It is intuitive that the minimum value over all possible decompositions of $E_{\mathrm{T}}^{\mathrm{miss}}$ of the variable thus calculated will be lower than the end point for the decay on a single leg. This quantity is defined as

$$m_{\mathrm{T2}}(\mathbf{p}_{\mathrm{T},1}, \mathbf{p}_{\mathrm{T},2}, \mathbf{q}_{\mathrm{T}}) = \min_{\mathbf{q}_{\mathrm{T},1}+\mathbf{q}_{\mathrm{T},2}=\mathbf{q}_{\mathrm{T}}} \{\max[\, m_{\mathrm{T}}(\mathbf{p}_{\mathrm{T},1}, \mathbf{q}_{\mathrm{T},1}), m_{\mathrm{T}}(\mathbf{p}_{\mathrm{T},2}, \mathbf{q}_{\mathrm{T},2})\,]\},$$

where m_{T} indicates the transverse mass,[1] $\mathbf{p}_{\mathrm{T},1}$ and $\mathbf{p}_{\mathrm{T},2}$ are the transverse momentum vectors of two particles, and $\mathbf{q}_{\mathrm{T},1}$ and $\mathbf{q}_{\mathrm{T},2}$ are transverse momentum vectors with $\mathbf{q}_{\mathrm{T}} = \mathbf{q}_{\mathrm{T},1} + \mathbf{q}_{\mathrm{T},2}$. The minimisation is performed over all the possible decompositions of $\mathbf{q}_{\mathrm{T}}$. For $t\bar{t}$ or WW decays with $t \to bW$ and $W \to \ell\nu$, when the transverse momenta of the two leptons in each event are taken as $\mathbf{p}_{\mathrm{T},1}$ and $\mathbf{p}_{\mathrm{T},2}$, and $\mathbf{p}_{\mathrm{T}}^{\mathrm{miss}}$ as $\mathbf{q}_{\mathrm{T}}$, $m_{\mathrm{T2}}(\mathbf{p}_{\mathrm{T}}(\ell_1), \mathbf{p}_{\mathrm{T}}(\ell_2), \mathbf{p}_{\mathrm{T}}^{\mathrm{miss}})$ is bounded sharply from above by the mass of the W boson [113, 114]. In the $\tilde{t} \to b\tilde{\chi}_1^{\pm}$ decay mode the upper bound is strongly correlated with the mass difference between the chargino and the lightest neutralino. For the decay chain shown in Figure 1.7(b) the end point will be determined by the mass difference squared $m^2(\tilde{\chi}^{\pm}) - m^2(\tilde{\chi}_1^0)$, therefore the analysis will only have sensitivity when this quantity is larger than $m^2(W)$. The bound $m_{\mathrm{T2}} < m_W$ for SM events is quite sharp, and by selecting events with $m_{\mathrm{T2}} > m_W$ it is thus possible to dramatically enhance the signal over background ratio. For the Dark Matter model presented in Section 1.7 a linear combination with the $E_{\mathrm{T}}^{\mathrm{miss}}$ is used in order to maximise the discrimination power of the two variables [115].

$$\xi^{+} = m_{\mathrm{T2}} + 0.2 \cdot E_{\mathrm{T}}^{\mathrm{miss}} \tag{3.1}$$

[1]The transverse mass is defined by the equation $m_{\mathrm{T}}(\mathbf{p}_{\mathrm{T}}, \mathbf{q}_{\mathrm{T}}) = \sqrt{2|\mathbf{p}_{\mathrm{T}}||\mathbf{q}_{\mathrm{T}}|(1-\cos(\Delta\phi))}$, where $\Delta\phi$ is the angle between the particles of negligible mass with transverse momenta $\mathbf{p}_{\mathrm{T}}$ and $\mathbf{q}_{\mathrm{T}}$.

Figures 3.2 and 3.3 show the m_{T2} distribution for events with Same Flavour (SF) (electron–electron or muon–muon) and Different Flavour (DF) (electron–muon) leptons respectively. As shown in Figure 3.2 the SF selection consists mostly of events coming from Z/γ^*+jets process.

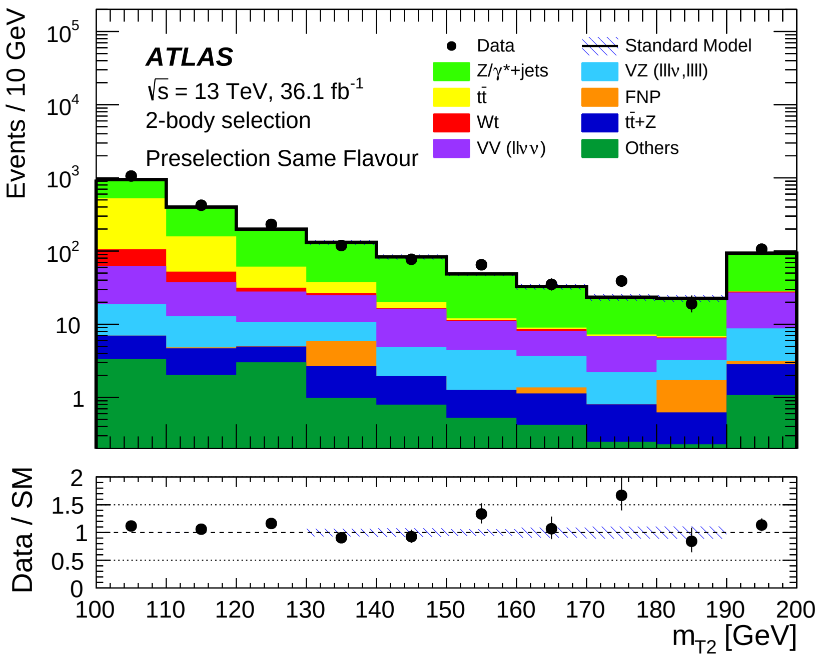

FIGURE 3.2: Distribution of m_{T2} for SF events. The contributions from all SM backgrounds are shown. The rightmost bin includes overflow events. For SF leptons a selection on the invariant mass of the leptons is applied to reduce the backgrounds with leptons from the decay of the Z boson.

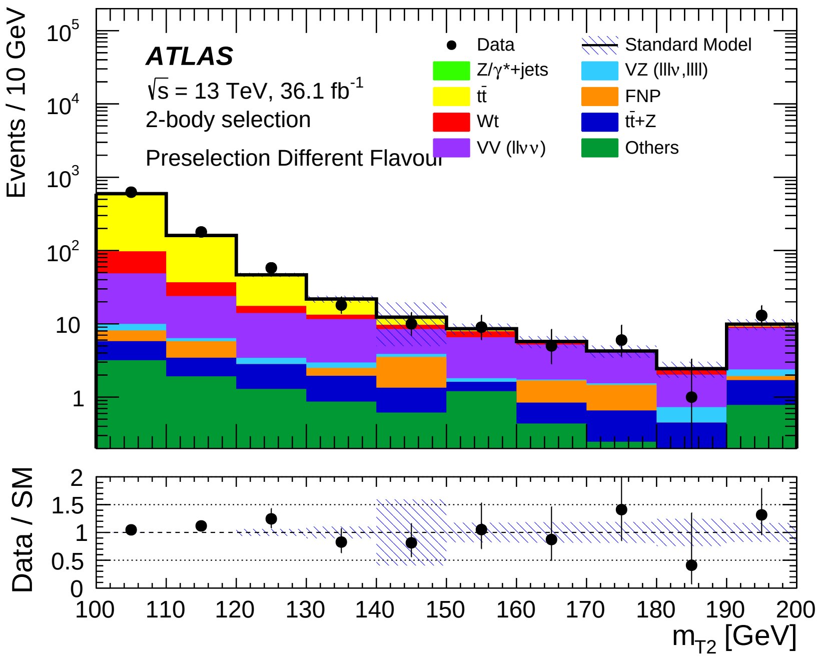

FIGURE 3.3: Distribution of m_{T2} for DF events. The contributions from all SM backgrounds are shown. The rightmost bin includes overflow events.

Other kinematic discriminators

Other sets of discriminating variables are used to further separate the signal from the SM backgrounds. The missing transverse momentum and the p_{T} of the leading leptons and jets are used to define these useful ratio variables:

$$R_{2\ell 2j} = \frac{E_{\mathrm{T}}^{\mathrm{miss}}}{E_{\mathrm{T}}^{\mathrm{miss}} + p_{\mathrm{T}}(\ell_1) + p_{\mathrm{T}}(\ell_2) + p_{\mathrm{T}}(j_1) + p_{\mathrm{T}}(j_2)} \tag{3.2}$$

$$R_{2\ell} = \frac{E_{\mathrm{T}}^{\mathrm{miss}}}{p_{\mathrm{T}}(\ell_1) + p_{\mathrm{T}}(\ell_2)} \tag{3.3}$$

The variables $R_{2\ell 2j}$ and $R_{2\ell}$ are used to reject backgrounds, e.g. Z/γ^*+jets, which peak at lower values than the signal.

Other variables employed are :

- $\mathbf{p}_{\mathrm{T,boost}}^{\ell\ell}$: defined as the vector

  $$\mathbf{p}_{\mathrm{T,boost}}^{\ell\ell} = \mathbf{p}_{\mathrm{T}}^{\mathrm{miss}} + \mathbf{p}_{\mathrm{T}}(\ell_1) + \mathbf{p}_{\mathrm{T}}(\ell_2).$$

  The $\mathbf{p}_{\mathrm{T,boost}}^{\ell\ell}$ variable, with magnitude $p_{\mathrm{T,boost}}^{\ell\ell}$, can be interpreted as the opposite of the vector sum of all the transverse hadronic activity in the event.

- $\Delta\phi_{\mathrm{boost}}$: the azimuthal angle between the $\mathbf{p}_{\mathrm{T}}^{\mathrm{miss}}$ vector and the $\mathbf{p}_{\mathrm{T,boost}}^{\ell\ell}$ vector [116].

- Δx: defined as

  $$\Delta x = \frac{2 \cdot (p_{\mathrm{z}}(\ell_1) + p_{\mathrm{z}}(\ell_2))}{E_{\mathrm{CM}}}$$

  where $E_{\mathrm{CM}} = 13$ TeV is used and $p_{\mathrm{z}}(\ell_1)$,$p_{\mathrm{z}}(\ell_2)$ are respectively the leading and sub-leading lepton longitudinal momenta. This variable helps to discriminate between gluon- and quark-initiated processes. The former tend to peak towards zero, while the latter tend to peak at higher values.

- $m_{b2\ell}^{\mathrm{min}}$ is the smallest invariant mass computed between the leading p_{T} b-tagged jet and each of the two leptons in the event. In events with two top quarks decaying dileptonically, at least one of the two mass combinations must be bounded from above by $m_{b2\ell}^{\mathrm{min}} < \sqrt{m_t^2 - m_W^2}$.

- $E_{\mathrm{T,corr}}^{\mathrm{miss}}$ is defined as the vectorial sum of the momentum of the same-flavour opposite-charge lepton pair to the $\mathbf{p}_{\mathrm{T}}^{\mathrm{miss}}$ vector.

3.3 Event selection

As previously mentioned, during Run 2 the LHC provides bunch collisions every 25 ns corresponding to a frequency of 40 MHz. The data-acquisition system cannot save each events at this frequency. For this reason an online event selection, called *trigger system* is employed in ATLAS to select only the most interesting events, characterised by hard scattering collision between partons inside the protons. In this analysis, events are accepted if they pass the trigger selection requiring a minimum of two electrons, two muons or an electron and a muon matched to the trigger objects. The p_{T} threshold of each triggers have been chosen in order to follow the conditions of the LHC with respect to the instantaneous luminosity available keeping the number of events recorded higher as possible. The triggers used are listed in Table 3.4.

Trigger Type	Trigger Name	Dataset
Di-electron	`HLT_2e12_lhloose_L12EM10VH`	2015
	`HLT_2e15_lhvloose_nod0_L12EM13VH`	2016
	`HLT_2e17_lhvloose_nod0`	
Di-muon	`HLT_mu18_mu8noL1`	2015
	`HLT_mu20_mu8noL1`	2016
	`HLT_mu22_mu8noL1`	
Electron-Muon	`HLT_e17_lhloose_mu14`	2015
	`HLT_e17_lhloose_nod0_mu14`	2016

TABLE 3.4: Triggers used in the analysis.

The off-line selection requires that the leading lepton has a p_{T} larger than 25 GeV and the sub-leading lepton a p_{T} larger than 20 GeV, ensuring that trigger efficiencies are constant in the relevant phase space.

Events are required to have exactly two signal leptons which must be of opposite electric charge (electrons, muons, or one of each) with an invariant mass (regardless of the flavours of the leptons in the pair) $m_{\ell\ell}$ greater than 20 GeV in order to remove leptons from low-mass resonances. Four signal regions (SRs) are defined. Three of them ($\mathrm{SRA}_{180}^{\text{2-body}}$,$\mathrm{SRB}_{140}^{\text{2-body}}$,$\mathrm{SRC}_{110}^{\text{2-body}}$) are then divided with respect to the flavour of the two leptons, same-flavour (SF) for pair of electrons or muons and different-flavour (DF) for the case of one electron and one muon. For SRt3 SF and DF leptons are not divided. Events with SF lepton pairs with $m_{\ell\ell}$ between 71.2 and 111.2 GeV are rejected, in order to reduce the contribution of leptons from the decay of the Z boson. No additional selection is applied to the $m_{\ell\ell}$ value of different-flavour (DF) lepton pairs.

The selections for $\mathrm{SRA}_{180}^{\text{2-body}}$, $\mathrm{SRB}_{140}^{\text{2-body}}$, $\mathrm{SRC}_{110}^{\text{2-body}}$ target the top squark two-body decays (Figures 1.7(b),1.7(a)) into either a bottom quark and a chargino, with the chargino decaying into the lightest neutralino and a W boson, or a near-mass-shell top quark and a neutralino. On the other side, the selection for SRt3 targets the associated production of DM with top quark pairs. In these decays, the kinematic properties of signal events are similar to those of $t\bar{t}$ events. In particular, when the top squarks are produced at rest the momenta carried by the neutralinos in the final state are small and the discrimination difficult. Better separation between signal events and the $t\bar{t}$ background can be obtained for top squark pairs which recoil from initial-state radiation (ISR).
The SR selections have been optimised by a simultaneous scan of the most discriminant variables presented in Section 3.2, assuming a 30% systematic uncertainty on the expected SM backgrounds, aiming at maximizing the discovery sensitivity[2]. The best cuts have been selected from the signal models not excluded by the latest Run 2 limits.

The signal regions are summarised in Table 3.5. The SRs denoted by $\mathrm{SR(A,B,C)}_x^{2-\mathrm{body}}$ targets SUSY models and x stands for the lower bound of the m_{T2} interval. SRt3 were optimised to target the DM model. Description of each of the SRs are presented in the following.

- $\mathrm{SRA}_{180}^{\text{2-body}}$ targets the stop decay into $b\tilde{\chi}_1^{\pm}$ (Figure 1.7(b)), in scenarios where $m_{\tilde{t}_1}$ - $m_{\tilde{\chi}_1^{\pm}}$ is below 10 GeV and the b-jets from the decay of the $\tilde{t}_1$ are too low in energy to be reconstructed. For this reason, b-jets with $p_{\mathrm{T}} > 25$ GeV are vetoed to reduce the contamination from SM processes including top quarks. No further requirement is imposed on the hadronic activity of the event. Events with SF leptons are required to have $m_{\ell\ell} > 111.2$ GeV and $R_{2\ell 2j} > 0.3$ to reduce the contamination from Z/γ^*+jets events. The contribution from diboson production is expected to be the dominant background in the SR and it is reduced

[2] computed using `RooStats::NumberCountingUtils::BinomialObsZ`

by requiring the events to have $\Delta x < 0.07$. Furthermore, events are required to have $m_{\mathrm{T2}} > 180$ GeV.

- $\mathrm{SRB}_{140}^{\text{2-body}}$ targets the stop decay into $b\tilde{\chi}_1^{\pm}$ (Figure 1.7(a)), in scenarios with a mass-splitting between the top squark and the chargino larger than 10 GeV, such that the jets from the hadronisation of b-quarks are expected to be detectable. At least two jets with $p_{\mathrm{T}} > 25$ GeV are required, with at least one of them being identified as a b-jet. Events from $t\bar{t}$ and Z/γ^*+jets production are suppressed by requiring $\Delta\phi_{\mathrm{boost}} < 1.5$. The main expected SM processes satisfying this selection are $t\bar{t}$ and $t\bar{t}$ $+Z$ with the Z boson decaying into neutrinos. A final selection of $m_{\mathrm{T2}} > 140$ GeV is applied. Because of the similar final state, this selection is the most sensitive to signal scenarios in which the $\tilde{t}_1$ decays into $t + \tilde{\chi}_1^0$, with large $m_{\tilde{t}_1}$ - $m_{\tilde{\chi}_1^0}$.
- $\mathrm{SRC}_{110}^{\text{2-body}}$ targets the stop decay into $t + \tilde{\chi}_1^0$(Figure 1.7(a)), in scenarios where $m_{\tilde{t}_1} \sim m_{\tilde{\chi}_1^0} + m_t$. Candidate events are required to have $E_{\mathrm{T}}^{\mathrm{miss}} > 200$ GeV and at least three jets with $p_{\mathrm{T}} > 25$ GeV, where one of the jets is interpreted as Initial State Radiation (ISR) jet. The other two jets are expected to arise from the decay of the top quarks in the final state. One of the jets in the event is required to be b-tagged, effectively separating the signal events from SM diboson production. The Z/γ^*+jets background is suppressed by requiring $R_{2\ell}$ to be larger than 1.2. Events are finally required to have $m_{\mathrm{T2}} > 110$ GeV.
- SRt3 targets DM produced in association with top quarks (Figure 1.11). In this events selection, a linear combination of m_{T2} and the $E_{\mathrm{T}}^{\mathrm{miss}}$ called $\xi^+$is used, in order to maximise the discrimination power of the two variables. Further requirements are placed on $\Delta\phi_{\mathrm{boost}}$ and $m_{b2\ell}^{\mathrm{min}}$. Both variables are used to further reject residual contamination from reducible backgrounds for this selection. The requirement on this variable reject $Z(\ell^+\ell^-)$+jets events where the $E_{\mathrm{T}}^{\mathrm{miss}}$ arises from jet mismeasurements, while retaining a large fraction of the signal.

	$\text{SRA}_{180}^{2\text{-body}}$		$\text{SRB}_{140}^{2\text{-body}}$		$\text{SRC}_{110}^{2\text{-body}}$		SRt3	
Lepton flavour	SF	DF	SF	DF	SF	DF	SF	DF
$p_{\text{T}}(\ell_1)[GeV]$	> 25		> 25		> 25		> 25	
$p_{\text{T}}(\ell_2)[GeV]$	> 20		> 20		> 20		> 20	
$m_{\ell\ell}$ [GeV]	> 111.2	> 20	[20, 71.2] or > 111.2	> 20	[20, 71.2] or > 111.2	> 20	[20, 71.2] or > 111.2	> 20
n_{jets}	–		≥ 2		≥ 3		≥ 1	
$n_{b\text{-jets}}$	$= 0$		≥ 1		≥ 1		≥ 1	
$p_{\text{T}}(j_1)$ [GeV]	> 20		> 20		> 20		> 30	
$p_{\text{T}}(bj_1)$ [GeV]	–		> 20		> 20		> 30	
$R_{2\ell 2j}$	> 0.3	–	–		–		–	
$R_{2\ell}$	–		–		> 1.2		–	
Δx	< 0.07		–		–		–	
$\Delta\phi_{\text{boost}}$	–		< 1.5		–		< 0.8	
$E_{\text{T}}^{\text{miss}}$ [GeV]	–		–		> 200		–	
$m_{b2\ell}^{\text{min}}$ [GeV]	–		–		–		< 170	
m_{T2} [GeV]	> 180		> 140		> 110		> 100	
ξ^+ [GeV]	–		–		–		> 170	

TABLE 3.5: Signal region definitions.

3.4 Simulated Samples

Monte Carlo (MC) simulated event samples are used to aid in the estimation of the background from SM processes and to model the SUSY signal.

The event generator, parton shower and hadronisation generator, cross-section normalisation, parton distribution function (PDF) set and underlying-event tuned parameter set (tune) of these samples are given in Table 3.6, and more details of the event generator configurations can be found in Refs. [117–120].

Cross-sections calculated at next-to-next-to-leading order (NNLO) in QCD including resummation of next-to-next-to-leading logarithmic (NNLL) soft gluon terms were used for top quark production processes using powheg-box v2 [121] for the event generator and Pythia 6.428 [122] for the parton shower generator.

For production of top quark pairs in association with vector or Higgs bosons, cross-sections calculated at next-to-leading order (NLO) were used, and the event generator cross-sections calculated by Sherpa (at NLO for most of the processes) are used when normalising the multi-boson backgrounds.

In all MC samples, except those produced by Sherpa [123], the EvtGen v1.2.0 program [124] was used to model the properties of the bottom and charm hadron decays. Additional MC samples are used when estimating systematic uncertainties, as detailed in Section 3.11. SUSY signal samples were generated from leading-order (LO) matrix elements with up to two extra partons, using the MadGraph5 aMC@NLO event generator. The SUSY signals used Pythia 8.186 [126] for the modelling of the SUSY decay chain, parton showering, hadronisation and the description of the underlying event. Parton luminosities were provided by the NNPDF23LO PDF set. Jet–parton matching was realised following the CKKW-L prescription [143], with a matching scale set to one quarter of the pair-produced superpartner mass. In all cases, the mass of the top quark was fixed at 172.5 GeV. Signal cross-sections were calculated to next-to-leading order in the strong coupling constant, adding the resummation of soft gluon emission at next-to-leading-logarithmic accuracy (NLO+NLL) [44, 144, 145]. The nominal cross-sections and their uncertainties were taken from an envelope of cross-section predictions using different PDF sets and factorisation and renormalisation scales, as described in Ref. [45]. The SUSY samples were generated assuming a 100% branching ratio into the respective final states.

For the pMSSM inspired models, the mass spectrum of sparticles was calculated using Softsusy 3.7.3 [146] and cross-checked with SPheno 3.3.8 [147, 148] and Suspect 2.5 [149]. Hdecay and Sdecay, included in Susy-Hit [150] were used to generate decay tables of the SUSY particles.

The event generation for the dark-matter signal samples followed the prescriptions in Ref. [151]. Events were generated from leading-order (LO) matrix elements using the MadGraph generator v2.3.3 [125] interfaced to Pythia v8.212 with the A14 tune for the modelling of the top-quark decay chain (when applicable), parton showering, hadronisation and the description of the underlying event. The renormalisation and factorisation scale choice adopted is the default MadGraph dynamical scale as documented in Ref. [152]. The samples were generated in the 5-flavour scheme. The PDF set NNPDF23LO was used, adopting $\alpha_S = 0.130$ and either the 5-flavour or the 4-flavour scheme consistently with the choice made for generating the events. The jet–parton matching was realised following the CKKW-L prescription. For the $t\bar{t}$ $+\phi/a$ model the matching scale was set to one quarter of the mass of the particle mediating the interaction between the SM and DM sectors. The matching scale was set to 30 GeV. The coupling g between the colour-neutral mediator for the $t\bar{t}$ $+\phi/a$ and $b\bar{b}$ $+\phi/a$ models and both the SM and the dark sector was assumed to be one, which implies pure Yukawa-type couplings between the mediator and the SM quarks. This choice impacts the mediator width and cross-section calculations for these models, but it was shown to have no significant impact on the kinematic properties [151]. The production cross-section was computed at NLO accuracy in the strong coupling constant α_S using the MadGraph5 aMC@NLO generator with the NNPDF30NLO PDF set using $\alpha_S = 0.118$. For this procedure a dynamical scale equal to $P_T/2$ was adopted, with P_T being the scalar sum of the transverse momenta of all final-state particles. The flavour scheme adopted is consistent with that used for event generation. For the mass range in which this analysis is sensitive, the NLO value of the cross-sections for the $t\bar{t}+\phi/a$ model is about 25% larger than the corresponding LO value [129, 130]. This is driven by the MadGraph minimum b-jet p_T requirement due to the strong dependence of the NLO cross-section on this parameter.

To simulate the effects of additional pp collisions in the same and nearby bunch crossings, additional interactions were generated using the soft QCD processes of Pythia 8.186 [126] with the A2 tune [153] and the MSTW2008LO PDF set [79], and they were overlaid onto each simulated hard-scatter event. The MC samples were reweighed to the pile-up distribution observed in the data. The MC samples were processed through an ATLAS detector simulation [154] based on Geant4 [155] or, in the case of $t\bar{t}t$ and the SUSY signal samples, a fast simulation using a parametrisation of the calorimeter response and Geant4 for the other parts of the detector [156]. All MC samples are reconstructed in the same manner as the data. Corrections derived from data control samples are applied to simulated events to account for differences between data and simulation in reconstruction efficiencies, momentum scale and resolution of leptons and in the efficiency and false positive rate for identifying jets resulting from the hadronisation of b-quarks.

Physics process	Event generator	Parton shower generator	Cross-section normalisation	PDF set	Tune
SUSY Signals	MadGraph5 aMC@NLO 2.2.3 [125]	Pythia 8.186 [126]	NLO+NLL [40–45]	NNPDF23LO [127]	A14 [128]
Dark-matter Signals	MadGraph 2.3.3 [125]	Pythia 8.212 [126]	NLO [129, 130]	NNPDF23LO [127]	A14 [128]
Z/γ^*+jets	Sherpa 2.2.1 [123]	Sherpa 2.2.1 [123]	NNLO [131]	NLO CT10 [127]	Sherpa default
$t\bar{t}$	powheg-box v2 [121]	Pythia 6.428 [122]	NNLO+NNLL [132–137]	NLO CT10	Perugia2012 [138]
Wt	powheg-box v2	Pythia 6.428	NNLO+NNLL [139]	NLO CT10	Perugia2012
$t\bar{t}W/Z/\gamma^*$	MadGraph5 aMC@NLO 2.2.2	Pythia 8.186 [126]	NLO [125]	NNPDF23LO	A14
Diboson	Sherpa 2.2.1 [123]	Sherpa 2.2.1 [123]	Generator NLO	NLO CT10	Sherpa default
$t\bar{t}h$	MadGraph5 aMC@NLO 2.2.2	Herwig 2.7.1 [140]	NLO [141]	CTEQ6L1 [142]	A14
Wh, Zh	MadGraph5 aMC@NLO 2.2.2	Pythia 8.186 [126]	NLO [141]	NNPDF23LO	A14
$t\bar{t}WW$, $t\bar{t}t\bar{t}$	MadGraph5 aMC@NLO 2.2.2	Pythia 8.186 [126]	NLO [125]	NNPDF23LO	A14
tZ, tWZ, $t\bar{t}t$	MadGraph5 aMC@NLO 2.2.2	Pythia 8.186 [126]	LO	NNPDF23LO	A14
Triboson	Sherpa 2.2.1 [123]	Sherpa 2.2.1 [123]	Generator LO, NLO	CT10	Sherpa default

Table 3.6: Simulated signal and background event samples: the corresponding event generator, parton shower generator, cross-section normalisation, PDF set and underlying-event tune are shown.

Kinematic distributions studies

A comparison between 2015 and 2016 data and MC simulation is made for the main observables used in the analysis. The distributions are also shown separately for the same and different flavour channels. The events are selected requiring $m_{\mathrm{T2}} > 100$ GeV, $m_{\ell\ell} > 20$ GeV and for SF leptons $m_{\ell\ell} < 71.2$ GeV and $m_{\ell\ell} > 111.2$ GeV.

Figure 3.4 and 3.5 show the p_{T} distribution of the leading lepton at the preselection level for same and different flavour respectively. Figure 3.6 and 3.7 show the p_{T} distribution of the sub-leading lepton at the preselection level for same and different flavour respectively. Figure 3.10 and 3.11 show the jets multiplicity distribution for same and different flavour respectively. Figure 3.8 and 3.9 show distribution of the b-tagged jets multiplicity for same and different flavour respectively. Figure 3.12 and 3.13 show the $E_{\mathrm{T}}^{\mathrm{miss}}$ distribution for same and different flavour respectively. The overall agreement between data and Monte Carlo is consistent within uncertainties.

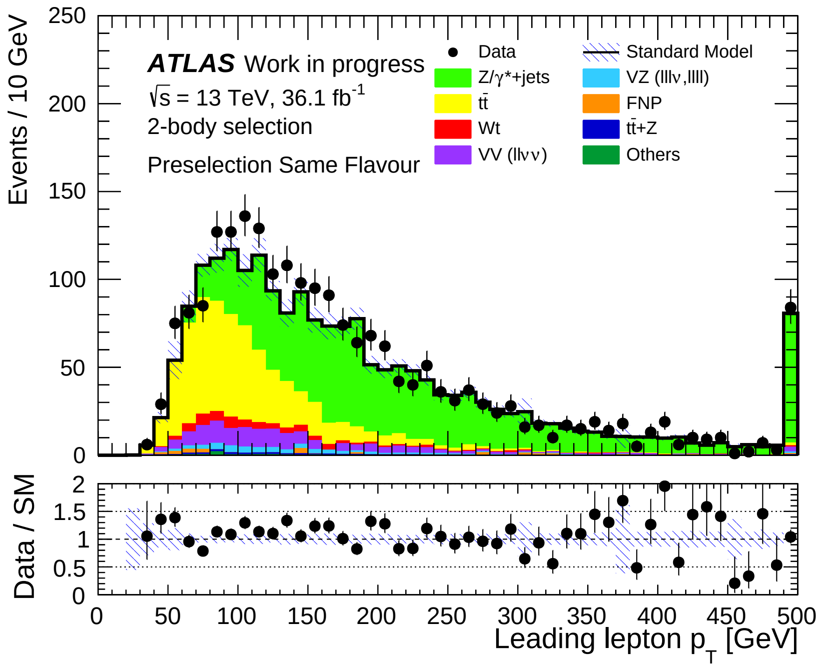

FIGURE 3.4: Distribution of p_T of the leading lepton for events satisfying the preselection criteria Same Flavour before the background fit. The contributions from all SM backgrounds are shown; the hatched bands represent the total statistical and systematic uncertainty. The rightmost bin includes overflow events.

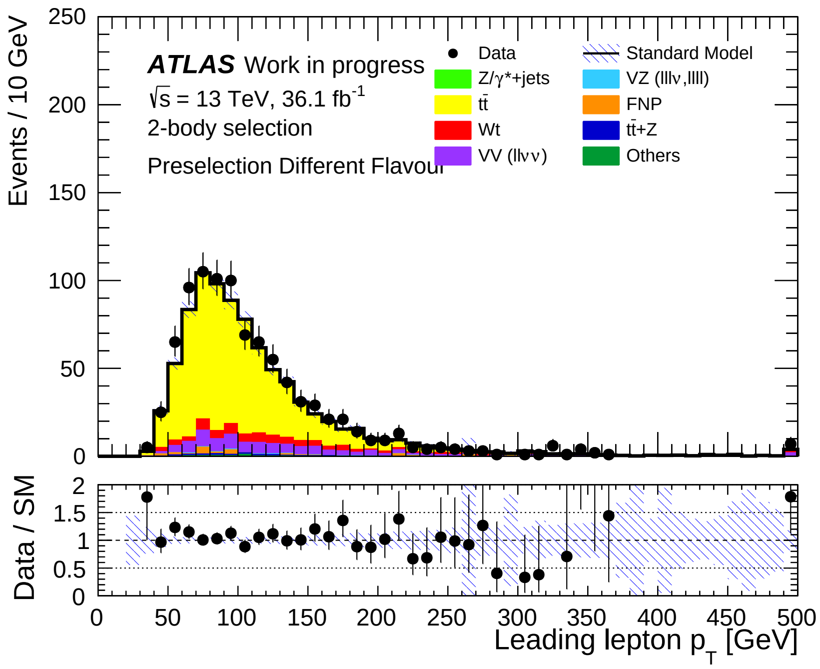

FIGURE 3.5: Distribution of p_T of the leading lepton for events satisfying the preselection criteria Different Flavour before the background fit. The contributions from all SM backgrounds are shown; the hatched bands represent the total statistical and systematic uncertainty. The rightmost bin includes overflow events.

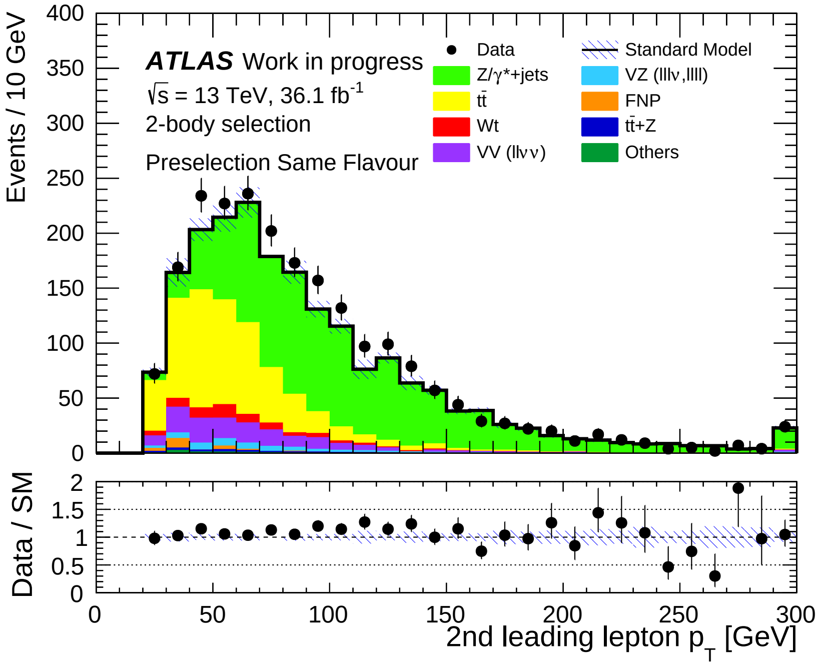

FIGURE 3.6: Distribution of p_T of the sub–leading for events satisfying the preselection criteria Same Flavour before the background fit. The contributions from all SM backgrounds are shown; the hatched bands represent the total statistical and systematic uncertainty. The rightmost bin includes overflow events.

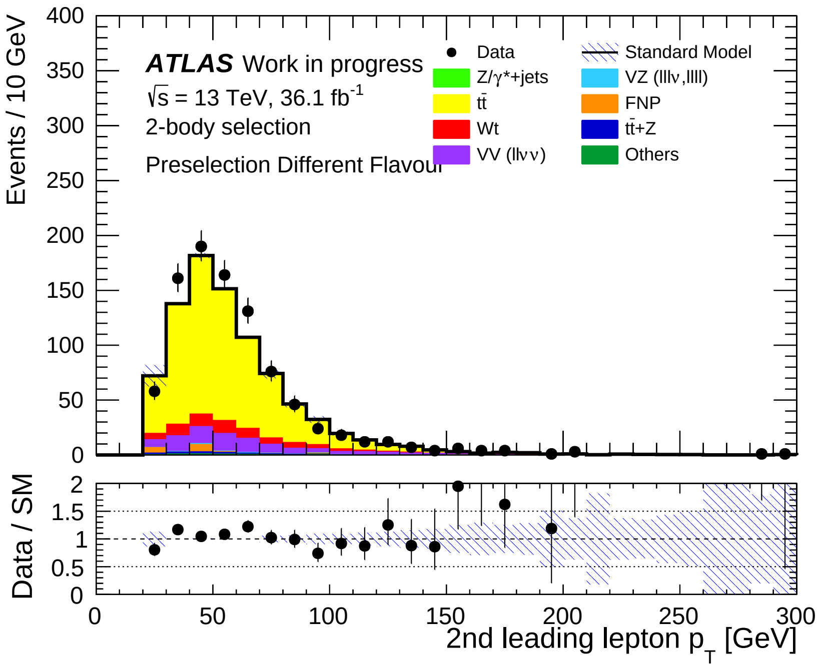

FIGURE 3.7: Distribution of p_T of the sub–leading for events satisfying the preselection criteria Different Flavour before the background fit. The contributions from all SM backgrounds are shown; the hatched bands represent the total statistical and systematic uncertainty. The rightmost bin includes overflow events.

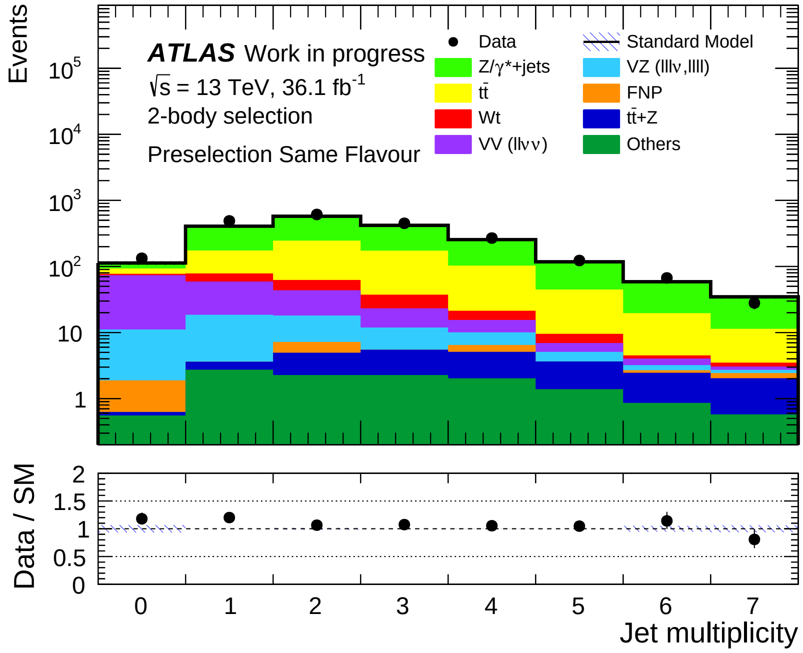

FIGURE 3.8: Distribution of b-tagged jets multiplicity for events satisfying the preselection criteria Same Flavour before the background fit. The contributions from all SM backgrounds are shown; the hatched bands represent the total statistical and systematic uncertainty. The rightmost bin includes overflow events.

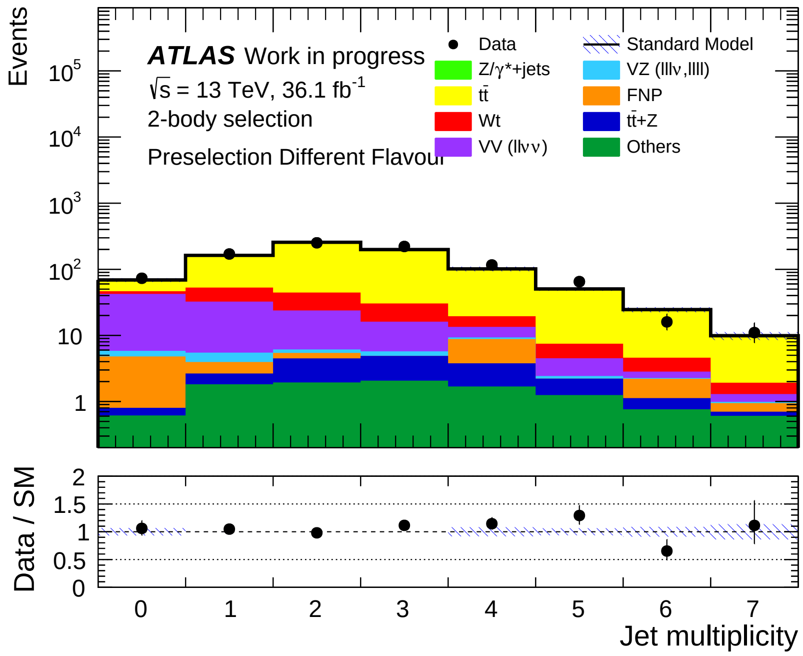

FIGURE 3.9: Distribution of b-tagged jet multiplicity for events satisfying the preselection criteria Different Flavour before the background fit. The contributions from all SM backgrounds are shown; the hatched bands represent the total statistical and systematic uncertainty. The rightmost bin includes overflow events.

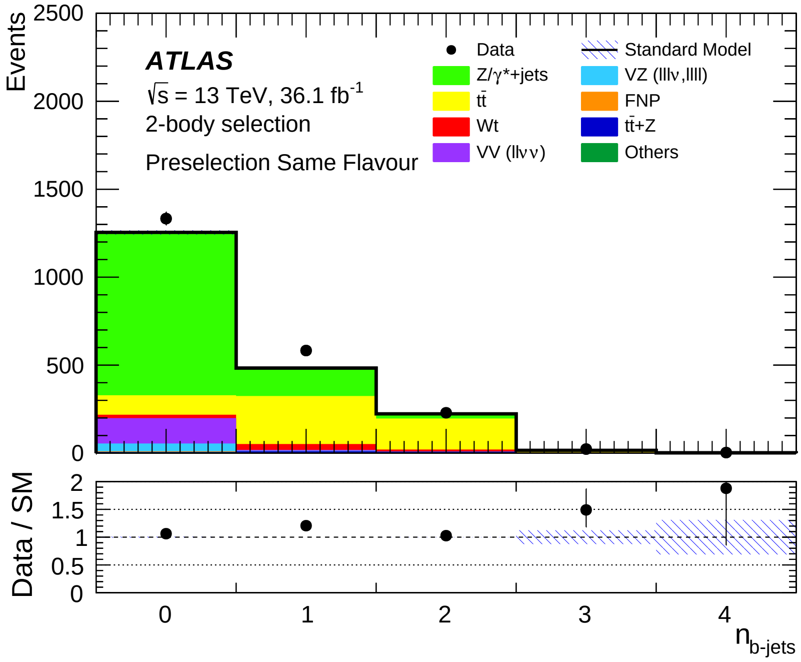

FIGURE 3.10: Distribution of jet multiplicity for events satisfying the preselection criteria Same Flavour before the background fit. The contributions from all SM backgrounds are shown; the hatched bands represent the total statistical and systematic uncertainty. The rightmost bin includes overflow events.

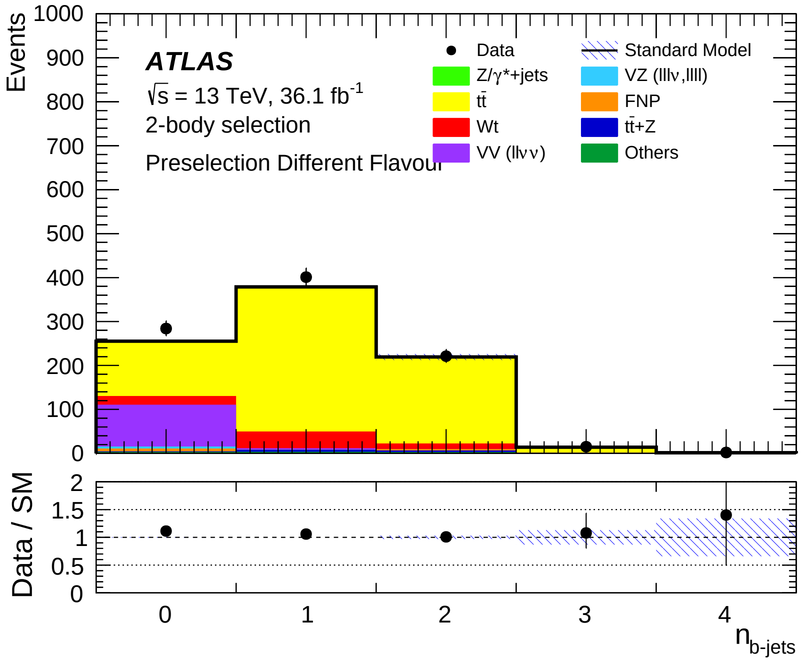

FIGURE 3.11: Distribution of jets multiplicity for events satisfying the preselection criteria Different Flavour before the background fit. The contributions from all SM backgrounds are shown; the hatched bands represent the total statistical and systematic uncertainty. The rightmost bin includes overflow events.

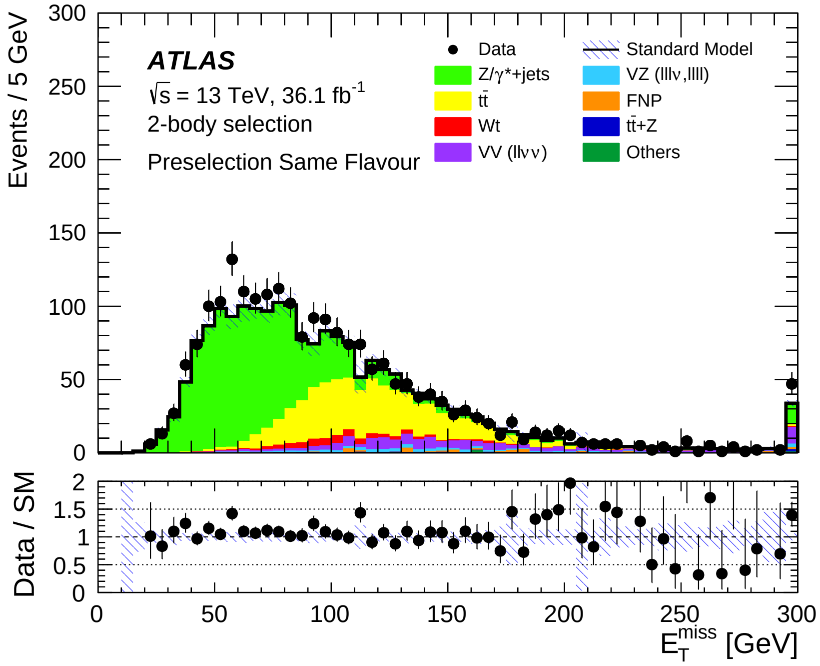

FIGURE 3.12: Distribution of $E_{\mathrm{T}}^{\mathrm{miss}}$ for events satisfying the preselection criteria Same Flavour before the background fit. The contributions from all SM backgrounds are shown; the hatched bands represent the total statistical and systematic uncertainty. The rightmost bin includes overflow events.

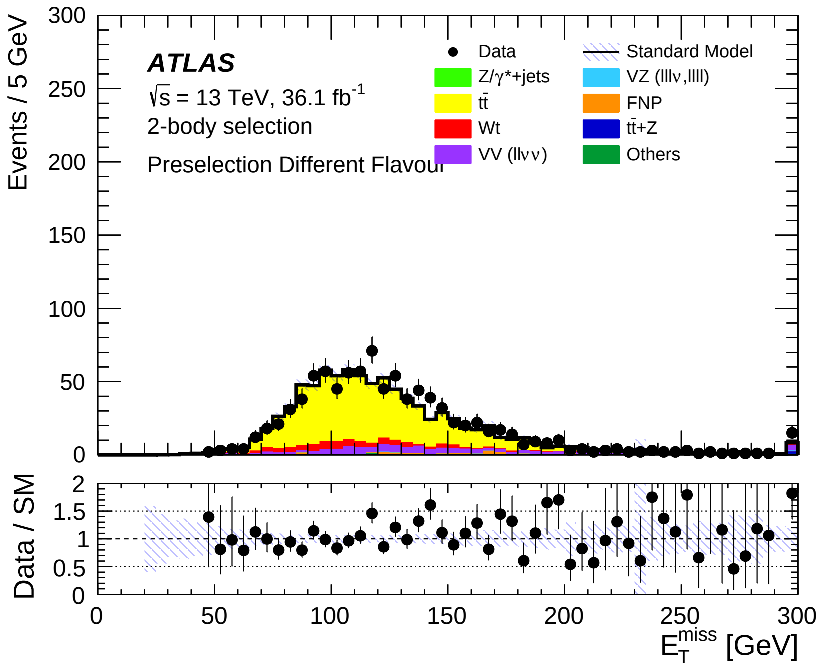

FIGURE 3.13: Distribution of $E_{\mathrm{T}}^{\mathrm{miss}}$ for events satisfying the preselection criteria Different Flavour before the background fit. The contributions from all SM backgrounds are shown; the hatched bands represent the total statistical and systematic uncertainty. The rightmost bin includes overflow events.

3.5 Standard Model background estimation

The main background processes in this analysis are diboson production in $\mathrm{SRA}^{\text{2-body}}_{180}$, and $t\bar{t}$ and $t\bar{t}$+Z in $\mathrm{SRB}^{\text{2-body}}_{140}$, $\mathrm{SRC}^{\text{2-body}}_{110}$ and SRt3. The contribution of these processes is estimated using a semi-data driven techniques. Taking, as an example, the $t\bar{t}$ process, the number of $t\bar{t}$ events in a given signal region X ($N^{X}_{t\bar{t}}$) is estimated rescaling the number of events in data in a control region (CR) by a transfer factor measured using MC event samples. The number of events N^{obs}_{CR} observed in each control region is related to the backgrounds yields by the equation

$$\begin{aligned} N^{obs}_{CR} = \mu_{t\bar{t}} \cdot N^{MC}_{t\bar{t},CR} + \mu_{VV\text{-}SF} \cdot N^{MC}_{VV\text{-}SF,CR} + \mu_{t\bar{t}Z} \cdot N^{MC}_{t\bar{t}Z,CR} \\ + \mu_{VZ} \cdot N^{MC}_{VZ,CR} + N^{MC}_{Others,CR} + N^{data}_{fakes} \end{aligned} \tag{3.4}$$

where $N^{MC}_{t\bar{t},CR}$, $N^{MC}_{VV\text{-}SF,CR}$, $N^{MC}_{t\bar{t}Z,CR}$ and $N^{MC}_{VZ,CR}$ are respectively the yields predicted by MC in the CR for $t\bar{t}$, Same Flavour diboson, $t\bar{t}$+Z and VZ background processes. The μ_i is the *transfer factor* that are applied to the background i. The *Others* category contains the contributions from $t\bar{t}$+W, $t\bar{t}$+h, $t\bar{t}$+WW, $t\bar{t}$+t, $t\bar{t}$+$t\bar{t}$, Wh, ggh and Zh production. The N^{data}_{fakes} corresponds to the number of events with fake and non-prompt lepton derived from data (See Section 3.10). The transfer factors $\mu_{t\bar{t}}, \mu_{VV\text{-}SF}, \mu_{t\bar{t}Z}$ and μ_{VZ} are determined by solving a system equation similar to Equation 3.4 one for each CRs. The transfer factors are then applied to evaluate the background expectation in the SRs:

$$\begin{aligned} N^{obs}_{SR} = \mu_{t\bar{t}} \cdot N^{MC}_{t\bar{t},SR} + \mu_{VV\text{-}SF} \cdot N^{MC}_{VV\text{-}SF,SR} + \mu_{t\bar{t}Z} \cdot N^{MC}_{t\bar{t}Z,SR} \\ + \mu_{VZ} \cdot N^{MC}_{VZ,SR} + N^{MC}_{Others,SR} + N^{data}_{fakes} \end{aligned} \tag{3.5}$$

The transfer factors and their uncertainties are calculated with a fit based on a profile likelihood method [157]. The likelihood function is defined $\mathcal{L}(n_s; \mu_i b_i, \theta)$ as follows:

$$\mathcal{L}(n_s; \mu_i, b_j, \theta) = Poiss(n_s | s(\mu_{sig}, \mu_i, b_j, \theta)) \times \left(\prod_{i \in CR} Poiss(n_i | s(\mu_i, b_j, \theta)) \right) \times N_{\text{syst}}(\theta_0, \theta) \ .$$

where:

- $Poiss(n_s|s)$ is a Poisson probability density function (pdf) describing the expected number of events n_s in each signal region, given the expectation s.
- The *transfer factors* μ_i are treated as free parameters which correspond to the overall normalisation scale of each of the background i.
- μ_{sig} is the signal strength for new physics to be tested. The fit with $\mu = 0$ corresponds to the background-only hypothesis while with $\mu = 1$ corresponds to the nominal signal + background hypothesis. This continuous parameter μ_{sig} is the parameter of interest.
- b is the number of background events in CRs or SR.
- N_{syst} models all the systematic uncertainties described in Section 3.11. Each Nuisance parameter (NP, θ) is described by a Gaussian centred on zero and of width one. Zero corresponds to the nominal rate in all regions, while ± 1 correspond to the "up" and "down" systematic variations. Systematic uncertainties which are one-sided are symmetrised. Different nuisance parameters are treated as uncorrelated.Uncertainties which affects both the background and the signal are considered as completely correlated.

Three different types of fits are considered:

	Control Region						
	$\mathrm{CR}_{t\bar{t}}^{\text{2-body}}$	$\mathrm{CR}_{t\bar{t},3j}^{\text{2-body}}$	CRTt3	$\mathrm{CR}_{VV\text{-SF}}^{\text{2-body}}$	$\mathrm{CR}_{t\bar{t}Z}$	CR_{VZ}	$\mathrm{CR}3\ell$
Corresponding transfer factor	$\mu_{t\bar{t},1}$	$\mu_{t\bar{t},2}$	$\mu_{t\bar{t},3}$	$\mu_{VV,SF}$	$\mu_{t\bar{t}Z,1}$	μ_{VZ}	$\mu_{t\bar{t}Z,2}$
Signal Region							
$\mathrm{SRA}_{180}^{\text{2-body}}$	×			×	×	×	
$\mathrm{SRB}_{140}^{\text{2-body}}$	×			×	×	×	
$\mathrm{SRC}_{110}^{\text{2-body}}$		×			×		
SRt3			×				×

Table 3.7: Summary of the Control Regions used to normalise the backgrounds for each of the signal regions

- In a *background-only fit*, only the background samples are considered. Any potential signal contamination is neglected. The observed number of events in each CR is used as a constraint and the corresponding μ_i terms as free parameters are determined. The resulting transfer factors are extrapolated to the SR and VR regions; the final error on the fitted total background in the CRs, VRs and SRs properly takes into account the correlation matrix between the different errors. validate the
- The model independent fit provides limits on any additional number of events in the SRs beyond the expected number of background events. This allow the results of the analysis to be interpreted in the contest of any generic model.
- The model dependent fit, also known as "exclusion fit", is a frequentist fit performed intending to study a specific signal model. The normalisation of the signal (μ_{sig}) in the SR is the Parameter Of Interest (POI) and this fit is performed taking into account signal contamination in the CRs. If there is no significant excess of events in the SRs, then exclusion limits can be placed on a specific signal model considered. In this scenario the statistical, modelling and experimental uncertainties on the signal samples are also taken into account and are treated in a similar manner as described above for the background uncertainties. The asymptotic calculator is used when performing the exclusion fit. The results of the exclusion fit when taking into account all of the signal mass scenarios allow an exclusion contour to be placed in the mass plane considered. In this search two mass plane are considered, the ($m_{\tilde{t}_1}, m_{\tilde{\chi}_1^0}$) for the SUSY searches and the mono-dimensional scan of ($m_{\phi/a}$ and m_χ) fixing one of the two parameters for the DM search. To construct an exclusion contour, a signal model hypothesis test is used. The model can be considered to be excluded at the 95% Confidence Level (CL), if the results of the hypothesis test return a p-value of > 0.05. In these scenarios the p-value is the probability of rejecting the background-only hypothesis. By performing the hypothesis test on the different mass point of the model, an exclusion contour (limit) can be produced. For the model-dependent exclusion limits, a shape fit of the m_{T2} distribution is performed for the $\mathrm{SRA}_{180}^{\text{2-body}}$ and $\mathrm{SRB}_{140}^{\text{2-body}}$ selections: the distribution is divided into bins of width 20 GeV, starting from $m_{\mathrm{T2}} = 120$ GeV; the last bin's low boundary corresponds to the requirement on the same variable in the definitions of $\mathrm{SRA}_{180}^{\text{2-body}}$ and $\mathrm{SRB}_{140}^{\text{2-body}}$; each bin is referred to as $\mathrm{SR(A,B)}_{x,y}^{2-\mathrm{body}}$, where x and y denote the low and high edges m_{T2} of the bin.

The background only fit is used to calculated the normalisation of the main SM backgrounds. In the following, the seven CRs are defined: three to normalise the $t\bar{t}$ background, one for same flavour leptons coming from diboson process, two to normalise the contribution of $t\bar{t}$+Z and one to normalise the 3 leptons contribution of diboson process (ZW, ZZ).

Overlapping regions ($\mathrm{CR}_{t\bar{t}}^{\text{2-body}}$,$\mathrm{CR}_{t\bar{t},3j}^{\text{2-body}}$ and CRTt3 or $\mathrm{CR}_{t\bar{t}Z}$ and CRTt3), are only included in independent background fits, so that no correlation is introduced. The expected signal contamination in the CRs is generally below 5%. The CR selection definitions are summarised respectively in Table 3.8.

	$CR^{2\text{-body}}_{t\bar{t}}$	$CR^{2\text{-body}}_{t\bar{t},3j}$	CRTt3	$CR^{2\text{-body}}_{VV\text{-SF}}$	$CR_{t\bar{t}Z}$	CR_{VZ}	$CR3\ell$
Leptons	2, DF	2	2	2, SF	3	3	3
m_{T2} [GeV]	[100, 120]	[60, 100]		[100, 120]	–	–	–
$p^{\ell\ell}_{T,\text{boost}}$ [GeV]	–	–		< 25	–	–	–
$\Delta\phi_{\text{boost}}$	–	–		–	–	–	–
$R_{2\ell 2j}$	–	–		> 0.3	–	–	–
$n_{b\text{-jets}}$	≥ 1	≥ 1	≥ 1	0	≥ 2 or $= 1$	0	≥ 2 or $= 1$
n_{jets}	–	≥ 3	≥ 1	–	≥ 3 or ≥ 4	–	≥ 3 or ≥ 4
$E^{\text{miss}}_{T,\text{corr}}$ [GeV]	–	–		–	> 120	> 120	–
E^{miss}_{T} [GeV]		> 200		–	–	–	–
$R_{2\ell}$	–	< 1.2		–	–	–	–
ξ^{+}[GeV]	–		<150	–	–	–	–
$m^{\text{min}}_{b2\ell}$[GeV]	–		<170	–	–	–	–
$\xi^{+}_{\ell\ell}$[GeV]	–	–	–	–	–	–	>120
$m^{\text{min}}_{2b\ell}$[GeV]	–	–	–	–	–	–	<170

TABLE 3.8: Control region definitions. The common selection defined in Section 3.3 also applies to all regions except $CR_{t\bar{t}Z}$ and CR_{VZ} and $CR3\ell$, which require three leptons including one same-flavour opposite-charge pair with $|m_{\ell\ell} - m_Z| < 20$ GeV.

3.6 Control regions for $t\bar{t}$

The events passing the $\mathrm{CR}^{\text{2-body}}_{t\bar{t}}$ $\mathrm{CR}^{\text{2-body}}_{t\bar{t},3j}$ and CRTt3 selection requirement have been investigated to check the modelling of the $t\bar{t}$ background in simulation. In order to reduce the contribution of Z/γ^* and select a region enriched of the $t\bar{t}$ process, events with different flavour leptons (one electron and one muon) are selected. The b-tagged jet multiplicity and $E_{\mathrm{T}}^{\mathrm{miss}}$ distribution for events passing the $\mathrm{CR}^{\text{2-body}}_{t\bar{t}}$selection is shown in Figure 3.14, 3.15. The MC contribution for the $t\bar{t}$ background and for all the other backgrounds is shown in Table 3.9 for $\mathrm{CR}^{\text{2-body}}_{t\bar{t}}$, in Table 3.10 for $\mathrm{CR}^{\text{2-body}}_{t\bar{t},3j}$ and in Table 3.11 for CRTt3. The b-tagged jet multiplicity $n_{b\text{-jets}}$ distribution in the $\mathrm{CR}^{\text{2-body}}_{t\bar{t}}$region is shown in Figure 3.14. In Figure 3.15, the $E_{\mathrm{T}}^{\mathrm{miss}}$ distribution in the $\mathrm{CR}^{\text{2-body}}_{t\bar{t}}$region is presented.

	$\mathrm{CR}^{\text{2-body}}_{t\bar{t}}$
Total SM Events	559 ± 7.96
$t\bar{t}$	504 ± 3.22
Wt	44 ± 6
Z/γ^*+jets	$0.02^{+0.05}_{-0.02}$
VV-DF	2.2 ± 0.8
VZ	0.18 ± 0.12
$t\bar{t}$ +Z	3.57 ± 0.21
Others	3.8 ± 0.4
Fake and non-prompt	1.6 ± 0.9

TABLE 3.9: Expected contribution in the $\mathrm{CR}^{\text{2-body}}_{t\bar{t}}$. The “Others” category contains the contributions from $t\bar{t}W$, $t\bar{t}h$, $t\bar{t}WW$, $t\bar{t}t$, $t\bar{t}t\bar{t}$, Wh, ggh and Zh production. Combined statistical and systematic uncertainties are included.

	$\mathrm{CR}^{\text{2-body}}_{t\bar{t},3j}$
Total SM Events	228.93 ± 72.18
$t\bar{t}$	201 ± 16
$t\bar{t}$ +Z	1.23 ± 0.32
Wt	23 ± 7
VV	1.69 ± 0.30
Z/γ^*+jets	0.05 ± 0.02
Others	1.91 ± 0.12

TABLE 3.10: Expected contribution in the $\mathrm{CR}^{\text{2-body}}_{t\bar{t},3j}$. The “Others” category contains the contributions from $t\bar{t}W$, $t\bar{t}h$, $t\bar{t}WW$, $t\bar{t}t$, $t\bar{t}t\bar{t}$, Wh, ggh and Zh production. Combined statistical and systematic uncertainties are included.

	CRTt3
Total SM Events	219.74 ± 3.17
$t\bar{t}$	204.96 ± 0.02
$t\bar{t}$+Z	2.03 ± 0.32
Wt	9.0 ± 2.6
VV	0.67 ± 0.41
Fake and non-prompt	$0.0^{+0.3}_{-0.0}$
Others	3.1 ± 1.2

TABLE 3.11: Expected contribution in the CRTt3. The “Others” category contains the contributions from $t\bar{t}W$, $t\bar{t}h$, $t\bar{t}WW$, $t\bar{t}t$, $t\bar{t}t\bar{t}$, Wh, ggh and Zh production. Combined statistical and systematic uncertainties are included.

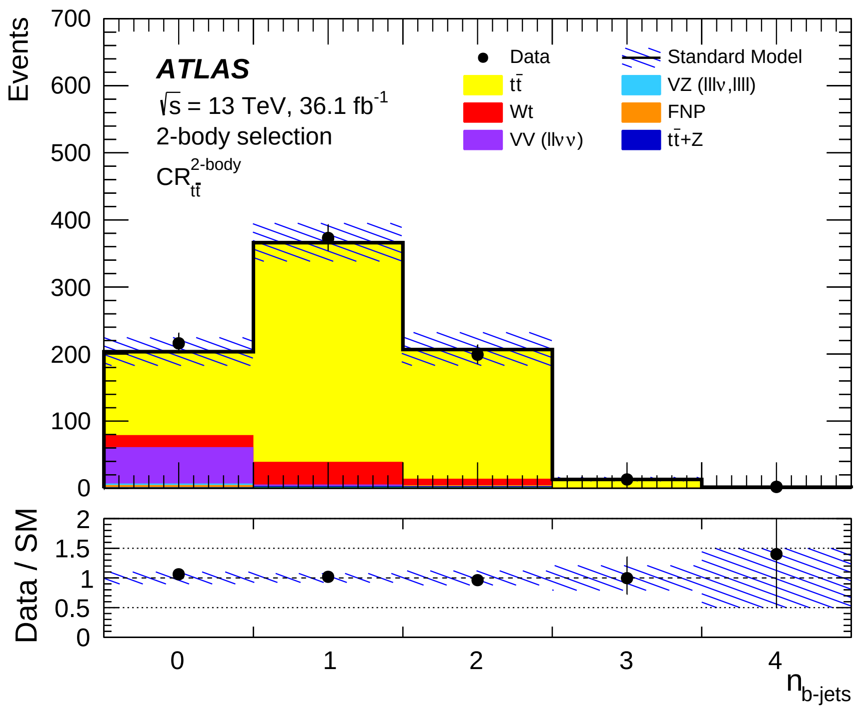

FIGURE 3.14: Distribution of the b-tagged jet multiplicity $n_{b\text{-jets}}$ in the $\mathrm{CR}_{t\bar{t}}^{2\text{-body}}$ region after the $\mathrm{SRA}_{180}^{2\text{-body}}$ background fit. The contributions from all SM backgrounds are shown; the hatched bands represent the total statistical and detector-related systematic uncertainty. The rightmost bin includes overflow events.

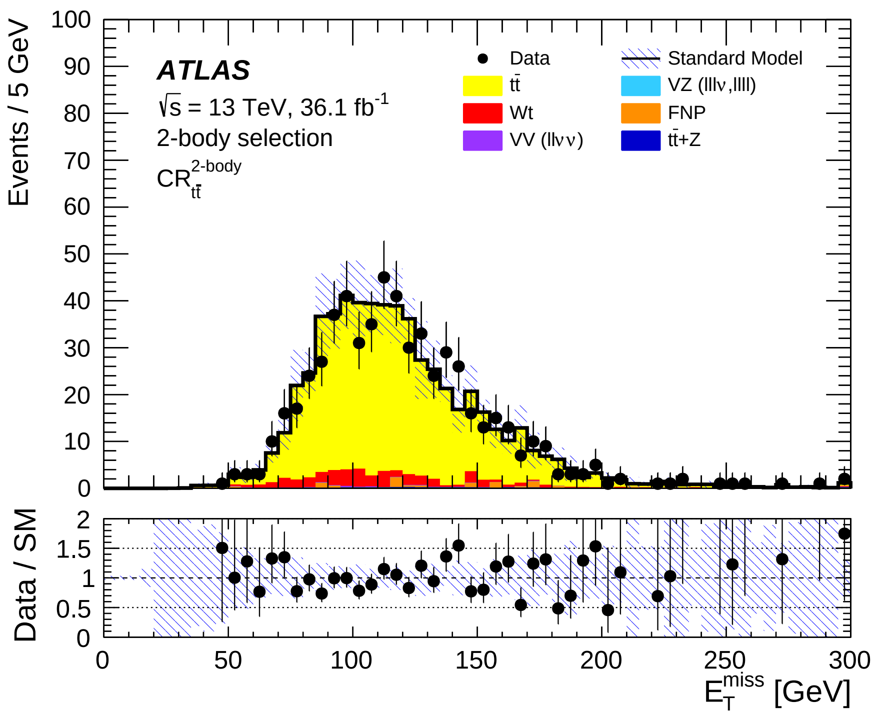

FIGURE 3.15: Distribution of the $E_{\mathrm{T}}^{\mathrm{miss}}$ in the $\mathrm{CR}_{t\bar{t}}^{2\text{-body}}$ region after the $\mathrm{SRA}_{180}^{2\text{-body}}$ background fit. The contributions from all SM backgrounds are shown; the hatched bands represent the total statistical and detector-related systematic uncertainty. The rightmost bin includes overflow events.

3.7 Control region for Diboson

The events passing the $\mathrm{CR}^{\text{2-body}}_{VV\text{-SF}}$ selection requirements are investigated to check the modelling of the diboson (WW,ZZ,WZ) background. The $R_{2\ell 2j}$ distribution and $\mathbf{p}^{\ell\ell}_{\mathrm{T,boost}}$ distribution in the $\mathrm{CR}^{\text{2-body}}_{VV\text{-SF}}$ are shown in Figure 3.16 and 3.16 respectively.

	$\mathrm{CR}^{\text{2-body}}_{VV\text{-SF}}$
Total SM Events	199.06 ± 18.22
$t\bar{t}$	13.9 ± 3.4
Wt	4.0 ± 1.5
Z/γ^{*}+jets	19 ± 10
VV-SF	122.5 ± 9.9
VZ	38.8 ± 6.4
$t\bar{t}$ +Z	$0.08^{+0.09}_{-0.08}$
Others	0.41 ± 0.18
Fake and non-prompt	0^{+5}_{-0}

TABLE 3.12: Expected contribution in the $\mathrm{CR}^{\text{2-body}}_{VV\text{-SF}}$. The "Others" category contains the contributions from $t\bar{t}W$, $t\bar{t}h$, $t\bar{t}WW$, $t\bar{t}t$, $t\bar{t}t\bar{t}$, Wh, ggh and Zh production. Combined statistical and systematic uncertainties are included.

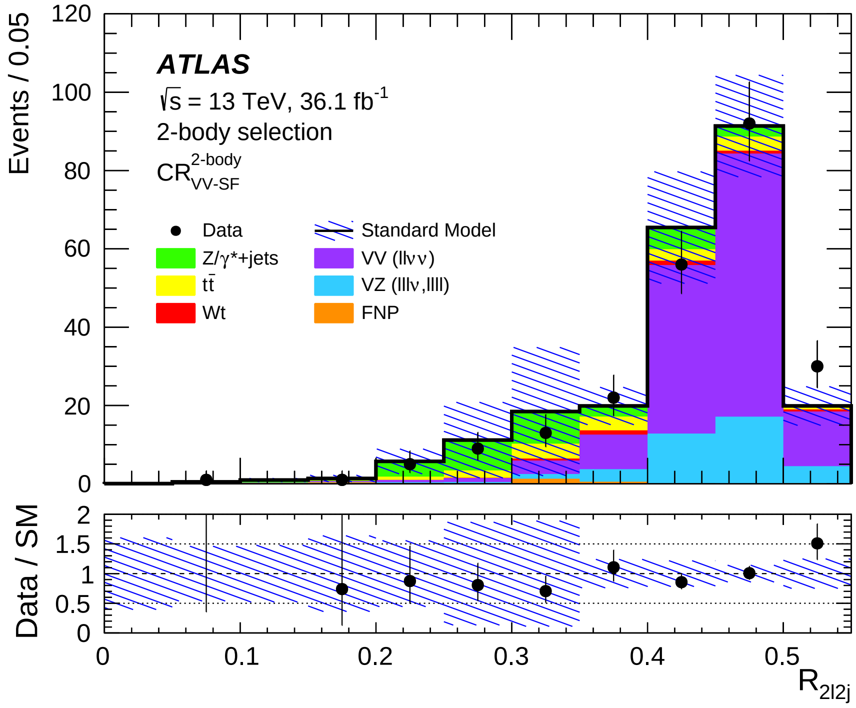

FIGURE 3.16: $R_{2\ell 2j}$ distribution in the $\mathrm{CR}^{\text{2-body}}_{VV\text{-SF}}$ after the $\mathrm{SRA}^{\text{2-body}}_{180}$ background fit. The contributions from all SM backgrounds are shown; the hatched bands represent the total statistical and detector-related systematic uncertainty. The rightmost bin includes overflow events.

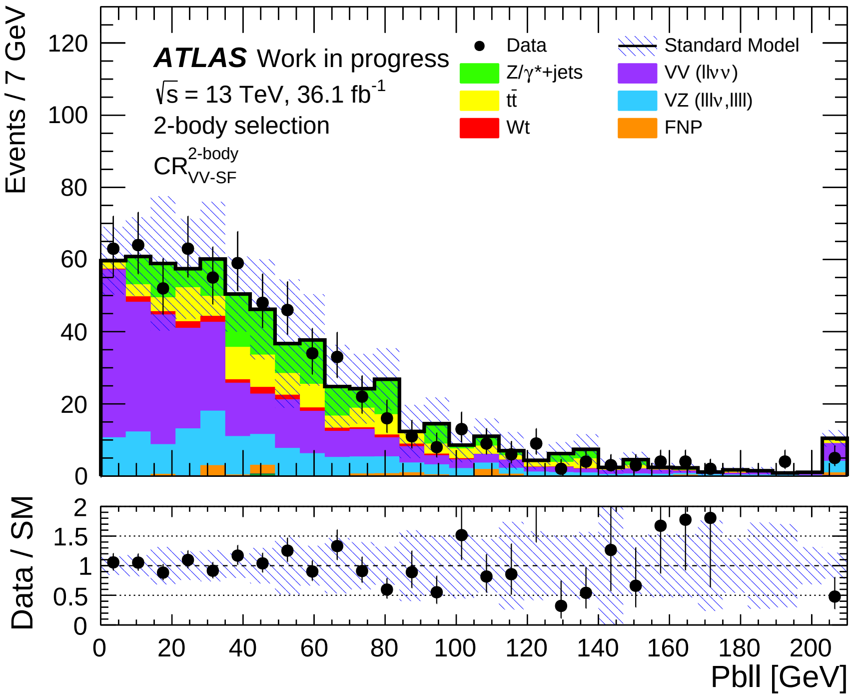

FIGURE 3.17: $\mathbf{p}^{\ell\ell}_{\mathrm{T,boost}}$ distribution in the $\mathrm{CR}^{\text{2-body}}_{VV\text{-SF}}$ after the $\mathrm{SRA}^{\text{2-body}}_{180}$ background fit. The contributions from all SM backgrounds are shown; the hatched bands represent the total statistical and detector-related systematic uncertainty. The rightmost bin includes overflow events.

3.8 Control region for ttZ

In the $\mathrm{CR}_{t\bar{t}Z}$ and CRTZt3 regions, events with three charged leptons including one same-flavour opposite-charge pair with $|m_{\ell\ell} - m_Z| < 20$ GeV are selected. In order to mimic the kinematics of the $t\bar{t}$ $+Z$ events with invisible Z decays, a corrected $E_{\mathrm{T}}^{\mathrm{miss}}$ variable, $E_{\mathrm{T,corr}}^{\mathrm{miss}}$, is defined by vectorially adding the momentum of the same-flavour opposite-charge lepton pair to the $\mathbf{p}_{\mathrm{T}}^{\mathrm{miss}}$ vector. The $E_{\mathrm{T,corr}}^{\mathrm{miss}}$ variable is used to define the selection criteria in the $\mathrm{CR}_{t\bar{t}Z}$ region. For CRTZt3, the $\xi_{\ell\ell}^{+}$ variable is used. The distribution of $E_{\mathrm{T,corr}}^{\mathrm{miss}}$ in the $\mathrm{CR}_{t\bar{t}Z}$ region is shown in Figure 3.18. The distribution of $\xi_{\ell\ell}^{+}$ in the CRTZt3 region is shown in Figure 3.19. In Figure 3.20, various kinematic variables are shown.

	$\mathrm{CR}_{t\bar{t}Z}$
Total SM Events	99.8 ± 7.81
VZ	17.64 ± 2.14
$t\bar{t}$ $+Z$	56 ± 1.2
Others	14.5 ± 1.4
Fake and non-prompt	12 ± 7

TABLE 3.13: Expected contribution in the $\mathrm{CR}_{t\bar{t}Z}$. The "Others" category contains the contributions from $t\bar{t}W$, $t\bar{t}h$, $t\bar{t}WW$, $t\bar{t}t$, $t\bar{t}t\bar{t}$, Wh, ggh and Zh production. Combined statistical and systematic uncertainties are included.

	CRTZt3
Total SM Events	106.46 ± 8.7
$t\bar{t}$+Z	67.85
VV	14.4 ± 2.2
Fake and non-prompt	10.6 ± 5.3
Others	13.6 ± 6.5

TABLE 3.14: Expected contribution in the CRTZt3. The "Others" category contains the contributions from $t\bar{t}W$, $t\bar{t}h$, $t\bar{t}WW$, $t\bar{t}t$, $t\bar{t}t\bar{t}$, Wh, ggh and Zh production. Combined statistical and systematic uncertainties are included. .

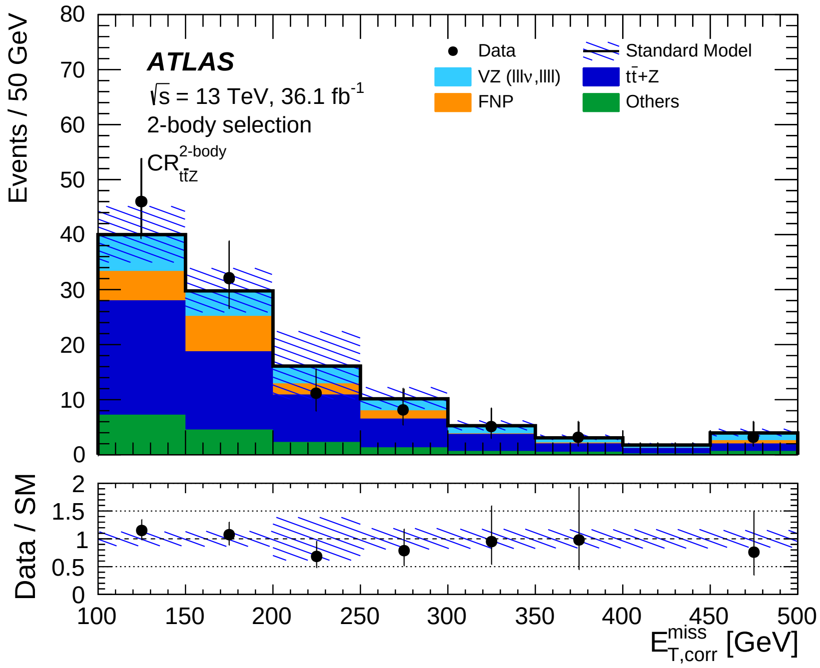

FIGURE 3.18: $E_{\mathrm{T,corr}}^{\mathrm{miss}}$ distribution in the $\mathrm{CR}_{t\bar{t}Z}$ after the $\mathrm{SRA}_{180}^{\text{2-body}}$ background fit. The contributions from all SM backgrounds are shown; the hatched bands represent the total statistical and detector-related systematic uncertainty. The rightmost bin includes overflow events.

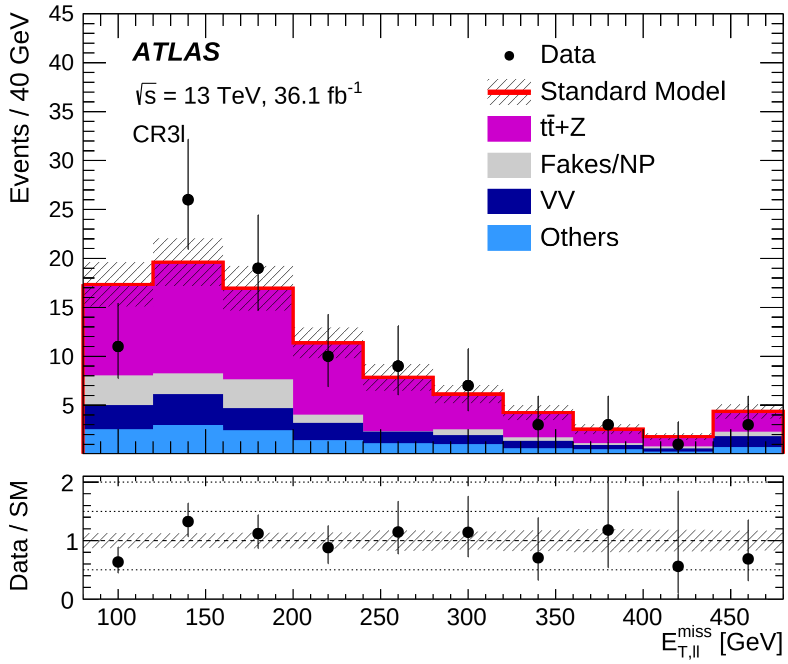

FIGURE 3.19: $E_{\mathrm{T},\ell\ell}^{\mathrm{miss}}$ distribution in the CR3ℓ after the SRt3 background fit. The contributions from all SM backgrounds are shown; the hatched bands represent the total statistical and detector-related systematic uncertainty. The rightmost bin includes overflow events.

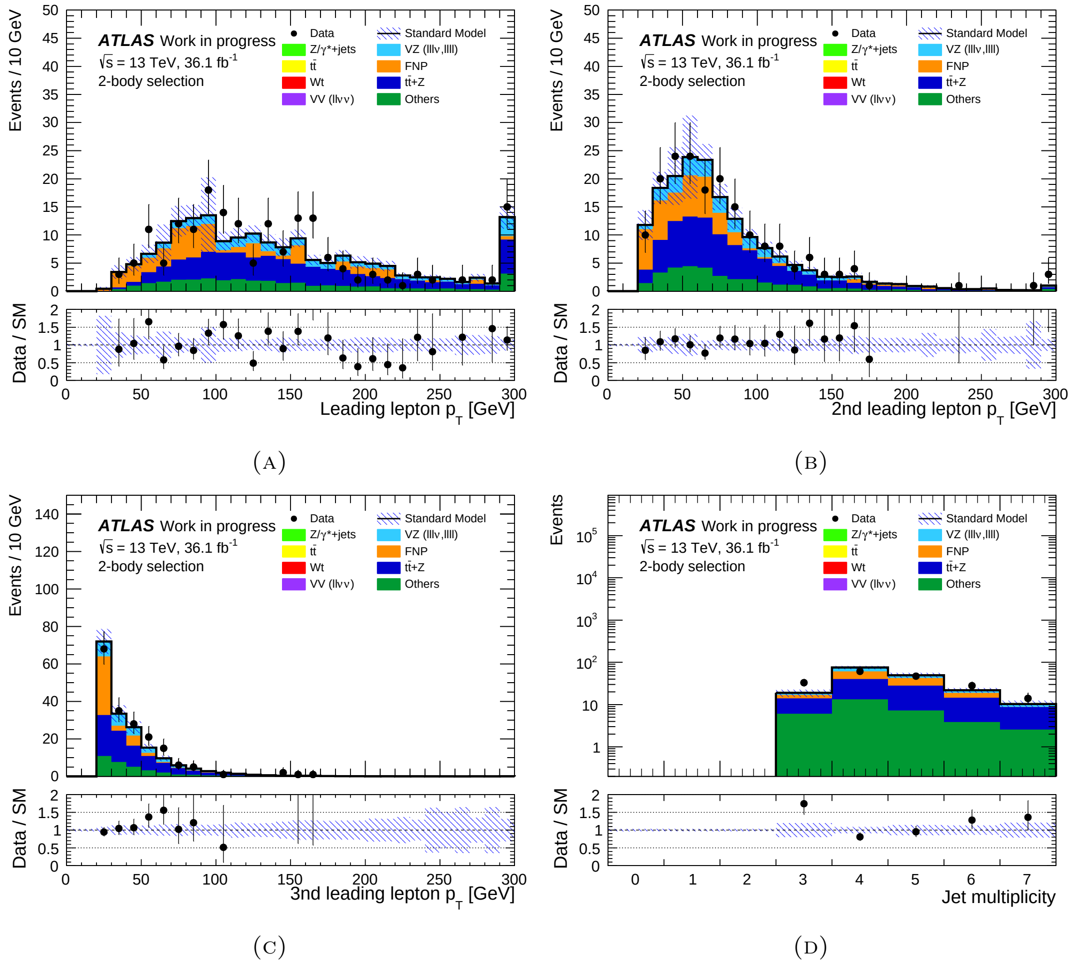

FIGURE 3.20: p_{T} distribution of the 3 leading leptons (A,B,C) in the $\mathrm{CR}_{t\bar{t}Z}$ after the $\mathrm{SRB}^{\text{2-body}}_{140}$ background fit and on the right bottom the jets multiplicity (D) in the $\mathrm{CR}_{t\bar{t}Z}$ after the $\mathrm{SRA}^{\text{2-body}}_{180}$ background fit. The contributions from all SM backgrounds are shown; the hatched bands represent the total statistical and detector-related systematic uncertainty. The right-most bin includes overflow events.

3.9 Control region for WZ and ZZ (VZ)

In the CR$_{VZ}$ region, events with three charged leptons including one same-flavour opposite-charge pair with $|m_{\ell\ell} - m_Z| < 20$ GeV are selected. In order to be orthogonal with respect to CR$_{t\bar{t}Z}$, a veto on b-jets activity is applied. In Figure 3.22, the distribution of $E_{\mathrm{T,corr}}^{\mathrm{miss}}$ is shown. In Figure 3.23, various kinematic variables are shown.

	CR$_{VZ}$
Total SM Events	842 ± 35.42
VZ	735 ± 6
$t\bar{t}$ $+Z$	11 ± 1.3
Others	10.3 ± 0.9
Fake and non-prompt	86 ± 34

TABLE 3.15: Expected contribution in the CR$_{VZ}$. The "Others" category contains the contributions from $t\bar{t}W$, $t\bar{t}h$, $t\bar{t}WW$, $t\bar{t}t$, $t\bar{t}t\bar{t}$, Wh, ggh and Zh production. Combined statistical and systematic uncertainties are included.

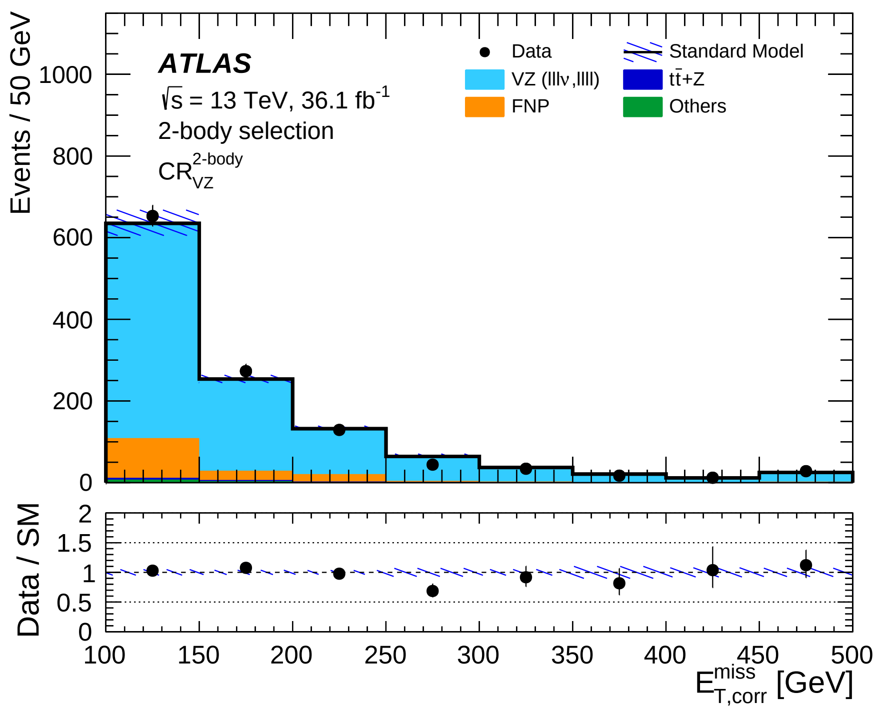

FIGURE 3.21

FIGURE 3.22: $E_{\mathrm{T,corr}}^{\mathrm{miss}}$ distribution in the CR$_{VZ}$ after the SRA$_{180}^{\text{2-body}}$ background fit. The contributions from all SM backgrounds are shown; the hatched bands represent the total statistical and detector-related systematic uncertainty. The rightmost bin includes overflow events.

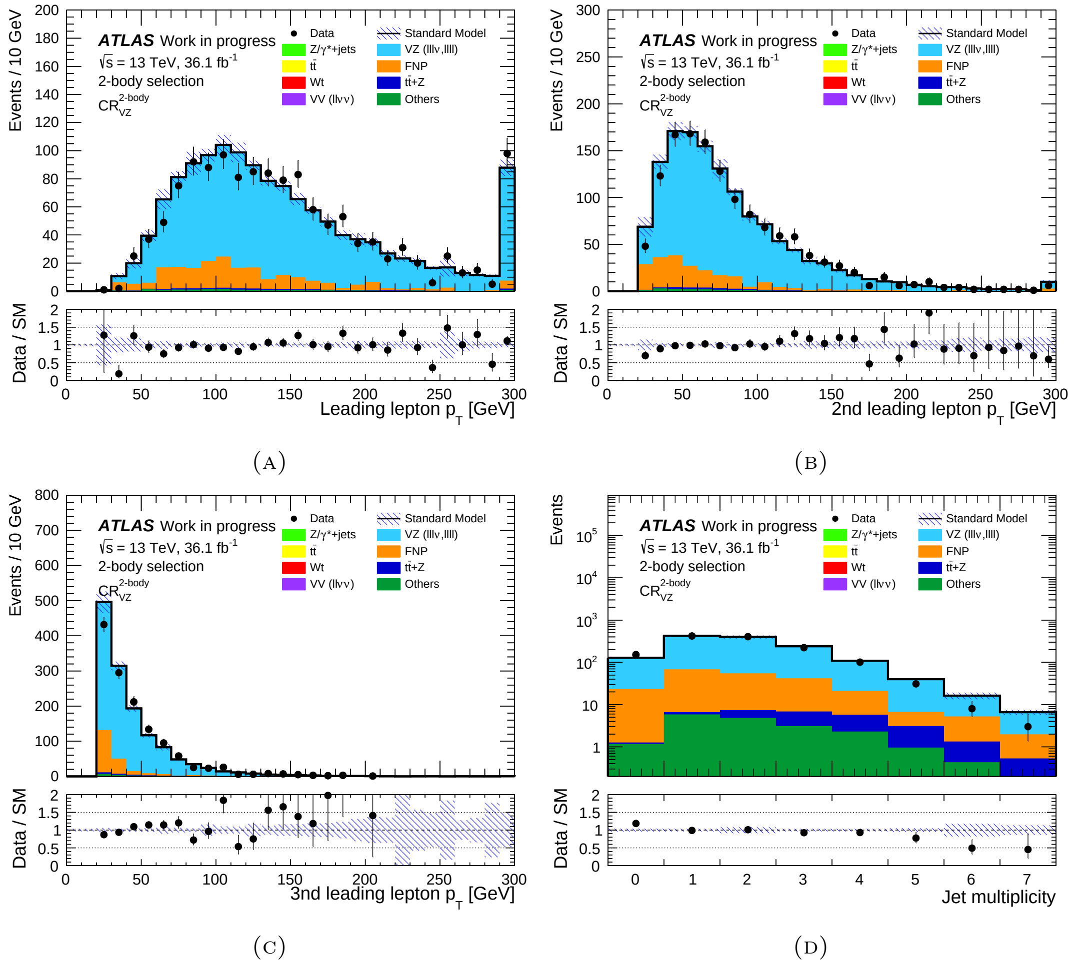

(A) (B) (C) (D)

FIGURE 3.23: p_{T} distribution of the 3 leading leptons (A,B,C) in the CR$_{VZ}$ after the SRB$^{\text{2-body}}_{140}$ background fit and on the right bottom the jets multiplicity (D) in the CR$_{VZ}$ after the SRB$^{\text{2-body}}_{140}$ background fit. The contributions from all SM backgrounds are shown; the hatched bands represent the total statistical and detector-related systematic uncertainty. The right-most bin includes overflow events.

3.10 Fake and non prompt leptons

The background due to jets misidentified as leptons (hereafter referred to as “fake” leptons) and non-prompt leptons is collectively referred to as Fake and Non Prompt (FNP).

This background has a small but non-negligible rate in the SRs and CRs considered in this analysis. In all these regions fake leptons can arise from double-fake sources from the QCD multi-jet background, such as $b\bar{b}$, $c\bar{c}$, where both jets fake a lepton, or from real-fake sources such as $t\bar{t}$ and W/Z+jets, where one lepton is prompt and the other one is a misidentified jet. Jets can fake leptons when they include hadrons that decay in flight into leptons or because there is a photon conversion during electromagnetic showering. Muons can also be faked by very energetic jets which enter in the muon spectrometer.

The estimation of this background is performed using a data-driven technique which makes use of the Matrix Method. It is estimated from data with a method similar to that described in Refs. [158, 159].

Two types of lepton identification criteria are defined for this background estimation method: `tight` and `loose`, corresponding to signal and baseline leptons described in Section 3.1. The method makes use of the number of observed events containing `loose`–`loose`, `loose`–`tight`, `tight`–`loose` and `tight`–`tight` lepton pairs in a given regions.

In order to estimate the Fake and Non Prompt background, three quantity are measured.

First, the real efficiency (r) is measured using Z candidate events selected from the main single lepton triggers. By requiring one *tight* lepton with $p_T > 30$ GeV, and using the second lepton as a probe, the fraction of `loose` probe leptons which pass the `tight` cuts (i.e. the real probability) can be measured. Each of the two leptons can be used as a probe if the other one pass the tag criteria. Two `loose` electrons or muons with $|\eta| < 2.5$ are required. Their invariant mass is required to be within $81 < m_{\ell\ell} < 101$ GeV. The real probability is then measured as a function of p_{T}, η. The results are shown in Figure 3.24 and Figure 3.25 for electrons and muons respectively as a function of η and p_{T} of the lepton.

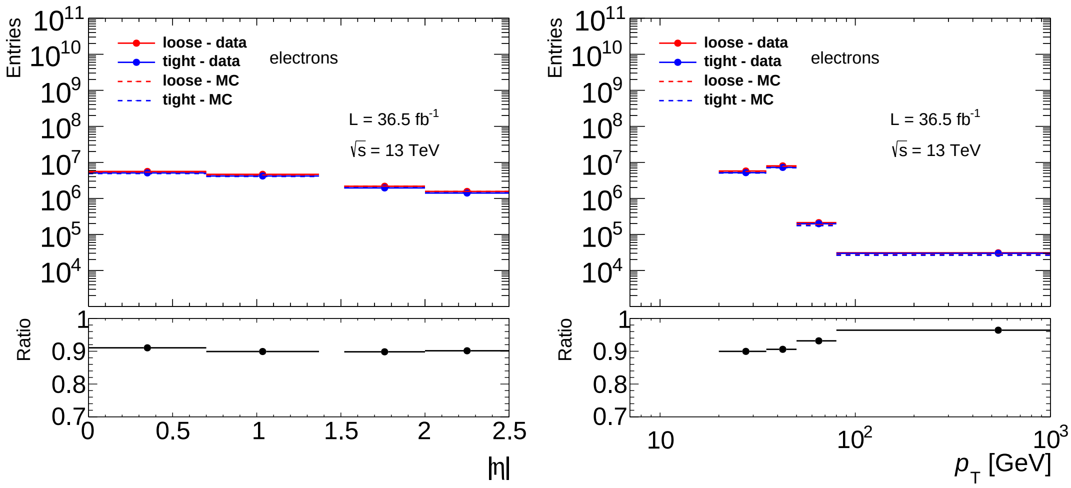

(A) (B)

FIGURE 3.24: Distribution of the pseudorapidity and p_{T} for `loose` and `tight` electron candidates in Z events. The ratio of `tight/loose` data is shown in the bottom pad

Second step is the measurement of the fake rate (f). A selection with same charge eμ events is applied, with a tag-and-probe method similar to the one used to measure the real efficiencies. This method relies on the small amount of SM processes that can result in a same electric charge eμ final state, so that when a tight lepton is selected, the other one is most likely to be fake. This measurement can be biased by processes containing two real opposite electric charge, different flavours leptons, like $t\bar{t}$ and $Z \to \tau\tau$ or WW, in which the charge of the leptons is wrongly identified. This contamination is evaluated using MC simulations. The results are shown in Figure 3.26 and Figure 3.27 for electrons and muons respectively as a function of η and p_{T}.

The last step is the measurement of the Fake and Non-Prompt background. The number of events with a `loose-loose`, `loose-tight`, and `tight-tight` lepton pairs (N_{TT}, $N_{Tl} + N_{lT}$ and N_{ll} respectively) are measured. Inverting the equation

$$\begin{pmatrix} N_{TT} \\ N_{Tl} \\ N_{lT} \\ N_{ll} \end{pmatrix} = M \begin{pmatrix} N_{LL}^{RR} \\ N_{LL}^{RF} \\ N_{LL}^{FR} \\ N_{LL}^{FF} \end{pmatrix} \tag{3.6}$$

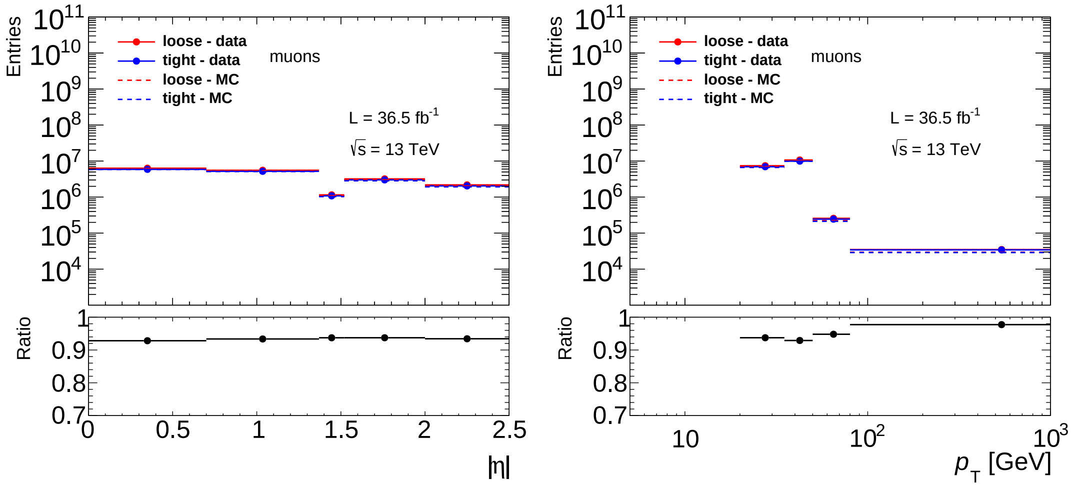

(A) (B)

FIGURE 3.25: Distribution of the pseudorapidity and p_T for `loose` and `tight` muon candidates in Z events. The ratio of `tight/loose` data is shown in the bottom pad

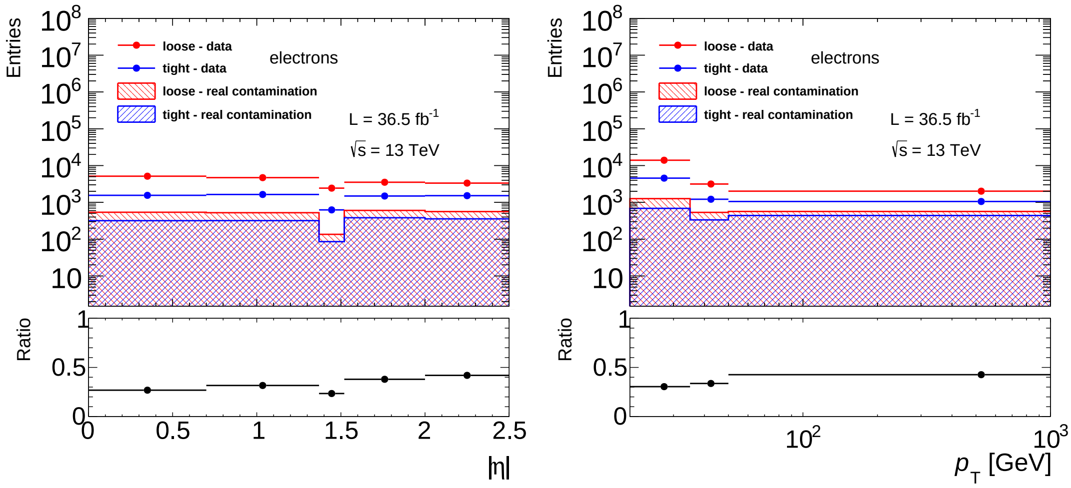

(A) (B)

FIGURE 3.26: Distribution of the pseudorapidity and p_T for `loose` and tight electron candidates in the $e\mu$SS selection. The data ratio of `tight/loose` after the real contamination subtraction is shown in the bottom pad.

with:

$$M = \begin{pmatrix} r_1 r_2 & r_1 f_2 & f_1 r_2 & f_1 f_2 \\ r_1(1-r_2) & r_1(1-f_2) & f_1(1-r_2) & f_1(1-f_2) \\ (1-r_1)r_2 & (1-r_1)f_2 & (1-f_1)r_2 & (1-f_1)f_2 \\ (1-r_1)(1-r_2) & (1-r_1)(1-f_2) & (1-f_1)(1-r_2) & (1-f_1)(1-f_2) \end{pmatrix} \tag{3.7}$$

where it is understood that the fake rates f_i and the real efficiencies r_i depend on lepton characteristics such as p_T, η, etc., and therefore are labelled accordingly. The number of events with double-fake and fake-real tight leptons (N_{TT}^{FF} and $N_{TT}^{RF} + N_{TT}^{FR}$ respectively) can thus be obtained

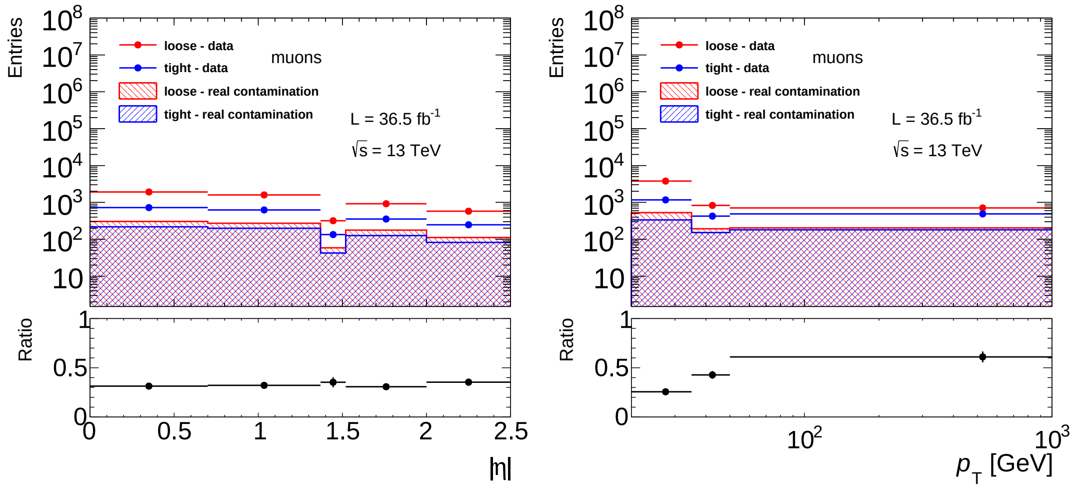

(A) (B)

FIGURE 3.27: Distribution of the pseudorapidity and p_T for `loose` and tight electron candidates in the $e\mu$SS selection. The data ratio of `tight/loose` after the real contamination subtraction is shown in the bottom pad.

from the number of events with double-fake and fake-real `loose` leptons (N_{LL}^{FF} and $N_{LL}^{RF} + N_{LL}^{FR}$)

$$\begin{cases} N_{TT}^{RR} = N_{LL}^{RR} r_1 r_2 \\ N_{TT}^{RF} = N_{LL}^{RF} r_1 f_2 \\ N_{TT}^{FR} = N_{LL}^{FR} f_1 r_2 \\ N_{TT}^{FF} = N_{LL}^{FF} f_1 f_2 \end{cases} \tag{3.8}$$

Equation 3.6 is solved for every single event with two `loose` leptons, computing its probability $w_i = N_{FF} + N_{FR} + N_{RF}$ to be an event with at least one non-prompt leptons. The sum of the probabilities w_i of all the events (which can be done for any selection or bin of an histogram) is the Fake and non prompt background estimation.

3.11 Systematic uncertainties

Various systematic uncertainties have been taken in account. The systematic uncertainties are used in the evaluation of the MC background predictions or to compute the uncertainties related to the transfer factor and propagate it to the predicted yields in the SR when the background is constrained, using the fitting method described in Section 3.5.

The primary sources of systematic uncertainty are related to the Jet Energy Scale (JES), Jet Energy Resolution (JER), and the theoretical and MC modelling uncertainties in the backgrounds. The statistical uncertainty for the simulated samples are also taken into account. The effect of the systematic uncertainties is evaluated for all signal samples and background processes. Since the normalisation of the dominant background processes is extracted in dedicated CR, the systematic uncertainties only affect the extrapolation to the signal regions in these cases. Uncertainties due to the limited number of data events in the CRs are also included in the fit for each region.

- The JES and JER uncertainties are derived as a function of the p_{T} and η of the jet, as well as of the pile-up conditions and the jet flavour composition of the selected jet sample [109]. Uncertainties associated to the modelling of the b-tagging efficiencies for b-jets, c-jets and light-flavour jets [160, 161] are also considered.
- The systematic uncertainties related to the modelling of $E_{\mathrm{T}}^{\mathrm{miss}}$ in the simulation are estimated by propagating the uncertainties in the energy and momentum scale of electrons, muons and jets, as well as the uncertainties in the resolution and scale of the soft term [100].
- Lepton reconstruction efficiency, energy scale, energy resolution and in the modelling of the trigger efficiency [91, 112], are found to have a small impact on the results and are generally negligible compared to the other detector-related uncertainties.
- The uncertainties in the modelling of the $t\bar{t}$ and single-top backgrounds in simulation are estimated by varying the renormalisation and factorisation scales by a factor of two, as well as the amount of initial- and final-state radiation used to generate the samples [117]. Uncertainties in the parton shower modelling are assessed as the difference between the predictions from POWHEG showered with PYTHIA and HERWIG, and those due to the event generator choice by comparing POWHEG and MADGRAPH5 aMC@NLO [117].
- An uncertainty due to the interference between $t\bar{t}$ and single top quark Wt production is assigned by comparing the predictions of dedicated LO MADGRAPH 2.5 samples. These samples are used to compare the predictions for $t\bar{t}$ and Wtb with the inclusive $WWbb$ process, where the same production diagrams are included, but top quarks are not required to be on-shell.
- The diboson background MC modelling uncertainties are estimated by varying up and down by a factor of two the renormalisation, factorisation and resummation scales used to generate the sample [162].
- For $t\bar{t}$+Z production, the predictions from the MADGRAPH5 aMC@NLO and SHERPA event generators are compared and the full difference between the respective predictions is assigned as an uncertainty. Uncertainties related to the choice of renormalisation and factorisation scales are assessed by varying the corresponding generator parameters up and down by a factor of two around their nominal values [163].
- The uncertainties related to the choice of QCD renormalisation and factorisation scales in Z/γ^*+jets events are assessed by varying the corresponding generator parameters up and down by a factor of two around their nominal values. Uncertainties due to our choice of the resummation scale and the matching scale between the matrix element and the parton shower are estimated by varying up and down by a factor of two the corresponding parameters in SHERPA.
- The cross-sections used to normalise the MC samples are varied according to the uncertainty in the cross-section calculation, i.e., 5.3% uncertainty for single top quark Wt-channel [164], 6% for diboson, 13% for $t\bar{t}W$ and 12% for $t\bar{t}Z$ production [125]. For $t\bar{t}WW$, tZ, tWZ, $t\bar{t}h$, $t\bar{t}t$, $t\bar{t}t\bar{t}$, and triboson production processes, which constitute a small background, a 50% uncertainty in the event yields is assumed.
- Systematic uncertainties are assigned to the FNP background estimate to account for potentially different compositions (heavy flavour, light flavour or photon conversions) between the signal and control regions, as well as for the contamination from prompt leptons in the regions used to measure the probabilities for `loose` fake or non-prompt leptons to satisfy the tight signal criteria. Parametrisations of these probabilities are independently derived from $t\bar{t}$- and multi-jet-enriched same-charge dilepton samples. The $t\bar{t}$-enriched sample is used to derive the parametrisation from which the central prediction for the FNP background is obtained. The full difference between the predictions derived from the $t\bar{t}$ and the multi-jet parametrisation is assigned as the systematic uncertainty in the central FNP prediction and symmetrised.

- A 3.2% uncertainty in the luminosity measurement is also taken into consideration for all signal and background estimates that are directly derived from MC simulations.

Table 3.16 summarises the contributions of the different sources of systematic uncertainty in the total SM background predictions in the signal regions. The total systematic uncertainty ranges between 15% and 46%, with the dominant sources being the size of the MC event samples, the JES and $E_{\mathrm{T}}^{\mathrm{miss}}$ modelling, the numbers of events in the CRs and the $t\bar{t}$ theoretical uncertainties.

Theory uncertainties in the signal acceptance are taken into account. These are computed by varying the strong coupling constant α_s, the renormalization and factorization scales, the CKKW scale used to match the parton shower and matrix element descriptions and the parton shower tunes. These uncertainties range between 10 and 30% depending on the mass difference $m_{\tilde{t}_1} - m_{\tilde{\chi}_1^0}$.

Signal Region	$SRA^{2\text{-body}}_{180}$ SF	$SRA^{2\text{-body}}_{180}$ DF	$SRB^{2\text{-body}}_{140}$ SF	$SRB^{2\text{-body}}_{140}$ DF	$SRC^{2\text{-body}}_{110}$ SF	$SRC^{2\text{-body}}_{110}$ DF	SRt3
Total SM background uncertainty	21%	32%	15%	21%	35%	38%	28 %
Diboson theoretical uncertainties	4.0%	5.9%	–	–	–	–	–
$t\bar{t}$ theoretical uncertainties	–	–	4.2%	6.6%	12%	13%	11 %
Wt theoretical uncertainties	–	–	–	1.9%	–	5.4%	–
$t\bar{t}$-Wt interference	–	–	1.8%	7.9%	–	–	–
MC statistical uncertainties	13%	28%	12%	13%	15%	15%	18%
VV normalisation	14%	–	–	–	–	–	–
$t\bar{t}$ normalisation	–	–	–	–	16%	15%	2.0 %
$t\bar{t}+Z$ normalisation	–	–	7.6%	9.9%	8.5%	10%	7.1 %
Jet energy scale	6.9%	3.1%	4.1%	6.4%	13%	22%	8.2 %
Jet energy resolution	–	–	–	–	12%	16%	<1 %
$E_{\mathrm{T}}^{\mathrm{miss}}$ modelling	5.0%	13%	2.2%	3.2%	26%	23%	12 %
b-tagging	–	–	3.0%	1.5%	–	–	<1 %
Pile-up reweighting	2.0%	3.2%	1.1%	4.3%	2.9%	4.6%	<1%
Lepton modelling	1.3%	2.1%	–	1.1%	–	–	–
Fake and non-prompt leptons	–	–	7.4%	–	4.0%	–	7.9 %

TABLE 3.16: Sources of systematic uncertainty in the SM background estimates, estimated after the background fits. The values are given as relative uncertainties in the total expected background event yields in the SRs. Entries marked "–" indicate either a negligible contribution or an uncertainty that does not apply (for example the normalisation uncertainty for a background whose normalisation is not fitted for that specific signal region). MC statistics refer to the statistical uncertainty from the simulated event samples. The individual components can be correlated and therefore do not necessarily add up in quadrature to the total systematic uncertainty.

3.12 Background-only fit results

The results of the background fits, as well as the MC expected background composition before the fit, are reported in Table 3.17 for the CRs used in the $\text{SRA}_{180}^{\text{2-body}}$ and $\text{SRB}_{140}^{\text{2-body}}$ background fits, and in Table 3.18 for the CRs used in the $\text{SRC}_{110}^{\text{2-body}}$ background fit. The normalisation for fitted backgrounds are found to be consistent with the theoretical predictions, when uncertainties are considered. By construction, in the CRs the yields observed and predicted by the fits are the same.

	$\text{CR}_{t\bar{t}}^{\text{2-body}}$	$\text{CR}_{VV\text{-SF}}^{\text{2-body}}$	$\text{CR}_{t\bar{t}Z}$	CR_{VZ}
Observed events	587	213	91	836
Fitted SM Events	587 ± 24	213 ± 15	91 ± 10	836 ± 29
$t\bar{t}$	532 ± 25	14 ± 4	–	–
Wt	44 ± 6	4.0 ± 1.5	–	–
Z/γ^*+jets	$0.02^{+0.05}_{-0.02}$	19 ± 10	–	–
VV-SF	–	135 ± 18	–	–
VV-DF	2.2 ± 0.8	–	–	–
VZ	0.18 ± 0.12	38 ± 7	17.5 ± 2.5	730 ± 50
$t\bar{t}$ +Z	2.2 ± 0.8	0.07 ± 0.07	47 ± 12	8.9 ± 2.5
Others	3.8 ± 0.4	0.41 ± 0.18	14.5 ± 1.4	10.3 ± 0.9
Fake and non-prompt	1.6 ± 0.9	0^{+5}_{-0}	12 ± 7	86 ± 34
Fit input, $t\bar{t}$	504	14	–	–
Fit input, VV-SF	–	122	–	–
Fit input, VZ	0.18	39	18	735
Fit input, $t\bar{t}$ +Z	3.57	0.08	56	11

Table 3.17: Background-only fit results for the CRs of the $\text{SRA}_{180}^{\text{2-body}}$ and $\text{SRB}_{140}^{\text{2-body}}$. The nominal predictions from MC simulation are given for comparison for those backgrounds ($t\bar{t}$, VV-SF, $t\bar{t}Z$ and VZ) that are normalised to data in dedicated CRs. The "Others" category contains the contributions from $t\bar{t}W$, $t\bar{t}h$, $t\bar{t}WW$, $t\bar{t}t$, $t\bar{t}t\bar{t}$, Wh, ggh and Zh production. Combined statistical and systematic uncertainties are included. Entries marked "–" indicate a negligible contribution.

	$\text{CR}_{t\bar{t},3j}^{\text{2-body}}$	$\text{CR}_{t\bar{t}Z}$
Observed events	212	91
Fitted SM Events	212 ± 15	91 ± 10
$t\bar{t}$	184 ± 16	–
$t\bar{t}$ +Z	1.03 ± 0.32	47 ± 12
Wt	23 ± 7	–
VV	1.69 ± 0.30	17.7 ± 2.2
Z/γ^*+jets	0.05 ± 0.02	–
Others	1.91 ± 0.12	14.6 ± 1.0
Fake and non-prompt	–	12 ± 7
Fit input, $t\bar{t}$	201	–
Fit input, $t\bar{t}$ +Z	1.23	56

Table 3.18: Background fit results for the CRs of the $\text{SRC}_{110}^{\text{2-body}}$. The nominal predictions from MC simulation are given for comparison for those backgrounds ($t\bar{t}$ and $t\bar{t}Z$) that are normalised to data in dedicated CRs. The "Others" category contains the contributions from $t\bar{t}W$, $t\bar{t}h$, $t\bar{t}WW$, $t\bar{t}t$, $t\bar{t}t\bar{t}$, Wh, ggh and Zh production. Combined statistical and systematic uncertainties are included. Entries marked "–" indicate a negligible contribution.

	CRTt3	CRTZt3
Observed events	245	92
Fitted SM Events	245 ± 16	92.1 ± 9.6
$t\bar{t}$	231 ± 16	-
$t\bar{t}$+Z	1.60 ± 0.47	53 ± 13
Wt	9.0 ± 2.6	-
VV	0.67 ± 0.41	14.4 ± 2.2
Fakes/NP	$0.0^{+0.3}_{-0.0}$	10.6 ± 5.3
Others	3.1 ± 1.2	13.6 ± 6.5
Fit input, $t\bar{t}$	204.96	-
Fit input, $t\bar{t}$+Z	2.03	67.85

Table 3.19: Background fit results for the CRs of the SRt3. The nominal predictions from MC simulation are given for comparison for those backgrounds ($t\bar{t}$ and $t\bar{t}Z$) that are normalised to data in dedicated CRs. The "Others" category contains the contributions from Z/γ^*+jets, $t\bar{t}W$, $t\bar{t}h$, $t\bar{t}WW$, $t\bar{t}t$, $t\bar{t}t\bar{t}$, Wh, ggh and Zh production. Combined statistical and systematic uncertainties are included. Entries marked "–" indicate a negligible contribution.

3.13 Validation of the background prediction

In order to verify the validity of the results of the background fit, four validation regions are designed with the selection described in Table 3.20. They are orthogonal from both the corresponding control and signal regions. Good agreement, within one standard deviation from the post-fit expectation, is observed between data and MC simulation in the VRs.

	$\mathrm{VR}^{\text{2-body}}_{t\bar{t}}$	$\mathrm{VR}^{\text{2-body}}_{t\bar{t},3j}$	$\mathrm{VR}^{\text{2-body}}_{VV\text{-DF}}$	VRTt3
Leptons	2, DF	2	2, DF	2
m_{T2} [GeV]	> 120	> 100	[100, 120]	> 100
ξ^+	–	–	–	> 170
$m^{\min}_{b2\ell}$ [GeV]	–	–	–	< 170
n_{jets}	≥ 2	≥ 3	-	≥ 1
$n_{b\text{-jets}}$	≥ 1	≥ 1	0	≥ 1
$p_{\mathrm{T}}(j_1)$ [GeV]	> 20	> 20	> 20	> 30
$p_{\mathrm{T}}(bj_1)$ [GeV]	–	> 20	> 20	> 30
$p^{\ell\ell}_{\mathrm{T,boost}}$ [GeV]	–	–	< 25	
$\Delta\phi_{\text{boost}}$	> 1.5	–	–	> 1.5
$E_{\mathrm{T}}^{\text{miss}}$ [GeV]	–	> 200	–	
$R_{2\ell}$	–	< 1.2	–	

Table 3.20: Validation region definitions. The common selection defined in Section 3.3 also applies to all regions.

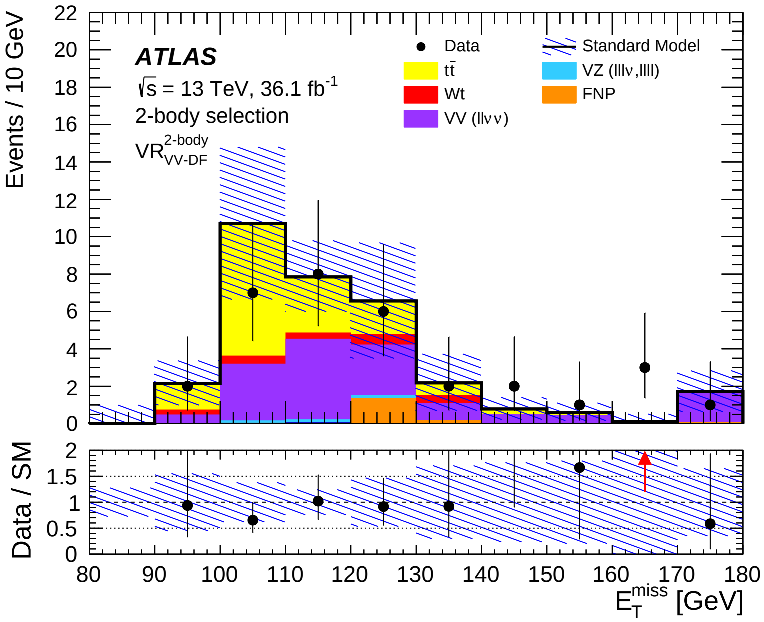

FIGURE 3.28: Distribution of $E_{\mathrm{T}}^{\mathrm{miss}}$ for events satisfying all the $\mathrm{VR}_{VV\text{-DF}}^{\text{2-body}}$ selections, after the background fit. The contributions from all SM backgrounds are shown; the hatched bands represent the total statistical and detector-related systematic uncertainty. The rightmost bin includes overflow events.

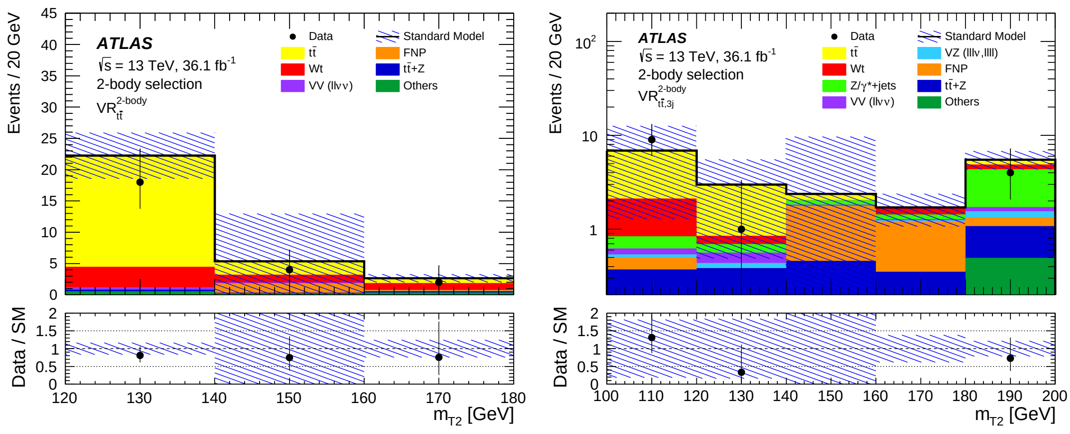

(A) (B)

FIGURE 3.29: Distribution of m_{T2} for events satisfying all the $\mathrm{VR}_{t\bar{t}}^{\text{2-body}}$ (A) and $\mathrm{VR}_{t\bar{t},3j}^{\text{2-body}}$ (B) selections, after the background fit. The contributions from all SM backgrounds are shown; the hatched bands represent the total statistical and detector-related systematic uncertainty. The rightmost bin includes overflow events.

	$\mathrm{VR}^{\text{2-body}}_{VV\text{-DF}}$	$\mathrm{VR}^{\text{2-body}}_{t\bar{t}}$
Observed events	32	24
Fitted SM events	31 ± 8	29 ± 8
$t\bar{t}$	14 ± 5	20.6 ± 3.1
Wt	2.0 ± 1.3	5.1 ± 3.3
Z/γ^*+jets	0.04 ± 0.01	0.10 ± 0.03
VV-SF	–	–
VV-DF	13.9 ± 3.5	0.55 ± 0.14
VZ	$0.2^{+0.2}_{-0.2}$	0.09 ± 0.03
$t\bar{t}+Z$	0.05 ± 0.02	0.5 ± 0.2
Others	0.17 ± 0.05	1.2 ± 0.1
Fake and non prompt	0.69 ± 0.07	1^{+7}_{-1}
Fit input, $t\bar{t}$	14 ± 5	19.5 ± 2.9
Fit input, VV-SF	–	–
Fit input, VZ	$0.18^{+0.24}_{-0.18}$	0.09 ± 0.03
Fit input, $t\bar{t}+Z$	0.05 ± 0.02	0.65 ± 0.10

TABLE 3.21: Background fit results for the VRs in the $\mathrm{SRA}^{\text{2-body}}_{180}$ and $\mathrm{SRB}^{\text{2-body}}_{140}$. The nominal expectations from MC simulation are given for comparison for those backgrounds ($t\bar{t}$, VV-SF, $t\bar{t}Z$ and VZ) that are normalised to data in dedicated CRs. The "Others" category contains the contributions from $t\bar{t}W$, $t\bar{t}h$, $t\bar{t}WW$, $t\bar{t}t$, $t\bar{t}t\bar{t}$, Wh, ggh and Zh production. Combined statistical and systematic uncertainties are included. Entries marked "–" indicate a negligible contribution.

	$\mathrm{VR}^{\text{2-body}}_{t\bar{t},3j}$
Observed events	14
Fitted SM events	19 ± 8
$t\bar{t}$	8 ± 4
$t\bar{t}$ +Z	1.5 ± 0.5
Wt	2.2 ± 0.6
VV	0.8 ± 0.2
Z/γ^*+jets	3.3 ± 0.5
Others	1.13 ± 0.15
Fake and non-prompt	$2.5^{+7.2}_{-2.5}$
Fit input, $t\bar{t}$	9 ± 6
Fit input, $t\bar{t}$ +Z	1.81 ± 0.27

TABLE 3.22: Background fit results for the VR in the $\mathrm{SRC}^{\text{2-body}}_{110}$. The nominal expectations from MC simulation are given for comparison for those backgrounds ($t\bar{t}$, $t\bar{t}$ +Z) that are normalised to data in dedicated CRs. The "Others" category contains the contributions from $t\bar{t}W$, $t\bar{t}h$, $t\bar{t}WW$, $t\bar{t}t$, $t\bar{t}t\bar{t}$, Wh, ggh and Zh production. Combined statistical and systematic uncertainties are included.

	VRTt3
Observed events	35
Fitted SM events	38.0 ± 7.5
$t\bar{t}$	22.3 ± 6.7
$t\bar{t}+Z$	1.58 ± 0.42
Wt	3.60 ± 0.61
VV	1.02 ± 0.25
Fake and non-prompt	$0.0^{+0.3}_{-0.0}$
Others	9.5 ± 2.2
Fit input, $t\bar{t}$	19.83
Fit input, $t\bar{t}+Z$	2.00

TABLE 3.23: Background fit results for $\mathrm{VR}^{\text{2-body}}_{t\bar{t},3j}$ in the SRt3. The nominal expectations from MC simulation are given for comparison for those backgrounds ($t\bar{t}$, $t\bar{t}$ +Z) that are normalised to data in dedicated CRs. The "Others" category contains the contributions from $t\bar{t}W$, $t\bar{t}h$, $t\bar{t}WW$, $t\bar{t}t$, $t\bar{t}t\bar{t}$, Wh, ggh and Zh production. Combined statistical and systematic uncertainties are included.

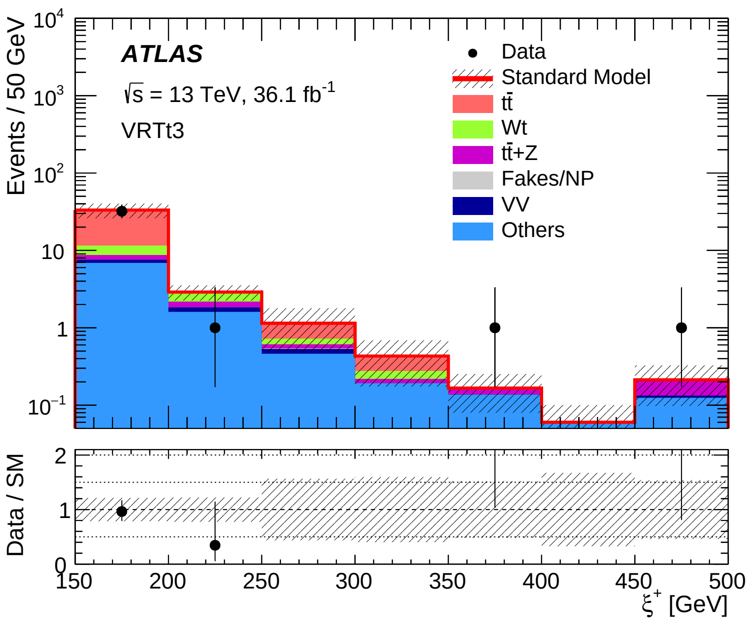

FIGURE 3.30: Distribution of ξ^+ for events satisfying all the VRTt3 selection, after the background fit. The contributions from all SM backgrounds are shown; the hatched bands represent the total statistical and detector-related systematic uncertainty. The rightmost bin includes overflow events.

3.14 Results

Figure 3.31 shows the comparison of the observed data (n_{obs}) with the predicted SM background (n_{exp}) in the $\mathrm{SRA}_{180}^{\text{2-body}}$,$\mathrm{SRB}_{140}^{\text{2-body}}$,$\mathrm{SRC}_{110}^{\text{2-body}}$and associated VRs. These SRs presented in this work corresponds to the one on the left. The definition of the other SRs and the corresponding results in the right part of the plot are presented in [101].

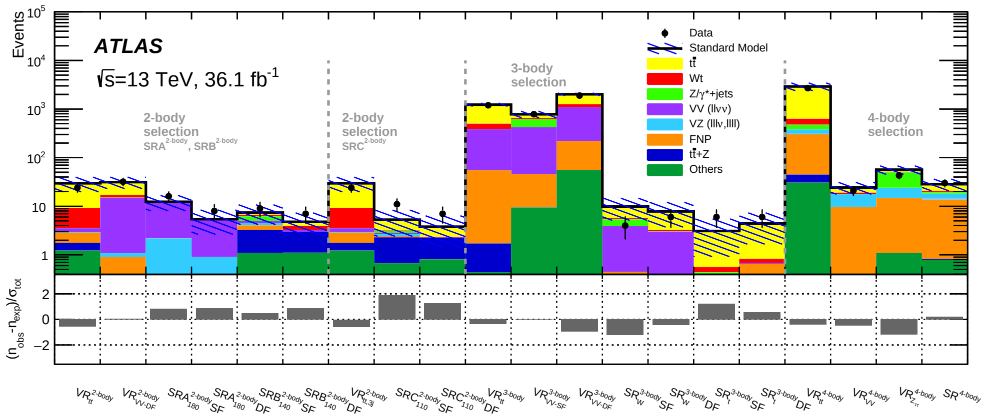

FIGURE 3.31: Comparison of the observed data (n_{obs}) with the predicted SM background (n_{exp}) in the SRs and associated VRs. The background predictions are obtained using the background-only fit configuration, and the hatched area around the SM prediction represents the total statistical and systematic uncertainty. The bottom panel shows the difference between data and the predicted SM background divided by the total uncertainty (σ_{tot}). [101]

In Figure 3.32, the comparison of the data with the post-fit SM prediction of the background in SRt3 is shown. For the definition of the other SRs and the corresponding results shown in the left part of the plot, look [102].

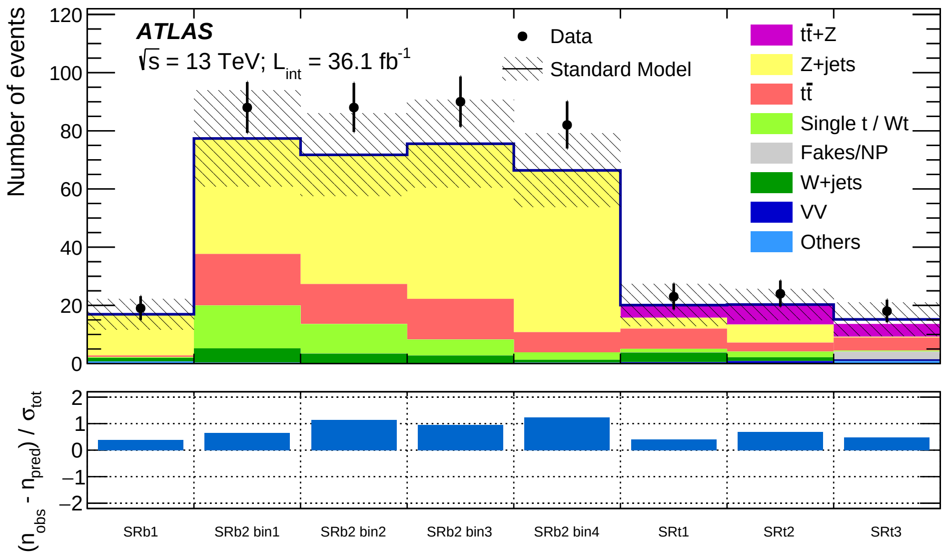

FIGURE 3.32: Comparison of the data with the post-fit SM prediction of the background in the SRs. The different background components are denoted by the colour specified in the legend. All systematic uncertainties defined in Sect. 3.11 and statistical uncertainties are included in the shaded band. The lower panel shows the pulls in each VR. The total uncertainty σ_{tot} includes systematic and Poisson uncertainties for each given region [102].

SR A

The number of events in $\mathrm{SRA}^{\text{2-body}}_{180}$ is reported in Table 3.24 and compared to the fitted SM background. The selection criteria for $\mathrm{SRA}^{\text{2-body}}_{180}$ are described in Table 3.5. The distribution of m_{T2} for event with Same Flavour or Different Flavour passing the $\mathrm{SRA}^{\text{2-body}}_{180}$ selection criteria, except the one on m_{T2} are shown in Figures 3.33, 3.34. The estimated SM yields in $\mathrm{SRA}^{\text{2-body}}_{180}$ are determined with a background fit simultaneously determining the normalisations of the background contributions from $t\bar{t}$, diboson with a SF lepton pair, $t\bar{t}+Z$ and diboson with more than two charged leptons by including $\mathrm{CR}^{\text{2-body}}_{t\bar{t}}$, $\mathrm{CR}^{\text{2-body}}_{VV\text{-SF}}$, $\mathrm{CR}_{t\bar{t}Z}$ and CR_{VZ} in the likelihood minimisation. No significant excess over the SM prediction is observed, as can be seen from the background-only fit results which are shown in Table 3.17 for $\mathrm{SRA}^{\text{2-body}}_{180}$. Table 3.25 reports the observed and expected yields for the SRs used for the computation of the exclusion limits. The distribution of the p_{T} of the leading and sub-leading leptons, of Δx and the jets multiplicity for events passing the $\mathrm{SRA}^{\text{2-body}}_{180}$ selection criteria, except the one on m_{T2} are shown respectively in Figure 3.35, 3.36 and 3.37.

	$\mathrm{SRA}^{\text{2-body}}_{180}$ SF	$\mathrm{SRA}^{\text{2-body}}_{180}$ DF
Observed events	16	8
Fitted SM Events	12.3 ± 2.6	5.4 ± 1.7
Z/γ^*+jets	0.35 ± 0.21	–
Fake and non-prompt	$0.00^{+0.30}_{-0.00}$	$0.00^{+0.30}_{-0.00}$
VV-DF	–	4.5 ± 1.5
VV-SF	9.8 ± 2.5	–
VZ	1.91 ± 0.31	0.52 ± 0.17
$t\bar{t}+Z$	0.08 ± 0.03	0.15 ± 0.06
Others	0.18 ± 0.02	0.24 ± 0.07
Fit input, $t\bar{t}$	–	–
Fit input, VV-SF	8.8	–
Fit input, VZ	1.9	0.52
Fit input, $t\bar{t}+Z$	0.09	0.17

Table 3.24: Background fit results for $\mathrm{SRA}^{\text{2-body}}_{180}$. The nominal predictions from MC simulation are given for comparison for those backgrounds ($t\bar{t}$, VV-SF, $t\bar{t}Z$ and VZ) that are normalised to data in dedicated CRs. The "Others" category contains the contributions from $t\bar{t}W$, $t\bar{t}h$, $t\bar{t}WW$, $t\bar{t}t$, $t\bar{t}t\bar{t}$, Wh, ggh and Zh production. Combined statistical and systematic uncertainties are included. Entries marked "–" indicate a negligible contribution. The "Others" contribution to $\mathrm{SRB}^{\text{2-body}}_{140}$ is dominated by $t\bar{t}W$.

	Lepton flavour	$\mathrm{SRA}^{2-\mathrm{body}}_{120,140}$	$\mathrm{SRA}^{2-\mathrm{body}}_{140,160}$	$\mathrm{SRA}^{2-\mathrm{body}}_{160,180}$
Observed events	SF	22	6	10
Fitted SM Events		20.0 ± 4.6	11.0 ± 2.5	5.6 ± 1.8
Observed events	DF	27	6	7
Fitted SM Events		23.8 ± 4.2	10.8 ± 2.1	6.4 ± 1.3

Table 3.25: Background fit results for $\mathrm{SR(A)}^{2-\mathrm{body}}_{x,y}$ regions, where x and y denote the low and high edges of the bin. Combined statistical and systematic uncertainties are included. Uncertainties in the predicted background event yields are treated as being symmetric.

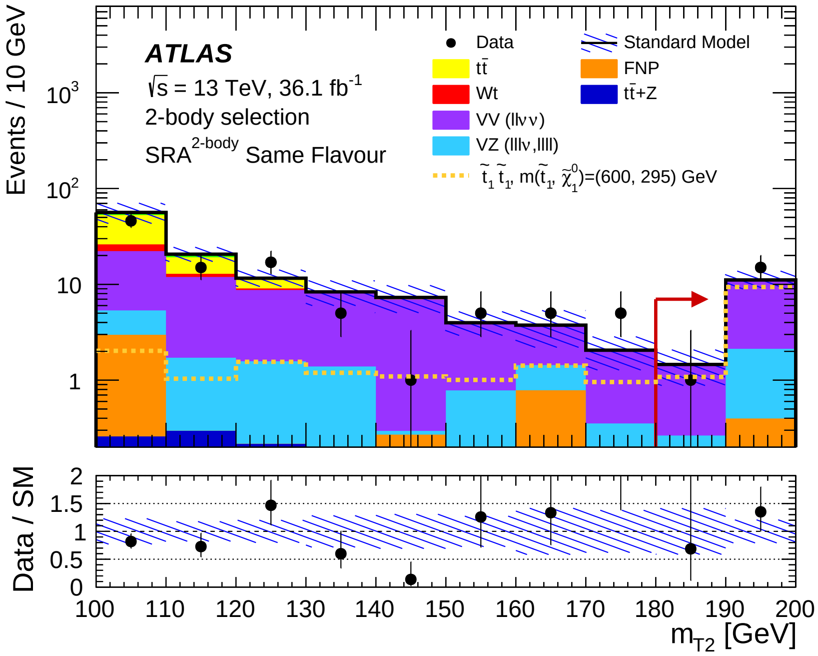

FIGURE 3.33: Distributions of m_{T2} for events satisfying the selection criteria in the $\mathrm{SRA}_{180}^{\text{2-body}}$ Same Flavour, except for the one on m_{T2}, after the background fit. The contributions from all SM backgrounds are shown; the hatched bands represent the total statistical and systematic uncertainty. The rightmost bin includes overflow events. A reference top squark pair production signal models is overlayed for comparison. Red arrows indicate the signal region selection criteria.

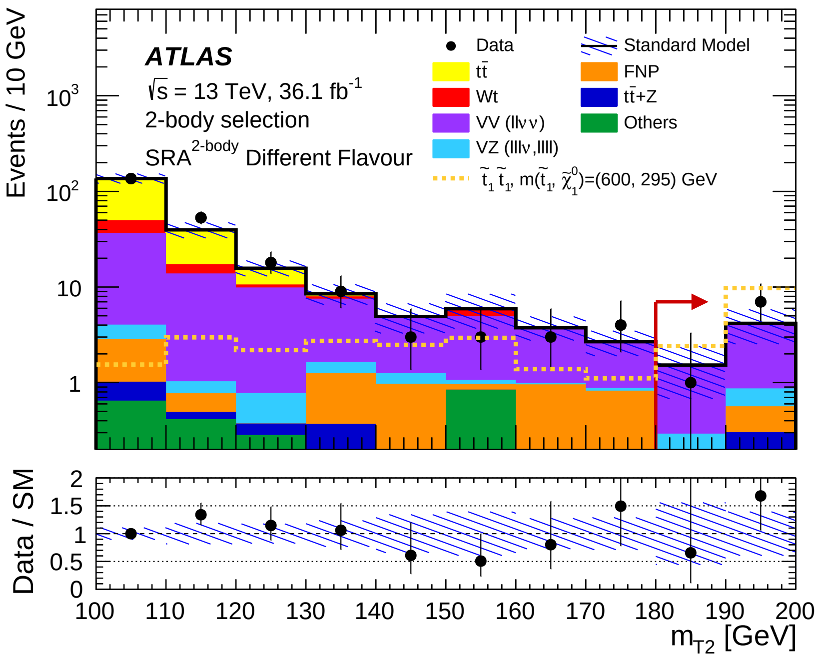

FIGURE 3.34: Distributions of m_{T2} for events satisfying the selection criteria in the $\mathrm{SRA}_{180}^{\text{2-body}}$ Different Flavour, except for the one on m_{T2}, after the background fit. The contributions from all SM backgrounds are shown; the hatched bands represent the total statistical and systematic uncertainty. The rightmost bin includes overflow events. A reference top squark pair production signal models is overlayed for comparison. Red arrows indicate the signal region selection criteria.

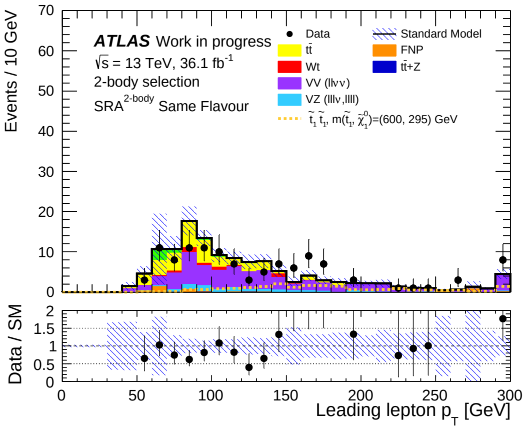

(A)

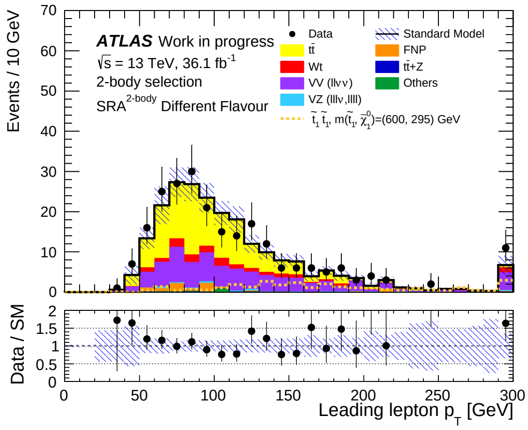

(B)

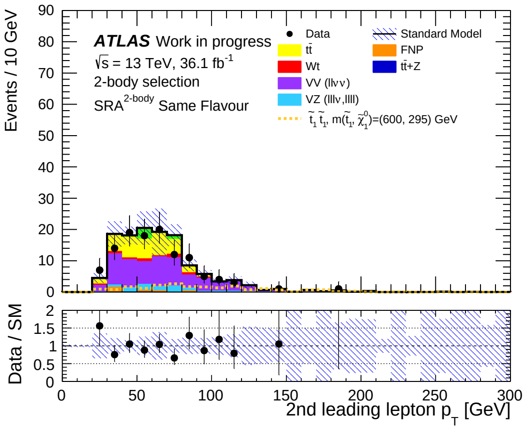

(C)

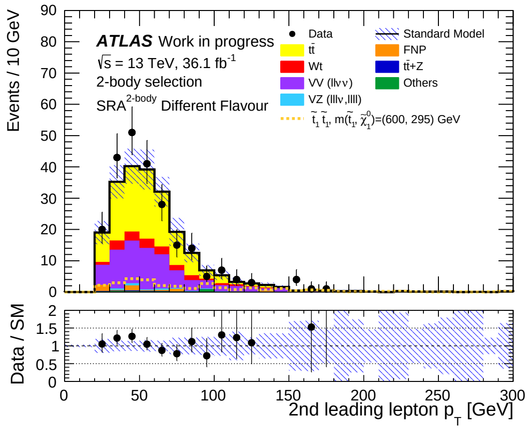

(D)

FIGURE 3.35: Distributions of the p_{T} of the leading (A,B) and sub-leading (C,D) leptons for events satisfying the selection criteria in the $\mathrm{SRA}^{\text{2-body}}_{180}$ Same Flavour (left) and $\mathrm{SRA}^{\text{2-body}}_{180}$ Different Flavour (right), except for the one on m_{T2}, after the background fit. The contributions from all SM backgrounds are shown; the hatched bands represent the total statistical and systematic uncertainty. The rightmost bin includes overflow events. A reference top squark pair production signal models is overlayed for comparison.

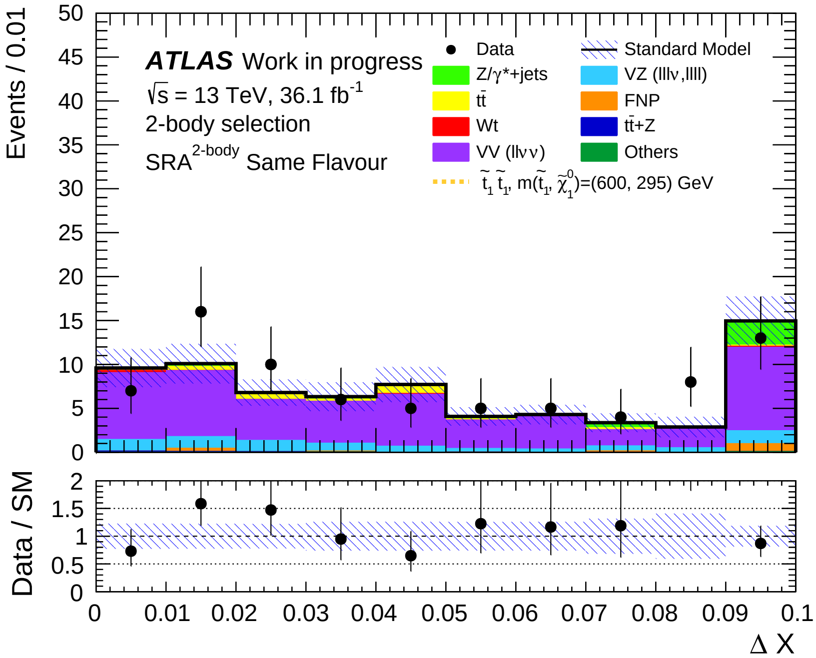

(A)

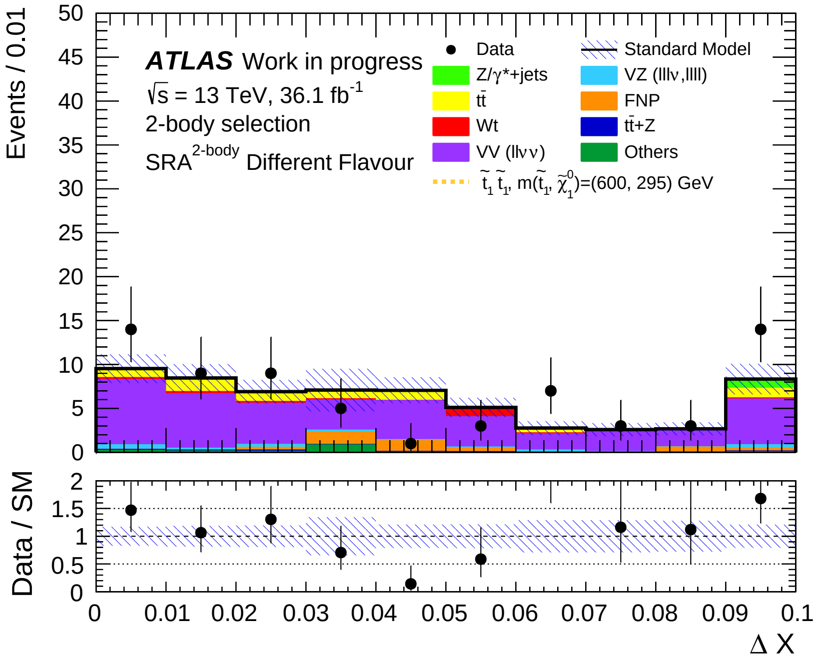

(B)

FIGURE 3.36: Distributions of Δx for events satisfying the selection criteria in the $\text{SRA}^{\text{2-body}}_{180}$ Same Flavour (A) and $\text{SRA}^{\text{2-body}}_{180}$ Different Flavour (B), except for the one on Δx, after the background fit. The contributions from all SM backgrounds are shown; the hatched bands represent the total statistical and systematic uncertainty. The rightmost bin includes overflow events.

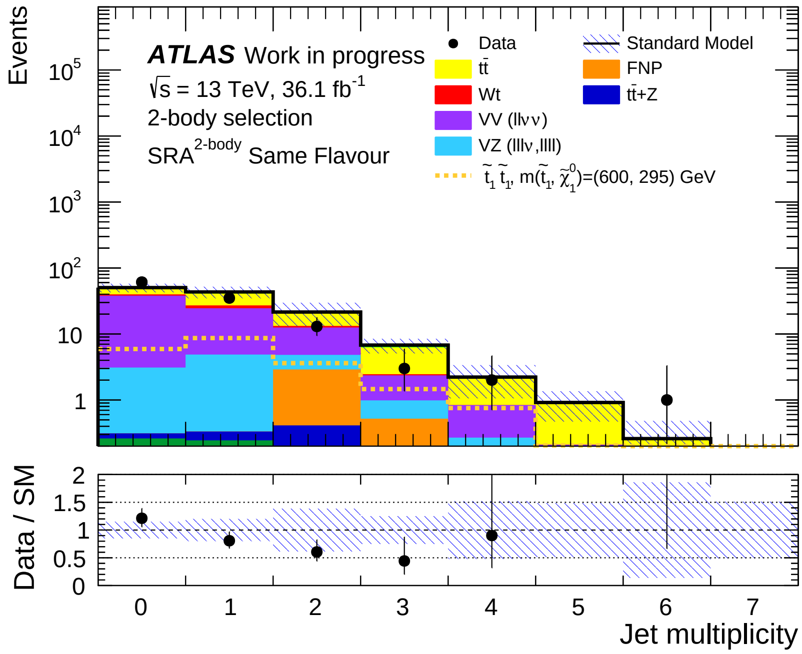

(A)

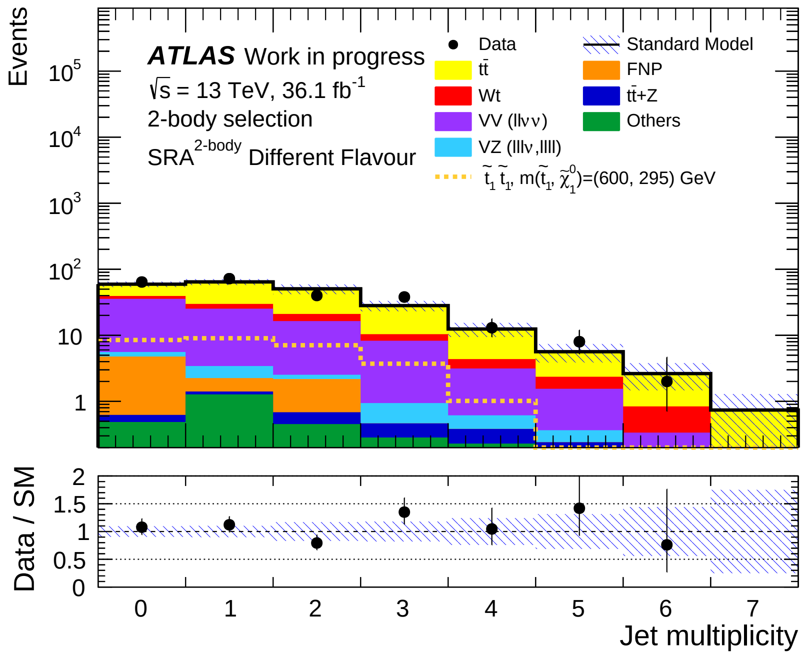

(B)

FIGURE 3.37: Distributions of the jet multiplicity for events satisfying the selection criteria in the $\mathrm{SRA}_{180}^{\text{2-body}}$ Same Flavour (A) and $\mathrm{SRA}_{180}^{\text{2-body}}$ Different Flavour (B), except for the one on the jet multiplicity, after the background fit. The contributions from all SM backgrounds are shown; the hatched bands represent the total statistical and systematic uncertainty. The rightmost bin includes overflow events. A reference top squark pair production signal models is overlayed for comparison.

SR B

The number of events in $\mathrm{SRB}_{140}^{\text{2-body}}$ is reported in Table 3.26 and compared to the total expected background. The selection criteria for $\mathrm{SRB}_{140}^{\text{2-body}}$ are described in Table 3.5. The distribution of m_{T2} for event with Same Flavour or Different Flavour passing the $\mathrm{SRB}_{140}^{\text{2-body}}$ selection criteria, except the one on m_{T2} are shown in Figure 3.38, 3.39. The estimated SM yields in $\mathrm{SRB}_{140}^{\text{2-body}}$ are determined with a background fit simultaneously determining the normalisations of the background contributions from $t\bar{t}$, diboson with a SF lepton pair, $t\bar{t}+Z$ and diboson with more than two charged leptons by including $\mathrm{CR}_{t\bar{t}}^{\text{2-body}}$, $\mathrm{CR}_{VV\text{-SF}}^{\text{2-body}}$, $\mathrm{CR}_{t\bar{t}Z}$ and CR_{VZ} in the likelihood minimisation. No significant excess over the SM prediction is observed, as can be seen from the background-only fit results which are shown in Table 3.26 for $\mathrm{SRB}_{140}^{\text{2-body}}$. Table 3.27 reports the observed and expected yields for the SRs used for the computation of the exclusion limits.

	$\mathrm{SRB}_{140}^{\text{2-body}}$ SF	$\mathrm{SRB}_{140}^{\text{2-body}}$ DF
Observed events	9	7
Fitted SM Events	7.4 ± 1.1	4.8 ± 1.0
$t\bar{t}$	0.8 ± 0.4	0.8 ± 0.5
Wt events	0.38 ± 0.29	0.7 ± 0.5
Z/γ^*+jets	1.24 ± 0.32	0.03 ± 0.01
Fake and non-prompt	0.8 ± 0.5	$0.00^{+0.30}_{-0.00}$
VV-DF	–	0.23 ± 0.06
VV-SF	0.39 ± 0.11	–
VZ	0.53 ± 0.14	0.04 ± 0.01
$t\bar{t}+Z$	2.3 ± 0.6	1.8 ± 0.5
Others	1.10 ± 0.16	1.11 ± 0.16
Fit input, $t\bar{t}$	0.78	0.8
Fit input, VV-SF	0.35	–
Fit input, VZ	0.54	0.04
Fit input, $t\bar{t}+Z$	2.6	2.2

TABLE 3.26: Background fit results for $\mathrm{SRB}_{140}^{\text{2-body}}$. The nominal predictions from MC simulation are given for comparison for those backgrounds ($t\bar{t}$, VV-SF, $t\bar{t}Z$ and VZ) that are normalised to data in dedicated CRs. The "Others" category contains the contributions from $t\bar{t}W$, $t\bar{t}h$, $t\bar{t}WW$, $t\bar{t}t$, $t\bar{t}t\bar{t}$, Wh, ggh and Zh production. Combined statistical and systematic uncertainties are included. Entries marked "–" indicate a negligible contribution. The "Others" contribution to $\mathrm{SRB}_{140}^{\text{2-body}}$ is dominated by $t\bar{t}W$.

	Lepton flavour	$\mathrm{SRB}_{120,140}^{2-\text{body}}$
Observed events	SF	17
Fitted SM Events		16.3 ± 6.2
Observed events	DF	13
Fitted SM Events		16.1 ± 5.3

TABLE 3.27: Background fit results for $\mathrm{SR(B)}_{x,y}^{2-\text{body}}$ regions, where x and y denote the low and high edges m_{T2} of the bin. Combined statistical and systematic uncertainties are included. Uncertainties in the predicted background event yields are quoted as being symmetric.

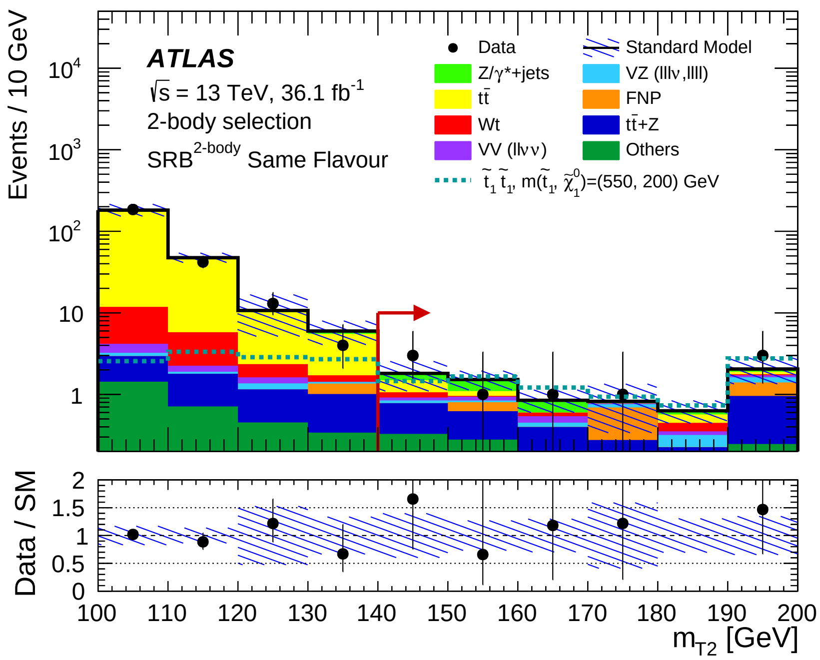

FIGURE 3.38: Distributions of m_{T2} for events satisfying the selection criteria in the $\mathrm{SRB}^{\text{2-body}}_{140}$ Same Flavour, except for the one on m_{T2}, after the background fit. The contributions from all SM backgrounds are shown; the hatched bands represent the total statistical and systematic uncertainty. The rightmost bin includes overflow events. A reference top squark pair production signal models is overlayed for comparison. Red arrows indicate the signal region selection criteria.

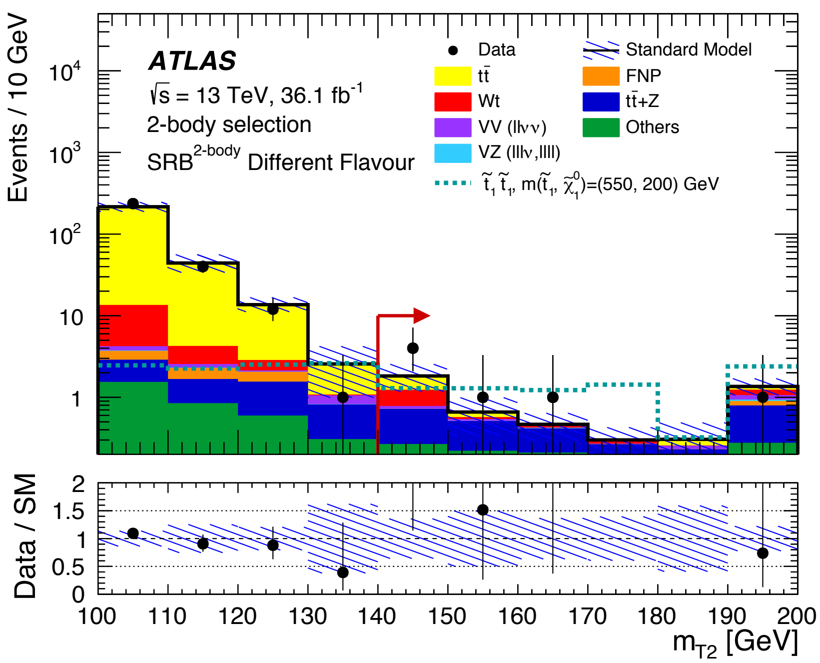

FIGURE 3.39: Distributions of m_{T2} for events satisfying the selection criteria in the $\mathrm{SRB}^{\text{2-body}}_{140}$ Different Flavour, except for the one on m_{T2}, after the background fit. The contributions from all SM backgrounds are shown; the hatched bands represent the total statistical and systematic uncertainty. The rightmost bin includes overflow events. A reference top squark pair production signal models is overlayed for comparison. Red arrows indicate the signal region selection criteria.

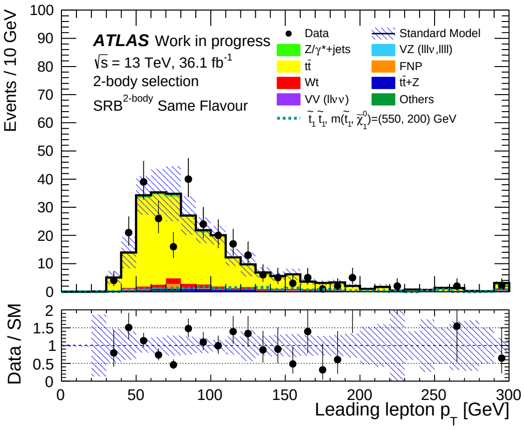

(A)

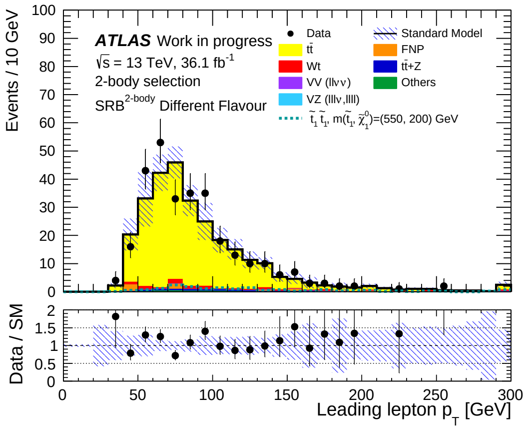

(B)

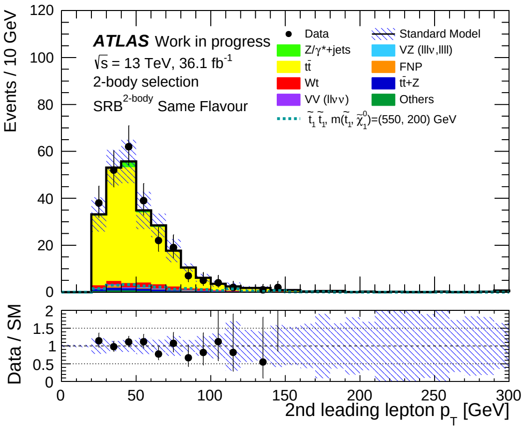

(C)

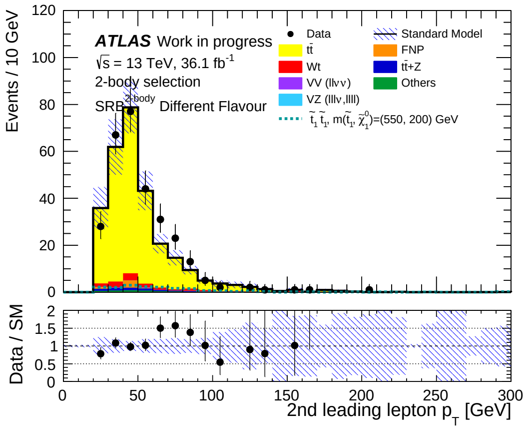

(D)

FIGURE 3.40: Distributions of p_{T} of the leading (A,B) and sub-leading (C,D) leptons for events satisfying the selection criteria in the $\mathrm{SRB}^{\text{2-body}}_{140}$ Same Flavour (left) and Different Flavour (right), except for the one on m_{T2}, after the background fit. The contributions from all SM backgrounds are shown; the hatched bands represent the total statistical and systematic uncertainty. The rightmost bin includes overflow events.

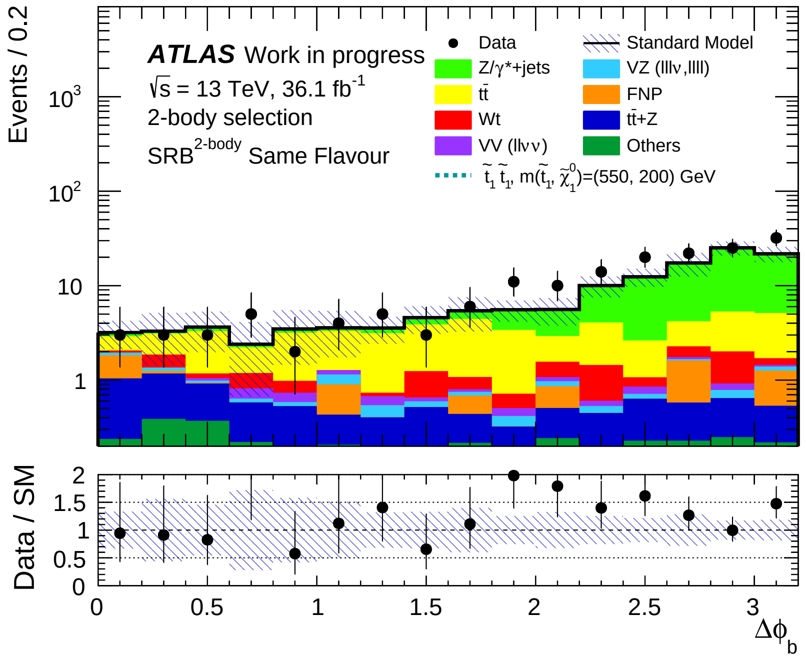

(A)

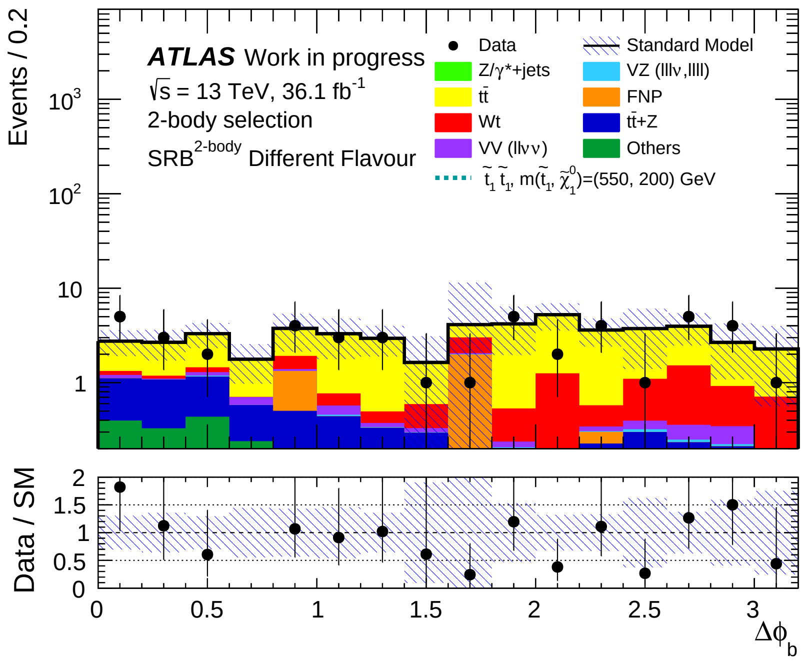

(B)

FIGURE 3.41: Distributions of $\Delta\phi_{\text{boost}}$ for events satisfying the selection criteria in the SRB$^{\text{2-body}}_{140}$ Same Flavour (A) and Different Flavour (B), except for the one on $\Delta\phi_{\text{boost}}$, after the background fit. The contributions from all SM backgrounds are shown; the hatched bands represent the total statistical and systematic uncertainty. The rightmost bin includes overflow events.

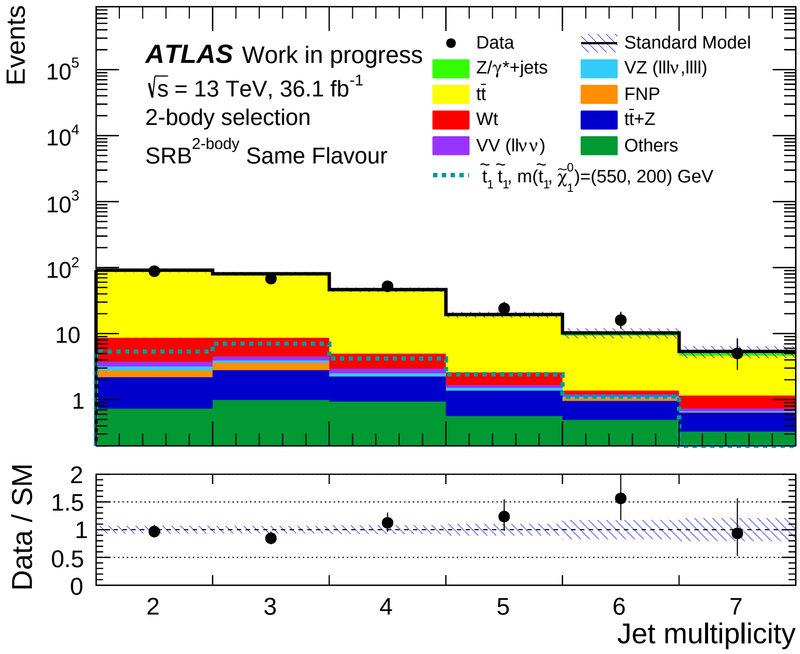

(A)

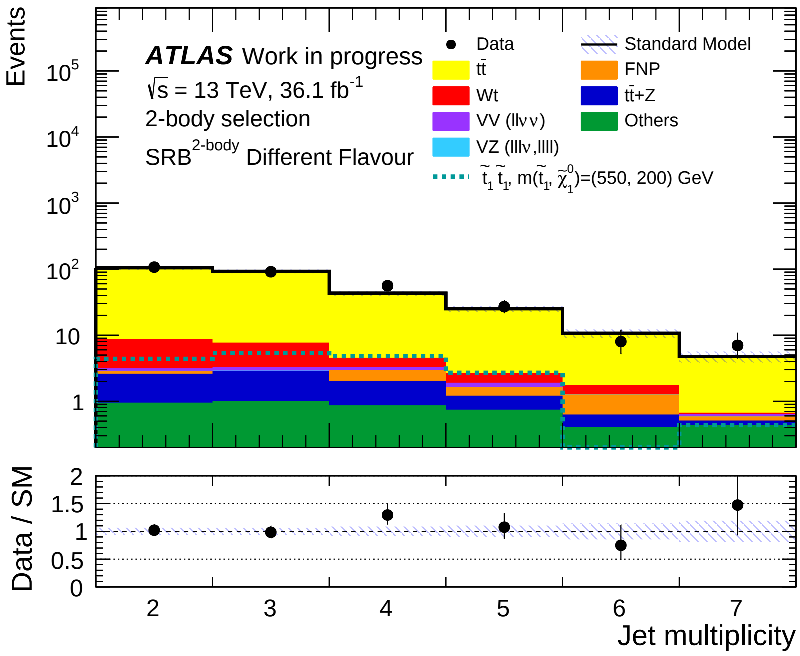

(B)

FIGURE 3.42: Distributions of the jet multiplicity for events satisfying the selection criteria in the $\mathrm{SRB}^{\text{2-body}}_{140}$ Same Flavour (A) and Different Flavour (B), except for the one on m_{T2}, after the background fit. The contributions from all SM backgrounds are shown; the hatched bands represent the total statistical and systematic uncertainty. The rightmost bin includes overflow events.

SR C

The number of events in $\mathrm{SRC}^{\text{2-body}}_{110}$ are compared to the total expected background. The selection criteria for $\mathrm{SRC}^{\text{2-body}}_{110}$ are described in Table 3.5. The distribution of m_{T2} for event with Same Flavour or Different Flavour passing the $\mathrm{SRC}^{\text{2-body}}_{110}$ selection criteria, except the one on m_{T2} are shown in Figure 3.43, 3.44. The estimated SM yields in $\mathrm{SRC}^{\text{2-body}}_{110}$ are determined with a background fit simultaneously determining the normalisations of the background contributions from $t\bar{t}$ and $t\bar{t}+Z$ by including $\mathrm{CR}^{\text{2-body}}_{t\bar{t},3j}$ and $\mathrm{CR}_{t\bar{t}Z}$ in the likelihood minimisation. A is found in No slight but not significant excess over the SM prediction is observed, as can be seen from the background-only fit results which are shown in Table 3.28. No significant excess over the SM prediction is observed. The fit results are shown in Table 3.28 for $\mathrm{SRC}^{\text{2-body}}_{110}$.

	$\mathrm{SRC}^{\text{2-body}}_{110}$ SF	$\mathrm{SRC}^{\text{2-body}}_{110}$ DF
Observed events	11	7
Fitted SM Events	5.3 ± 1.8	3.8 ± 1.5
$t\bar{t}$	2.1 ± 1.3	1.4 ± 1.2
$t\bar{t}$ +Z	1.6 ± 0.5	1.4 ± 0.5
Wt	$0.05^{+0.09}_{-0.05}$	$0.00^{+0.23}_{-0.00}$
$VV{+}VZ$	0.33 ± 0.06	0.12 ± 0.04
Z/γ^*+jets	$0.3^{+0.5}_{-0.3}$	–
Others	0.67 ± 0.13	0.81 ± 0.15
Fake and non-prompt	$0.18^{+0.41}_{-0.18}$	$0.00^{+0.02}_{-0.00}$
Fit input, $t\bar{t}$	2.3	1.6
Fit input, $t\bar{t}$ +Z	1.9	1.70

Table 3.28: Background fit results for $\mathrm{SRC}^{\text{2-body}}_{110}$. The nominal predictions from MC simulation are given for comparison for those backgrounds ($t\bar{t}$ and $t\bar{t}Z$) that are normalised to data in dedicated CRs. The "Others" category contains the contributions from $t\bar{t}W$, $t\bar{t}h$, $t\bar{t}WW$, $t\bar{t}t$, $t\bar{t}t\bar{t}$, Wh, ggh and Zh production. Combined statistical and systematic uncertainties are included. Entries marked "–" indicate a negligible contribution.

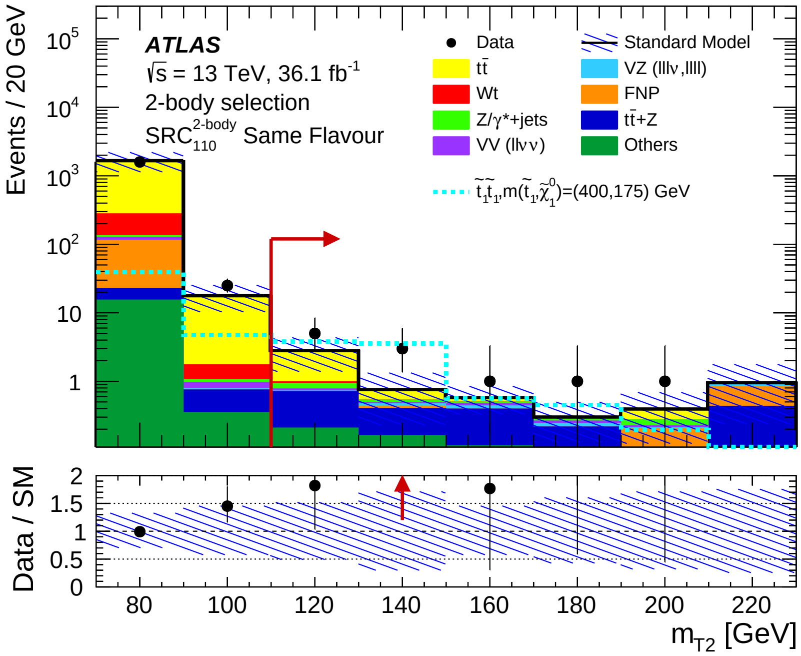

FIGURE 3.43: Distributions of the m_{T2} for events satisfying the selection criteria in the $\mathrm{SRC}_{110}^{\text{2-body}}$Same Flavour, except for the one on the m_{T2}, after the background fit. The contributions from all SM backgrounds are shown; the hatched bands represent the total statistical and systematic uncertainty. The rightmost bin includes overflow events. A reference top squark pair production signal models is overlayed for comparison.

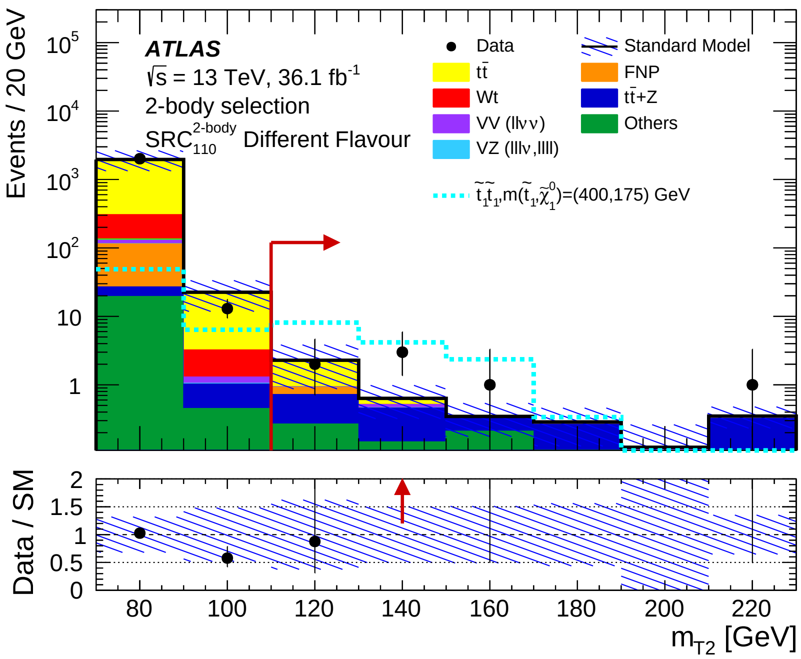

FIGURE 3.44: Distributions of the m_{T2} for events satisfying the selection criteria in the $\mathrm{SRC}_{110}^{\text{2-body}}$Different Flavour, except for the one on the m_{T2}, after the background fit. The contributions from all SM backgrounds are shown; the hatched bands represent the total statistical and systematic uncertainty. The rightmost bin includes overflow events. A reference top squark pair production signal models is overlayed for comparison.

SRt3

The number of events in SRt3 are compared to the total expected background. The selection criteria for SRt3 are described in Table 3.5. The estimated SM yields in SRt3 are determined with a background fit simultaneously determining the normalisations of the background contributions from $t\bar{t}$ and $t\bar{t}+Z$ by including CRTt3 and CR3ℓ in the likelihood minimisation. No significant excess over the SM prediction is observed, as can be seen from the background-only fit results which are shown in Table 3.28.

	SRt3
Observed events	18
Fitted SM Events	15.2 ± 4.3
$t\bar{t}$	4.5 ± 2.5
$t\bar{t}$+Z	4.4 ± 1.9
Wt	$0.33^{+0.53}_{-0.33}$
VV	0.61 ± 0.25
Fake and non-prompt	2.7 ± 1.3
Others	2.69 ± 0.93
Fit input, $t\bar{t}$	4.0
Fit input, $t\bar{t}$+Z	5.6

Table 3.29: Fit results in SRt3 for an integrated luminosity of 36.1 fb^{-1}. The background normalisation parameters are obtained from the background-only fit in the CRs and are applied to the SRs. Pre-fit values are also shown. Small backgrounds are indicated as Others (see text for details). Benchmark signal models yields are given for each SR. The uncertainties in the yields include statistical uncertainties and all systematic uncertainties defined in Sect. 3.11.

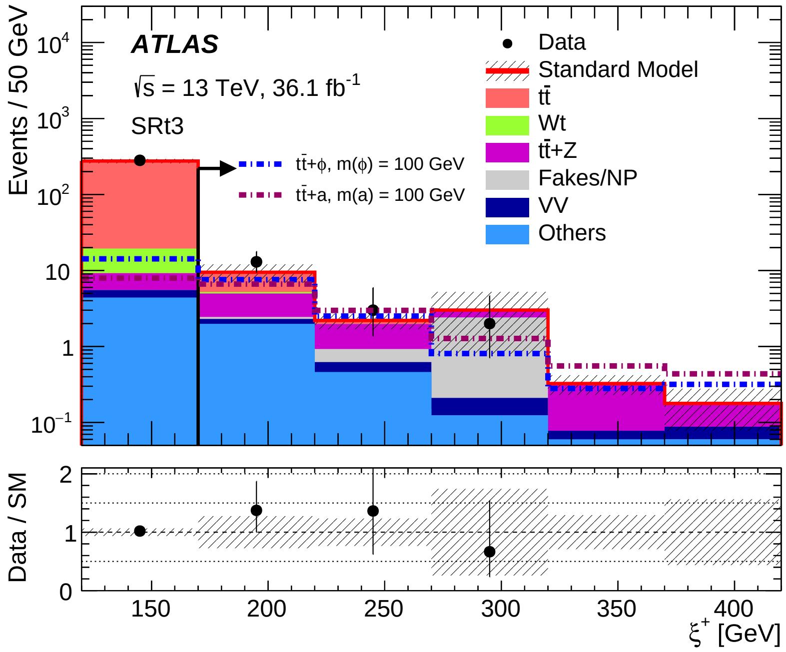

FIGURE 3.45: Distributions of $\xi^+$for events satisfying the selection criteria in the SRt3, except for the one on the jet multiplicity, after the background fit. The contributions from all SM backgrounds are shown; the hatched bands represent the total statistical and systematic uncertainty. The rightmost bin includes overflow events. Reference DM signal models are overlayed for comparison.

3.15 Interpretation

The observed yields in each SR is compared with the SM expectations using the frequentist significance tests introduced in Section 3.5.

Two different sets of exclusion limits are derived for models of new physics beyond the SM. Since no excess of events in data is observed, model independent limits at 95% of C.L. are derived on the product $\sigma \times \epsilon \times \mathcal{A}$, where σ is the non-SM cross section, ϵ the selection efficiency, and $\mathcal{A}$ the acceptance of kinematic cuts. The selection efficiency and acceptance of kinematic cuts are presented in the Appendix B. The limit on the visible cross-section σ_{vis} of new physics, defined as the ratio between the upper limit at 95% CL on the number of signal events S^{95} and the integrated luminosity, is derived in each SR by performing a fit which includes the observed yield in the SR as a constraint, and a free signal yield in the SR as an additional process. Model-independent upper limits are presented in Table 3.30.

Model-dependent limits are computed for the various scenarios presented in Section 1.6 and 1.7. Profile likelihood fits are performed including the expected signal yield and its associated uncertainties in the CRs and SRs. When setting limits, the regions included in the m_{T2} shape fits ($\text{SRA}^{2-\text{body}}_{x,y}$ and $\text{SRB}^{2-\text{body}}_{x,y}$) are statistically combined. The CL_s method [165] is used to derive all the exclusion confidence levels. All limits are quoted at 95% CL. Two types of CLs values are considered: CLs_{exp} is obtained is considering the median of the background pdf as "data" in the signal regions, and provides an estimate of the expected sensitivity of the analysis; CLs_{obs} is obtained when the observed data is used in the signal regions. CLs values below 0.05 allow to exclude the given signal model under test at 95% confidence level. These limits assume negligible signal contamination in the CRs. This assumption leads to conservative results when

Signal Region	$\sigma_{\rm vis}$ [fb]	S^{95}_{obs}	S^{95}_{exp}	$p(s=0)$
$\mathrm{SRA}^{\text{2-body}}_{180}$ SF	0.37	13.2	10^{+4}_{-3}	0.20
$\mathrm{SRA}^{\text{2-body}}_{180}$ DF	0.26	9.5	$7.0^{+3.0}_{-1.8}$	0.19
$\mathrm{SRB}^{\text{2-body}}_{140}$ SF	0.24	8.6	$7.2^{+2.7}_{-1.8}$	0.28
$\mathrm{SRB}^{\text{2-body}}_{140}$ DF	0.23	8.4	$6.0^{+2.7}_{-1.3}$	0.19
$\mathrm{SRC}^{\text{2-body}}_{110}$ SF	0.36	13.0	$7.4^{+3.1}_{-2.0}$	0.05
$\mathrm{SRC}^{\text{2-body}}_{110}$ DF	0.26	9.5	$6.3^{+2.5}_{-1.6}$	0.12
SRt3	0.44	15.9	13^{+5}_{-2}	0.33

TABLE 3.30: Model-independent 95% CL upper limits on the visible cross-section ($\sigma_{\rm vis}$) of new physics, the visible number of signal events (S^{95}_{obs}), the visible number of signal events (S^{95}_{exp}) given the expected number of background events (and $\pm 1\sigma$ excursions of the expected number), and the discovery p-value ($p(s=0)$), all calculated with pseudo-experiments, are shown for each SR.

comparing with model-dependent limits for models that predict a sizeable contamination in the CRs.

Limits for simplified models in which pair-produced $\tilde{t}_1$ decay with 100% branching ratio into a top quark and $\tilde{\chi}^0_1$ are shown in the $\tilde{t}_1$–$\tilde{\chi}^0_1$ mass plane in Figure 3.46. The SRs presented in this chapter cover the two body decay scenario. Top squark masses up to 720 GeV are excluded for a massless lightest neutralino. Neutralino masses up to 300 GeV are excluded for $m_{\tilde{t}_1} = 645$ GeV.

Limits are shown for a class of simplified models in which only pair-produced $\tilde{t}_1$ decaying with 100% branching ratio into the lightest chargino ($\tilde{\chi}^{\pm}_1$) and a b-quark are considered. Figure 3.47 shows the interpretation in the $\tilde{t}_1$–$\tilde{\chi}^0_1$ mass plane assuming that $m_{\tilde{t}_1}$ - $m_{\tilde{\chi}^{\pm}_1} = 10$ GeV. Top squark masses up to 700 GeV are excluded for an LSP mass up to 200 GeV.

Limits are set on a pMSSM model presented in Section 1.6. Top squark masses up to about 700 GeV are excluded for a lightest neutralino of about 280 GeV. The sensitivity for low values of $m_{\tilde{\chi}^0_1}$ is limited by the $m_{\rm T2}$ selection acceptance, since $m_{\tilde{\chi}^{\pm}_1} - m_{\tilde{\chi}^0_1}$ is reduced by assuming $M_2 = 2M_1$.

The results of SRt3 are used to set limits on the production cross-section of colour-neutral mediator models decaying into dark-matter particles. Figures 3.49 and 3.50 show upper limits at 95% CL on the signal cross-section scaled to the signal cross-section for coupling $g = 1$, denoted by $\sigma/\sigma(g = 1.0)$. These are the most stringent limits to date on $t\bar{t} + \phi/a$ models. These limits are obtained both as a function of the mediator mass, assuming a specific DM mass of 1 GeV (Figure 3.49), and as a function of the DM mass, assuming a specific mediator mass of 10 GeV (Figure 3.50). Both the scalar and pseudoscalar mediator cases are considered. The sensitivity for $t\bar{t} + \phi/a$ on-shell decays is approximately constant for masses below 100 GeV, with SRt3 excluding the $g = 1$ assumption for scalar mediator masses up to 50 GeV. For a given mediator mass the acceptance of the analysis is independent of the value of the DM mass as long as $m(\phi/a) > 2 \cdot m(\chi)$ is fulfilled and width effects can be neglected. Under these conditions, exclusion limits for DM masses differing from the one presented can be inferred from the result shown in Figure 3.49.

For each dark-matter and mediator mass pair, the exclusion limit on the production cross-section of colour-neutral scalar mediator particles can be converted into a limit on the spin-independent DM–nucleon scattering cross-section using the procedure described in Ref. [166]. The results can thus be compared with the results from direct-detection experiments. The most stringent

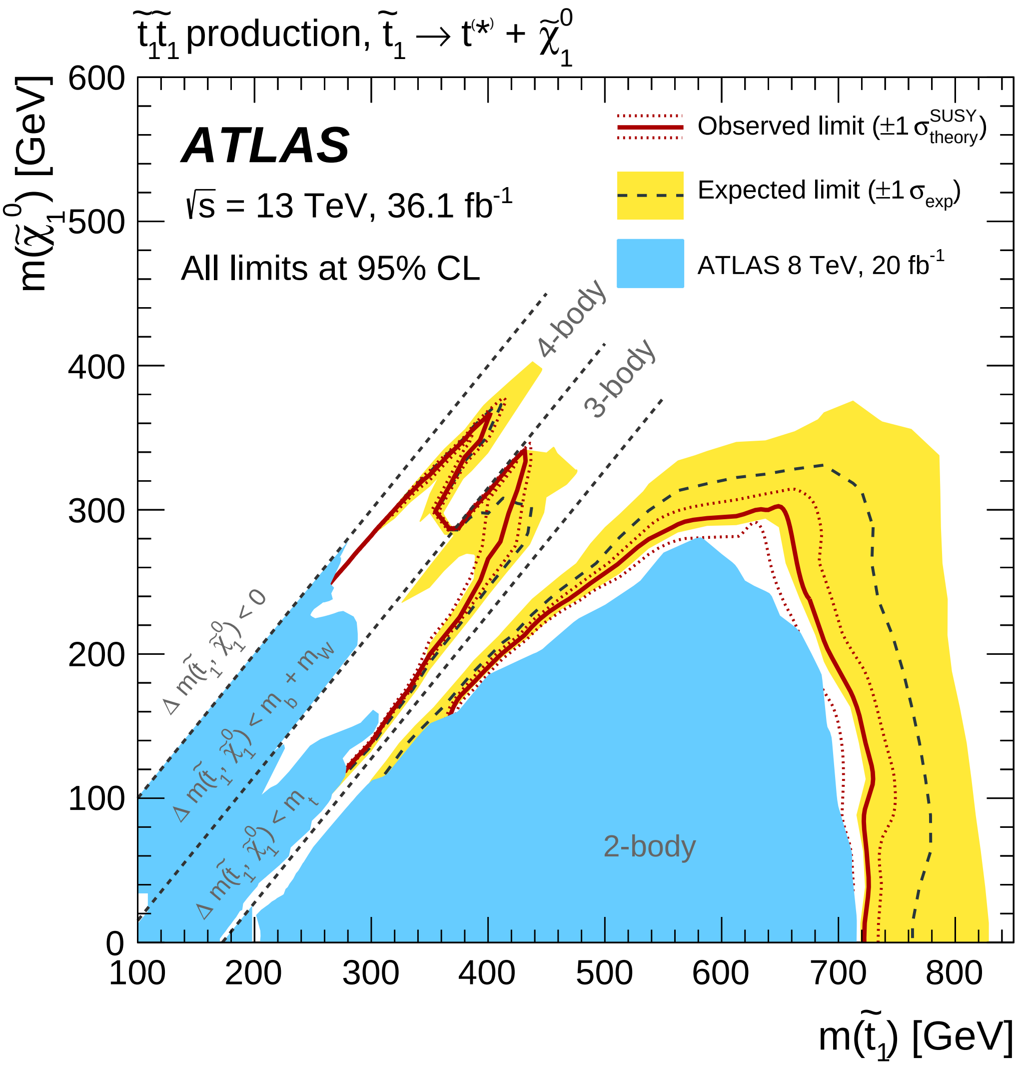

FIGURE 3.46: Exclusion contour for a simplified model assuming $\tilde{t}_1$ pair production, decaying via $\tilde{t}_1 \rightarrow t^{(*)}\tilde{\chi}^0_1$ with 100% branching ratio. The dashed grey line and the shaded yellow band are the expected limit and its $\pm1\sigma$ uncertainty. The thick solid red line is the observed limit for the central value of the signal cross-section. The expected and observed limits do not include the effect of the theoretical uncertainties in the signal cross-section. The dotted lines show the effect on the observed limit when varying the signal cross-section by $\pm1\sigma$ of the theoretical uncertainty. The shaded blue areas show the observed exclusion from the ATLAS $\sqrt{s} = 8$ TeV analyses [49].

limits, provided by SRt3, are used for this purpose. Figure 3.51 shows the constraints from this analysis expressed as exclusion limits at 90% CL in the plane defined by the dark-matter mass and the scattering cross-section. The black line indicates the exclusion contour derived from the observed limits in the top part of Figure 3.49, where mediator masses between 10 GeV and 500 GeV are considered. The maximum value of the DM–nucleon scattering cross-section displayed corresponds to the result obtained for a mediator mass of 10 GeV. The results of this analysis are compared with the results from the LUX [167], PandaX-II [168], XENON [169], SuperCDMS [170] and CRESST-II [171] experiments. The comparison is model-dependent, and therefore valid only for the specific models considered in this paper. For pseudoscalar mediator models, the predicted dark-matter cross-sections in these direct-detection experiments is suppressed by velocity-dependent terms. As a result, direct-detection limits on spin-independent

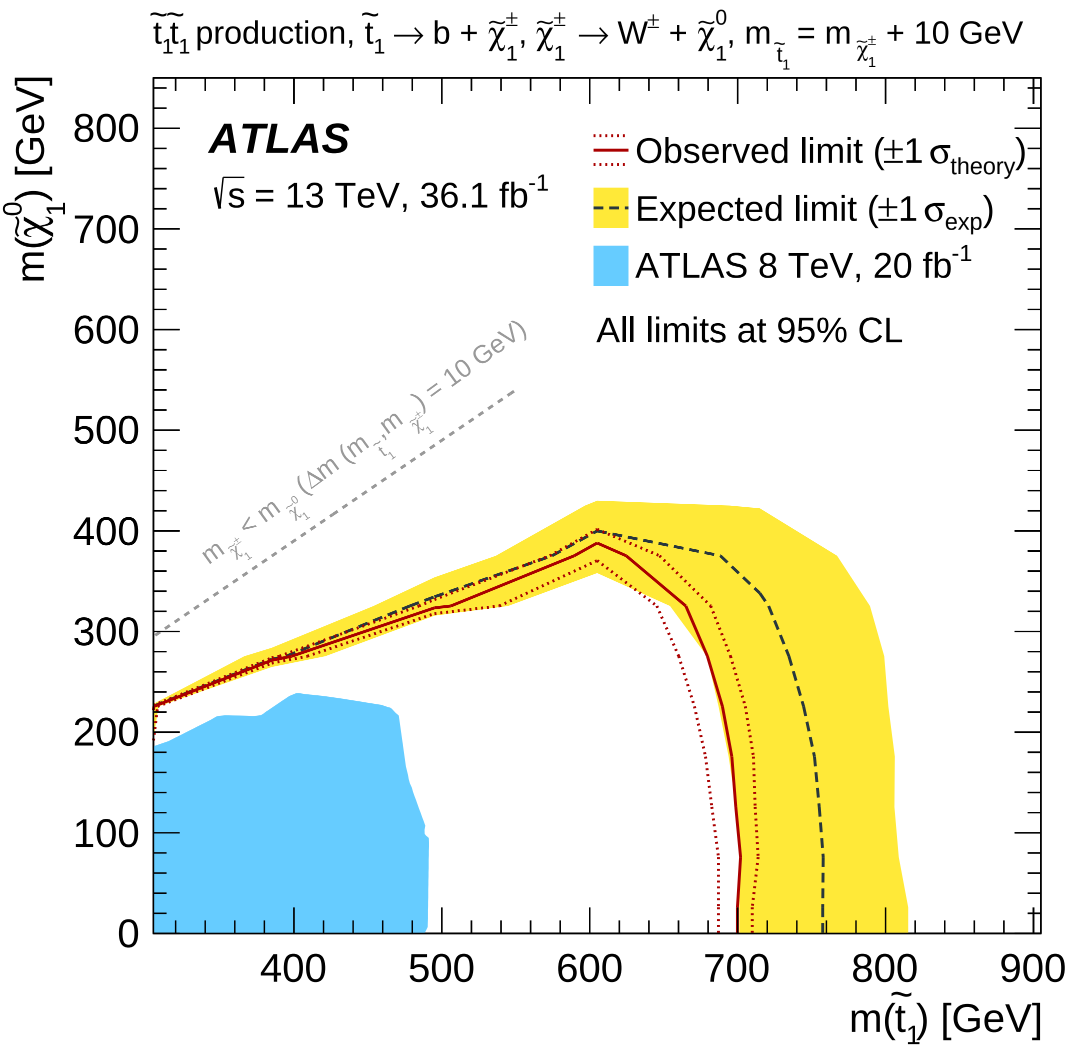

FIGURE 3.47: Exclusion contour for a simplified model assuming $\tilde{t}_1$ pair production, decaying via $\tilde{t}_1 \to b\tilde{\chi}_1^\pm$ with 100% branching ratio. The lightest chargino mass is assumed to be close to the stop mass, $m_{\tilde{\chi}_1^\pm} = m_{\tilde{t}_1} - 10$ GeV. The dashed grey line and the shaded yellow band are the expected limit and its $\pm 1\sigma$ uncertainty. The thick solid red line is the observed limit for the central value of the signal cross-section. The expected and observed limits do not include the effect of the theoretical uncertainties in the signal cross-section. The dotted lines show the effect on the observed limit when varying the signal cross-section by $\pm 1\sigma$ of the theoretical uncertainty. The shaded blue area shows the observed exclusion from the ATLAS $\sqrt{s} = 8$ TeV analysis [49].

DM–nucleon scattering cross-section are several orders of magnitude worse than the ones obtained in this analysis, and therefore not presented.

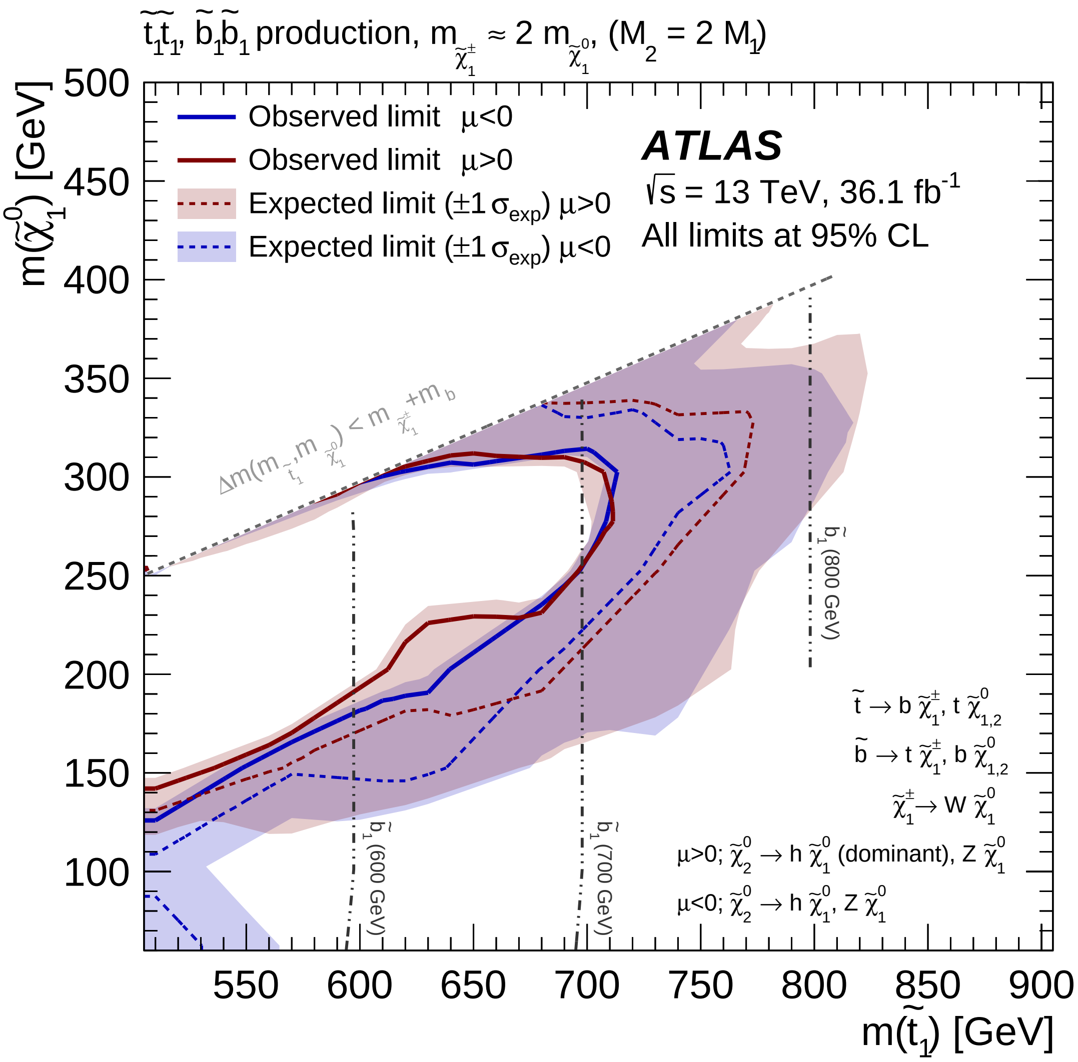

FIGURE 3.48: Exclusion contour as a function of $m_{\tilde{t}_1}$ and $m_{\tilde{\chi}_1^0}$ in the pMSSM model. Pair production of $\tilde{t}_1$ and $\tilde{b}_1$ are considered. Limits are set for both the positive (red in the figure) and negative (blue in the figure) values of μ. The dashed and dotted grey lines indicate constant values of the $\tilde{b}_1$ mass. The signal models included within the shown contours are excluded at 95% CL. The dashed lines and the shaded band are the expected limit and its $\pm 1\sigma$ uncertainty. The thick solid line is the observed limit for the central value of the signal cross-section. The expected and observed limits do not include the effect of the theoretical uncertainties in the signal cross-section.

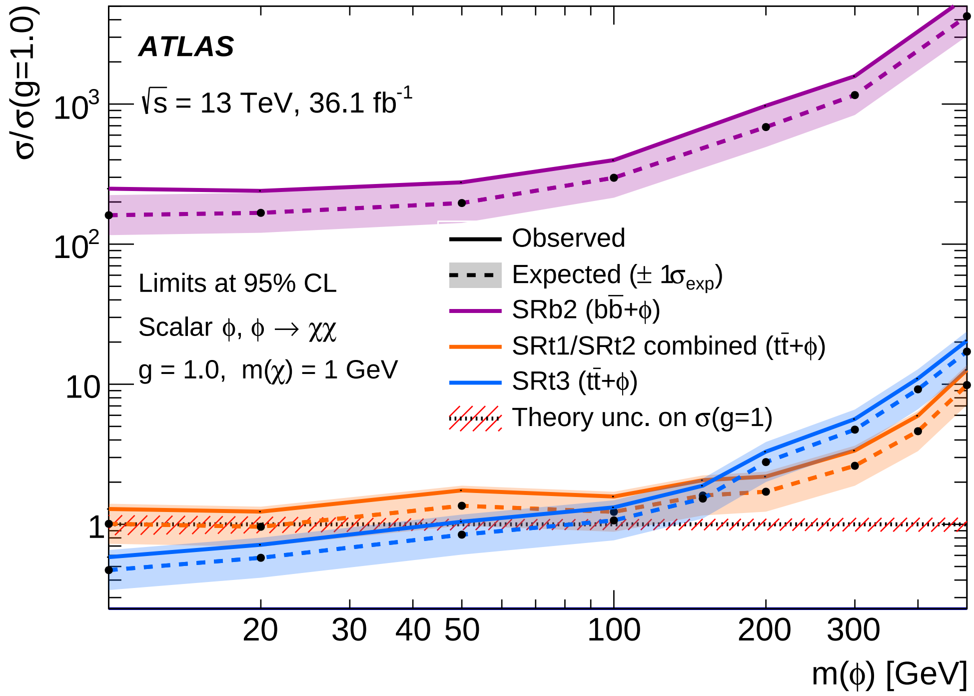

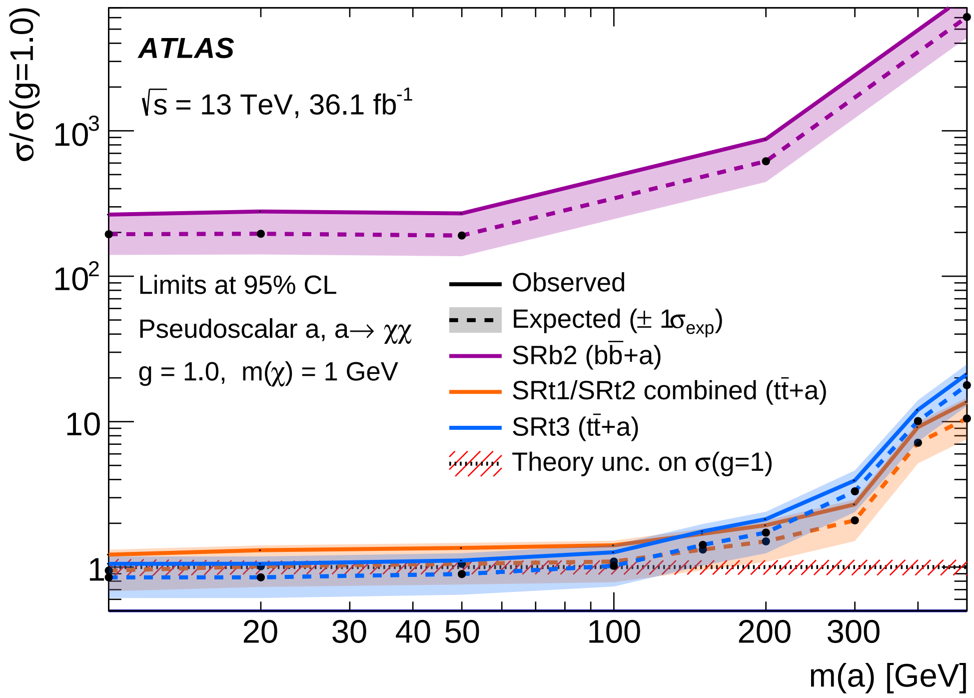

FIGURE 3.49: Exclusion limits for colour-neutral $t\bar{t}/b\bar{b} + \phi$ scalar (top) and $t\bar{t}/b\bar{b} + a$ pseudoscalar (bottom) models as a function of the mediator mass for a DM mass of 1 GeV. The limits are calculated at 95% CL and are expressed in terms of the ratio of the excluded cross-section to the nominal cross-section for a coupling assumption of $g = g_q = g_\chi = 1$. The solid (dashed) lines shows the observed (expected) exclusion limits for the different signal regions, according to the colour code specified in the legend. To derive the results for the fully hadronic $t\bar{t}$ final state the region SRt1 or SRt2 providing the better expected sensitivity is used.

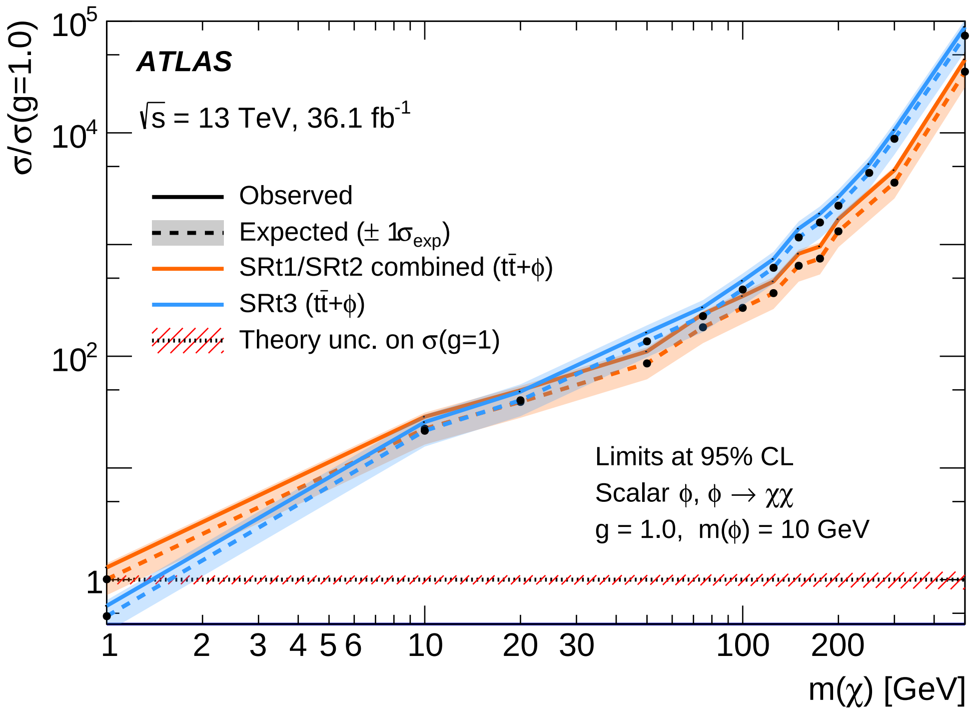

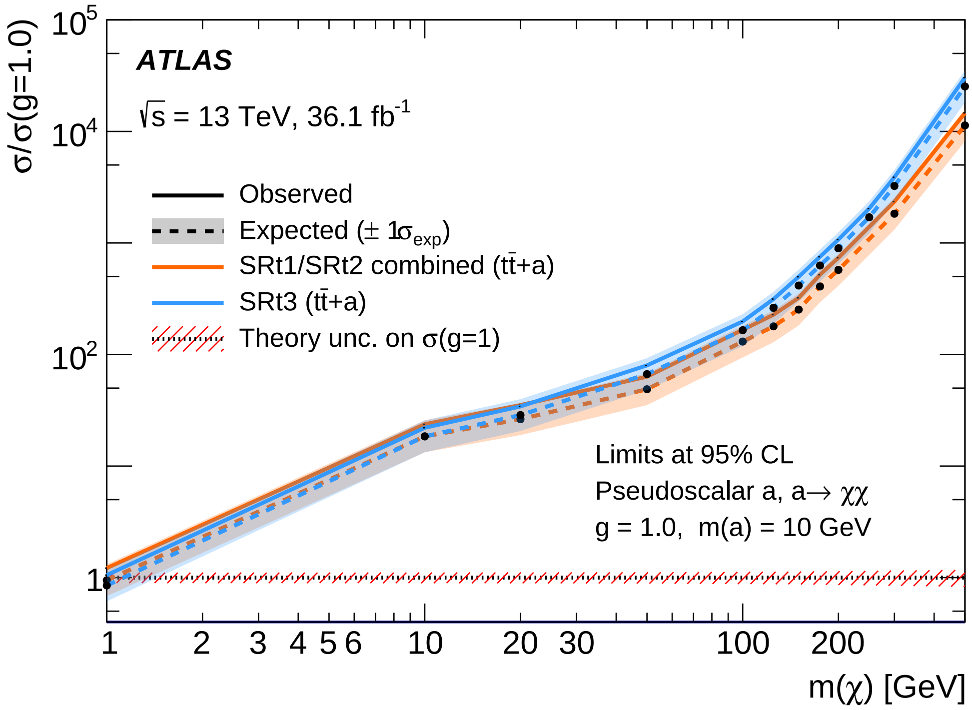

FIGURE 3.50: Exclusion limits for colour-neutral $t\bar{t} + \phi$ scalar (top) and $t\bar{t} + a$ pseudoscalar (bottom) models as a function of the DM mass for a mediator mass of 10 GeV. The limits are calculated at 95% CL and are expressed in terms of the ratio of the excluded cross-section to the nominal cross-section for a coupling assumption of $g = g_q = g_\chi = 1$. The solid (dashed) lines shows the observed (expected) exclusion limits for the different signal regions, according to the colour code specified in the legend. To derive the results for the fully hadronic $t\bar{t}$ final state the region SRt1 or SRt2 providing the better expected sensitivity is used.

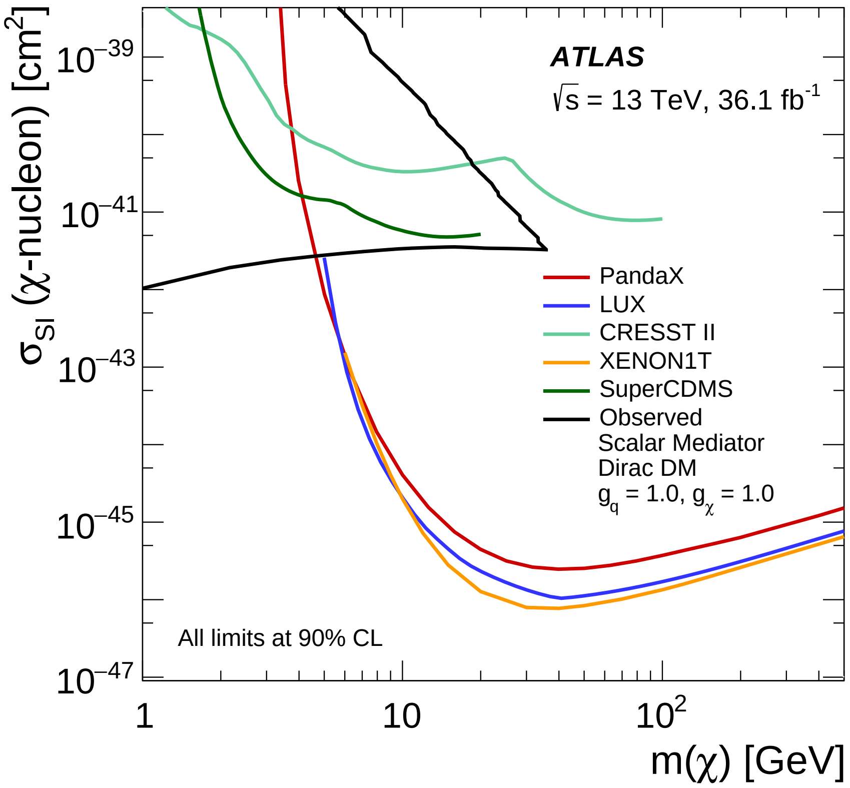

FIGURE 3.51: Comparison of the 90% CL limits on the spin-independent DM–nucleon cross-section as a function of DM mass between these results and the direct-detection experiments, in the context of the colour-neutral simplified model with scalar mediator. The black line indicates the exclusion contour derived from the observed limits of SRt3. Values inside the contour are excluded. The exclusion limit is compared with limits from the LUX [167], PandaX-II [168], XENON [169], SuperCDMS [170] and CRESST-II [171] experiments.

Chapter 4

HL–LHC and the ATLAS Upgrade

The LHC program is divided into different data taking Runs as reported in Figure 4.1. Between each Run, few years of shutdown, called Long Shutdown (LS) are foreseen for maintenance and installation of upgrades. The analysis presented in the previous Chapter, examined the 36.1 fb^{-1} of data collected in the beginning of the Run 2 period between 2015 and 2016.

By the end of Run 2 in 2018, the LHC is expected to have delivered more than $\sim$150 fb^{-1} of proton-proton collisions with an instantaneous luminosity of $\sim 2 \times 10^{34}$ $\text{cm}^{-2}\text{s}^{-1}$ and an average number of collisions per bunch crossing $\langle\mu\rangle \sim 40$. In the next two years, the Long Shutdown 2 will follow (2019-20), during which the injection chain is foreseen to be modified to allow for instantaneous luminosities up to $\sim 5{\times}10^{34}$ $\text{cm}^{-2}\text{s}^{-1}$ and the centre of mass energy will be increased to 14 TeV thus reaching the nominal LHC energy. During Run 3, the average number of proton-proton collisions per bunch crossing is expected to be $\langle\mu\rangle \sim 80$ and the data collected up to the next Long Shutdown 3 will amount to $\sim$ 300 fb^{-1}.
After the LS3 (2024-2026), the upgrade project of the LHC, called the High Luminosity-LHC (HL–LHC), is planned to be ready during late 2026. This project intends to increase the instantaneous luminosity of the proton-proton collisions to more than $7.5 \cdot 10^{34}\,\text{cm}^{-2}\text{s}^{-1}$, with an $\langle\mu\rangle \sim 200$ with the goal to deliver more than 3000 fb^{-1} during the 10 years of operation.

During the LS3 period, major upgrades of the all the ATLAS detector will be needed allowing full exploitation of the LHC physics programme. The upgrades are required to cope with increased particle multiplicity, the large pile-up and huge radiation doses. A fully silicon based detector called Inner Tracker (ITk) will replace the current ATLAS Inner Detector. The current Liquid Argon calorimetry and the Tile Calorimeter are expected to be fully operational also during the HL-LHC. Upgrades will concern all the readout electronics and power supplies because of radiation tolerance limits and because the on-detector front-end electronics cannot operate with the trigger rates and latencies required. With the new readout, an higher resolution information will be available at the lowest level of the trigger system. The Muon Spectrometer upgrade focuses primarily on the improvement of the performance of the muon trigger chambers. A complete upgrade of the Trigger and Acquisition (TDAQ) will be installed. The readout capacity will be increased from the actual 100kHz to 1MHz and the data-output sent into storage from 1kHz to 10kHz. The tracking information coming from ITk and the full calorimeter granularity will be available in the trigger architecture. In the next section the ITk project will be introduced.

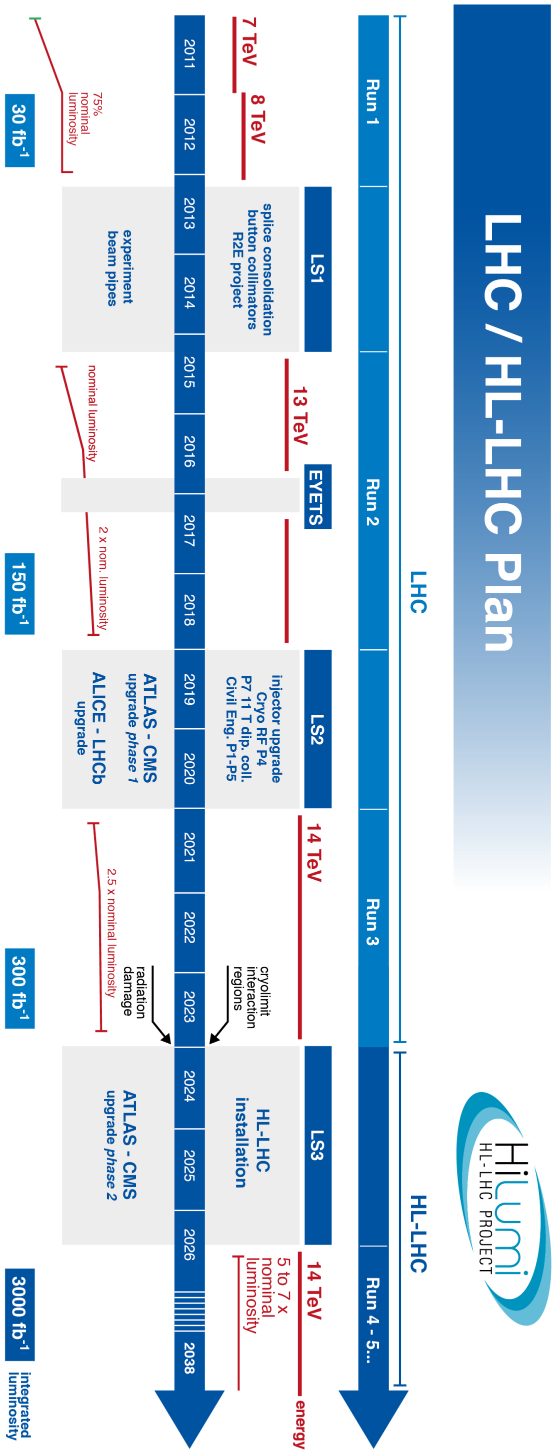

Figure 4.1: The schedule for the LHC and HL–LHC is reported.

4.1 The Inner Tracker

The Inner Tracker (ITk) will be a fully silicon based detector which will be able to maintain good performance up to fluences expected after 10 years of data taking in the harsh environment The current design foresees a Pixel Detector in the inner part and a strip detector in the outer one (Figure 4.2). A pixel detector, composed of five barrel layers and four end-cap ring layers, will be installed to provide hermetic tracking coverage up to $|\eta| = 4$. The strip detector will be composed of four barrel layers and six disks on each side of the end-cap [172].

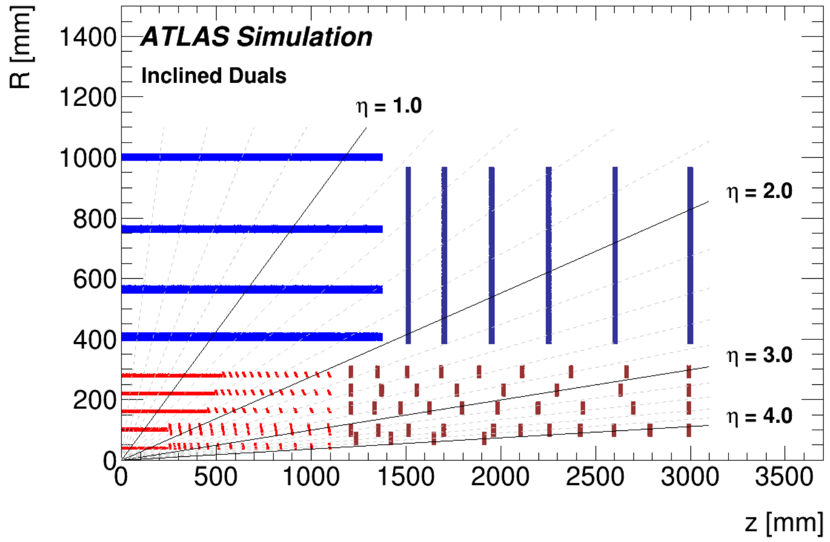

FIGURE 4.2: A schematic layout of the current design of the ITk for the HL–LHC phase. Only one quadrant and only active detector elements are shown for both diagrams. The active elements of the barrel and end-cap Strip Detector are shown in blue, for the Pixel Detector the sensors are shown in red for the barrel layers and in dark red for the end-cap rings. The horizontal axis is along the beam line with zero being the interaction point. The vertical axis is the radius measured from the interaction region [173].

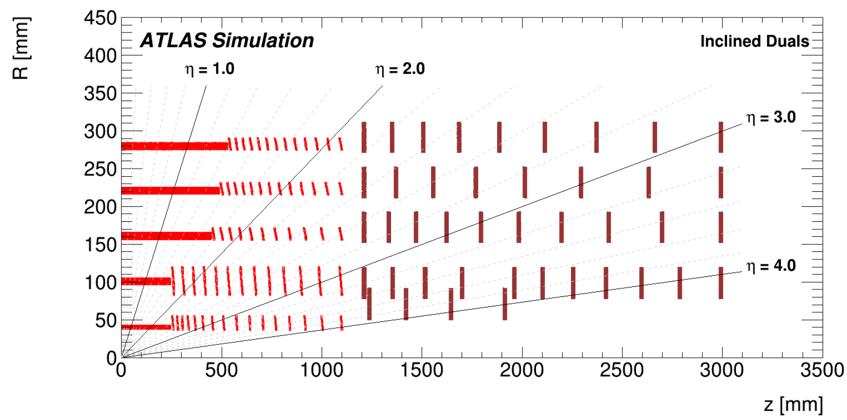

FIGURE 4.3: Zoom into the Pixel Detector. Only one quadrant and only active detector elements are shown for both diagrams. The sensors of the Pixel Detector are shown in red for the barrel layers and in dark red for the end-cap rings. The horizontal axis is along the beam line with zero being the interaction point. The vertical axis is the radius measured from the interaction region [173].

The current Pixel Detector layout [174] is an evolution of the layout presented in the Strip TDR [172]. Two novel design ideas have been implemented. The first one is the inclined barrel

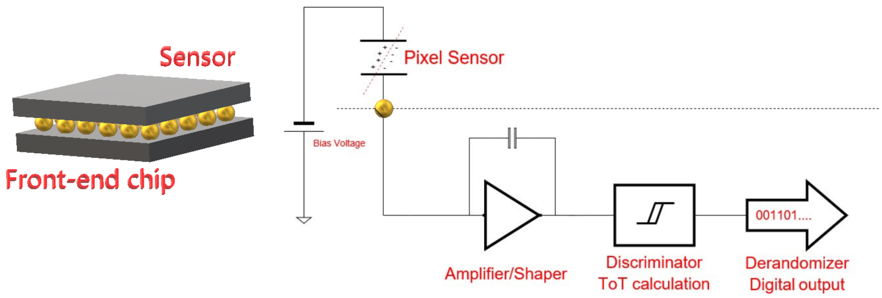

FIGURE 4.4: Schematic view of a hybrid pixel module. [173].

stave design (Figure 4.3); for $\eta > 1.5$, the flat barrel stave is prolonged with a section with inclined modules. This allows to minimise the degradation of the performance due to material in the transition region between the barrel and the end-cap section. Moreover, it allows to reduce the amount of silicon needed as inclined modules have a larger angular coverage in this region. The second novel concept is the end-cap ring system. The pixel rings extend the coverage in z and allow routing the service separately along each ring layers. This two new concepts have been introduced to keep the number of hits more stable as a function η considering both the hits coming from the Pixel and the Strip detector. In particular, using the inclined allow to keep the number of hits above 9 in all η region except very close to η of 4.

The staves and the rings will be populated by so-called "hybrid module" similar to the one adopted for the present ATLAS Pixel Detector and for the IBL. They made of two parts: a passive high resistivity silicon sensor and a front-end read-out chip fabricated in CMOS technology. The two parts are joined using a high density connection technique called "bump-bonding". A schematic of the elements of a hybrid pixel module is presented in Figure 4.4.

Three size of module will be used: single read-out chip modules $20 \times 20\ mm^2$ in the inclined section of barrel layer 0; duals read-out chip modules of $20 \times 40\ mm^2$ in size for the flat section of barrel layer 0 and, still to be defined, in the inclined section of the barrel layers 2 to 4. Quads read-out chip modules of $40 \times 40\ mm^2$ in size will be used for the remaining parts of the detector.

Due to the increased luminosity and the associated increase in the rate of proton-proton collisions, the expected radiation levels in the ATLAS ITk will increase by roughly an order of magnitude compared to the present Inner Detector. Radiation background simulations have been performed for the ITk using PYTHIA [126] event generator and the FLUKA [175] particle transport code. The expected fluences and the dose distributions for the Pixel Detector are shown in Figure 4.5. While fluences in the innermost layers of the ITk pixel barrel region are dominated by particles coming directly from the interaction point, the fluences in the outer barrel layers and the pixel end-cap region are increasingly dominated by particles coming from secondary interactions in the calorimeter, beam-line and pixel service material.

To cope with the harsh environment expected at the HL–LHC, different approaches are being developed for pixel detectors. For the innermost layer 3D silicon detectors will be used. They are intrinsically more radiation tolerant than other available sensor technologies because the distance between the electrodes, which penetrate the sensor bulk perpendicular to the surface, are decoupled from the device thickness. This distance can be chosen to be significantly smaller than the thickness of the standard planar sensors where the electrodes are implanted in the surface of the device. The shorter distance between the electrodes leads to less charge trapping from radiation induced defects and lower operational voltage. Planar sensors are the baseline for the other Layer of ITk.

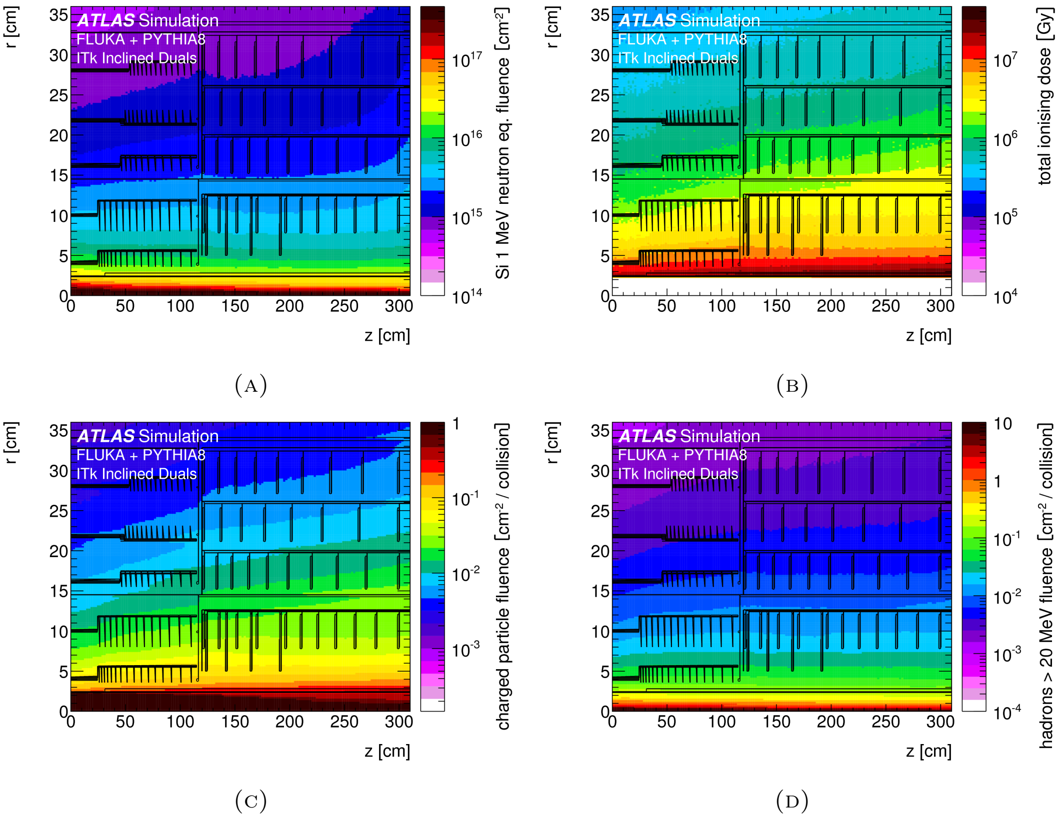

Figure 4.5: The fluence and dose distributions for the Pixel Detector. (A) 1 MeVneutron equivalent fluence. (B) Total ionising dose. (C) Charged particle fluence. (D) Hadron fluence for energies greater than 20 MeV. The (A) and (B) plots are normalised to 4ab^{-1}.

Detector Part	Inclined Duals Layout [m^2]
Inner Barrel Flat	0.52
Inner Barrel Inclined	1.00
Inner Barrel Total	1.51
End-cap Inner Rings	0.94
Outer Barrel Flat	4.49
Outer Barrel Inclined	2.30
Outer Barrel Total	6.79
End-cap Outer Rings	3.50
Barrel Total	8.30
End-cap Rings Total	4.44
Total	12.74

Table 4.1: Summary of the pixel surface needed for the different parts of the detector.

Table 4.1 summarises the total silicon surface needed for the different parts of the detector. In total the pixel surface is 12.55 m^2 . In total, more than 10k modules will be constructed of which $\sim$ 500 single module chip, 3.2k dual module chip and $\sim$ 6.5k quad module chip.

4.2 Monolithic CMOS pixel

A new approach towards a pixel module is a "monolithic module" with pixel sensor and read-out chip being one entity, in contrast to the traditional "hybrid" pixel module described in the previous section.

The monolithic CMOS sensor technology is being investigated for the outer layers of the pixel detector of ITk. In this region the requirements for radiation hardness and hit rate can be relaxed and a fully monolithic design could be a viable approach. This technology would reduce potentially the power consumption per chip and decrease the material in front of the calorimeter system. Furthermore, production costs would be reduced and production yields is improved since commercial process can be used. The most striking difference with respect to the hybrid sensors is the absence of the bump bonding process. The monolithic CMOS technology can house the charge collection, the analog amplification and the digital electronics in the same silicon wafer. The charge collection is obtained by applying a reverse bias voltages (HV) of the order of 100 V. The combination of high voltage and CMOS technology is a novel concept for a monolithic devices [176]. Thanks to this a fast charge collection is possible, profiting from the signal obtained by charge drift. The analog and digital circuitries are usually implemented in the a deep n-wells to be decoupled from the charge collection region in the p-substrate. The radiation hardness is improved thanks to multiple nested wells which give the embedded CMOS electronics sufficient shielding. As shown in the Figures 4.5(a) and 4.5(b) the 1 MeV neutron equivalent dose for the sensor in the outer layer is evaluated to be up to 10^{15} $n_{\mathrm{eq}}/\mathrm{cm}^2$ and a total ionising dose of 10^6 Gy.

Two different sensor designs have been developed in the ATLAS CMOS Collaboration with the goal to produce a fully monolithic CMOS module; a solution with a *small fill factor* and another with a *large fill factor*

In this *Small fill factor* design the electronics are placed outside the charge collection wells. Figure 4.6 shows a schematic cross section of a sensor with small fill factor. In addition the analog and digital circuitries are placed in separate wells minimising their cross talk. Noise and power consumption are minimised by the small capacitance between the electronic and the charge collection well. In order to increase the depletion region and further increase radiation hardness a process modification was developed by implanting a planar n-layer in epitaxial layer p^+ [177].

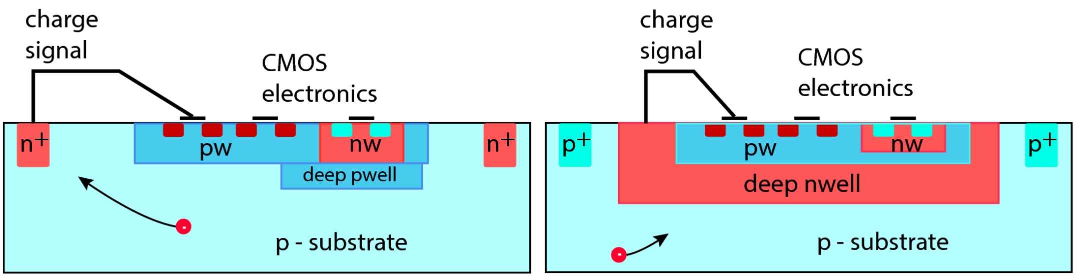

(A) (B)

FIGURE 4.6: Schematic cross-section of a CMOS sensor with small (A) and large (B) fill factor technologies. In the small fill factor the charge collection node is placed outside the CMOS electronics area, while in the large fill factor the charge collecting deep nwell encloses the complete CMOS electronics [173].

The *large fill factor* design maximises the charge collection with a large electrode. The digital and the analog circuitries are implemented inside a common charge collecting well. Radiation

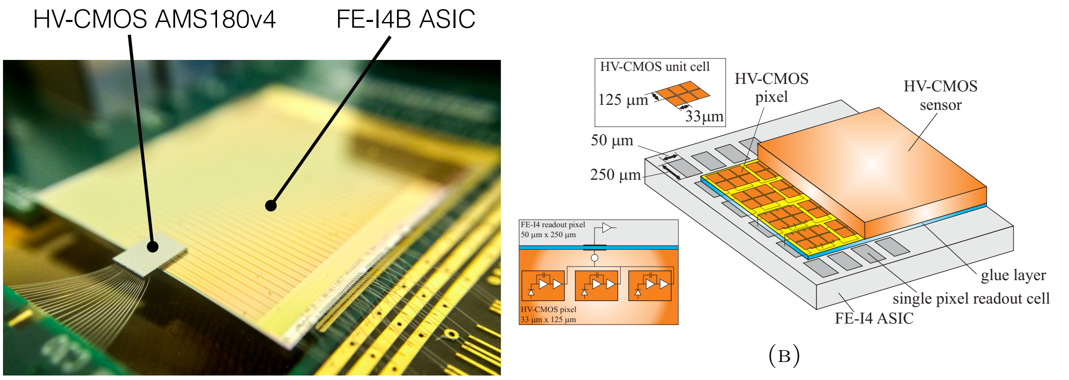

(A) (B)

FIGURE 4.7: (A) Assembly of a FE-I4 pixel readout chip to HV-CMOS *CCPDv4* sensor via capacitive coupling [179]. (B) Schematic representation (not in scale) of the HV-CMOS to FE-I4B connections. The bottom-left inset shows how three HV-CMOS pixels (forming a so-called *macro-pixel*) are capacitively coupled to a single FE-I4B readout pixel.

hardness is achieved due to the electrode size and the depletion thickness. Figure 4.6 shows a schematic cross section of a sensor with large fill factor.

I characterized a prototype sensor designed using a *large fill factor* design. This sensor, referred to as *CCPDv4*, is the 4^{th} revision of a series of prototypes using the AMS H18 process in $180nm$. The resistivity of the substrate is $10\,\Omega$cm with a total sensor size of 2.4×2.9 mm^2 and a thickness of $250\,\mu$m (Figure 4.7). Different pixel types are implemented in this sensor. The characterizations is focused on the *STime* Pixel on the HV-CMOS sensor with a pixel size of 33×125 μm^2. Each pixel contains an amplifier and a discriminator, together with a 4-bit in-pixel DAC that allows for the tuning of the individual pixel thresholds. All the electronics are implemented in the deep N-well (Figure 4.6).

The *CCPDv4* sensors are glued to the FE-I4B readout chip [178] using Araldite 2011 non-conductive epoxy glue as shown in Figure 4.7. Glue is used so that the sensor electrodes and the input pads of the readout channels form capacitors. This assembly is called Capacitively Coupled Pixel Detector (CCPD) Digital signal coming out from the *CCPDv4* is readout using the well known FE-I4B.

Since the pixel size of the *CCPDv4* and the FE-I4B are different in size (33×125 μm^2 and $250 \times 50\mu m^2$ respectively), a unit cell, made by six HV-CMOS pixels, corresponds to two FE-I4 pixels (see Figure 4.7) is considered. In this respect, a *macro-pixel* is defined as the set of three HV-CMOS single pixels (half the unit-cell) connected to a single FE-I4B readout pixel. For simplicity of operation in the testbeam, the signal amplitude of the discriminator output of each of these three sub-pixels were set to the same voltage level.

In order to test the radiation tolerance of this sensor, different samples have been irradiated with neutron and proton:

- One sample with 1 MeV neutron equivalent dose of $1 \cdot 10^{15}$ $n_{\text{eq}}/\text{cm}^2$ at the TRIGA reactor in Ljubljana [180]
- One sample with 1 MeV neutron equivalent dose of $5 \cdot 10^{15}$ $n_{\text{eq}}/\text{cm}^2$ at the TRIGA reactor in Ljubljana [180]
- One sample with a 18 MeV proton beam with an equivalent dose of $1.3 \cdot 10^{14}$ $n_{\text{eq}}/\text{cm}^2$ at the Bern Cyclotron Laboratory [181, 182]
- One sample with a 18 MeV proton beam with an equivalent dose of $5 \cdot 10^{14}$ $n_{\text{eq}}/\text{cm}^2$ at the Bern Cyclotron Laboratory [181, 182]

In Section 4.3, the Bern Cyclotron irradiation facility is presented. The measurement of the dose delivered to the samples is also described. In Section 4.4, the results obtained during a beam test on *CCPDv4* prototype are presented.

4.3 Irradiation campaign at the Bern Cyclotron

A medical cyclotron is in operation at the Bern University Hospital (Inselspital) [181]. It is a commercial IBA18/18 cyclotron, accelerating H^- to 18 MeV [183]. The facility (See Figure 4.8) can be operated for research activities during the day time while radio isotope production for medical purpose is running over-night.

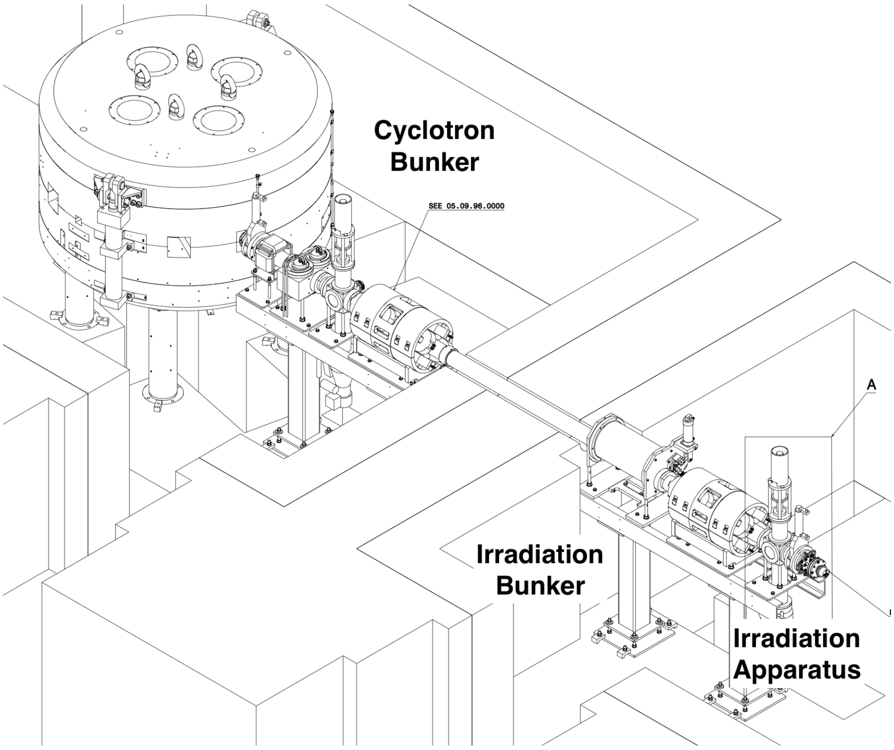

Figure 4.8: Diagram of the cyclotron facility, the cyclotron bunker is separated from the irradiation bunker where the irradiation apparatus is located. This facilitates the access to the device under irradiation due to the low level of activity in the irradiation bunker which is below 2 µSv per hour.

Proton extraction is achieved by stripping off the electrons from the negative H^- ions with 5 µm thick pyrolytic carbon foils. The accelerated protons are steered by an X-Y magnet system and are directed towards a collimator. The focusing of the beam is realised using two quadrupole doublets; the first is located in the cyclotron bunker and the second in the irradiation bunker (Figure 4.8). A 1.8 m thick wall divides the bunkers and is necessary to stop the fast neutron flux generated during isotope production. For the same reason, a movable cylindrical neutron shutter is located inside the beam pipe while the beam transfer line is not in use. Two beam viewers are present in the line allowing for beam current measurements. The facility is equipped with an external 6.5 m long Beam Transfer Line (BTL) which delivers the beam in a irradiation bunker. Despite the design of the cyclotron for high current operation (with maximum of 150 µA), operation with currents at the pA level is possible.

The dose delivered to the exposed sensors is essential to link the evolution of the device performance to the bulk and surface damages caused by the radiation. Protons interact with the the material by means of ionisation and nuclear processes. The dose due to ionisation ($\mathcal{D}_{ion}$) and nuclear ($\mathcal{D}_{nuc}$) processes can be calculated with Equation 4.1:

$$\mathcal{D} = \phi \cdot \frac{1}{\rho} \left(\frac{dE}{dx}_{ion} + \frac{dE}{dx}_{nucl} \right) = \mathcal{D}_{ion} + \mathcal{D}_{nucl}; \tag{4.1}$$

where ϕ is the fluence, defined as number of incident particles per unit area, ρ the density of the target and $\frac{dE}{dx}_{ion/nuc}$ is the average energy loss per unit of length in a given material for either ionisation or nuclear interactions. The effects of nuclear interaction are often compared to a reference 1 MeV neutron fluence as can be seen in Equation 4.2

$$\phi(1\,\mathrm{MeV} \quad n_{eq}) = \frac{\int_0^{+\infty} D(E)\phi(E)dE}{D(1\mathrm{MeV} \quad \mathrm{n_{eq}})}. \tag{4.2}$$

where $\phi(E)$ is the fluence of certain kind of particles at a given energy E and D is the damage function which depends upon the target material, the characteristics of the incident particle (energy, mass and electrical charge). The measurement of the fluence is used to assess the dose, for both nuclear and ionising phenomena, if the proton energy and the material properties are known. The fluence can be obtained by measuring the beam current:

$$\phi = \int_{t_0}^{t_1} \frac{j(t)}{Q_e} dt; \tag{4.3}$$

where $j(t)$ is the current per unit area, Q_e is the charge of the proton and $[t_0, t_1]$ is the time interval of the irradiation. A measurement of the current per unit area during the irradiation allows to measure the dose rate and at the same time to have a complete history of the irradiation. In particular, the dose rate measurement is relevant for identyfing non-linear phenomena which are typical in electronics, as presented in Ref. [184].

A dedicated irradiation setup was developed for the measurement of $j(t)$. The method relies on the extraction of the central part of the beam to irradiate the device, while dumping the outermost part of the beam for measuring the current density. It is important to operate the cyclotron so that the delivered beam has a constant intensity per unit surface in the transverse plane. The transverse uniformity guarantees a uniform irradiation of the device and as well as a constant beam density over the dump area. The beam profile is flat within 20% up to 40 mm in both the vertical and the horizontal directions. The irradiation setup is shown in Figure 4.9. It is composed of two detectors: a two-dimensional beam profile detector and a collimator to measure the density current and to extract the beam with a custom profile. The extraction window consists in a 300 µm thick aluminum layer. A 2D movable stage completes the system, allowing for the irradiation of large surface devices, up to $30 \times 30\,\mathrm{cm}^2$, or the irradiation of several devices without accessing the irradiation bunker. The 2D-stage has a 10 µm precision.

The current density is measured with a dedicated collimator, developed at the University of Bern. The cross-section of such colimator is shown in Figure 4.10. It consists of three aluminum rings: the shaping ring, the high-voltage ring, and the beam dump. Each of the rings is 5 mm thick, this thickness was optimised considering that 18 MeV protons have a range of 1.6 mm in aluminum.

The proton beam coming from the BTL enters the system of collimators through a 40 mm diameter opening and is further shaped through the shaping ring of 35 mm inner diameter. After the shaping ring, the proton beam hits a dump ring, which also acts as collimator, allowing the

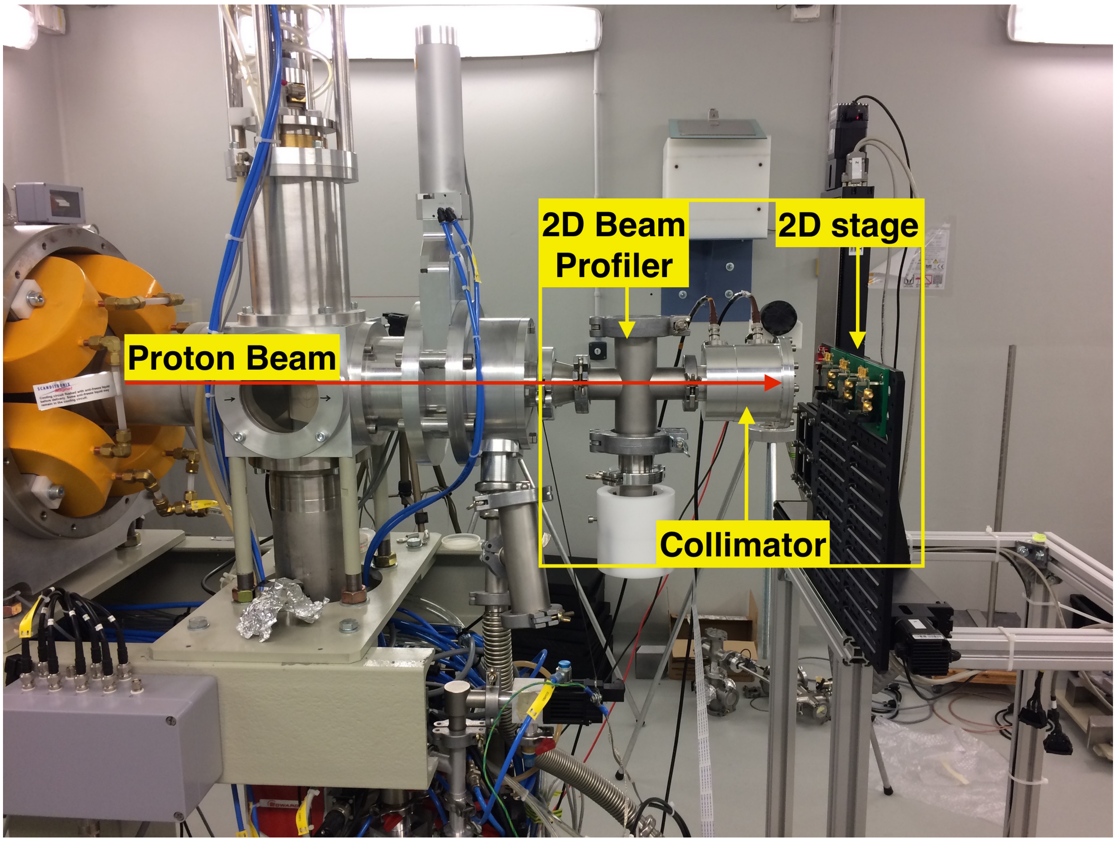

FIGURE 4.9: Irradiation setup at the Bern Cyclotron. It consists of the two-dimensional beam profiler, for measuring the beam transverse profile, and the the collimator system for the current measurement and the beam shaping. The 2D stage, for alignment of the devices under irradiation, is visible on the right.

beam to be extracted via a dedicated opening. Finally the beam is extracted into air through a 300 µm aluminum window. The part of the beam absorbed by the beam dump is used for the current density measurement. The dump ring is electrically connected to a high precision ammeter, which has a precision of 0.01 fA in the current measurement.

When the protons hit the aluminum surface of the beam dump, they extract secondary electrons. This phenomenon can lead to an overestimation of the current up to $\sim 20\,\%$ and it has been documented in Ref. [185]. In order to prevent this to happen, the system is biased with high-voltage. In particular an intermediate high voltage ring is then placed between the shaping ring and the dump ring. The high-voltage ring has an inner diameter of 37.5 mm and is biased at -100 V, preventing the extraction of secondary electrons in the dump ring. The bias voltage is provided by an ammeter.

The entire system is operated in vacuum in order to prevent air ionisation. This is necessary to avoid the beam to produce electrons which would be collected at the dump affecting the current measurement. For this reason the system is kept at $\sim 10^{-8}$ bar, the vacuum system is the one provided by the BTL.

The current per unit area $j(t)$ is calculated according to Equation 4.4:

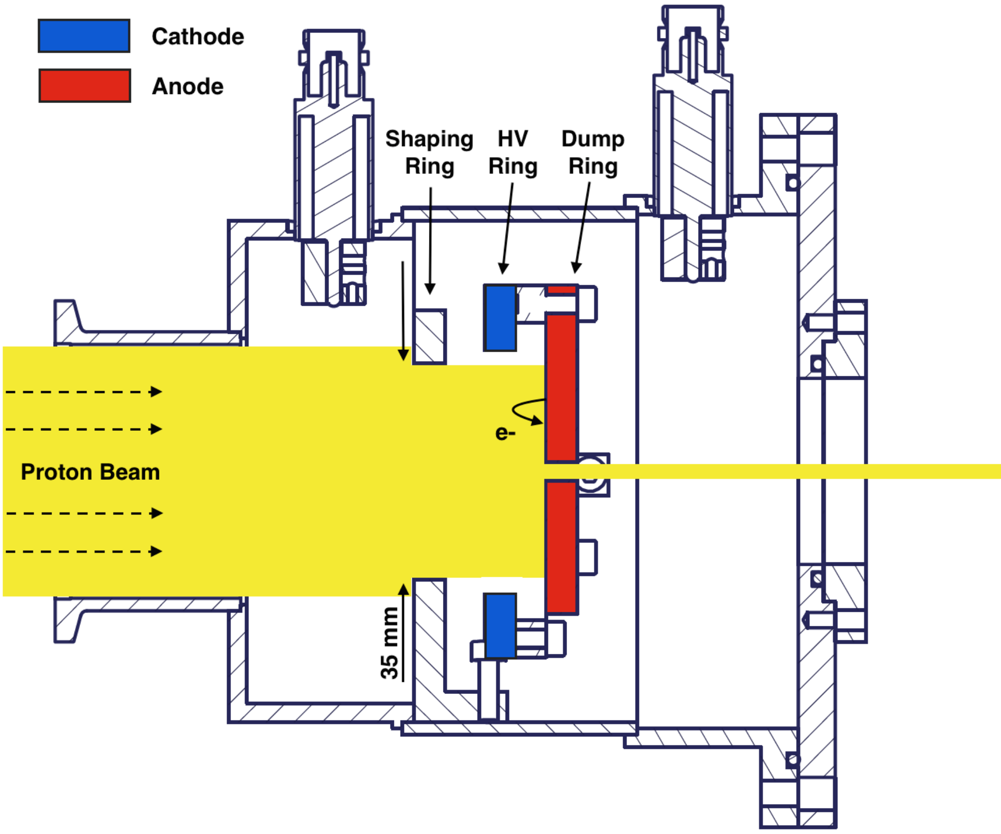

FIGURE 4.10: Cross section of the collimator system. The proton beam coming from the cyclotron enters the collimators system through an opening circular window of 40 mm. The beam is reduced to 35 mm diameter by means of a shaping ring. At this stage a flat beam of 35 mm diameter approaches the dump ring. This acts as a collimator, so that part of the beam is extracted and delivered to the device under test through an aluminum extraction window, 300 µm thick. The rest of the beam is absorbed on the dump ring so that the current density is measured. When hitting the dump rings, the protons produce secondary electrons at the aluminum surface. For this reason a high voltage ring is in between the shaping ring and the dump ring. A bias voltage of −100 V is applied, so that the electrons are pushed back to the dump ring.

$$j(t) = \frac{i(t)}{A_{BD}} \cdot \Lambda \,; \tag{4.4}$$

$$A_{BD} = \pi \cdot r^2 - A_{open} = 9.62\,\text{cm}^2 - A_{open} \,; \tag{4.5}$$

$$\Lambda = \frac{\rho_{extraction}}{\rho_{dump}} \,. \tag{4.6}$$

The current measured at the dump ring $i(t)$ is divided by the enlightened surface area A_{BD} and corrected for beam inhomogeneities. The area A_{BD} is calculated in Equation 4.5 and it depends on A_{open}, which is the extraction area. A correction factor Λ takes in account the measurement of the two-dimensional beam profile. It is calculated as in Equation 4.6, where $\rho_{extraction}$ is the beam density at the extraction area and ρ_{dump} the one at the dump ring surface.

The other important factor to take into account for the dose measurement is the stopping power. The stopping power depends on the beam energy and the material of the device under irradiation. The beam energy of the Bern Cyclotron was measured to be 18.3±0.4 MeV [186]. The additional

Material	$\frac{1}{\rho}\frac{dE}{dx}_{ion}$ [MeV $\frac{cm^2}{g}$]	$\frac{1}{\rho}\frac{dE}{dx}_{nuc}$ [MeV $\frac{cm^2}{g}$]
Silicon	23.25	0.011
Silicon dioxide	24.31	0.012
Aluminum	22.67	0.011
Plastic scintillator (Vyniltoluene)	30.12	0.015
Mylar	28.06	0.013
Photographic emulsion	18.30	0.009

TABLE 4.2: Stopping power for different material in case of proton beam of 16.7 MeV. The values are obtained from the NIST database.

aluminium thickness of 300µm of the extraction window needs to be taken in account. The mean energy was estimated to be 16.7 ± 0.5MeV after the extraction window.

Table 4.2 shows the stopping power and the hardness factor for several materials considering a 16.7 MeV proton beam. The dose profile needs to be calculated depending on the material on the device under irradiation and its thickness. For example the protons will lose ~ 0.55MeV in the first 100 µm in silicon.

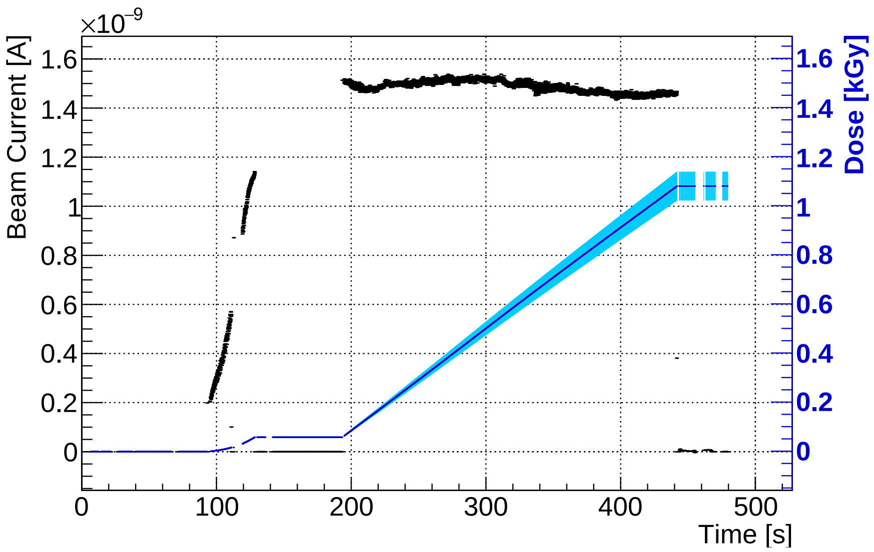

FIGURE 4.11: Observed beam current during an irradiation with the estimated delivered dose given a silicon device

Figure 4.11 shows the beam current intercepted by the dump ring and the dose measured during an irradiation. The blue curve represents the dose, where the light blue error bar takes in consideration a 5% uncertainty on the stopping power value and 500 µm uncertainty on the acceptance radius of the dump ring. The experimental uncertainty on the current was measured to be negligible. The final uncertainty on the dose determination was estimated to be 6 % of the dose value. A stability of approximatively 20% of the beam current can be achieved with a manual adjustment of the beam. A software for online beam monitoring has been developed to provide the current and the dose measurement in real time. Data are updated every 250 ms. Figure 4.11 shows data-taking example from irradiation that took place to evaluate the performance of the cyclotron. In the first 140 s the beam current is increasing. After 200 s the current is constant within 5% and the beam parameters were kept constant until the end of the irradiation. The beam was shut down temporarily in 2 occasions because of user request.

4.4 Beam test results for HV-CMOS pixel sensor prototype

The *CCPDv4* samples have been tested in Autumn 2015 and Spring 2016 at the H8 beamline of the CERN SPS (Super Proton Synchrotron), that provides a 180 GeV π^+ beam. In order to test this samples the FE-I4 Telescope [187] based on RCE readout system was used. This telescope consists of 6 planes of ATLAS Insertable B-Layer (IBL) double-chip (DC) pixel modules [85] arranged in two arms of three module each.

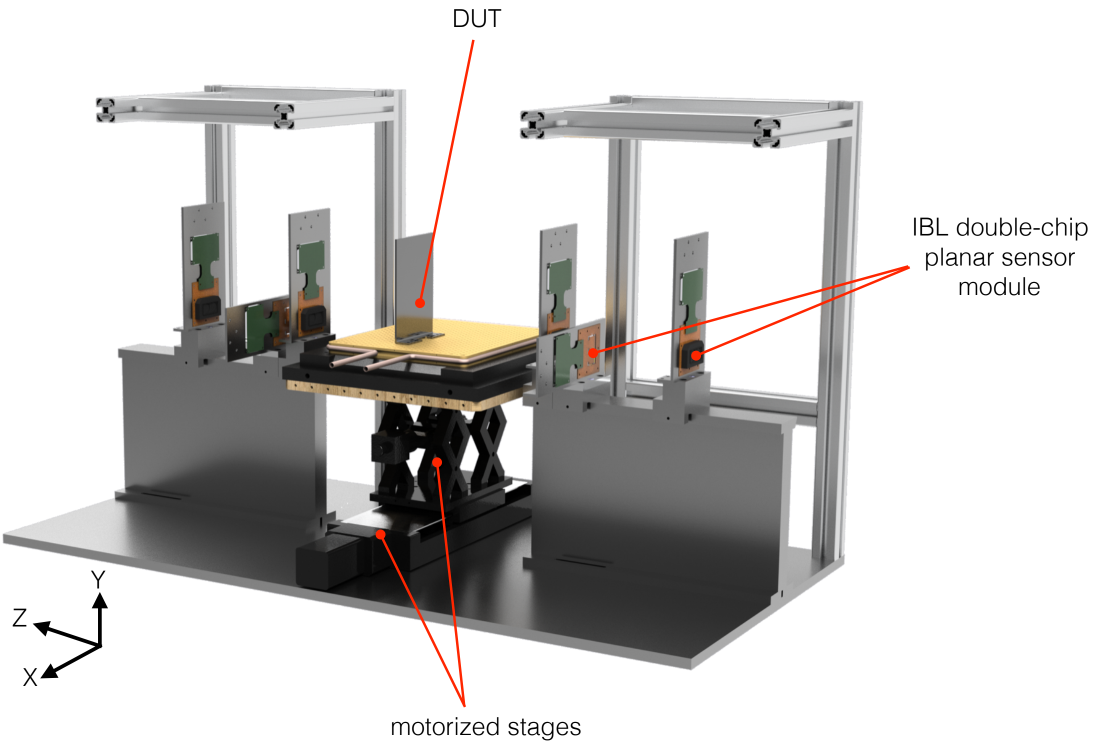

FIGURE 4.12: A rendered view of the FE-I4 beam telescope. The coordinate system is defined with the Z-axis along the beam-axis, the Y-axis pointing vertically upwards and the X-axis pointing horizontally.

The raw data coming from the six planes of the telescope were analysed using a software based on Judith [188]. This program was written in C++ package and originally was developed for the Kartel telescope (composed of six MIMOSA-26 pixel sensors [189]). The Judith package has been adapted for the FE-I4 telescope configuration and its module geometries.

The reconstructed charged particle trajectories called *tracks* are compared to the hit response of the *CCPDv4*. The internal alignment of the six telescope planes is performed using a iterative algorithm that minimises the difference between the hit position measured in the plane being aligned and the predicted hit position from the track extrapolation into the plane. Pixels that show a much greater occupancy (*noisy pixels*) with respect to its contiguous, has been masked. The first telescope plane is kept fixed at its nominal position to create the reference position for the other telescope planes. The alignment algorithm allow to correct for the translations in the transverse plane (XY) and the rotation along the Z axis. Upper limits on the spatial resolution of the telescope were found to be 11.7 μm and 8.3 μm in the XY plane at the Device Under Test (DUT) position.

After the internal alignment of the telescope planes, the reconstructed tracks are used to align the DUT. The small size of the DUT didn't allow to correct for rotation along the Z axis but only X-Y translation. Single track events were selected. Tracks are required to have a good χ^2

from the track fit and small gradient with respect to the beam axis. The goodness of the fit was estimated looking at the un-bias residual distributions at the DUT after alignment along X and Y (Figure 4.13).

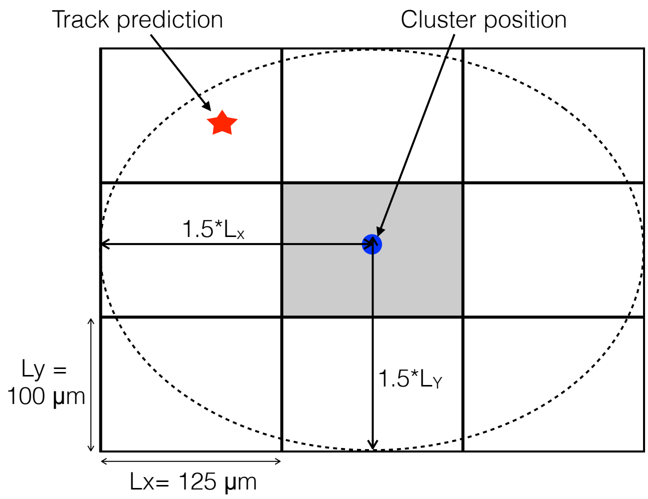

(A)

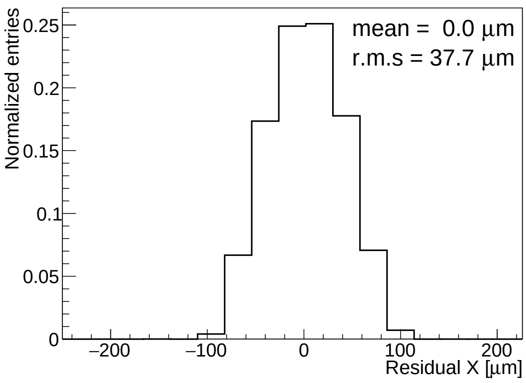

(B)

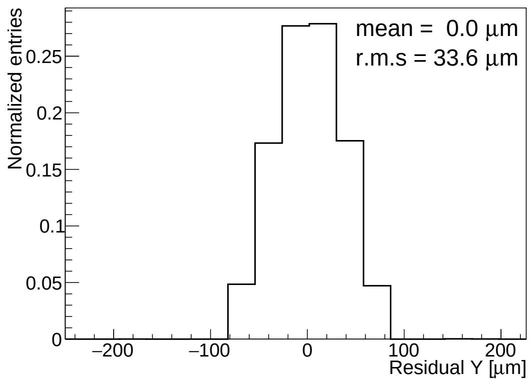

(C)

FIGURE 4.13: (a) Graphical depiction of the search area used to compute the hit efficiency. Normalised residual distributions of the 1×10^{15} $n_{\text{eq}}/\text{cm}^2$ DUT along the x (b) and y (c) directions.

The r.m.s. of the residual distributions (Figure 4.13(b), 4.13(c)) are in good agreement with the expected intrinsic resolutions of the *macro-pixel* along the X ($\sigma_{x,\text{exp}}$) and Y-directions ($\sigma_{y,\text{exp}}$)[1].

The hit efficiency ϵ has been calculated using Equation 4.7 as the ratio between the number of clusters in the DUT that match the reconstructed tracks from the beam telescope and the number of good reconstructed tracks that are predicted to penetrate the DUT within its active area.

$$\epsilon = \frac{N_{tracks}^{matched}}{N_{tracks}^{total}} \tag{4.7}$$

The search area for tracks is an ellipse with the major and minor radii being 1.5 macro-pixel pitches in x and y coordinates around the centre of the cluster, i.e. 150 μm and 187.5μm respectively (see also Figure 4.13(a)).

[1] $\sigma_{x,\text{exp}} = \frac{125\ \mu\text{m}}{\sqrt{12}} = 36.1\ \mu\text{m}$; $\sigma_{y,\text{exp}} = \frac{100\ \mu\text{m}}{\sqrt{12}} = 28.9\ \mu\text{m}$, respectively

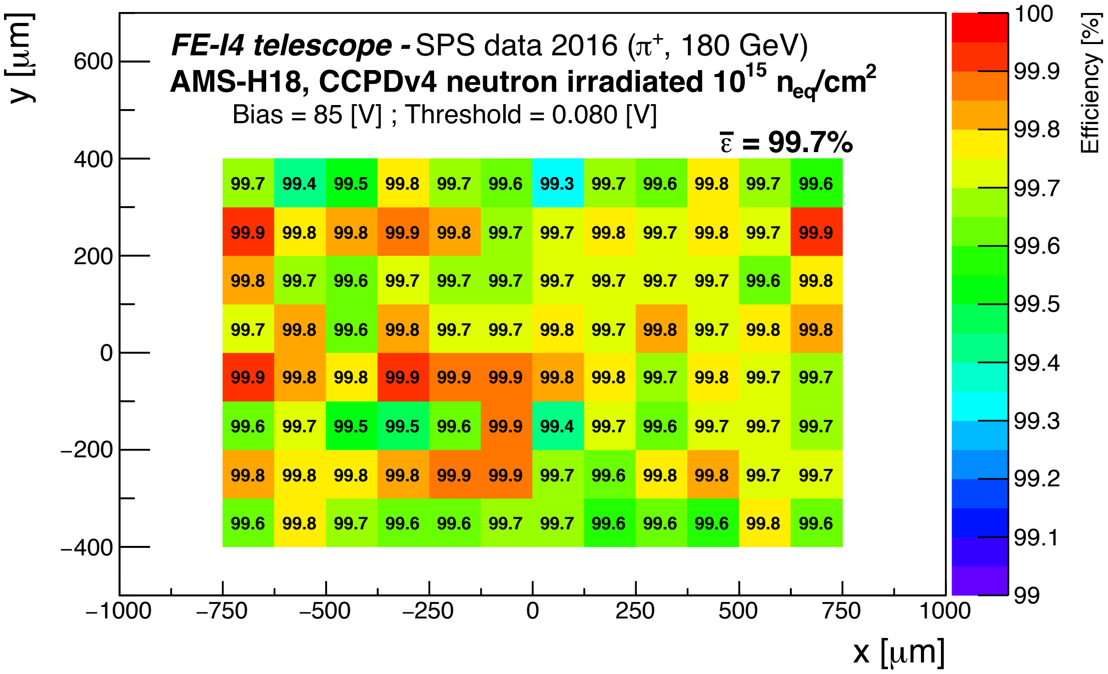

FIGURE 4.14: Hit efficiency map for *CCPDv4* neutron-irradiated with 1×10^{15} $n_{\mathrm{eq}}/\mathrm{cm}^2$; the colour scale is only ranging from 99% to 100% [179].

In Figure 4.14a, the hit efficiency for the STime pixels in this sample at a bias voltage of 85 V and using a threshold of 80 mV is shown.

The hit efficiency was also studied as a function of the bias voltage for different samples irradiated with neutrons or protons. These results are reported in Figure 4.15. A plateau is reached after about 40 V. Increasing the bias voltage results in a higher efficiency in particular for the lowest and highest fluence.

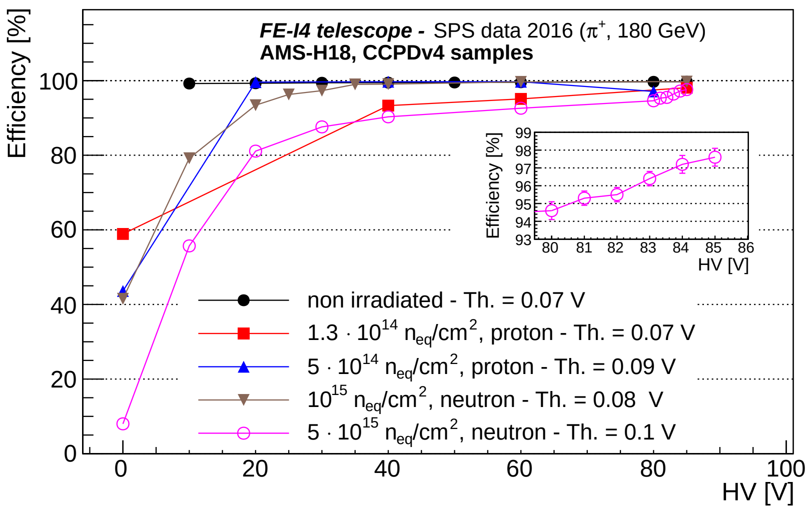

FIGURE 4.15: Average hit efficiency as a function of applied bias voltage obtain using the FE-I4 Telescope at the SPS H8 beamline with 180 MeV pion beam. The inset shows the sudden increase in efficiency between 80 and 85 V, which can be attributed to charge multiplication. The thresholds of 70, 80, 90 and 100 mV are assumed to be equivalent to 600, 690, 770 and 860 e^-.

In highly irradiated (above 10^{15} $n_{\mathrm{eq}}/\mathrm{cm}^2$) planar and 3D pixel sensors, it has been demonstrated that the high electric field combined with trapping due to radiation damage can lead to charge multiplication due to impact ionisation when sufficient high voltage is applied to the sensors [190]. This fact generates an increase of the signal associated to the passage of a particle, which is correlated to the increase in noise and leakage current in the device. For the 5×10^{15} $n_{\mathrm{eq}}/\mathrm{cm}^2$ sample, a sudden increase in detection efficiency is observed between 80 and 85V, as shown in the insert of Figure 4.15. This measurement is correlated with a similar increase in leakage current of the device. Such a behaviour was not expected and was not observed for the other devices irradiated with lower fluences and can be interpreted as evidence for the existence of the charge multiplication process in HV-CMOS devices, as previously observed in planar and 3D pixel sensors.
Threshold scans were conducted to study their dependencies on the hit efficiency and they are shown in Figure 4.16. The results show an increase of efficiency between 1.3×10^{14} $n_{\mathrm{eq}}/\mathrm{cm}^2$ and 5×10^{14} $n_{\mathrm{eq}}/\mathrm{cm}^2$ and then a loss of efficiency with increasing dose. This behaviour is due to acceptor removal phenomena and is supported also by edge-TCT results [191]. For each sample the threshold has been optimised in order to equalise the response of the individual pixel sensors.

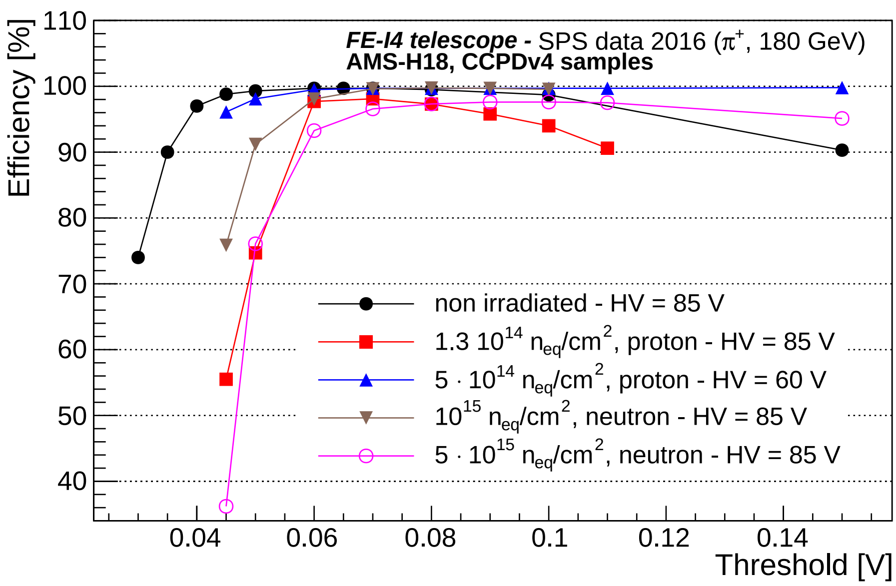

FIGURE 4.16: Efficiency as a function of threshold. The two vertical dashed-lines indicate the operating region for which the DUT efficiency is larger than 99.5%.

From Figure 4.16, three regions can be identified

- for very high thresholds there is a loss of events, and thus hit efficiency, due to low charge signals not being detected
- for low threshold settings, the discriminators trigger on noise events and the dead time associated induces the measured inefficiency
- in between there is a stable plateau, which is widest for the intermediate fluences, while for 1.3×10^{14} and 5×10^{15} $n_{\mathrm{eq}}/\mathrm{cm}^2$ the lack of signal due to small depletion depth or increased trapping, respectively, reduces the span of the plateau region, i.e. of the operation point

Some more insight can be gained when looking at the timing distribution for different applied bias voltages in Figure 4.17(a). As expected, the events still registered without any applied bias voltage are slow and very broad in their timing. The time resolution gradually increases with the increasing electric field causing faster collection.

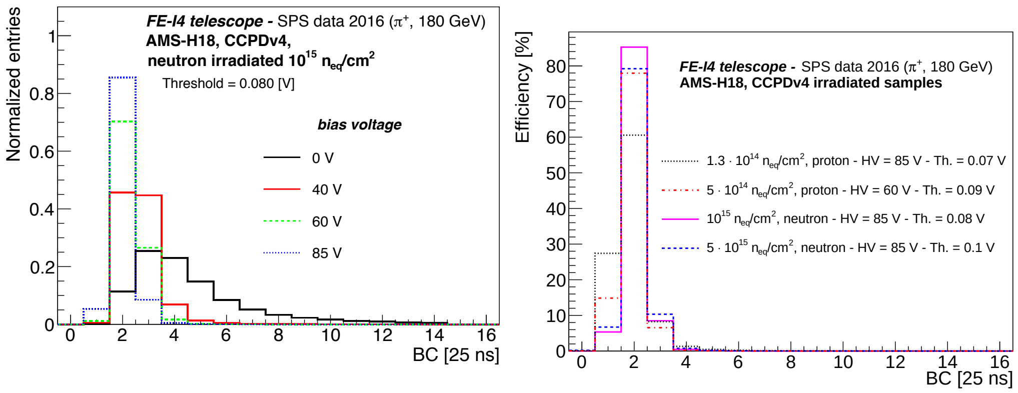

(A) (B)

FIGURE 4.17: (A) Timing for a CCPDv4 sensor for four values of the bias voltage. (B) Timing distributions for the four irradiated CCPDv4 samples at the operational bias voltages

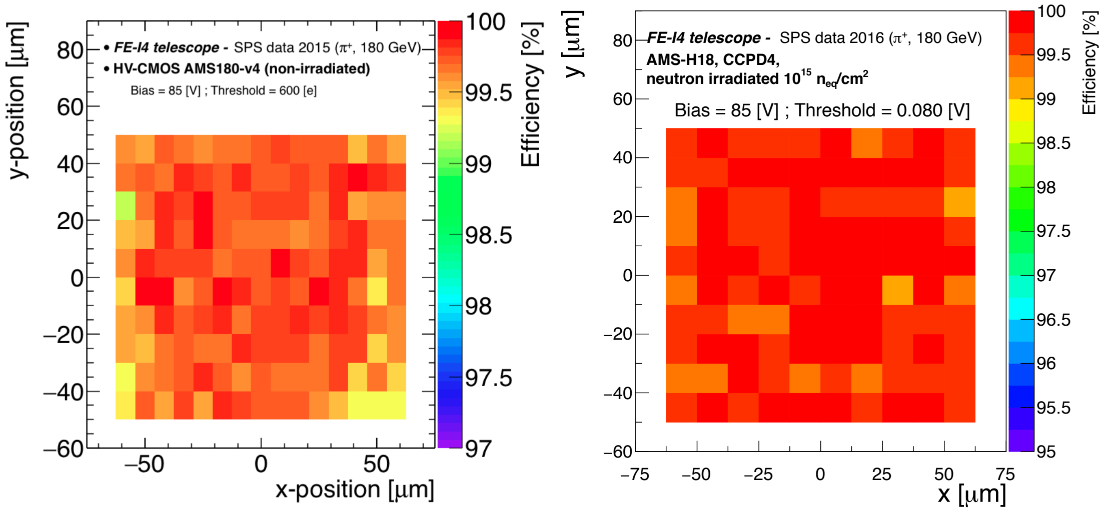

(A) (B)

FIGURE 4.18: The efficiency inside a *macro-pixel* of 125 μm $\times$ 100 μm. [179, 192]

Figure 4.17(b) shows the timing distributions of the four irradiated samples. Clearly, most events are collected within one timing bin. It appears that a cumulative in-time efficiency of better than 95% is achievable in 3 BCs for all fluences that have been investigated.

The resolution of the telescope allowed to study the hit efficiency with sub-pixel resolution. It was found that there is no significant loss of hit efficiency in any region of the *macro-pixel* 125×100 μm^2 for the optimal value of the threshold and the bias voltage. Figures 4.18 show the results for both unirradiated sample (left) and for a neutron irradiated sample (right).

Chapter 5

Sensitivity prospect at the High Luminosity LHC

In this chapter, the expected discovery and exclusion reach for a search for top squark pair production in simplified SUSY models analysing up to 3 ab^{-1} of pp collision data at the High Luminosity LHC (HL–LHC) with $\sqrt{s}$=14 TeV is presented. This search explore what is the possible gain of the new Inner Tracker (ITk) described in Chapter 4.

This search is also motivated by the limited sensitivity to top squark pair production in scenarios with compressed mass spectra. The considered model is top squark pair production decaying via $\tilde{t}_1 \rightarrow t\tilde{\chi}_1^0$, as shown in Figure 5.1, with both top quarks decaying leptonically. This model is targeted in a compressed mass spectra with the mass difference between the $\tilde{t}_1$ and the $\tilde{\chi}_1^0$ close to the top mass.

$$m(\tilde{t}_1) - m(\tilde{\chi}_1^0) = 173 \text{ GeV} \tag{5.1}$$

This phase space region is particularly challenging since the expected signal resembles the SM $t\bar{t}$ background.

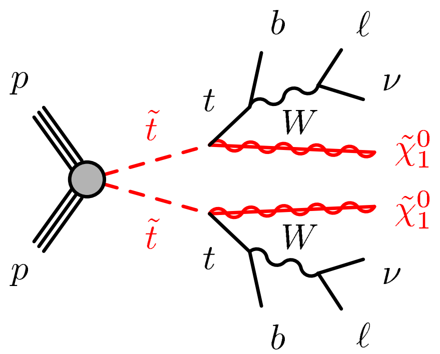

FIGURE 5.1: Diagram representing the two-body decay into an on-shell top quark and the lightest neutralino ($\tilde{t}_1 \rightarrow t\tilde{\chi}_1^0$).

The choice of this model is motivated by the interest in performing measurements of possible new phenomena exploiting this final state and, in particular, and by the understanding of the capability of the new Inner Tracker described in the previous chapter. The analysis presented below has been released in a public note [193].

5.1 Performance of the ATLAS Detector at the HL-LHC

The effects of the upgraded ATLAS Detector and in particular of the new Inner Tracker (ITk) are taken into account using parametrised detector response functions, efficiencies and fake rates that are applied to truth level quantities. These parametrisations are derived from detector performance studies based on GEANT 4 simulation of the ATLAS Detector in the condition expected during HL-LHC. The latest understanding of the detector geometry and the performance of the electron identification and isolation, b-tagging, muon reconstruction and trigger are taken into account following the one described in Ref [194]. The latest expected tracking, jet and missing transverse energy performance are considered following Ref [195]. In order to emulate the pile-up condition during HL-LHC, pile-up jets are overlaid on the hard-scatter events accordingly to the expected pileup conditions.

Such an approach allows the flexibility of fully exploring optimal selections that apply for the much larger integrated luminosity expected to be delivered during HL-LHC. Extrapolations from present analyses are also used when appropriate, for instance when data-driven background estimates play a vital role in the physics analysis.

5.2 Simulated samples

The Monte Carlo (MC) simulated event samples took into account the 14 TeVcentre-of-mass-energy and these samples are used to predict the background from SM processes and to model the SUSY signal. The most relevant MC samples have equivalent luminosities of at least 3 ab^{-1}.

The production of $t\bar{t}$ and single top-quarks in the Wt channel [117] are generated using the POWHEG-Box v2 [196–198] interfaced to the PYTHIA 8.186 [126] parton shower model. The A14 set of tuned parameters [128] is used together with the CT10 PDF set [127]. The top quark mass is assumed to be 172.5 GeV. The $t\bar{t}$ and Wt events are normalised to the NNLO + NNLL [137] (NLO) QCD cross-sections.

Events containing W and Z bosons with associated jets (W+jets and Z/γ^*+jets) are produced using the SHERPA v1.4.1 [123] generator with massive b/c-quarks to improve the treatment of the associated production of W and Z bosons with heavy flavour jets. The expected W+jets, Z+jets and diboson yields are normalised to the SHERPA predictions.

Diboson processes with four charged leptons (ℓ), three charged leptons and one neutrino, or two charged leptons and two neutrinos are simulated using the SHERPA v2.1.1 generator [162]. The matrix elements contain the WW, WZ and ZZ processes and all other diagrams with four or six electroweak vertices (such as same-electric-charge W boson production in association with two jets, $W^{\pm}W^{\pm}jj$). The CT10 parton distribution function (PDF) set is used for all SHERPA samples in conjunction with a dedicated tuning of the parton shower parameters developed by the SHERPA authors. The generator cross-sections (at NLO for most of the processes) are used when normalising these backgrounds.

Samples of $t\bar{t}W$,$t\bar{t}Z$, including non-resonant Z/γ^* contributions and $t\bar{t}WW$ production are generated at LO with MADGRAPH5 aMC@NLO [125] v2.2.2 interfaced to the PYTHIA 8.186 parton shower model, with up to two ($t\bar{t}$ W), one ($t\bar{t}$ Z) or no ($t\bar{t}$ WW) extra partons included in the matrix element [163]. MADGRAPH5 aMC@NLO is also used to simulate the tZ, tWZ, $t\bar{t}t\bar{t}$ and $t\bar{t}$ t processes. The A14 tune is used together with the NNPDF23LO PDF set [199]. The $t\bar{t}$ W, $t\bar{t}$ Z, $t\bar{t}$ WW and $t\bar{t}t\bar{t}$ events are normalised to their NLO cross-sections [125] while the generator cross-section is used for tZ, tWZ and $t\bar{t}$ t.

Production of a Higgs boson in association with a $t\bar{t}$ pair is simulated using MadGraph5 aMC@NLO v2.2.2 interfaced to Herwig 2.7.1 [140]. The UEEE5 underlying-event tune is used together with the CTEQ6L1 [142] (matrix element) and CT10 (parton shower) PDF sets. Simulated samples of SM Higgs boson production in association with a W or Z boson are produced with Pythia 8.186, using the A14 tune and the NNPDF23LO PDF set. For normalisation purposes, cross-sections calculated at NLO [141] are used.

The SUSY signal samples are generated using LO matrix elements with up to two extra partons, with the MadGraph5 aMC@NLO v2.2.3 generator. The modelling of the SUSY decay chain, parton showering, hadronisation and the description of the underlying event are simulated with Pythia 8.186, using the A14 tune. Parton luminosities are provided by the NNPDF23LO PDF set. The jet-parton matching is realised following the CKKW-L prescription [143], with a matching scale set to one quarter of the pair-produced superpartner mass. Signal cross-sections are calculated to next-to-leading order in the strong coupling constant, adding the resummation of soft gluon emission at next-to-leading-logarithmic accuracy (NLO+NLL) [44, 144, 145]. The nominal cross-section and the uncertainty are taken from an envelope of cross-section predictions using different PDF sets and factorisation and renormalisation scales [200].

In all MC samples, except those produced by Sherpa, the EvtGen v1.2.0 program [124] is used to model the properties of the bottom and charm hadron decays.

5.3 Event selection

Electrons, muons and jets are selected following the same requests presented in Section 3.1. The missing transverse energy ($E_{\mathrm{T}}^{\mathrm{miss}}$) at generator level is instead computed as the vectorial sum of the momenta of neutral weakly-interacting particles (neutrinos and neutralinos). It is then smeared to simulate the detector response, with a function parametrised in the average number of interactions per bunch crossing μ and the scalar sum of energy in the calorimeter $\sum E_T$. Many simulated samples have been generated with an $E_{\mathrm{T}}^{\mathrm{miss}}$ filter of 100 GeV at generator level in order to reduce the needed MC statistics. It is necessary to determine which selection on the smeared $E_{\mathrm{T}}^{\mathrm{miss}}$ becomes fully efficient with respect to the generator-level filter. The optimal value has been found to be 300 GeV, as shown in Figure 5.2.

Events are accepted if they contain either exactly two electrons, two muons or one electron and one muon. Furthermore, events are also required to contain at least two b-jets from the $t\bar{t}$ decay. The selected simulated events are than reweighted by the expected efficiencies of the lepton trigger, reconstruction and identification in the HL-LHC conditions.

The considered SUSY models are characterised by a small mass splitting between the $\tilde{t}_1$ and $\tilde{\chi}_1^0$. This implies that the top quark and the $\tilde{\chi}_1^0$ are generally produced with very small momentum, hence it is necessary to select events where the $\tilde{t}_1$ $\tilde{t}_1$ system is boosted by the recoil of at least one energetic ISR jet. Since di-leptonic final states are selected, the $\tilde{t}_1$ pair is identified by the two leptons and the two leading b-jets in the event ($\tilde{t}_1$ **system**). The additional jets are grouped together and they are assigned to the ISR system.

Different discriminators and kinematic variables are used in the analysis to separate the signal from the SM background.

- $min\{\Delta\phi(jet_{ISR}, E_{\mathrm{T}}^{\mathrm{miss}})\}$ is the minimum azimuthal angular distance between each jet assigned to the ISR system and the $E_{\mathrm{T}}^{\mathrm{miss}}$.
- $\Delta\phi(jet_{ISR1}, E_{\mathrm{T}}^{\mathrm{miss}})$ is the azimuthal angular distance between the leading jet assigned to the ISR system and the $E_{\mathrm{T}}^{\mathrm{miss}}$.

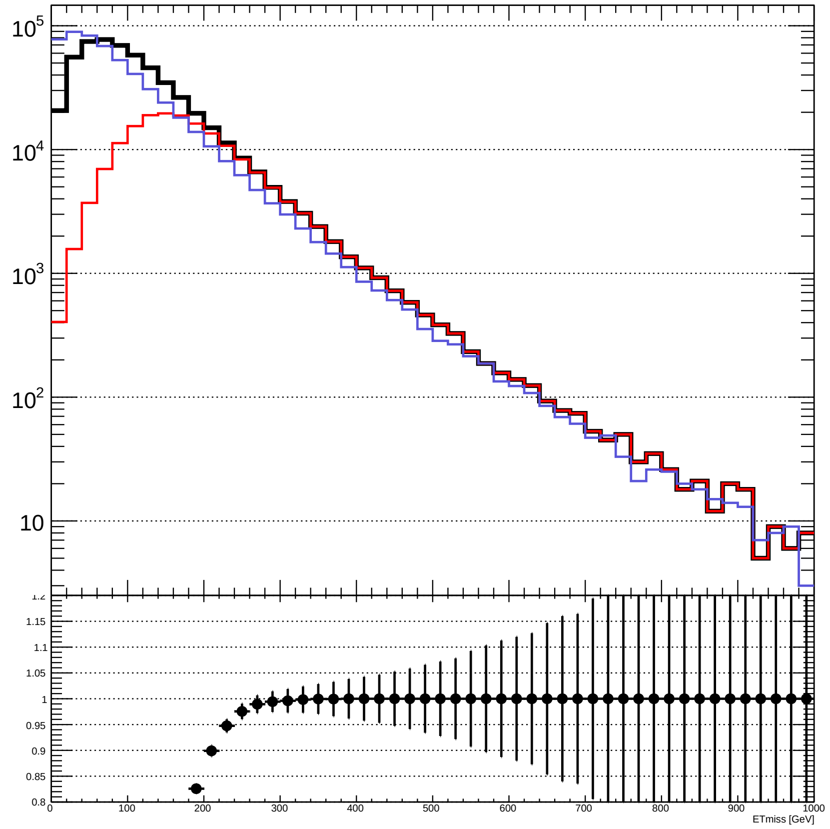

FIGURE 5.2: The top shows the $E_{\mathrm{T}}^{\mathrm{miss}}$ distribution for a $t\bar{t}+Z$ MC sample. The blue line shows the generator-level $E_{\mathrm{T}}^{\mathrm{miss}}$ distribution. The black line shows the smeared $E_{\mathrm{T}}^{\mathrm{miss}}$ distribution for an inclusive sample, while the red line shows the smeared $E_{\mathrm{T}}^{\mathrm{miss}}$ distribution for the same sample when a generator-level cut of 100 GeV is applied. The bottom shows the turn on curve, with full efficiency reached at $E_{\mathrm{T}}^{\mathrm{miss}} = 300$ GeV.

- $R_{\ell\ell}$: the ratio of $E_{\mathrm{T}}^{\mathrm{miss}}$ and the scalar sum of the lepton transverse momenta;

$$R_{\ell\ell} = \frac{E_{\mathrm{T}}^{\mathrm{miss}}}{p_{\mathrm{T}}(\ell_1) + p_{\mathrm{T}}(\ell_2)} \tag{5.2}$$

- m_{T2} as described in Section 3.2.

5.4 Selection optimisation

The SR optimisation has been done scanning a set of discriminating variables, assuming a flat 30% systematic uncertainty on the expected SM backgrounds and aiming at maximising the discovery sensitivity (z_N). A minimum of 2 signal events and a total SM background yield larger than 0.8 with a statistical uncertainty smaller than 50% have been required during the optimisation scan.

Only the most discriminating variables have been retained in the final selection. These are shown in Figure 5.3–5.5 after applying all selection criteria except for m_{T2} and the variable being plotted ($R_{2\ell}$, the leading ISR jet p_{T} or $E_{\mathrm{T}}^{\mathrm{miss}}$). Figure 5.6 shows the m_{T2} distribution after the application of all other selection criteria.

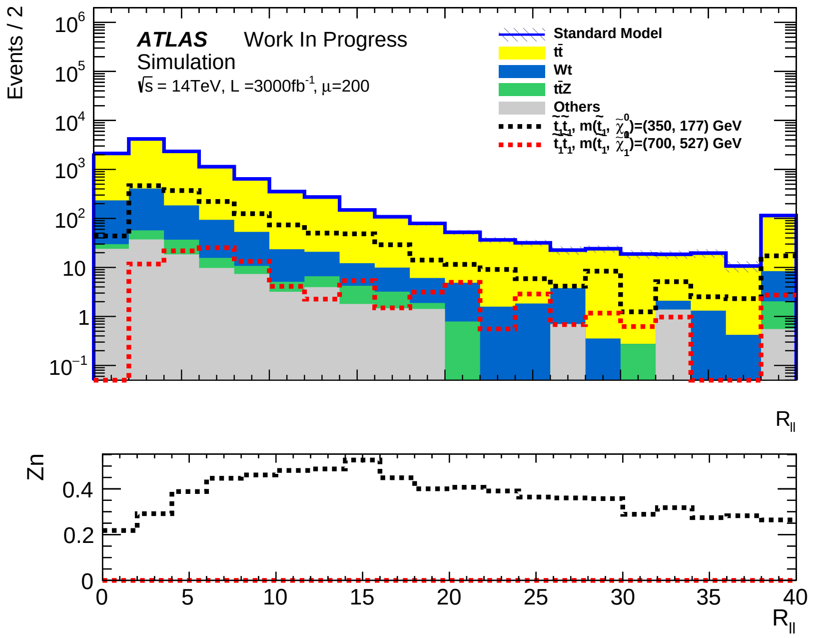

FIGURE 5.3: $R_{2\ell}$ distribution for events passing all SR selection criteria except for the ones on m_{T2} and $R_{2\ell}$ itself for an integrated luminosity of 3000 fb^{-1}. The contributions from all SM backgrounds are shown, and the hashed band represents the statistical uncertainty on the total SM background prediction. The expected distributions for two signal models are also shown as dashed lines for comparison. The bottom shows the expected z_N as a function of the cut (integrating to the right).

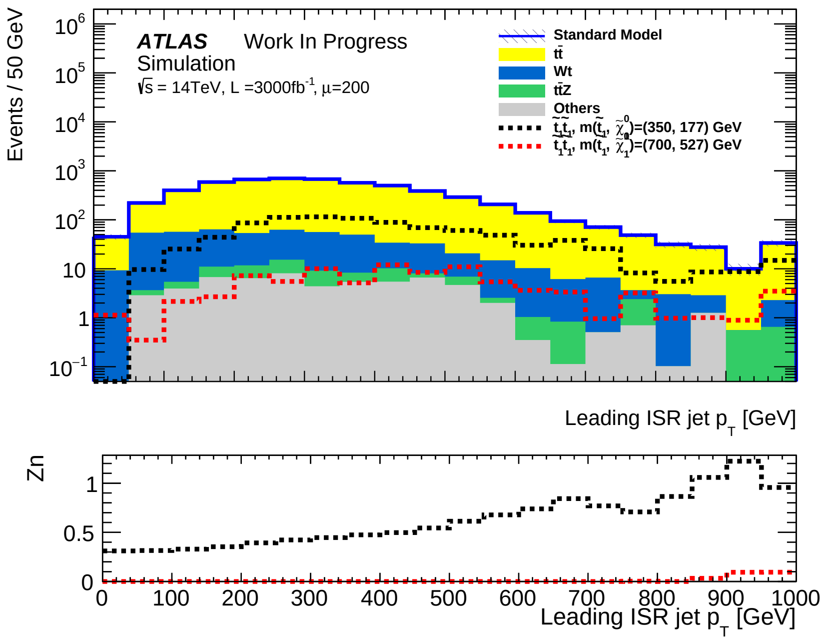

FIGURE 5.4: Leading ISR jet p_{T} distribution for events passing all SR selection criteria except for the ones on m_{T2} and the leading ISR jet p_{T} itself for an integrated luminosity of 3000 fb^{-1}. The contributions from all SM backgrounds are shown, and the hashed band represents the statistical uncertainty on the total SM backgroun prediction. The expected distributions for two signal models are also shown as dashed lines for comparison. The bottom shows the expected z_N as a function of the cut (integrating to the right).

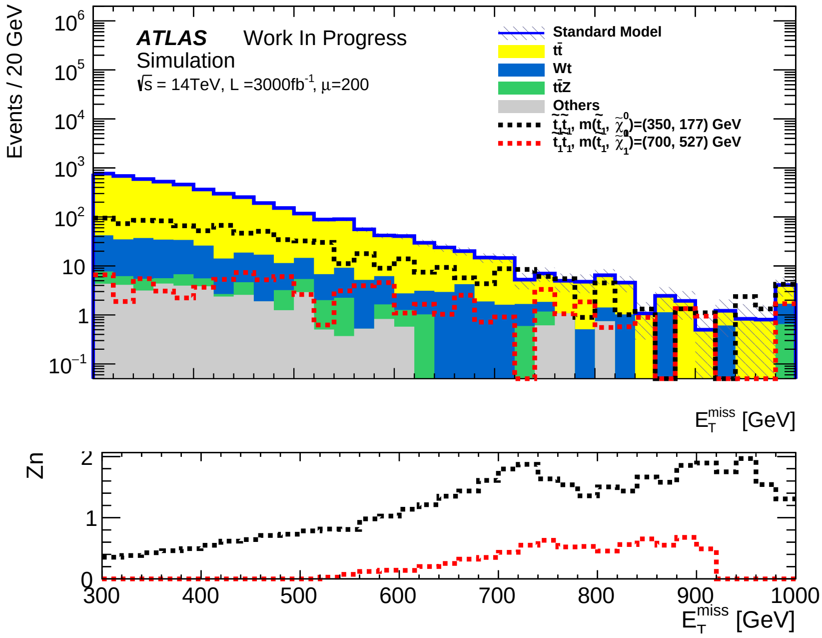

FIGURE 5.5: $E_{\rm T}^{\rm miss}$ distribution for events passing all SR selection criteria except for the ones on $m_{\rm T2}$ and $E_{\rm T}^{\rm miss}$ itself for an integrated luminosity of 3000 fb^{-1}. The contributions from all SM backgrounds are shown, and the hashed band represents the statistical uncertainty on the total SM backgroun prediction. The expected distributions for two signal models are also shown as dashed lines for comparison. The bottom shows the expected z_N as a function of the cut (integrating to the right).

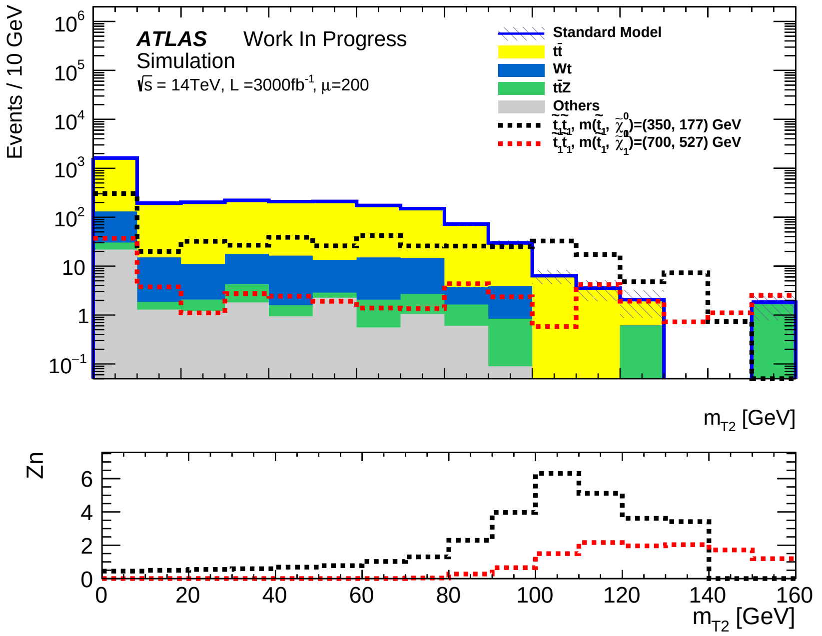

FIGURE 5.6: $m_{\rm T2}$ distribution after applying all SR selection criteria except for that on $m_{\rm T2}$ itself for an integrated luminosity of 3000 fb^{-1}. The contributions from all SM backgrounds are shown, and the hashed band represents the statistical uncertainty on the total SM backgroun prediction. The expected distributions for two signal models are also shown as dashed lines for comparison. The bottom shows the expected z_N as a function of the cut (integrating to the right).

5.5 Signal Region definition

The contribution of SM processes including an on-shell Z boson decaying leptonically is reduced by vetoing events with a same flavour opposite sign lepton pair with 81.2 GeV $< m_{\ell\ell} <$ 101.2 GeV. $R_{\ell\ell}$ is required to be above 6, to further reduce the SM backgrounds, which peak at lower values. $min\{\Delta\phi(jet_{ISR}, E_{\mathrm{T}}^{\mathrm{miss}})\}$ is required to be larger than 0.4, to reject events where the $E_{\mathrm{T}}^{\mathrm{miss}}$ comes from mis-measured jets. Events are required to have at least one jet associated to the ISR system with the leading ISR jet with $p_{\mathrm{T}} >$ 300 GeV and $\Delta\phi(jet_{ISR1}, E_{\mathrm{T}}^{\mathrm{miss}}) > 2$, to ensure to be in the recoiling configuration. Figure 5.7 shows the expected $E_{\mathrm{T}}^{\mathrm{miss}}$ and leading ISR jet p_{T} distributions for events passing all the requirements described so far.

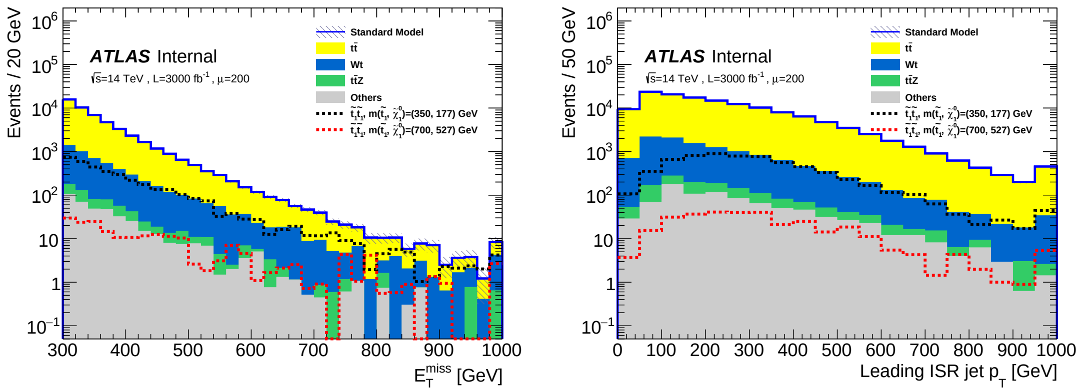

FIGURE 5.7: Distributions of $E_{\mathrm{T}}^{\mathrm{miss}}$ (left) and the leading ISR jet p_{T} (right) for events passing the $m_{\ell\ell}$, $min\{\Delta\phi(jet_{ISR}, E_{\mathrm{T}}^{\mathrm{miss}})\}$ and $\Delta\phi(jet_{ISR1}, E_{\mathrm{T}}^{\mathrm{miss}})$ requirements described in Section 5.3 and with $E_{\mathrm{T}}^{\mathrm{miss}}$ >300 GeV. The contributions from all SM backgrounds are shown, and the hashed band represents the statistical uncertainty on the total SM background prediction. The expected distributions for signal models with $m_{\tilde{t}_1}$ = 350 GeV and $m_{\tilde{t}_1}$ = 700 GeV are also shown as dashed lines for comparison.

The signal region (SR) is then also defined selecting events with $E_{\mathrm{T}}^{\mathrm{miss}} >$ 350 GeV, and $m_{\mathrm{T2}} >$ 100 GeV.

	SR
$m_{\ell\ell}$ [GeV] (SF lepton pairs only)	$m_{\ell\ell} < 81.2$ or $m_{\ell\ell} > 101.2$
$min\{\Delta\phi(jet_{ISR}, E_{\mathrm{T}}^{\mathrm{miss}})\}$	>0.4
$\Delta\phi(jet_{ISR1}, E_{\mathrm{T}}^{\mathrm{miss}})$	>2
$R_{2\ell}$	>6
$E_{\mathrm{T}}^{\mathrm{miss}}$ [GeV]	$>$ 350
Leading ISR jet p_{T} [GeV]	$>$ 300
m_{T2} [GeV]	>100

TABLE 5.1: Summary of the analysis selection criteria (see text for details).

Figure 5.8 shows the m_{T2} distribution for events passing all the SR requirements except for the one on m_{T2} itself.

The main backgrounds that survive the selections are $t\bar{t}$ events that exceed the expected m_{T2} endpoint at the W mass because of the finite detector resolution, and the irreducible $t\bar{t}+Z$ (with $Z \to \nu\nu$) background. A summary of the SR selections is presented in Table 5.1.

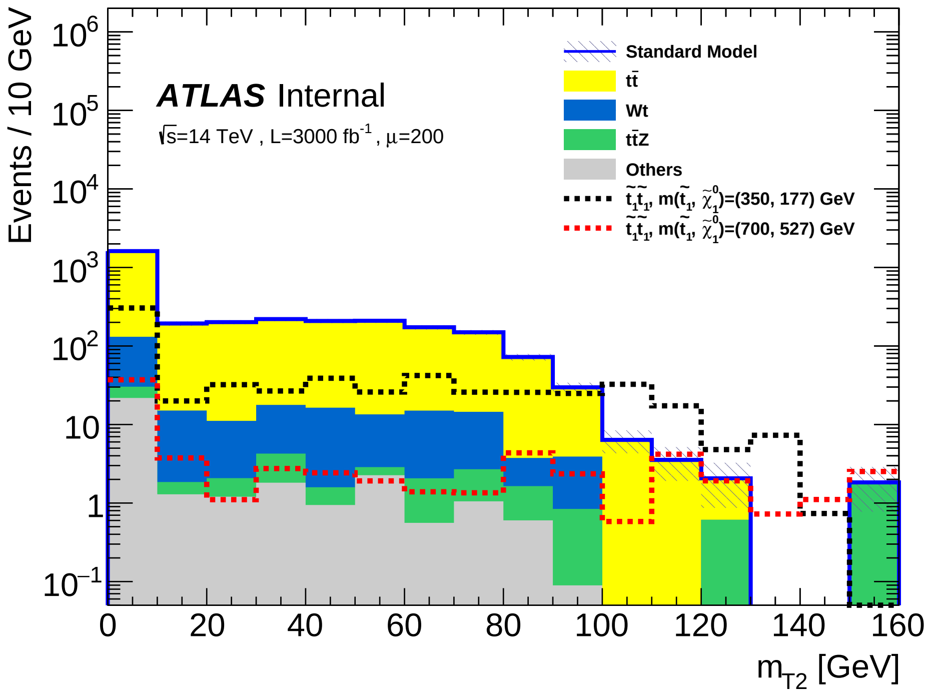

FIGURE 5.8: Distribution of m_{T2} for events passing all SR selection requirements, except that on m_{T2} itself. The contributions from all SM backgrounds are shown, and the hashed band represents the statistical uncertainty on the total SM background prediction. The expected distributions for signal models with $m_{\tilde{t}_1} = 350$ GeV and $m_{\tilde{t}_1} = 700$ GeV are also shown as dashed lines for comparison.

5.6 Results and interpretation

Table 5.2 shows the expected yields in the SR for each background source, together with two benchmark signal models.

	SR
Expected Standard Model	13.8 ± 6.5
$t\bar{t}$	11.4 ± 5.1
$t\bar{t} + Z$	2.4 ± 1.5
Others	$0.0^{+1.8}_{-0.0}$
$\tilde{t}_1\ \tilde{t}_1\ m(\tilde{t}_1, \tilde{\chi}_1^0) = (350, 177)$ GeV	62.7 ± 7.5
$\tilde{t}_1\ \tilde{t}_1\ m(\tilde{t}_1, \tilde{\chi}_1^0) = (700, 527)$ GeV	11.0 ± 2.0

TABLE 5.2: Expected yields in the SR together with their statistical uncertainties, for an integrated luminosity of 3000 fb^{-1}. The expected numbers of events for two signal samples ($m_{\tilde{t}_1} = 350$ GeV, $m_{\tilde{\chi}_1^0} = 177$ GeV and $m_{\tilde{t}_1} = 700$ GeV, $m_{\tilde{\chi}_1^0} = 527$ GeV) are also reported.

Scans of expected discovery significance and 95% CL limits are shown in Figure 5.9 and 5.10 as a function of the $\tilde{t}_1$ mass. The 5σ discovery potential for the full HL-LHC dataset is expected to extend up to $m_{\tilde{t}_1} = 480$ GeV, while in the absence of a signal, $\tilde{t}_1$ masses up to 700 GeV are expected to be excluded at 95% CL.

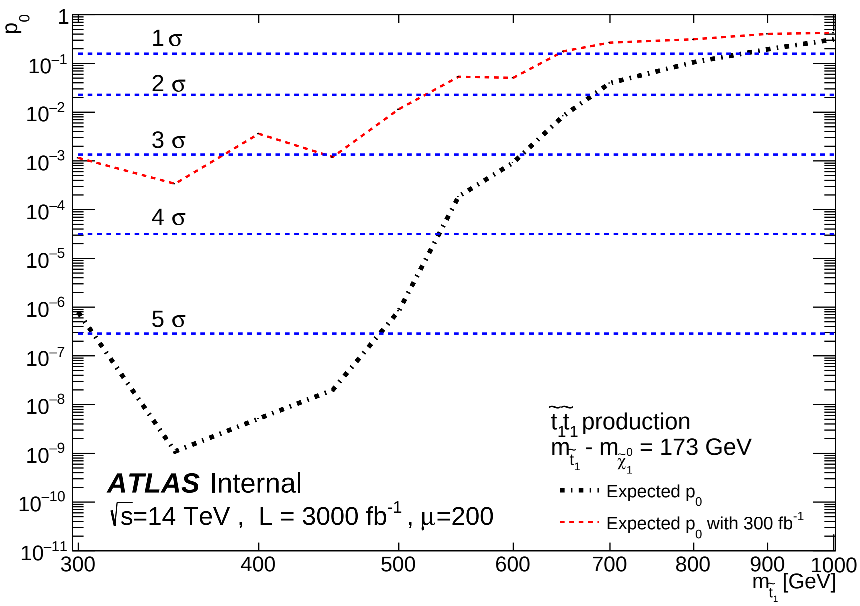

FIGURE 5.9: Expected compatibility, in terms of p-value p_0, with the background-only hypothesis from the analysis of 3000 fb^{-1}of 14 TeV proton-proton collision data as a function of the $\tilde{t}_1$ mass, for $m_{\tilde{t}_1} - m_{\tilde{\chi}_1^0} = 173$ GeV and assuming BR($\tilde{t}_1 \rightarrow t\tilde{\chi}_1^0$) = 1. The sensitivity from the analysis of 300 fb^{-1}of 14 TeV collision data is also shown as a red dashed line for comparison.

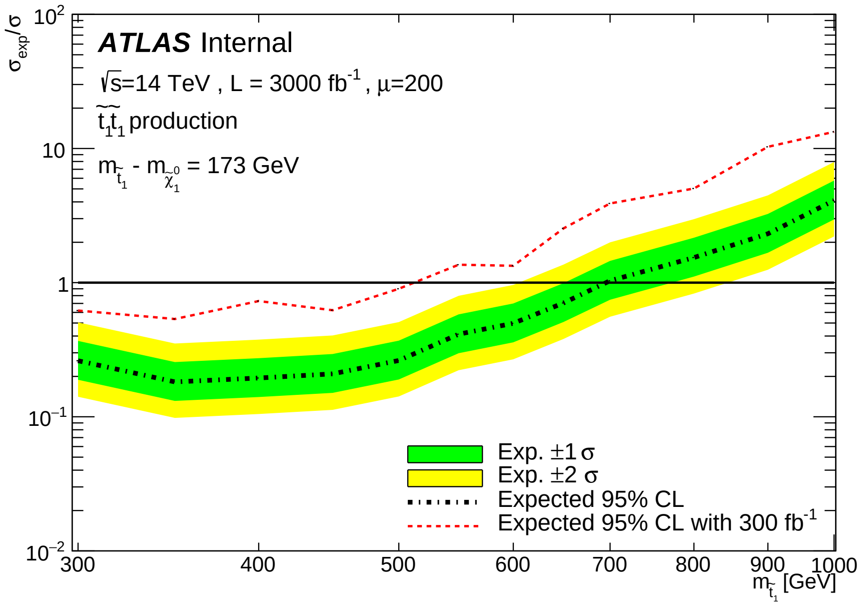

FIGURE 5.10: Exclusion limits at 95% CL shown as the ratio between the cross-section limit σ and the nominal NLO+NLL prediction σ_{theory} from the analysis of 3000 fb^{-1}of 14 TeV proton-proton collision data as a function of the $\tilde{t}_1$ mass, for $m_{\tilde{t}_1} - m_{\tilde{\chi}_1^0} = 173$ GeV and assuming BR($\tilde{t}_1 \rightarrow t\tilde{\chi}_1^0$) = 1. The shaded bands show the effect on the limit of respectively one and two sigma variations on the background prediction. The sensitivity from the analysis of 300 fb^{-1}of 14 TeV collision data is also shown as a red dashed line for comparison.

The sensitivity to heavy SUSY particles will be increased significantly with the analysis of ATLAS data collected in proton-proton collisions at the LHC design centre-of-mass-energy of $\sqrt{s} = 14\,\text{TeV}$. Feasibility studies on benchmark SUSY scenarios for direct top squark production are carried out with MC simulated events generated at $\sqrt{s} = 14$ TeV, and with corrections accounting for the detector response applied to the generator-level particles. A dataset of $3\,\text{ab}^{-1}$ extends the discovery potential for $\tilde{t}_1\,\tilde{t}_1$ production up to 480 GeV and the exclusion sensitivity up to masses of about 700 GeV, assuming $\tilde{t}_1 \rightarrow t\tilde{\chi}_1^0$ and $m_{\tilde{t}_1} - m_{\tilde{\chi}_1^0} = 173$ GeV with both top quarks decaying leptonically. The fully hadronic and semi-leptonic channels, which have not been considered in this study, are likely to further extend this reach. The latest results for $\tilde{t}_1 \rightarrow t\tilde{\chi}_1^0$ already exclude the potential discovery region presented in this chapter. Future improvements in the understanding of experimental and theoretical systematic uncertainties on the SM backgrounds will provide additional gains in sensitivity.

Chapter 6

Conclusion

During my Ph.D. I worked in the framework ATLAS collaboration and had the pleasure to sign more than 200 ATLAS publications and directly contribute to several of them. My involvement was particularly active in the search for new physics beyond the Standard Model and in the detector development toward the High Luminosity programme of LHC.

The data analysis work presented in this thesis is based on the data collected by the ATLAS detector during 2015 and 2016 at $\sqrt{s} = 13$ TeV centre mass energy and correspond to 36.1 fb^{-1} of integrated luminosity. I targeted two specific models involving the existence of new physics beyond the Standard Model: the first assume the existence of Dark Matter particles which is produced in association with top quark pairs via a scalar or pseudoscalar mediator; the second is a simplified model based on Supersymmetry (SUSY). In particular, I targeted the decay lightest top squark $\tilde{t}_1$. I defined and developed different data events selections to target both of the two models reported before. The data analysis presented focused on the final state with two lepton (electrons or muons) of opposite electric charge. The number of observed events potentially indicating the existence of new physics beyond the Standard Model was found to be consistent with the Standard Model expectations. Through a statistical analysis of the data, I was able to set world-leading limits on models involving the existence of new particles from Dark Matter and Supersymmetry. In details, I set limits on the production cross-section of colour-neutral mediator models decaying into DM particles. Both the scalar and pseudoscalar mediator cases were considered. These limits were obtained both as a function of the mediator mass, assuming a specific DM mass of 1 GeV and as a function of the DM mass, assuming a specific mediator mass of 10 GeV. For a DM mass particle of 1 GeV, scalar mediator masses up to 50 GeV were excluded at 95% CL. The result obtained assuming the scalar mediator was converted in a limit on the spin-independent DM–nucleon scattering cross-section allowing to straight away compare it with the limits obtained by the past fixed target experiments. For DM mass particle of 1GeV, production cross-section higher than 10^{-42} was excluded at 90% CL. For simplified SUSY model considering only the lightest top squark $\tilde{t}_1$ and the lightest neutralino $\tilde{\chi}_1^0$, top squark masses below 720 GeV for massless neutralino and neutralino masses below 300 GeV for $m(\tilde{t}_1) = 650$ GeV were excluded at 95% CL. Similar limits were also set on a phenomenological Minimal Supersimmetric Standard Model. I also presented model-independent limits that will allow reinterpretations of the presented results using other models, which predict decays into di-lepton final states in association with invisible particles. My original results were reported in two peer review papers published in December 2017 and January 2018 in The European Physical Journal C (EPJC), C77(12):898, 2017 [101] and C78(1):18, 2018 [102].

The non-observation of new particles in the decay process considered in my studies doesn't close all the possibility to find new physics beyond the Standard Model in the next years. The study of the remaining data available in Run 2 will be certainly a unique opportunity to further investigate possible physics beyond the Standard Model. In particular, SUSY models with heavier lightest Supersymmetric particles or models characterised by compress mass spectra are now accessible with the amount of integrated luminosity collected during 2017 and 2018. Concerning Dark Matter particles produced in association with top quarks, more complex models can now be targeted. In particular, it would be very interesting to consider a two-Higgs-doublet model with the addition of a pseudoscalar mediator a (2HDMa) [201]. The two-Higgs-doublet model is a typical extension of the SM Higgs sector where a second Higgs doublet is added. This model is inspired by SUSY and it allows also the reproduce the baryon asymmetry measured in the Universe [202]. The pseudoscalar mediator is responsible for the connection between the DM particles and the Standard Model particles as $SM \rightarrow a \rightarrow \chi\chi$. Results of this model could have a direct impact on the determination of the parameters space still accessible with the LHC. Would be also very important to tackle another challenging open question in nature: Dark Energy (DE). DE is believed to constitute up to $\sim 70\%$ of the Universe and to cause its expansion in an accelerated rate [21]. Recently proposed scalar DE models [203] suggests that the signature with a top quark pairs plus missing transverse energy is very sensitive to the coupling between the SM matter and the DE scalar field. Thus, would be very interesting to also apply the di-lepton signature to this type of model.

As a related experimental activity, I also investigated a new silicon pixel sensor technology based on a "monolithic" approach. In this thesis, I presented studies of a beam test done at the H8 line at the CERN Super Proton Synchrotron (SPS) using pixel sensor prototypes using this technology. I developed the reconstruction algorithm and results of the measurements showed excellent performance and high efficiency for both non-irradiated sample (99.9%) and irradiated samples. The 95% of the charge signal is collected in 75 ns which corresponds to three LHC bunch crossing of 25 ns. This is a promising characteristic for future prototypes. My original results were reported in JINST 11 (2016) no.07, P07019 and JINST 13 (2018) no.02, P02011 [179, 192]. New prototypes designed to fulfil the requirements expected for ITk have been produced and are now being tested. In particular, the focus is to implement a digital circuitry compatible with the expected ITk readout.

Appendices

Appendix A

Upper limits on signal cross section

Upper limits on the signal cross section for all the signal regions discussed in Chapter 3 are presented.

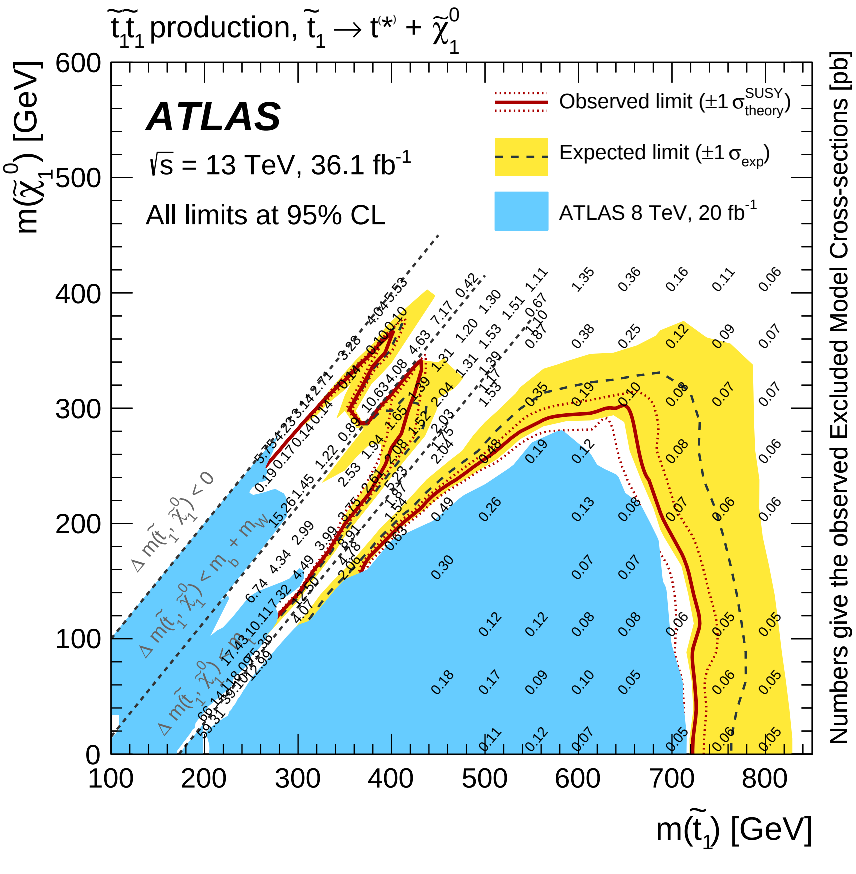

FIGURE A.1: Upper limits on cross-sections (in pb) at 95% CL for each signal model, assuming $\tilde{t}_1$ pair production, decaying via $\tilde{t}_1 \to t\tilde{\chi}_1^0$ with 100% branching ratio. The numbers of the plot give the observed excluded model cross-sections measured in fb

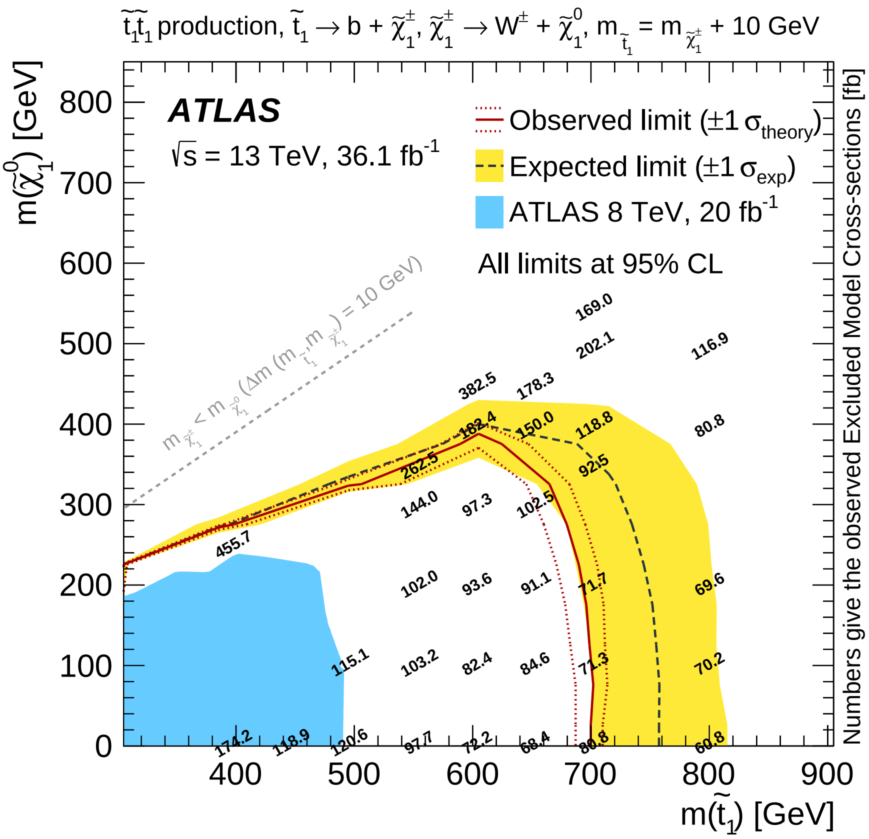

FIGURE A.2: Upper limits on cross-sections (in fb) at 95% CL for each signal model, assuming $\tilde{t}_1$ pair production, decaying via $\tilde{t}_1 \to b\tilde{\chi}_1^{\pm}$ with 100% branching ratio. The lightest chargino mass is assumed to be close to the stop mass, $m_{\tilde{\chi}_1^{\pm}} = m_{\tilde{t}_1} - 10$ GeV. The numbers of the plot give the observed excluded model cross-sections measured in fb

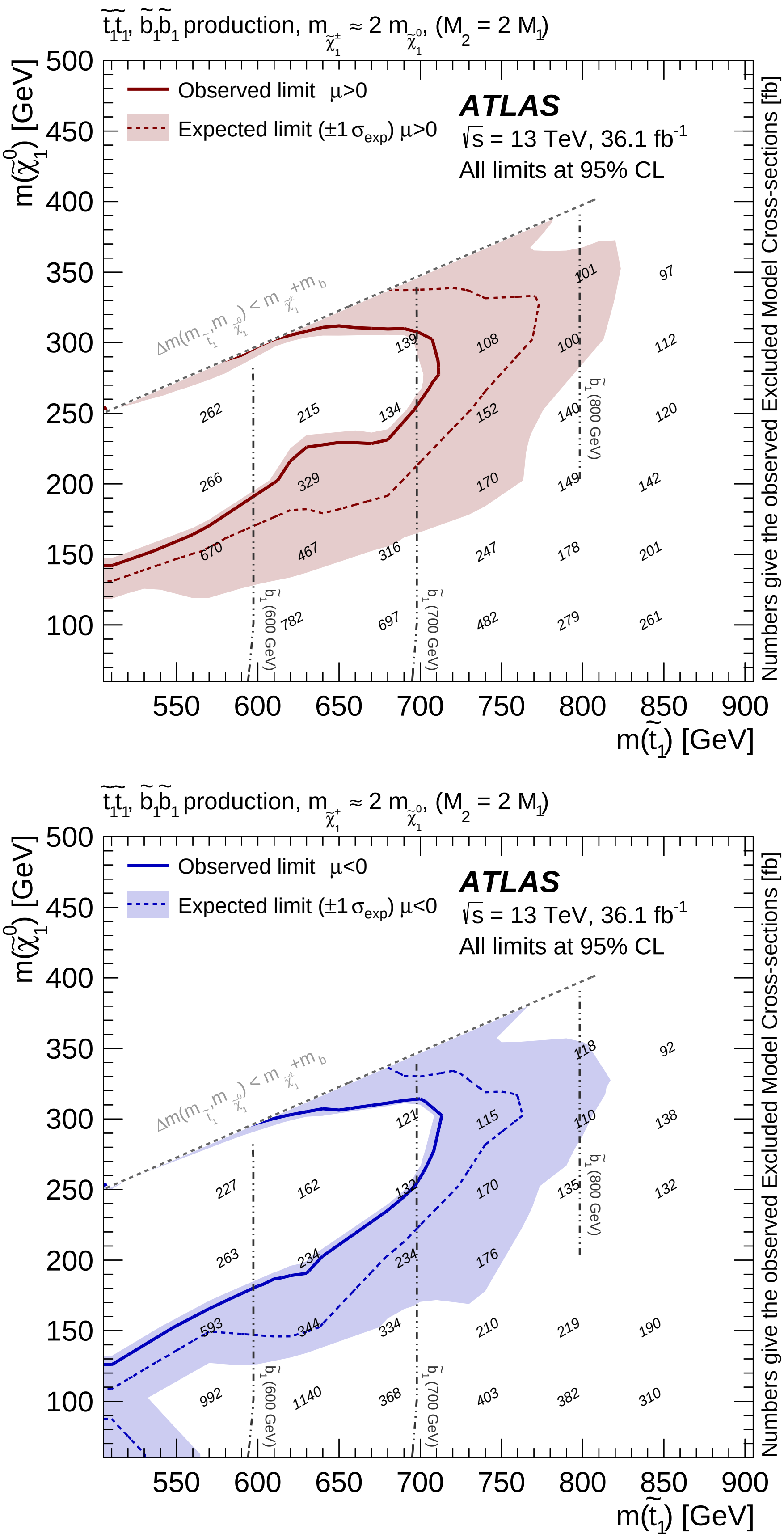

FIGURE A.3: Upper limits on cross-sections (in fb) at 95% CL for each signal model, assuming the pMSSM model described in the text. Pair production of $\tilde{t}_1$ and $\tilde{b}_1$ are considered. Limits are set for both positive (top) and negative (bottom) values of μ.The numbers of the plot give the observed excluded model cross-sections measured in fb

Appendix B

Acceptance and efficiency

Acceptance and efficiency for all the signal region discussed in Chapter 3 are presented.

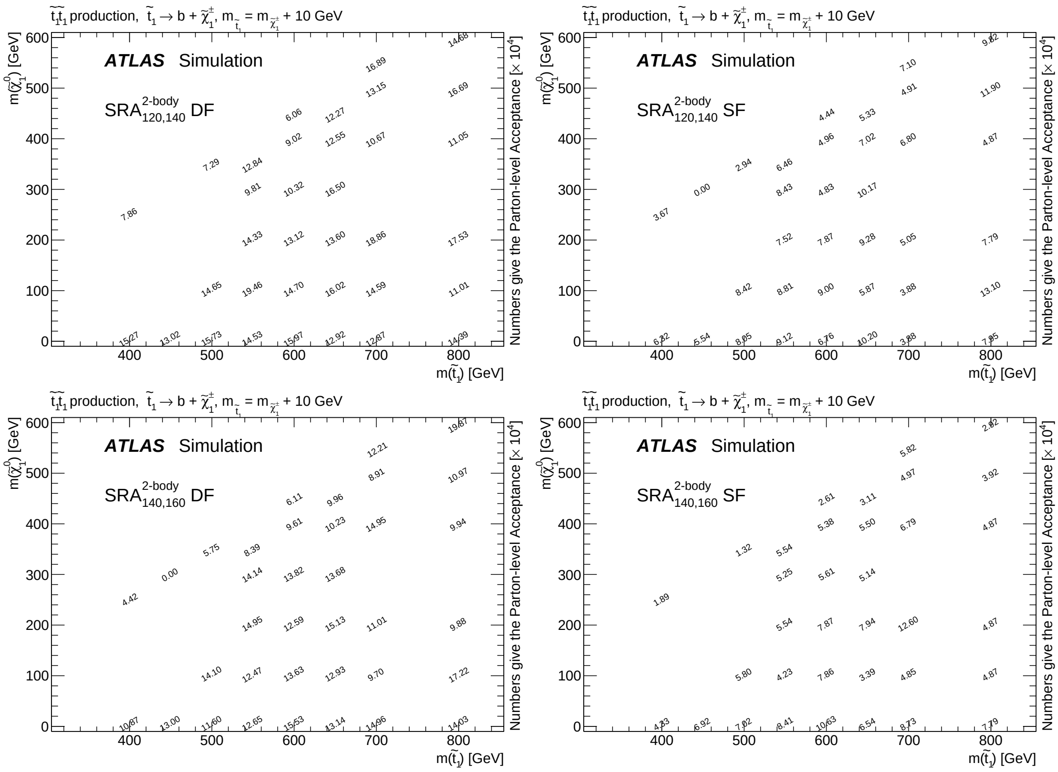

FIGURE B.1: $\text{SRA}_{120,140}^{2-\text{body}}$ DF (first row - left), $\text{SRB}_{120,140}^{2-\text{body}}$ SF (first row - right), $\text{SRA}_{140,160}^{2-\text{body}}$ DF (second row - left), $\text{SRB}_{140,160}^{2-\text{body}}$ SF (second row - right) acceptance for each signal model, assuming $\tilde{t}_1$ pair production, decaying via $\tilde{t}_1 \to b\tilde{\chi}_1^{\pm}$ with 100% branching ratio. The lightest chargino mass is assumed to be close to the stop mass, $m_{\tilde{\chi}_1^{\pm}} = m_{\tilde{t}_1} - 10$ GeV.

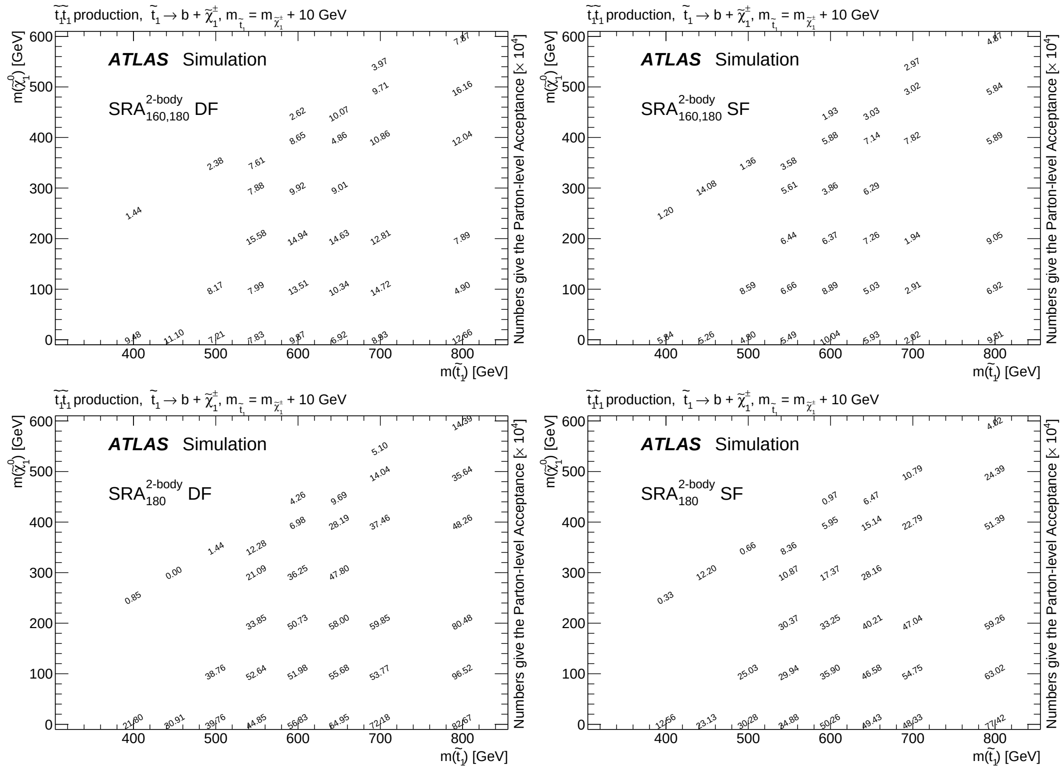

FIGURE B.2: $\text{SRA}^{2-\text{body}}_{160,180}$ DF (first row - left), $\text{SRB}^{2-\text{body}}_{160,180}$ SF (first row - right) and $\text{SRA}^{2\text{-body}}_{180}$DF (second row - left) and $\text{SRA}^{2\text{-body}}_{180}$SF (second row - right) acceptance for each signal model, assuming $\tilde{t}_1$ pair production, decaying via $\tilde{t}_1 \to b\tilde{\chi}_1^{\pm}$ with 100% branching ratio. The lightest chargino mass is assumed to be close to the stop mass, $m_{\tilde{\chi}_1^{\pm}} = m_{\tilde{t}_1} - 10$ GeV.

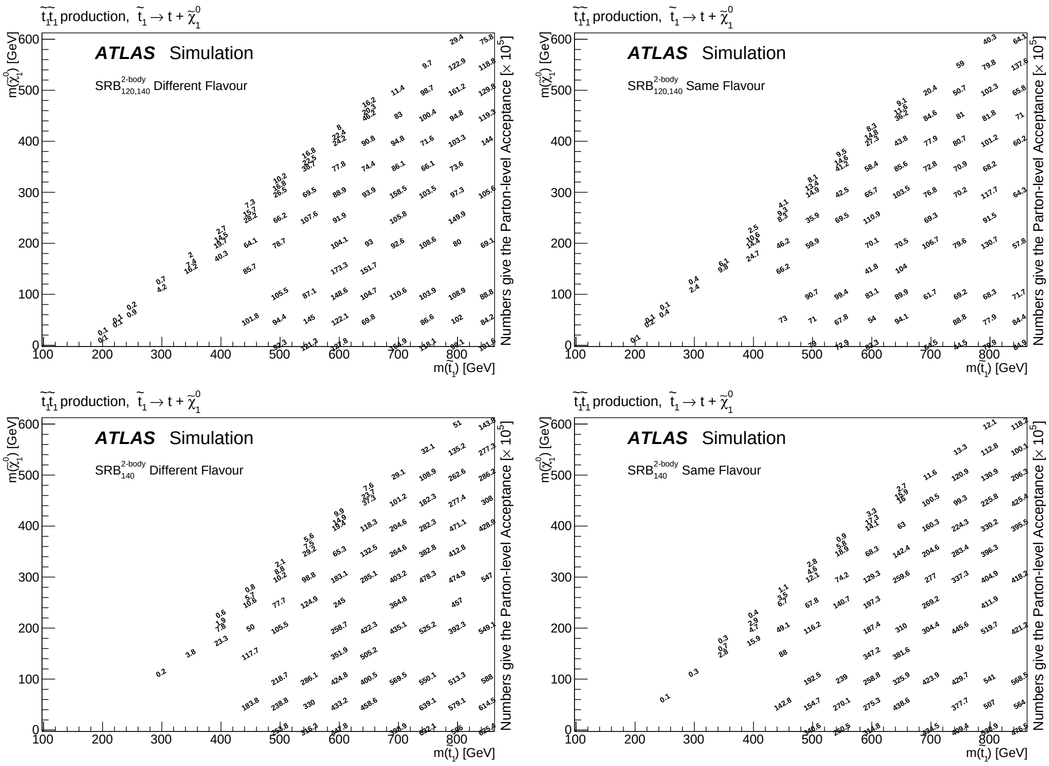

FIGURE B.3: $\text{SRB}^{2-\text{body}}_{120,140}$ DF (first row - left), $\text{SRB}^{2-\text{body}}_{120,140}$ SF (first row - right), $\text{SRB}^{\text{2-body}}_{140}$DF (second row - left) and $\text{SRB}^{\text{2-body}}_{140}$SF (second row - left) acceptance for each signal model, assuming $\tilde{t}_1$ pair production, decaying via $\tilde{t}_1 \to t\tilde{\chi}^0_1$ with 100% branching ratio.

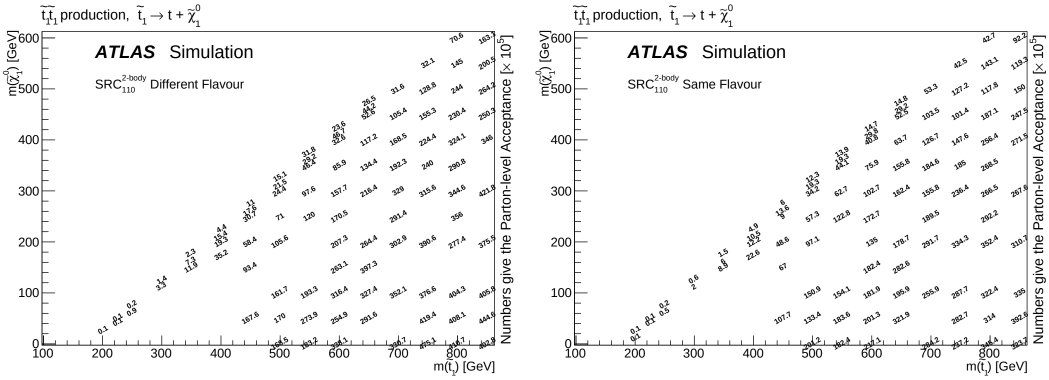

FIGURE B.4: $\text{SRC}^{\text{2-body}}_{110}$ DF (left) and $\text{SRC}^{\text{2-body}}_{110}$ SF (right) acceptance for each signal model, assuming $\tilde{t}_1$ pair production, decaying via $\tilde{t}_1 \to t\tilde{\chi}^0_1$ with 100% branching ratio.

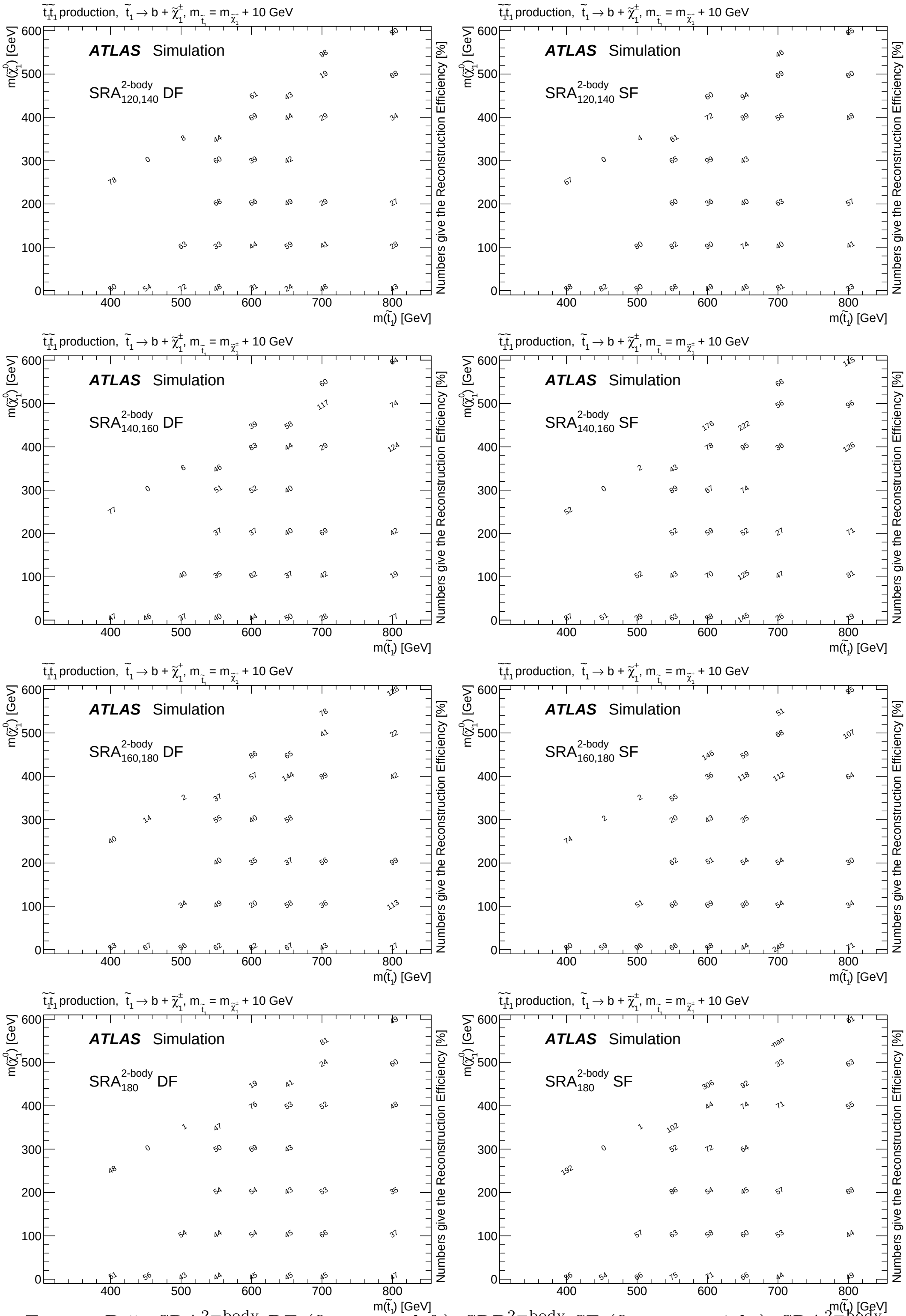

FIGURE B.5: $SRA^{2-\text{body}}_{120,140}$ DF (first row - left), $SRB^{2-\text{body}}_{120,140}$ SF (first row - right), $SRA^{2-\text{body}}_{140,160}$ DF (second row - left), $SRB^{2-\text{body}}_{140,160}$ SF (second row - right), $SRA^{2-\text{body}}_{160,180}$ DF (third row - left), $SRB^{2-\text{body}}_{160,180}$ SF (third row - right) and $SRA^{2\text{-body}}_{180}$DF and $SRA^{2\text{-body}}_{180}$SF efficiency for each signal model, assuming $\tilde{t}_1$ pair production, decaying via $\tilde{t}_1 \rightarrow b\tilde{\chi}_1^{\pm}$ with 100% branching ratio. The lightest chargino mass is assumed to be close to the stop mass, $m_{\tilde{\chi}_1^{\pm}} = m_{\tilde{t}_1} - 10$ GeV.

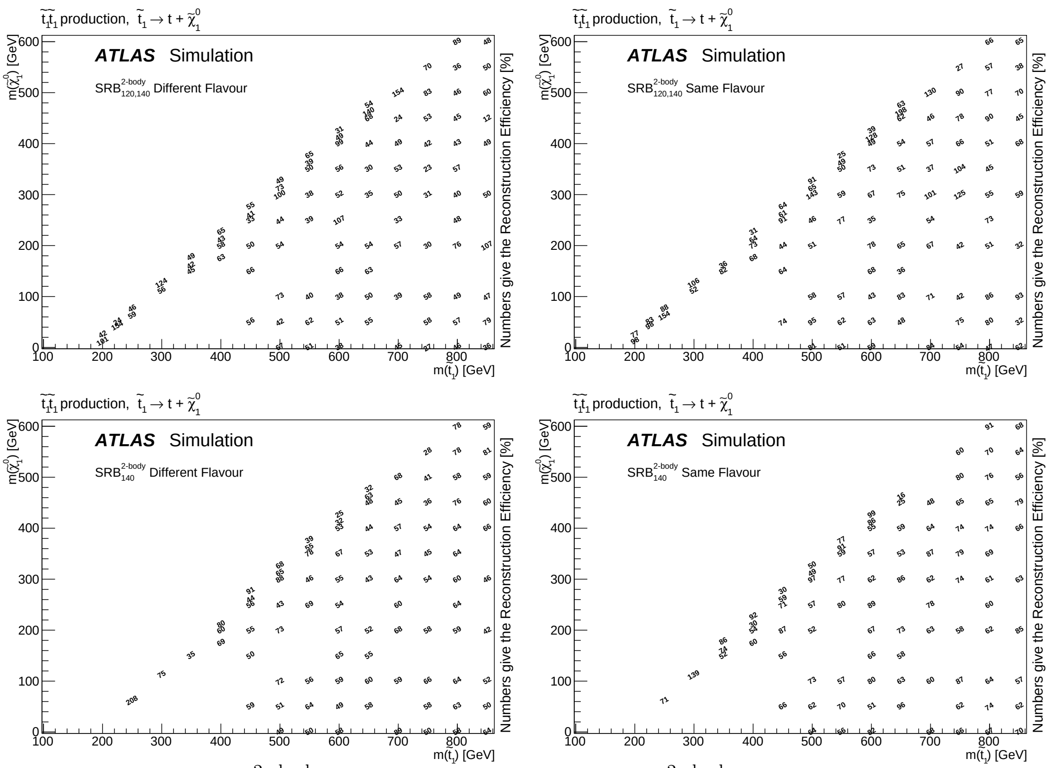

Figure B.6: $\text{SRB}^{2-\text{body}}_{120,140}$ DF (first row - left), $\text{SRB}^{2-\text{body}}_{120,140}$ SF (first row - right), $\text{SRB}^{2\text{-body}}_{140}$DF(second row - left) and $\text{SRB}^{2\text{-body}}_{140}$SF(second row - right) efficiency for each signal model, assuming $\tilde{t}_1$ pair production, decaying via $\tilde{t}_1 \rightarrow t\tilde{\chi}_1^0$ with 100% branching ratio.

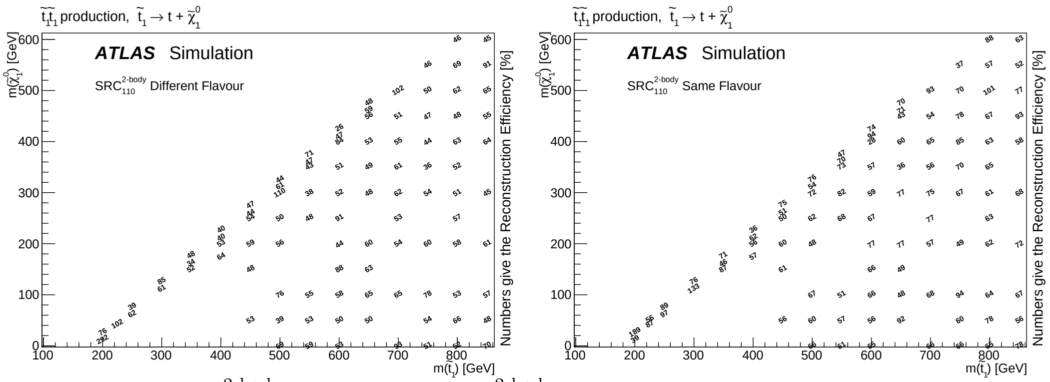

Figure B.7: $\text{SRC}^{2\text{-body}}_{110}$ DF (left) and $\text{SRC}^{2\text{-body}}_{110}$ SF (right) efficiency for each signal model, assuming $\tilde{t}_1$ pair production, decaying via $\tilde{t}_1 \rightarrow t\tilde{\chi}_1^0$ with 100% branching ratio.

$m(\phi)$ [GeV]	$m(\chi)$ [GeV]	acc. SRt3	eff. SRt3
10	1	$4.15{\cdot}10^{-5}$	0.70
20	1	$8.25{\cdot}10^{-5}$	0.54
50	1	$2.14{\cdot}10^{-4}$	0.52
100	1	$6.99{\cdot}10^{-4}$	0.55
150	1	$1.46{\cdot}10^{-3}$	0.59
200	1	$2.13{\cdot}10^{-3}$	0.56
300	1	$3.85{\cdot}10^{-3}$	0.56
400	1	$4.74{\cdot}10^{-3}$	0.57
500	1	$5.35{\cdot}10^{-3}$	0.61
600	1	$5.34{\cdot}10^{-3}$	0.61
1000	1	$6.54{\cdot}10^{-3}$	0.60
10	10	$2.39{\cdot}10^{-4}$	0.67
10	20	$6.37{\cdot}10^{-4}$	0.59
10	50	$2.20{\cdot}10^{-3}$	0.57
10	75	$3.79{\cdot}10^{-3}$	0.62
10	100	$4.61{\cdot}10^{-3}$	0.63
10	125	$5.26{\cdot}10^{-3}$	0.64
10	150	$5.23{\cdot}10^{-3}$	0.56
10	175	$5.54{\cdot}10^{-3}$	0.60
10	200	$6.11{\cdot}10^{-3}$	0.58
10	250	$5.99{\cdot}10^{-3}$	0.63
10	300	$6.61{\cdot}10^{-3}$	0.56
10	500	$8.37{\cdot}10^{-3}$	0.55

TABLE B.1: Acceptance and efficiency of the SRt3 selections to the colour-neutral simplified model samples with scalar mediator decaying into dark matter pairs produced in association with top-quark pairs ($t\bar{t} + \phi$).

$m(a)$ [GeV]	$m(\chi)$ [GeV]	acc. SRt3	eff. SRt3
10	1	$1.27{\cdot}10^{-3}$	0.54
20	1	$1.36{\cdot}10^{-3}$	0.54
50	1	$1.68{\cdot}10^{-3}$	0.56
100	1	$2.35{\cdot}10^{-3}$	0.57
150	1	$2.89{\cdot}10^{-3}$	0.52
200	1	$3.18{\cdot}10^{-3}$	0.59
300	1	$4.04{\cdot}10^{-3}$	0.52
400	1	$4.41{\cdot}10^{-3}$	0.56
500	1	$5.04{\cdot}10^{-3}$	0.59
600	1	$5.54{\cdot}10^{-3}$	0.56
1000	1	$6.72{\cdot}10^{-3}$	0.55
10	10	$2.03{\cdot}10^{-3}$	0.54
10	20	$2.42{\cdot}10^{-3}$	0.58
10	50	$3.42{\cdot}10^{-3}$	0.55
10	75	$4.14{\cdot}10^{-3}$	0.59
10	100	$4.46{\cdot}10^{-3}$	0.61
10	125	$4.69{\cdot}10^{-3}$	0.62
10	150	$5.19{\cdot}10^{-3}$	0.57
10	175	$5.15{\cdot}10^{-3}$	0.58
10	200	$5.61{\cdot}10^{-3}$	0.56
10	250	$6.29{\cdot}10^{-3}$	0.21
10	300	$6.26{\cdot}10^{-3}$	0.57
10	500	$7.67{\cdot}10^{-3}$	0.57

TABLE B.2: Acceptance and efficiency of the SRt3 selections to the colour-neutral simplified model samples with pseudo-scalar mediator decaying into dark matter pairs produced in association with top-quark pairs ($t\bar{t}+a$).

Bibliography

[1] Planck Collaboration, *Planck 2015 results - XIII. Cosmological parameters*, AA **594** (2016) A13, https://doi.org/10.1051/0004-6361/201525830.

[2] Komatsu, E. et Al., *Seven-year Wilkinson Microwave Anisotropy Probe (WMAP) Observations: Cosmological Interpretation*, The Astrophysical Journal Supplement **192** (2011) 18, arXiv:1001.4538 [astro-ph.CO].

[3] G. Steigman and M. S. Turner, *Cosmological constraints on the properties of weakly interacting massive particles*, Nuclear Physics B **253** (1985) 375 – 386, http://www.sciencedirect.com/science/article/pii/0550321385905371.

[4] G. D'Ambrosio, G. F. Giudice, G. Isidori, and A. Strumia, *Minimal flavor violation: An Effective field theory approach*, Nucl. Phys. **B645** (2002) 155–187, arXiv:hep-ph/0207036 [hep-ph].

[5] Y. Golfand and E. Likhtman, *Extension of the Algebra of Poincare Group Generators and Violation of p Invariance*, JETP Lett. **13** (1971) 323–326.

[6] D. Volkov and V. Akulov, *Is the neutrino a goldstone particle?*, Phys. Lett. B **46** (1973) 109–110.

[7] J. Wess and B. Zumino, *Supergauge transformations in four dimensions*, Nucl. Phys. B **70** (1974) 39–50.

[8] J. Wess and B. Zumino, *Supergauge invariant extension of quantum electrodynamics*, Nucl. Phys. B **78** (1974) 1.

[9] S. Ferrara and B. Zumino, *Supergauge invariant Yang-Mills theories*, Nucl. Phys. B **79** (1974) 413.

[10] A. Salam and J. A. Strathdee, *Super-symmetry and non-Abelian gauges*, Phys. Lett. B **51** (1974) 353–355.

[11] G. R. Farrar and P. Fayet, *Phenomenology of the production, decay, and detection of new hadronic states associated with supersymmetry*, Phys. Lett. B **76** (1978) 575–579.

[12] H. Goldberg, *Constraint on the Photino Mass from Cosmology*, Phys. Rev. Lett. **50** (1983) 1419–1422, https://link.aps.org/doi/10.1103/PhysRevLett.50.1419.

[13] J. Ellis, J. Hagelin, D. Nanopoulos, K. Olive, and M. Srednicki, *Supersymmetric relics from the big bang*, Nuclear Physics B **238** (1984) 453 – 476, http://www.sciencedirect.com/science/article/pii/0550321384904619.

[14] S. L. Glashow, *Partial-symmetries of weak interactions*, Nuclear Physics **22** (1961) 579 – 588, http://www.sciencedirect.com/science/article/pii/0029558261904692.

[15] S. Weinberg, *A Model of Leptons*, Phys. Rev. Lett. **19** (1967) 1264–1266, http://link.aps.org/doi/10.1103/PhysRevLett.19.1264.

[16] A. Salam, *Weak and Electromagnetic Interactions*, Conf. Proc. **C680519** (1968) 367–377.

[17] G. 't Hooft and M. Veltman, *Regularization and renormalization of gauge fields*, Nuclear Physics B **44** (1972) 189–213.

[18] ATLAS Collaboration, *Observation of a new particle in the search for the standard model Higgs boson with the ATLAS detector at the LHC*, Phys. Lett. **B 716** (2012) 1–29, arXiv:1207.7214 [hep-ex].

[19] CMS Collaboration, *Observation of a new boson at a mass of 125 GeV with the CMS experiment at the LHC*, Phys. Lett. **B 716** (2012) 30–61, arXiv:1207.7235 [hep-ex].

[20] ATLAS Collaboration, *Summary plots from the ATLAS Standard Model physics group*, https://atlas.web.cern.ch/Atlas/GROUPS/PHYSICS/CombinedSummaryPlots/SM/.

[21] C. Patrignani et al., *Review of Particle Physics*, Chinese Physics C **C40** (2016) 100001, http://inspirehep.net/record/1489868.

[22] P. W. Higgs, *Broken symmetries, massless particles and gauge fields*, Physics Letters **12** (1964) 132–133.

[23] F. Englert and R. Brout, *Broken Symmetry and the Mass of Gauge Vector Mesons*, Phys. Rev. Lett. **13** (1964) 321–323, http://link.aps.org/doi/10.1103/PhysRevLett.13.321.

[24] G. S. Guralnik, C. R. Hagen, and T. W. B. Kibble, *Global Conservation Laws and Massless Particles*, Phys. Rev. Lett. **13** (1964) 585–587, http://link.aps.org/doi/10.1103/PhysRevLett.13.585.

[25] ATLAS Collaboration, *Observation of a new particle in the search for the Standard Model Higgs boson with the ATLAS detector at the LHC*, Phys. Lett. B **716** (2012) 1, arXiv:1207.7214 [hep-ex].

[26] CMS Collaboration, *Observation of a new boson at a mass of 125 GeV with the CMS experiment at the LHC*, Phys. Lett. B **716** (2012) 30, arXiv:1207.7235 [hep-ex].

[27] ATLAS and CMS Collaborations, *Combined Measurement of the Higgs Boson Mass in pp Collisions at $\sqrt{s} = 7$ and 8 TeV with the ATLAS and CMS Experiments*, Phys. Rev. Lett. **114** (2015) 191803, arXiv:1503.07589 [hep-ex].

[28] ATLAS and CMS Collaborations, *Measurements of the Higgs boson production and decay rates and constraints on its couplings from a combined ATLAS and CMS analysis of the LHC pp collision data at $\sqrt{s} = 7$ and 8 TeV*, JHEP **08** (2016) 045, arXiv:1606.02266 [hep-ex].

[29] R. Barbieri and G. F. Giudice, *Upper Bounds on Supersymmetric Particle Masses*, Nucl. Phys. B **306** (1988) 63.

[30] J. L. Feng, *Naturalness and the Status of Supersymmetry*, Annual Review of Nuclear and Particle Science **63** (2013) 351–382, https://doi.org/10.1146/annurev-nucl-102010-130447.

[31] F. Zwicky, *Die Rotverschiebung von extragalaktischen Nebeln*, Helvetica Physica Acta **6** (1933) 110–127.

[32] G. Bertone, D. Hooper, and J. Silk, *Particle dark matter: evidence, candidates and constraints*, Physics Reports **405** (2005) 279 – 390, http://www.sciencedirect.com/science/article/pii/S0370157304003515.

[33] Supernova Search Team Collaboration, A. G. Riess et al., *Observational evidence from supernovae for an accelerating universe and a cosmological constant*, Astron. J. **116** (1998) 1009–1038, arXiv:astro-ph/9805201 [astro-ph].

[34] Supernova Cosmology Project Collaboration, S. Perlmutter et al., *Measurements of Omega and Lambda from 42 high redshift supernovae*, Astrophys. J. **517** (1999) 565–586, arXiv:astro-ph/9812133 [astro-ph].

[35] *The Nobel Prize in Physics 2015*, http://www.nobelprize.org/nobel_prizes/physics/laureates/2015/press.pdf.

[36] S. Coleman and J. Mandula, *All Possible Symmetries of the S Matrix*, Phys. Rev. **159** (1967) 1251–1256, https://link.aps.org/doi/10.1103/PhysRev.159.1251.

[37] Super-Kamiokande Collaboration, C. Regis et al., *Search for proton decay via $p \to \mu^+ K^0$ in Super-Kamiokande I, II, and III*, Phys. Rev. D **86** (2012) 012006, arXiv:1205.6538 [hep-ex].

[38] A. Djouadi et al., *The Minimal supersymmetric standard model: Group summary report*, arXiv:hep-ph/9901246.

[39] C. F. Berger, J. S. Gainer, J. L. Hewett, and T. G. Rizzo, *Supersymmetry without prejudice*, JHEP **02** (2009) 023, arXiv:0812.0980 [hep-ph].

[40] W. Beenakker, R. Hopker, M. Spira, and P. Zerwas, *Squark and gluino production at hadron colliders*, Nucl. Phys. B **492** (1997) 51–103, arXiv:hep-ph/9610490 [hep-ph].

[41] A. Kulesza and L. Motyka, *Threshold resummation for squark-antisquark and gluino-pair production at the LHC*, Phys. Rev. Lett. **102** (2009) 111802, arXiv:0807.2405 [hep-ph].

[42] A. Kulesza and L. Motyka, *Soft gluon resummation for the production of gluino-gluino and squark-antisquark pairs at the LHC*, Phys. Rev. D **80** (2009) 095004, arXiv:0905.4749 [hep-ph].

[43] W. Beenakker, S. Brensing, M. Kramer, A. Kulesza, E. Laenen, et al., *Soft-gluon resummation for squark and gluino hadroproduction*, JHEP **12** (2009) 041, arXiv:0909.4418 [hep-ph].

[44] W. Beenakker, S. Brensing, M. n. Kramer, A. Kulesza, E. Laenen, L. Motyka, and I. Niessen, *Squark and gluino hadroproduction*, Int. J. Mod. Phys. A **26** (2011) 2637–2664, arXiv:1105.1110 [hep-ph].

[45] C. Borschensky, M. Krämer, A. Kulesza, M. Mangano, S. Padhi, et al., *Squark and gluino production cross sections in pp collisions at $\sqrt{s}$ = 13, 14, 33 and 100 TeV*, Eur. Phys. J. C **74** (2014) 3174, arXiv:1407.5066 [hep-ph].

[46] J. Alwall, M.-P. Le, M. Lisanti, and J. G. Wacker, *Searching for Directly Decaying Gluinos at the Tevatron*, Phys. Lett. B **666** (2008) 34–37, arXiv:0803.0019 [hep-ph].

[47] J. Alwall, P. Schuster, and N. Toro, *Simplified models for a first characterization of new physics at the LHC*, Phys. Rev. D **79** (2009) 075020, arXiv:0810.3921 [hep-ph].

[48] LHC New Physics Working Group Collaboration, D. Alves, *Simplified models for LHC new physics searches*, J. Phys. G **39** (2012) 105005, arXiv:1105.2838 [hep-ph].

[49] ATLAS Collaboration, *ATLAS Run 1 searches for direct pair production of third-generation squarks at the Large Hadron Collider*, Eur. Phys. J. C **75** (2015) 510, arXiv:1506.08616 [hep-ex].

[50] ATLAS Collaboration,, *Search for top squarks in final states with one isolated lepton, jets, and missing transverse momentum in* $\sqrt{s} = 13$ *TeV pp collisions with the ATLAS detector*, Phys. Rev. D **94** (2016) 052009, arXiv:1606.03903 [hep-ex].

[51] CMS Collaboration, *Search for top-squark pair production in the single-lepton final state in pp collisions at* $\sqrt{s} = 8$ *TeV*, Eur. Phys. J. C **73** (2013) 2677, arXiv:1308.1586 [hep-ex].

[52] CMS Collaboration, *Search for supersymmetry using razor variables in events with b-tagged jets in pp collisions at* $\sqrt{s} = 8$ *TeV*, Phys. Rev. D **91** (2015) 052018, arXiv:1502.00300 [hep-ex].

[53] CMS Collaboration, *Searches for supersymmetry using the* M_{T2} *variable in hadronic events produced in pp collisions at* 8 *TeV*, JHEP **05** (2015) 078, arXiv:1502.04358 [hep-ex].

[54] CMS Collaboration, *Search for direct pair production of supersymmetric top quarks decaying to all-hadronic final states in pp collisions at* $\sqrt{s} = 8$ *TeV*, Eur. Phys. J. C **76** (2016) 460, arXiv:1603.00765 [hep-ex].

[55] CMS Collaboration, *Searches for third-generation squark production in fully hadronic final states in proton–proton collisions at* $\sqrt{s} = 8$ *TeV*, JHEP **06** (2015) 116, arXiv:1503.08037 [hep-ex].

[56] CMS Collaboration, *Search for top squark pair production in compressed-mass-spectrum scenarios in proton–proton collisions at* $\sqrt{s} = 8$ *TeV using the* α_T *variable*, Phys. Lett. B **767** (2017) 403, arXiv:1605.08993 [hep-ex].

[57] CMS Collaboration, *Search for supersymmetry in events with soft leptons, low jet multiplicity, and missing transverse energy in proton–proton collisions at* $\sqrt{s} = 8$ *TeV*, Phys. Lett. B **759** (2016) 9, arXiv:1512.08002 [hep-ex].

[58] CMS Collaboration, *Search for direct pair production of scalar top quarks in the single- and dilepton channels in proton–proton collisions at* $\sqrt{s} = 8$ *TeV*, JHEP **07** (2016) 027, arXiv:1602.03169 [hep-ex].

[59] CMS Collaboration, *Search for new physics with the* M_{T2} *variable in all-jets final states produced in pp collisions at* $\sqrt{s} = 13$ *TeV*, JHEP **10** (2016) 006, arXiv:1603.04053 [hep-ex].

[60] CMS Collaboration, *Inclusive search for supersymmetry using razor variables in pp collisions at* $\sqrt{s} = 13$ *TeV*, Phys. Rev. D **95** (2017) 012003, arXiv:1609.07658 [hep-ex].

[61] CMS Collaboration, *A search for new phenomena in pp collisions at* $\sqrt{s} = 13$ *TeV in final states with missing transverse momentum and at least one jet using the* α_T *variable*, Eur. Phys. J. C **77** (2017) 294, arXiv:1611.00338 [hep-ex].

[62] CMS Collaboration, *Searches for pair production of third-generation squarks in* $\sqrt{s} = 13$ *TeV pp collisions*, Eur. Phys. J. C **77** (2017) 327, arXiv:1612.03877 [hep-ex].

[63] CMS Collaboration, *Search for supersymmetry in the all-hadronic final state using top quark tagging in pp collisions at* $\sqrt{s} = 13$ *TeV*, arXiv:1701.01954 [hep-ex].

[64] ATLAS Collaboration, *ATLAS Run 1 searches for direct pair production of third-generation squarks at the Large Hadron Collider*, Eur. Phys. J. C **75** (2015) 510, arXiv:1506.08616 [hep-ex].

[65] ATLAS Collaboration, *Summary of the ATLAS experiment's sensitivity to supersymmetry after LHC Run 1 — interpreted in the phenomenological MSSM*, JHEP **10** (2015) 134, arXiv:1508.06608 [hep-ex].

[66] T. Han, S. Padhi, and S. Su, *Electroweakinos in the Light of the Higgs Boson*, Phys. Rev. **D88** (2013) 115010, arXiv:1309.5966 [hep-ph].

[67] M. R. Buckley, D. Feld, and D. Goncalves, *Scalar Simplified Models for Dark Matter*, Phys. Rev. D **91** (2015) 015017, arXiv:1410.6497 [hep-ph].

[68] L. R. Evans and P. Bryant, *LHC Machine*, J. Instrum. **3** (2008) S08001. 164 p, This report is an abridged version of the LHC Design Report (CERN-2004-003).

[69] ATLAS Collaboration, *The ATLAS Experiment at the CERN Large Hadron Collider*, Journal of Instrumentation **3** (2008) S08003, http://stacks.iop.org/1748-0221/3/i=08/a=S08003.

[70] S. Myers, *The LEP Collider, from design to approval and commissioning*. John Adams' Lecture. CERN, Geneva, 1991. https://cds.cern.ch/record/226776. Delivered at CERN, 26 Nov 1990.

[71] *ECFA-CERN Workshop on Large Hadron Collider in the LEP tunnel*, Geneva, 1984, http://cds.cern.ch/record/154938.

[72] *LHC Design Report*, http://ab-div.web.cern.ch/ab-div/Publications/LHC-DesignReport.html.

[73] L. Evans and P. Bryant, *LHC Machine*, Journal of Instrumentation **3** (2008) S08001, http://stacks.iop.org/1748-0221/3/i=08/a=S08001.

[74] ALICE Collaboration , *The ALICE experiment at the CERN LHC*, Journal of Instrumentation **3** (2008) S08002, http://stacks.iop.org/1748-0221/3/i=08/a=S08002.

[75] CMS Collaboration, *The CMS experiment at the CERN LHC*, Journal of Instrumentation **3** (2008) S08004, http://stacks.iop.org/1748-0221/3/i=08/a=S08004.

[76] LHCb Collaboration, *The LHCb Detector at the LHC*, Journal of Instrumentation **3** (2008) S08005, http://stacks.iop.org/1748-0221/3/i=08/a=S08005.

[77] ATLAS Collaboration, *Measurements of long-range azimuthal anisotropies and associated Fourier coefficients for pp collisions at* $\sqrt{s} = 5.02$ *and* 13 *TeV and p+Pb collisions at* $\sqrt{s_{\mathrm{NN}}} = 5.02$ *TeV with the ATLAS detector*, arXiv:1609.06213 [hep-ex].

[78] ATLAS Collaboration, *Evidence for light-by-light scattering in heavy-ion collisions with the ATLAS detector at the LHC*, arXiv:1702.01625 [hep-ex].

[79] A. D. Martin, W. J. Stirling, R. S. Thorne, and G. Watt, *Parton distributions for the LHC*, Eur. Phys. J. C **63** (2009) 189–285, arXiv:0901.0002 [hep-ph].

[80] J. Stirling, *PARTON LUMINOSITY AND CROSS SECTION PLOTS*, http://www.hep.ph.ic.ac.uk/~wstirlin/plots/plots.html.

[81] ATLAS Collaboration, *ATLAS: letter of intent for a general-purpose pp experiment at the large hadron collider at CERN*, http://cds.cern.ch/record/291061.

[82] ATLAS Collaboration, *ATLAS detector and physics performance: Technical Design Report, 1*, https://cdsweb.cern.ch/record/391176.

[83] ATLAS Collaboration, *ATLAS detector and physics performance: Technical Design Report, 2*, https://cdsweb.cern.ch/record/391177.

[84] ATLAS Collaboration, *ATLAS Insertable B-Layer Technical Design Report*, Atlas-tdr-19, 2010, https://cds.cern.ch/record/1291633.

[85] ATLAS IBL Collaboration, *Prototype ATLAS IBL modules using the FE-I4A front-end readout chip*, Journal of Instrumentation **7** (2012) P11010, http://stacks.iop.org/1748-0221/7/i=11/a=P11010.

[86] M. Shochet, L. Tompkins, V. Cavaliere, P. Giannetti, A. Annovi, and G. Volpi, *Fast TracKer (FTK) Technical Design Report*, Tech. Rep. CERN-LHCC-2013-007. ATLAS-TDR-021, Jun, 2013. http://cds.cern.ch/record/1552953. ATLAS Fast Tracker Technical Design Report.

[87] ATLAS Collaboration, *Electron efficiency measurements with the ATLAS detector using the 2012 LHC proton–proton collision data*, ATLAS-CONF-2014-032, 2014, https://cds.cern.ch/record/1706245.

[88] ATLAS Collaboration, *Electron and photon energy calibration with the ATLAS detector using data collected in 2015 at $\sqrt{s} = 13$ TeV*, ATL-PHYS-PUB-2016-015, 2016, https://cds.cern.ch/record/2203514.

[89] ATLAS Collaboration, *Electron efficiency measurements with the ATLAS detector using the 2015 LHC proton–proton collision data*, ATLAS-CONF-2016-024, 2016, https://cds.cern.ch/record/2157687.

[90] ATLAS Collaboration,, *Electron and photon reconstruction and performance in ATLAS using a dynamical, topological cell clustering-based approach*, Tech. Rep. ATL-PHYS-PUB-2017-022, CERN, Geneva, Dec, 2017. https://cds.cern.ch/record/2298955.

[91] ATLAS Collaboration, *Muon reconstruction performance of the ATLAS detector in proton–proton collision data at $\sqrt{s} = 13$ TeV*, Eur. Phys. J. C **76** (2016) 292, arXiv:1603.05598 [hep-ex].

[92] ATLAS Collaboration, *Measurement of the muon reconstruction performance of the ATLAS detector using 2011 and 2012 LHC proton–proton collision data*, Eur. Phys. J. C **74** (2014) 3130, arXiv:1407.3935 [hep-ex].

[93] ATLAS Collaboration, *ATLAS Muon Combined Performance with 2017 and 2016 dataset*, MUON-2017-002, https://atlas.web.cern.ch/Atlas/GROUPS/PHYSICS/PLOTS/MUON-2017-002/.

[94] M. Cacciari, G. P. Salam, and G. Soyez, *The Anti-k(t) jet clustering algorithm*, JHEP **04** (2008) 063, arXiv:0802.1189 [hep-ph].

[95] M. Cacciari, G. P. Salam, and G. Soyez, *FastJet user manual*, Eur. Phys. J. C **72** (2012) 1896, arXiv:1111.6097 [hep-ph].

[96] ATLAS Collaboration, *Jet energy measurement and its systematic uncertainty in proton–proton collisions at $\sqrt{s} = 7$ TeV with the ATLAS detector*, Eur. Phys. J. C **75** (2015) 17, arXiv:1406.0076 [hep-ex].

[97] ATLAS Collaboration, *Jet energy scale measurements and their systematic uncertainties in proton–proton collisions at $\sqrt{s} = 13$ TeV with the ATLAS detector*, arXiv:1703.09665 [hep-ex].

[98] ATLAS Collaboration, *Optimisation of the ATLAS b-tagging performance for the 2016 LHC Run*, ATL-PHYS-PUB-2016-012, 2016, https://cds.cern.ch/record/2160731.

[99] ATLAS Collaboration, *Performance of missing transverse momentum reconstruction with the ATLAS detector in the first proton–proton collisions at $\sqrt{s} = 13$ TeV*, ATL-PHYS-PUB-2015-027, 2015, https://cds.cern.ch/record/2037904.

[100] ATLAS Collaboration, *Expected performance of missing transverse momentum reconstruction for the ATLAS detector at $\sqrt{s} = 13$ TeV*, ATL-PHYS-PUB-2015-023, 2015, https://cds.cern.ch/record/2037700.

[101] ATLAS Collaboration, *Search for direct top squark pair production in final states with two leptons in $\sqrt{s} = 13$ TeV pp collisions with the ATLAS detector*, Eur. Phys. J. **C77** (2017) 898, arXiv:1708.03247 [hep-ex].

[102] ATLAS Collaboration, *Search for dark matter produced in association with bottom or top quarks in $\sqrt{s} = 13$ TeV pp collisions with the ATLAS detector*, Eur. Phys. J. **C78** (2018) 18, arXiv:1710.11412 [hep-ex].

[103] C. G. Lester and D. J. Summers, *Measuring masses of semi-invisibly decaying particles pair produced at hadron colliders*, Phys. Lett. B **463** (1999) 99–103, arXiv:hep-ph/9906349.

[104] A. Barr, C. Lester, and P. Stephens, *A variable for measuring masses at hadron colliders when missing energy is expected; m_{T2}: the truth behind the glamour*, J. Phys. G **29** (2003) 2343–2363, arXiv:hep-ph/0304226 [hep-ph].

[105] ATLAS Collaboration, ATLAS Collaboration, *Luminosity determination in pp collisions at $\sqrt{s}$ = 8 TeV using the ATLAS detector at the LHC*, Eur. Phys. J. C **76** (2016) 653, arXiv:1608.03953 [hep-ex].

[106] ATLAS Collaboration, *Topological cell clustering in the ATLAS calorimeters and its performance in LHC Run 1*, arXiv:1603.02934 [hep-ex].

[107] M. Cacciari, G. P. Salam, and G. Soyez, *The anti-k_t jet clustering algorithm*, JHEP **04** (2008) 063, arXiv:0802.1189 [hep-ph].

[108] ATLAS Collaboration, *A measurement of the calorimeter response to single hadrons and determination of the jet energy scale uncertainty using LHC Run-1 pp-collision data with the ATLAS detector*, Eur. Phys. J. C **77** (2017) 26, arXiv:1607.08842 [hep-ex].

[109] ATLAS Collaboration, *Jet Calibration and Systematic Uncertainties for Jets Reconstructed in the ATLAS Detector at $\sqrt{s} = 13$ TeV*, ATL-PHYS-PUB-2015-015, 2015, https://cds.cern.ch/record/2037613.

[110] ATLAS Collaboration, *Tagging and suppression of pileup jets with the ATLAS detector*, ATLAS-CONF-2014-018, 2014, https://cds.cern.ch/record/1700870.

[111] ATLAS Collaboration, *Data-Quality Requirements and Event Cleaning for Jets and Missing Transverse Energy Reconstruction with the ATLAS Detector in Proton–Proton Collisions at a Center-of-Mass Energy of $\sqrt{s} = 7$ TeV*, ATLAS-CONF-2010-038, 2010, https://cds.cern.ch/record/1277678.

[112] ATLAS Collaboration, *Electron efficiency measurements with the ATLAS detector using 2012 LHC proton-proton collision data*, Eur. Phys. J. C **77** (2017) 195, arXiv:1612.01456 [hep-ex].

[113] W. S. Cho, K. Choi, Y. G. Kim, and C. B. Park, *Measuring superparticle masses at hadron collider using the transverse mass kink*, JHEP **02** (2008) 035, arXiv:0711.4526 [hep-ph].

[114] M. Burns, K. Kong, K. T. Matchev, and M. Park, *Using subsystem M_{T2} for complete mass determinations in decay chains with missing energy at hadron colliders*, JHEP **03** (2009) 143, arXiv:0810.5576 [hep-ph].

[115] U. Haisch, P. Pani, and G. Polesello, *Determining the CP nature of spin-0 mediators in associated production of dark matter and $t\bar{t}$ pairs*, JHEP **02** (2017) 131, arXiv:1611.09841 [hep-ph].

[116] ATLAS Collaboration, ATLAS Collaboration, *Search for direct top-squark pair production in final states with two leptons in pp collisions at $\sqrt{s} = 8$ TeV with the ATLAS detector*, JHEP **06** (2014) 124, arXiv:1403.4853 [hep-ex].

[117] ATLAS Collaboration, *Simulation of top-quark production for the ATLAS experiment at $\sqrt{s} = 13$ TeV*, ATL-PHYS-PUB-2016-004, 2016, https://cds.cern.ch/record/2120417.

[118] ATLAS Collaboration, *Monte Carlo Generators for the Production of a W or Z/γ^* Boson in Association with Jets at ATLAS in Run 2*, ATL-PHYS-PUB-2016-003, 2016, https://cds.cern.ch/record/2120133.

[119] ATLAS Collaboration, *Multi-boson simulation for 13 TeV ATLAS analyses*, ATL-PHYS-PUB-2016-002, 2016, https://cds.cern.ch/record/2119986.

[120] ATLAS Collaboration, *Modelling of the $t\bar{t}H$ and $t\bar{t}V (V = W, Z)$ processes for $\sqrt{s} = 13$ TeV ATLAS analyses*, ATL-PHYS-PUB-2016-005, 2016, https://cds.cern.ch/record/2120826.

[121] S. Alioli, P. Nason, C. Oleari, and E. Re, *A general framework for implementing NLO calculations in shower Monte Carlo programs: the POWHEG BOX*, JHEP **06** (2010) 043, arXiv:1002.2581 [hep-ph].

[122] T. Sjöstrand, S. Mrenna, and P. Z. Skands, *PYTHIA 6.4 physics and manual*, JHEP **05** (2006) 026, arXiv:hep-ph/0603175.

[123] T. Gleisberg, S. Hoeche, F. Krauss, M. Schonherr, S. Schumann, et al., *Event generation with SHERPA 1.1*, JHEP **0902** (2009) 007, arXiv:0811.4622 [hep-ph].

[124] D. J. Lange, *The EvtGen particle decay simulation package*, Nucl. Instrum. Meth. A **462** (2001) 152.

[125] J. Alwall, R. Frederix, S. Frixione, V. Hirschi, F. Maltoni, O. Mattelaer, H. S. Shao, T. Stelzer, P. Torrielli, and M. Zaro, *The automated computation of tree-level and next-to-leading order differential cross sections, and their matching to parton shower simulations*, JHEP **07** (2014) 079, arXiv:1405.0301 [hep-ph].

[126] T. Sjöstrand, S. Mrenna, and P. Z. Skands, *A brief introduction to PYTHIA 8.1*, Comput. Phys. Commun. **178** (2008) 852–867, arXiv:0710.3820 [hep-ph].

[127] H.-L. Lai, M. Guzzi, J. Huston, Z. Li, P. M. Nadolsky, J. Pumplin, and C. P. Yuan, *New parton distributions for collider physics*, Phys. Rev. D **82** (2010) 074024, arXiv:1007.2241 [hep-ph].

[128] ATLAS Collaboration, *ATLAS Pythia8 tunes to 7 TeV data*, ATL-PHYS-PUB-2014-021, 2014, https://cds.cern.ch/record/1966419.

[129] O. Mattelaer and E. Vryonidou, *Dark matter production through loop-induced processes at the LHC: the s-channel mediator case*, Eur. Phys. J. C **75** (2015) 436, arXiv:1508.00564 [hep-ph].

[130] M. Backovic, M. Krämer, F. Maltoni, A. Martini, K. Mawatari, and M. Pellen, *Higher-order QCD predictions for dark matter production at the LHC in simplified models with s-channel mediators*, Eur. Phys. J. C **75** (2015) 482, arXiv:1508.05327 [hep-ph].

[131] S. Catani, L. Cieri, G. Ferrera, D. de Florian, and M. Grazzini, *Vector boson production at hadron colliders: a fully exclusive QCD calculation at NNLO*, Phys. Rev. Lett. **103** (2009) 082001, arXiv:0903.2120 [hep-ph].

[132] M. Czakon, P. Fiedler, and A. Mitov, *Total Top-Quark Pair-Production Cross Section at Hadron Colliders Through $O(\alpha_S^4)$*, Phys. Rev. Lett. **110** (2013) 252004, arXiv:1303.6254 [hep-ph].

[133] M. Czakon and A. Mitov, *NNLO corrections to top pair production at hadron colliders: the quark-gluon reaction*, JHEP **01** (2013) 080, arXiv:1210.6832 [hep-ph].

[134] M. Czakon and A. Mitov, *NNLO corrections to top-pair production at hadron colliders: the all-fermionic scattering channels*, JHEP **12** (2012) 054, arXiv:1207.0236 [hep-ph].

[135] P. Bärnreuther, M. Czakon, and A. Mitov, *Percent-Level-Precision Physics at the Tevatron: Next-to-Next-to-Leading Order QCD Corrections to $q\bar{q} \to t\bar{t} + X$*, Phys. Rev. Lett. **109** (2012) 132001, arXiv:1204.5201 [hep-ph].

[136] M. Cacciari, M. Czakon, M. Mangano, A. Mitov, and P. Nason, *Top-pair production at hadron colliders with next-to-next-to-leading logarithmic soft-gluon resummation*, Phys. Lett. B **710** (2012) 612–622, arXiv:1111.5869 [hep-ph].

[137] M. Czakon and A. Mitov, *Top++: a program for the calculation of the top-pair cross-section at hadron colliders*, Comput. Phys. Commun. **185** (2014) 2930, arXiv:1112.5675 [hep-ph].

[138] P. Z. Skands, *Tuning Monte Carlo generators: the Perugia tunes*, Phys. Rev. D **82** (2010) 074018, arXiv:1005.3457 [hep-ph].

[139] N. Kidonakis, *Two-loop soft anomalous dimensions for single top quark associated production with a W- or H-*, Phys. Rev. D **82** (2010) 054018, arXiv:1005.4451 [hep-ph].

[140] G. Corcella et al., *HERWIG 6: an event generator for hadron emission reactions with interfering gluons (including supersymmetric processes)*, JHEP **01** (2001) 010, arXiv:hep-ph/0011363.

[141] LHC Higgs Cross Section Working Group, *Handbook of LHC Higgs Cross Sections: 2. Differential Distributions*, CERN-2012-002 (CERN, Geneva, 2012), arXiv:1201.3084 [hep-ph].

[142] J. Pumplin et al., *New generation of parton distributions with uncertainties from global QCD analysis*, JHEP **07** (2002) 012, arXiv:hep-ph/0201195.

[143] L. Lönnblad and S. Prestel, *Matching tree-level matrix elements with interleaved showers*, JHEP **03** (2012) 019, arXiv:1109.4829 [hep-ph].

[144] W. Beenakker, M. Kramer, T. Plehn, M. Spira, and P. M. Zerwas, *Stop production at hadron colliders*, Nucl. Phys. B **515** (1998) 3–14, arXiv:hep-ph/9710451.

[145] W. Beenakker, S. Brensing, M. Kramer, A. Kulesza, E. Laenen, and I. Niessen, *Supersymmetric top and bottom squark production at hadron colliders*, JHEP **08** (2010) 098, arXiv:1006.4771 [hep-ph].

[146] B. C. Allanach, *SOFTSUSY: a program for calculating supersymmetric spectra*, Comput. Phys. Commun. **143** (2002) 305–331, arXiv:hep-ph/0104145.

[147] W. Porod, *SPheno, a program for calculating supersymmetric spectra, SUSY particle decays and SUSY particle production at e+ e- colliders*, Comput. Phys. Commun. **153** (2003) 275–315, arXiv:hep-ph/0301101.

[148] W. Porod and F. Staub, *SPheno 3.1: Extensions including flavour, CP-phases and models beyond the MSSM*, Comput. Phys. Commun. **183** (2012) 2458–2469, arXiv:1104.1573 [hep-ph].

[149] A. Djouadi, J.-L. Kneur, and G. Moultaka, *SuSpect: A Fortran code for the supersymmetric and Higgs particle spectrum in the MSSM*, Comput. Phys. Commun. **176** (2007) 426–455, arXiv:hep-ph/0211331.

[150] A. Djouadi, M. M. Muhlleitner, and M. Spira, *Decays of supersymmetric particles: the program SUSY-HIT (SUspect-SdecaY-Hdecay-InTerface)*, Acta Phys. Polon. B **38** (2007) 635–644, arXiv:hep-ph/0609292.

[151] D. Abercrombie et al., *Dark Matter Benchmark Models for Early LHC Run-2 Searches: Report of the ATLAS/CMS Dark Matter Forum*, arXiv:1507.00966 [hep-ex].

[152] V. Hirschi and O. Mattelaer, *Automated event generation for loop-induced processes*, JHEP **10** (2015) 146, arXiv:1507.00020 [hep-ph].

[153] ATLAS Collaboration, *Summary of ATLAS Pythia 8 tunes*, ATLAS-PHYS-PUB-2012-003, 2012, https://cdsweb.cern.ch/record/1474107.

[154] ATLAS Collaboration, *The ATLAS Simulation Infrastructure*, Eur. Phys. J. C **70** (2010) 823, arXiv:1005.4568 [hep-ex].

[155] GEANT4 Collaboration, S. Agostinelli et al., *GEANT4: a simulation toolkit*, Nucl. Instrum. Meth. A **506** (2003) 250–303.

[156] ATLAS Collaboration, *The simulation principle and performance of the ATLAS fast calorimeter simulation FastCaloSim*, ATL-PHYS-PUB-2010-013, 2010, https://cds.cern.ch/record/1300517.

[157] G. Cowan, K. Cranmer, E. Gross, and O. Vitells, *Asymptotic formulae for likelihood-based tests of new physics*, Eur. Phys. J. **C71** (2011) 1554, arXiv:1007.1727 [physics.data-an], [Erratum: Eur. Phys. J.C73,2501(2013)].

[158] ATLAS Collaboration, *Measurement of the top quark-pair production cross section with ATLAS in pp collisions at $\sqrt{s} = 7$ TeV*, Eur. Phys. J. C **71** (2011) 1577, arXiv:1012.1792 [hep-ex].

[159] ATLAS Collaboration, *Measurement of the top quark pair production cross section in pp collisions at $\sqrt{s} = 7$ TeV in dilepton final states with ATLAS*, Phys. Lett. B **707** (2012) 459, arXiv:1108.3699 [hep-ex].

[160] ATLAS Collaboration, *Calibration of b-tagging using dileptonic top pair events in a combinatorial likelihood approach with the ATLAS experiment*, ATLAS-CONF-2014-004, 2014, https://cds.cern.ch/record/1664335.

[161] ATLAS Collaboration, *Calibration of the performance of b-tagging for c and light-flavour jets in the 2012 ATLAS data*, ATLAS-CONF-2014-046, 2014, https://cds.cern.ch/record/1741020.

[162] ATLAS Collaboration, *Multi-Boson Simulation for 13 TeV ATLAS Analyses*, ATL-PHYS-PUB-2016-002, 2016, https://cds.cern.ch/record/2119986.

[163] ATLAS Collaboration, *Modelling of the $t\bar{t}H$ and $t\bar{t}V$ $(V = W, Z)$ processes for $\sqrt{s} = 13$ TeV ATLAS analyses*, ATL-PHYS-PUB-2015-022, 2016, https://cds.cern.ch/record/2120826.

[164] P. Kant, O. M. Kind, T. Kintscher, T. Lohse, T. Martini, S. Mölbitz, P. Rieck, and P. Uwer, *HATHOR for single top-quark production: Updated predictions and uncertainty estimates for single top-quark production in hadronic collisions*, Comput. Phys. Commun. **191** (2015) 74–89, arXiv:1406.4403 [hep-ph].

[165] A. L. Read, *Presentation of search results: the CL_s technique*, J. Phys. G **28** (2002) 2693–2704.

[166] A. Boveia et al., *Recommendations on presenting LHC searches for missing transverse energy signals using simplified s-channel models of dark matter*, arXiv:1603.04156 [hep-ex].

[167] LUX Collaboration Collaboration, D. Akerib et al., *First results from the LUX dark matter experiment at the Sanford Underground Research Facility*, Phys. Rev. Lett. **112** (2014) 091303, arXiv:1310.8214 [astro-ph.CO].

[168] PandaX-II Collaboration, PandaX-II Collaboration, *Dark Matter Results from First 98.7 Days of Data from the PandaX-II Experiment*, Phys. Rev. Lett. **117** (2016) 121303, arXiv:1607.07400 [hep-ex].

[169] XENON Collaboration, XENON Collaboration, *First Dark Matter Search Results from the XENON1T Experiment*, arXiv:1705.06655 [astro-ph.CO].

[170] SuperCDMS Collaboration, SuperCDMS Collaboration, *New Results from the Search for Low-Mass Weakly Interacting Massive Particles with the CDMS Low Ionization Threshold Experiment*, Phys. Rev. Lett. **116** (2016) 071301, arXiv:1509.02448 [astro-ph.CO].

[171] CRESST Collaboration, CRESST Collaboration, *Results on light dark matter particles with a low-threshold CRESST-II detector*, Eur. Phys. J. C **76** (2016) 25, arXiv:1509.01515 [astro-ph.CO].

[172] ATLAS Collaboration, *Technical Design Report for the ATLAS Inner Tracker Strip Detector*, CERN-LHCC-2017-005, ATLAS-TDR-025 (2017), https://cds.cern.ch/record/2257755.

[173] ATLAS Collaboration, *ATLAS page for the Pixel TDR plots*, ITK-2018-001, https://atlas.web.cern.ch/Atlas/GROUPS/PHYSICS/PLOTS/ITK-2018-001/.

[174] ATLAS Collaboration, *Technical Design Report for the ATLAS ITk Pixel Detector*, Tech. Rep. ATL-COM-ITK-2017-073, CERN, Geneva, Dec, 2017. https://cds.cern.ch/record/2296611. This is the second and final circulation to the ATLAS collaboration.

[175] A. Ferrari, P. R. Sala, A. Fassò, and J. Ranft, *FLUKA: A multi-particle transport code (program version 2005)*. CERN Yellow Reports: Monographs. CERN, Geneva, 2005. https://cds.cern.ch/record/898301.

[176] I. Peric, *A novel monolithic pixelated particle detector implemented in high-voltage CMOS technology*, Nucl. Instr. Meth. Phys. Res. A **582** (2007) 876 – 885, VERTEX 2006.

[177] W. Snoeys, G. A. Rinella, H. Hillemanns, T. Kugathasan, M. Mager, L. Musa, P. Riedler, F. Reidt, J. V. Hoorne, A. Fenigstein, and T. Leitner, *A process modification for CMOS monolithic active pixel sensors for enhanced depletion, timing performance and radiation tolerance*, Nucl. Instr. Meth. Phys. Res. A **871** (2017) 90 – 96, http://www.sciencedirect.com/science/article/pii/S016890021730791X.

[178] M. Garcia-Sciveres, D. Arutinov, M. Barbero, R. Beccherle, S. Dube, D. Elledge, J. Fleury, D. Fougeron, F. Gensolen, D. Gnani, V. Gromov, T. Hemperek, M. Karagounis, R. Kluit, A. Kruth, A. Mekkaoui, M. Menouni, and J.-D. Schipper, *The FE-I4 pixel readout integrated circuit*, Nucl. Instr. Meth. Phys. Res. A **636** (2011) S155 – S159, http://www.sciencedirect.com/science/article/pii/S0168900210009551, 7th International ""Hiroshima"" Symposium on the Development and Application of Semiconductor Tracking Detectors.

[179] M. Benoit, S. Braccini, G. Casse, H. Chen, K. Chen, F. A. Di Bello, D. Ferrere, T. Golling, S. Gonzalez-Sevilla, G. Iacobucci, M. Kiehn, F. Lanni, H. Liu, L. Meng, C. Merlassino, A. Miucci, D. Muenstermann, M. Nessi, H. Okawa, I. Peric, M. Rimoldi, B. Ristic, M. V. Barrero Pinto, J. Vossebeld, M. Weber, T. Weston, W. Wu, L. Xu, and E. Zaffaroni, *Testbeam results of irradiated ams H18 HV-CMOS pixel sensor prototypes*, arXiv:1611.02669 [physics.ins-det].

[180] L. Snoj, G. Zerovnik, and A. Trkov, *Computational analysis of irradiation facilities at the JSI TRIGA reactor*, Applied Radiation and Isotopes **70** (2012) 483 – 488, http://www.sciencedirect.com/science/article/pii/S0969804311005963.

[181] S. Braccini, *The new bern PET cyclotron, its research beam line, and the development of an innovative beam monitor detector*, in *American Institute of Physics Conference Series*, F. D. McDaniel, B. L. Doyle, G. A. Glass, and Y. Wang, eds., pp. , 144–150. Apr., 2013.

[182] S. Braccini, *Particle Accelerators and Detectors for medical Diagnostics and Therapy*, arXiv:1601.06820 [physics.med-ph], https://inspirehep.net/record/1417027/files/arXiv:1601.06820.pdf.

[183] J. Anders, S. Braccini, T. Carzaniga, A. Ereditato, A. Fehr, F. Meloni, C. Merlassino, A. Miucci, M. Rimoldi, and M. Weber, *A facility for radiation hardness studies based on the Bern medical cyclotron*, arXiv:1803.01939 [physics.ins-det].

[184] ATLAS Collaboration,, *Irradiation induced effects in the FE-I4 front-end chip of the ATLAS IBL detector*, pp. , 1–4. 2016. arXiv:1611.00803 [physics.ins-det].

[185] M. Auger, S. Braccini, A. Ereditato, K. P. Nesteruk, and P. Scampoli, *Low current performance of the Bern medical cyclotron down to the pA range*, Measurement Science and Technology **26** (2015) 094006, http://stacks.iop.org/0957-0233/26/i=9/a=094006.

[186] K. P. Nesteruk, M. Auger, S. Braccini, T. S. Carzaniga, A. Ereditato, and P. Scampoli, *A system for online beam emittance measurements and proton beam characterization*, arXiv:1705.07486 [physics.acc-ph].

[187] M. Benoit, J. B. D. Mendizabal, F. D. Bello, D. Ferrere, T. Golling, S. Gonzalez-Sevilla, G. Iacobucci, M. Kocian, D. Muenstermann, B. Ristic, and A. Sciuccati, *The FE-I4 telescope for particle tracking in testbeam experiments*, JINST **11** (2016) P07003, http://stacks.iop.org/1748-0221/11/i=07/a=P07003.

[188] G. McGoldrick, M. Cerv, and A. GoriÅ¡ek, *Synchronized analysis of testbeam data with the Judith software*,.

[189] J. Baudot, G. Bertolone, A. Brogna, G. Claus, C. Colledani, Y. Degerli, R. De Masi, A. Dorokhov, G. Doziere, W. Dulinski, M. Gelin, M. Goffe, A. Himmi, F. Guilloux, C. Hu Guo, K. Jaaskelainen, M. Koziel, F. Morel, F. Orsini, and M. Winter, *First test results Of MIMOSA-26, a fast CMOS sensor with integrated zero suppression and digitized output*, 12, 2009.

[190] M. Benoit, A. Lounis, and N. Dinu, *Simulation of Radiation Damage Effects on Planar Pixel Guard Ring Structure for ATLAS Inner Detector Upgrade*, IEEE Transactions on Nuclear Science **56** (2009) 3236–3243.

[191] M. Rimoldi, *CMOS pixel sensor development for the ATLAS experiment at the High Luminosity-LHC*, Journal of Instrumentation **12** (2017) C12014, http://stacks.iop.org/1748-0221/12/i=12/a=C12014.

[192] M. Benoit, J. Bilbao de Mendizabal, G. Casse, H. Chen, K. Chen, F. A. Di Bello, D. Ferrere, T. Golling, S. Gonzalez-Sevilla, G. Iacobucci, F. Lanni, H. Liu, F. Meloni, L. Meng, A. Miucci, D. Muenstermann, M. Nessi, I. Perić, M. Rimoldi, B. Ristic, M. V. Barrero Pinto, J. Vossebeld, M. Weber, W. Wu, and L. Xu, *Results of the 2015 testbeam of a 180 nm AMS High-Voltage CMOS sensor prototype*, JINST **11** (2016) P07019, arXiv:1603.07798 [physics.ins-det].

[193] ATLAS Collaboration, *Prospects for a search for direct pair production of top squarks in scenarios with compressed mass spectra at the high luminosity LHC with the ATLAS Detector*, ATL-PHYS-PUB-2016-022, 2016, https://cds.cern.ch/record/2220904.

[194] ATLAS Collaboration, *Expected performance for an upgraded ATLAS detector at High-Luminosity LHC*, ATL-PHYS-PUB-2016-026, 2016, https://cds.cern.ch/record/2223839.

[195] ATLAS Collaboration, *Expected Performance of the ATLAS Inner Tracker at the High-Luminosity LHC*, ATL-PHYS-PUB-2016-025, 2016, https://cds.cern.ch/record/2222304.

[196] S. Frixione, P. Nason, and G. Ridolfi, *A Positive-weight next-to-leading-order Monte Carlo for heavy flavour hadroproduction*, JHEP **09** (2007) 126, arXiv:0707.3088 [hep-ph].

[197] P. Nason, *A New method for combining NLO QCD with shower Monte Carlo algorithms*, JHEP **11** (2004) 040, arXiv:hep-ph/0409146 [hep-ph].

[198] S. Frixione, P. Nason, and C. Oleari, *Matching NLO QCD computations with Parton Shower simulations: the POWHEG method*, JHEP **11** (2007) 070, arXiv:0709.2092 [hep-ph].

[199] R. D. Ball et al., *Parton distributions with LHC data*, Nucl. Phys. B **867** (2013) 244–289, arXiv:1207.1303 [hep-ph].

[200] M. Krämer, A. Kulesza, R. van der Leeuw, M. Mangano, S. Padhi, et al., *Supersymmetry production cross sections in pp collisions at* $\sqrt{s} = 7$ *TeV*,, arXiv:1206.2892 [hep-ph].

[201] M. Bauer, U. Haisch, and F. Kahlhoefer, *Simplified dark matter models with two Higgs doublets: I. Pseudoscalar mediators*, JHEP **05** (2017) 138, arXiv:1701.07427 [hep-ph].

[202] J. E. Kim, *Light pseudoscalars, particle physics and cosmology*, Physics Reports **150** (1987) 1 – 177, http://www.sciencedirect.com/science/article/pii/0370157387900172.

[203] P. Brax, C. Burrage, C. Englert, and M. Spannowsky, *LHC Signatures Of Scalar Dark Energy*, Phys. Rev. **D94** (2016) 084054, arXiv:1604.04299 [hep-ph].

Acknowledgements

I thank Prof. Dr. Antonio Ereditato for giving me the opportunity to do the PhD studies at the Albert Einstein Center for Fundamental Physics at the University of Bern. I thank Prof. Dr. Monica D'Onofrio for accepting to be the external referee and co-examiner. I also thank Dr. Thomas Becher for being the examiner of this thesis.
A special thank to Prof. Dr. Michele Weber for the review of this thesis and for the help, support and discussion we had on physics. I especially thank also Federico for closely following me day by day during the whole period. A big thank to Antonello for supporting me and teach me how to stay in the lab.
I would like to thank also all my colleagues that I met in Bern, Stefania, Maria Elena, Geoffrey, Gabriele, Tom, Yves, Claudia, Armin, Dean, John, Gianfranco, Saverio. Thank you guys for the help, the beers, the chats, and everything else we shared. Special thank to Marcella and Ciro.
Thank all of my physics friends, especially to Lidia, Pietro, Sabba, Lucia, Marco, Semola, Marta and Silvia for always been available. Big thank to my old friends, Bazu, Kemyo, Crive, Giudy, Chiara, Paolo, Jonny.
Finally, special thank to all my family for always believed and supported me.

Declaration of consent

on the basis of Article 28 para. 2 of the RSL05 phil.-nat.

Name/First Name: Marco Rimoldi

Matriculation Number: 14-139-133

Study program: Doktorat PHIL NAT

Bachelor ☐ Master ☐ Dissertation ☑

Title of the thesis: Search for physics beyond the Standard Model in di-lepton final state with the ATLAS experiment

Supervisor: Prof. Dr. Antonio Ereditato, Prof. Dr. Michele Weber

I declare herewith that this thesis is my own work and that I have not used any sources other than those stated. I have indicated the adoption of quotations as well as thoughts taken from other authors as such in the thesis. I am aware that the Senate pursuant to Article 36 para. 1 lit. r of the University Act of 5 September, 1996 is authorised to revoke the title awarded on the basis of this thesis. I allow herewith inspection in this thesis.

Bern, 25/06/2018

Place/Date

Signature

Curriculum Vitae

Rimoldi Marco

Personal Information

Name	Marco Rimoldi
Date & Place of Birth	August 27^{th} 1988, Segrate (MI), Italy.
Citizenship	Italian
Address	Waldheimstrasse 46, 3012 , Bern (CH), Switzerland
E-mail	marcorimo88@gmail.com
Telephone	+41 766720078

Education

January 2015 - July 2018 Ph.D in **Particle Physics** at the AEC/LHEP at the Universität Bern, Switzerland working in the **ATLAS Bern Group**.
Advisors: Prof. Dr. Antonio Ereditato, Prof. Dr. Michele Weber.

September 2011 - April 2014 Master degree in **Particle Physics**, Università degli Studi di Milano, Milano (Italy)
"Higgs mass measurement in the di-photon decay channel with the ATLAS experiment" (https://cds.cern.ch/record/1711780)
Advisors: Prof. Leonardo Carminati and Dr. Ruggero Turra.

September 2007 - July 2011 Bachelor's degree in **Physics**, Università degli Studi di Milano, Milano (Italy).
"Study of silicon pixel detectors in 3D technology for ATLAS"
Advisors: Prof. Attilio Andreazza and Dr. Chiara Meroni.

September 2002- June 2007 **High School Diploma**
Liceo Scientifico "Alexis Carrel", Milano (Italy).

Summary of research activities

March 2018- Present **Search for heavy top squark $\tilde{t}_1$ and Dark Matter particles with the ATLAS Detector using the Run 2**
I am currently involved in the search for third generation squarks in final states with two leptons and dark matter particles in association with heavy flavour quarks using the full Run 2 dataset.

December 2017- Present **Prospect for DM search at High Luminosity LHC**
I evaluated the prospects for a search for associated production of dark matter and top quark pairs at the High Luminosity LHC

September 2016 - January 2018 **Search for heavy top squark $\tilde{t}_1$ and Dark Matter particles with the ATLAS Detector using the 2015 and 2016 data:**
I was the main contributor to the search for third generation squarks in final states with two leptons from the conceptual design of the analysis to the approval, interpretation and publication of the results. I also contributed to the development of the event selections and results interpretation of a search for dark matter particles in association with heavy flavour quarks. Both results are based on the data collected during 2015 and 2016 by the ATLAS experiment.
[*Eur. Phys. J. C77 (2017) 898*, *Eur. Phys. J. C 78 (2018) 18*]

April 2016 - October 2016 **Prospect for top squarks search at High Luminosity LHC in scenarios with compressed mass spectra**
I investigated the prospects for a search for direct pair production of top squarks in scenarios with compressed mass spectra at the High Luminosity LHC. I was the main developer of this analysis and responsible of the generation of MC samples, optimisation of the events selection and interpretation of the results.
[*ATL-PHYS-PUB-2016-022*]

January 2016 - May 2016 **Development of a new irradiation facility for silicon sensors**
I worked in the development of a new irradiation facility at the Bern cyclotron. I developed the first beam current monitor crucial for measuring the dose delivered to the device under irradiation and I participated to the following irradiation campaign on silicon sensor.
[*arXiv:1803.01939*, *ATL-INDET-PUB-2017-001*]

January 2015 - May 2016 **Development of monolithic radiation hard pixel sensor technology**
I worked on the development of silicon pixel sensors in high-voltage CMOS technology. In particular, I focused on the sensor characterisation with lab measurements of CCPDv4 and H35 Demonstrator prototypes and the following preparation of a test beam campaign performed at the CERN SPS. I was main developer of reconstruction and analysis of the test beam data. The sensors were characterised both before and after proton and neutron irradiation. My work has resulted in this two peer reviewed publications
[*JINST 11 (2016) no.07, P07019*, *JINST 13 (2018) no.02, P02011*]

September 2011 - April 2014 **Higgs mass measurement in the di-photon decay channel**
As part of my master thesis project I contributed to the measurement of the Higgs boson mass in the di-photon decay channel. In particular, I studied and assess the photon energy systematic uncertainties which have been used in the publication of the mass measurement.
[*Phys.Rev.D90,052004*]

Publications

I am author in the ATLAS Collaboration with more than two hundred published papers *[INSPIRE record]*. Listed below, you can find the most important public documents (papers and proceedings and public documents) to which I gave major contributions.

October 2017 **"Search for the production of dark matter particles in association with heavy flavour quarks in pp collisions at $\sqrt{s} = 13$ TeV with the ATLAS detector"**,
The ATLAS Collaboration, *Eur. Phys. J. C 78 (2018) 18*

October 2017 **"CMOS pixel sensor development for the ATLAS experiment at the High Luminosity-LHC"**, M. Rimoldi on behalf of the ATLAS Collaboration, Proceedings for Position Sensitive Detector 11 ($PSD11$), 3rd - 8th September 2017, *Journal of Instrumentation 12 12 C12014*

August 2017 **"Search for direct top squark pair production in final states with two leptons in $\sqrt{s} = 13$ TeV pp collisions with the ATLAS detector"**,
The ATLAS Collaboration, *Eur. Phys. J. C77 (2017) 898*.

November 2016 **"Testbeam results of irradiated AMS H18 HV-CMOS pixel sensor prototypes"**,
M.Benoit et al., *JINST 13 (2018) no.02, P02011*

October 2016 **"Prospects for a search for direct pair production of top squarks in scenarios with compressed mass spectra at the high luminosity LHC with the ATLAS Detector"**,
The ATLAS Collaboration, ATL-PHYS-PUB-2016-022.

March 2016 **"Results of the 2015 testbeam of a 180 nm AMS High-Voltage CMOS sensor prototype"**,
M.Benoit et al., *JINST 11 (2016) no.07, P07019*

June 2014 **"Measurement of the Higgs boson mass from the $H \to \gamma\gamma$ and $H \to ZZ^* \to 4l$ channels with the ATLAS detector using 25 fb^{-1} of pp collision data"**,
The ATLAS Collaboration, *Phys.Rev.D90,052004*.

Communications at Conferences

June 2018 **"SUSY searches at the HL-LHC"** on behalf of the ATLAS and CMS Collaborations, HLHE2018, HL/HE-LHC Workshop, June 2018, CERN.

April 2018 **"Search for dark matter produced in association with bottom or top quarks in $\sqrt{s} = 13\ TeV$ pp collisions with the ATLAS detector"**,
Dark Matter @ LHC 2018 ($DM@LHC$), April 2018, Heidelberg.

September 2017 **"CMOS pixel development for the ATLAS experiment at HL-LHC"**,
Position Sensitive Detector 11 ($PSD11$), 3rd - 8th September 2017, Milton Keynes.

August 2017 **"Search for direct top squark pair production in final states with two leptons in $\sqrt{s} = 13\ TeV$ pp collisions with the ATLAS detector"**,
Joint Annual Meeting of SPS and OPG, Geneve.

September 2015	**"Development of HV-CMOS Pixel Sensors for the Phase-2 ATLAS upgrades"**, Joint Annual Meeting of OPG, SPG, OGAA und SGAA in Vienna, Austria.
September 2014	**"Misura della massa del Bosone di Higgs nel canale di decadimento in due fotoni con l'esperimento ATLAS."**, 100° Congresso Nazionale of the Societa Italiana di Fisica (SIF), Pisa, Italy.

Schools

February 2017	**CHIPP Winter School of Particle Physics 2017**, Sorenberg, Switzerland.
August 2016	**CERN-Fermilab HCP Summer School 2016**, Fermilab,US.
July 2012	**HASCO Summer School 2012**, Goettingen, Germany.

Teaching Experience

2015 - 2018	During my PhD, I was in charge for 3 semesters of the assistance of biology students in the General Physics course. For one semester I was assistant in the Particle Physics Master course for Physics Master students. For two semester I was assistant in the practikum Physics course for biology and medics students
2015-2018	I was in charge of the preparation and student assistance of the *International Masterclass* in Bern.
2007 - 2014	Private Math and Physics lessons to high school students.

Last updated: 22^{th} June 2018